

Heat and Mass Transfer Enhancement by Carbon Nanotubes and Supersonically-Blown Nanofibers

BY

SUMIT SINHA RAY

B.Met.E., Jadavpur University, Kolkata, India, 2011

THESIS

Submitted as a partial fulfillment of the requirements
for the degree of Doctor of Philosophy in Mechanical Engineering
in the Graduate College of the
University of Illinois at Chicago, 2016

Chicago, Illinois

Defense Committee

Alexander L. Yarin,	Chair and Advisor
W.J. Minkowycz,	Mechanical and Industrial Engineering
Jeremiah Abiade,	Mechanical and Industrial Engineering
Kumar Natesaiyer,	United States Gypsum Corporation
Alan Nicholls,	Research Resource Center, UIC

I dedicate this thesis to my mother Mrs. Manashi Sinha Ray, my father Mr. Sukumar Sinha Ray, my brother Dr. Suman Sinha Ray and my friend late Mr. Pritam Banerjee, without whose love and support it would never have been accomplished.

ACKNOWLEDGEMENTS

First and foremost I would like to express my gratitude to my advisor Professor Alexander Yarin for being my mentor. I would like to thank him from the core of my heart for all the counsel he has provided to me during my research to shape my thoughts and let me grow as a researcher. It has been a great honor for me to work with him as his PhD student. I will always be grateful for the ideas, directions and support he has provided to me and I hope to enjoy the fruits of those forever. His never ending aspiration for successful research has often enthralled me and inspired my work even amidst my turbulent times. His liveliness in teaching with loads of examples from past till date has amazed me. I am blessed to work with Professor Yarin and will always be thankful to him for allowing me to engage in research across various fields and encouraging me to think freely and impart those ideas. Without his consistent help and support, this dissertation would not have been possible.

I would like to thank my thesis committee members- Professor Alexander Yarin, Professor W. J. Minkowycz, Professor Jeremiah Abiade, Dr. Kumar Natesaiyer and Dr. Alan Nicholls, for their suggestions, support and assistance, which helped me in achieving my goals. Most importantly I would like to thank my parents who encouraged me to pursue research and extended their utmost support when I needed it most. I am blessed to have them in my life and it is them who will always have the most influence in my life, my decisions and my love for research. I will always be indebted to their undying love and sacrifice for my growth. At this occasion I would like to extend my special gratitude to my brother and co-researcher Dr. Suman Sinha Ray, who has always been like a mentor to me and has always helped me in my fruitful research experience. I would also like to thank my teacher late Mr. Dulal Chandra Bhattacharya who had been my source of inspiration from my childhood and

had always helped me to think independently. I would like to thank Professor Subir Paul from Jadavpur University who helped me during my first independent research during my undergraduate studies and extended his support. I would also like to thank Dr. Alan Nicholls, and Dr. Kebin Low for helping me with characterizations and assisting me with the analysis.

I will forever be thankful to all my lab mates whose help and support at all stages of this journey have been instrumental in completion of my PhD. I am grateful to my seniors and co-authors of my publications, Dr. Suman Sinha Ray and Dr. Rakesh Prasad Sahu. In addition, I would also like to thank all the undergraduate students: Hari Sriram, Nicholas McCarteny, Christopher Staszal, Mustafa Wahid, Chris Kim and Barak Stoltz, who helped me immensely in my experimental work. I would specially like to express my gratitude to Chris Kim and Barak Stoltz for their support during the time when I was hospitalized and temporarily incapacitated. I wish to express my sincere thanks to David Mecha, Eric Schmidt, John Grega, Jakub Walkosz, and Thomas Bruzan from the Scientific Instrument Shop for their significant contributions in making my experiments successful. I would like to express my utmost gratitude to my physician Dr. Mark Hutchinson and my physiotherapist Joshua McFarren who helped me to recover from my dreadful accident. Also last but not the least, I would like to thank all my friends, late Pritam, Srijit, Prithwish, Debjani, Suryani, Sudeshna, Anambar, Barak and all my well-wishers who have been a constant source of support and will always be.

S.S.R.

Some parts of this thesis have been published in peer-reviewed journals. Sections 2.1 and 3.1, and 4.3 of Chapter 4, were partially published in Journal of Material Chemistry C of the Royal Society of Chemistry (Sinha-Ray, Suman, Lee, M.W., Sinha-Ray, Sumit, An, S., Pourdeyhimi, B., Yoon, S.S. and Yarin, A.L. (2013), Supersonic nanoblowing: a new ultra-stiff phase of nylon 6 in 20–50 nm confinement, 1, 3491-3498). Sections 2.2, 3.2, and Chapter 5 were published in Journal of Membrane Science of ELSEVIER (Sinha-Ray, Sumit, Sinha-Ray, Suman, Yarin, A.L. and Pourdeyhimi, B. (2015a), Application of solution-blown 20–50 nm nanofibers in filtration of nanoparticles: The efficient van der Waals collectors, Journal of Membrane Science, 482, 132-150). Sections 2.3, 3.3, subsection 6.2.3 and subsection 6.3.1 of Chapter 6 were partially published in International Journal of Heat and Mass Transfer of ELSEVIER (Sahu, R.P., Sinha-Ray, Sumit, Sinha-Ray, Suman and Yarin, A.L., Pool Boiling of Novec 7300 and Self-Rewetting Fluids on Electrically-Assisted Supersonically Solution-Blown, Copper-Plated Nanofibers (2016), International Journal of Heat and Mass Transfer, 95, 83-93) and sections 2.3, 3.3 and the rest of Chapter 6 were partially published in International Journal of Heat and Mass Transfer of ELSEVIER (Sinha-Ray, Sumit, Zhang, W., Sinha-Ray, Suman, Sahu, R.P. and Yarin A.L. (2017), Pool boiling of Novec 7300 and DI water on nano-textured heater covered with supersonically blown or electrospun polymer nanofibers, International Journal of Heat and Mass Transfer, <http://dx.doi.org/10.1016/j.ijheatmasstransfer.2016.08.101>). Sections 2.4, 3.4 and Chapter 7 were published in Lab on Chip of the Royal Society of Chemistry (Sinha-Ray, Sumit, Sinha-Ray, Suman, Sriram, H. and Yarin, A.L. (2014), Flow of suspensions of carbon nanotubes carrying phase change materials through microchannels and heat transfer enhancement, 14,

494-508). Sections 2.5, 3.5 and Chapter 8 were published in Polymer of ELSEVIER (Sinha-Ray, Sumit, Sinha-Ray, Suman, Yarin, A.L. and Pourdeyhimi, B. (2015b), Theoretical and experimental investigation of physical mechanisms responsible for polymer nanofiber formation in solution blowing, Polymer, 56, 452-463). Permission letters given by the publisher are in the Appendix.

CONTRIBUTION OF AUTHORS

The work on supersonic solution blowing in Section 2.1, Section 3.1, and part of Chapter 4 (section 4.3) partially represents a published manuscript [Sinha-Ray, Suman et al. (2013)] for which I am one of the co-authors and I developed the experimental setup in our lab, conducted the experiments, performed Scanning Electron Microscopy and measured nanofiber sizes, while Dr. Lee developed the experimental setup in Korea University and performed characterization, Dr. Sinha-Ray also performed additional characterizations and was the first author. Rest of Chapter 4 represents an unpublished work relevant to the process. The work on filtration of nanoparticles in sections 2.2, 3.2 and Chapter 5 represents a published manuscript [Sinha-Ray, Sumit et al. (2015a)] where I am the primary author, and performed all the experiments and developed the theory and Dr. Sinha-Ray helped in analysis. The work on pool boiling of coolants on nanofiber nano-textured surface in Section 2.3, Section 3.3, and Chapter 6 represents two published manuscripts [Sahu et al. (2016); Sinha-Ray, Sumit et al. (2017)]. For subsections 6.2.3 and 6.3.1, I am one of the co-authors, developed the materials, co-designed the experimental setup, and performed several experiments. Dr. Sahu contributed in co-developing the experimental scheme, performing experiments and writing. Dr. Sinha-Ray assisted in analyzing the results. For the same subsections and the rest of Chapter 6, I am the primary author, developed materials, performed experiments and wrote the manuscript. Ms. Zhang assisted in performing the experiments and Dr. Sahu and Dr. Sinha-Ray assisted in the analysis. The work on nanoencapsulated phase change materials in sections 2.4, 3.4 and Chapter 7 represents a published manuscript [Sinha-Ray, Sumit et al. (2014)], where I am the primary author, designed the experimental scheme and performed the experiments. Mr. Sriram assisted with

the experiments and Dr. Sinha-Ray assisted with the analysis. The work on nanofiber formation by subsonic solution blowing in sections 2.5, and Chapter 8 represents a published manuscript [Sinha-Ray, Sumit et al. (2015b)] for which I am the primary author, developed the theory, performed the experiments and characterized the specimens. Dr. Sinha-Ray assisted in developing the theory. In all published works my advisor, Dr. Yarin, supervised the experimental and theoretical work and contributed to the writing of the manuscripts.

TABLE OF CONTENTS

<u>CHAPTER</u>	<u>PAGE</u>
1. INTRODUCTION	1
1.1 Polymer nanofibers in heat and mass transfer.....	2
1.2 Carbon nanotubes in thermal management.....	2
1.3 Thesis objectives.....	3
2. BACKGROUND AND LITERATURE SURVEY	5
2.1 Electrically assisted supersonic solution blowing.....	5
2.2 Application of nanofibers in filtration of nanoparticles.....	7
2.3 Pool Boiling of coolant on superheated microelectronic surface.....	11
2.4 Microelectronic cooling and phase change materials.....	14
2.5 Solution blowing.....	16
3. RESEARCH OUTLINE	18
3.1 Electrically assisted supersonic solution blowing.....	18
3.2 Application of solution-blown 20-50 nm nanofibers in filtration of nanoparticles.....	19
3.3 Pool boiling of coolants on nano-textured heater covered with ultrafine metalized and pure polymer nanofibers.....	20
3.4 Flow of suspensions of carbon nanotubes carrying phase change Materials for passive cooling of microelectronics.....	22
3.5 Theoretical and experimental investigation of solution blowing....	24
4. SUPERSONIC SOLUTION BLOWING FOR PRODUCTION OF 50 nm NANOFIBER.....	25
4.1 Introduction	25
4.2 Experiments.....	25
4.2.1 Materials.....	25
4.2.2 Solution preparation.....	26
4.2.3 Supersonic solution blowing.....	27
4.2.4 Characterization.....	30
4.3 Supersonic blowing of nylon 6.....	30
4.4 Supersonic solution blowing of different polymers.....	32
4.4.1 Polyvinylidene fluoride.....	32
4.4.2 Polyacrylonitrile.....	36
4.4.3 Polyvinyl alcohol.....	38
4.4.3 Polyethylene oxide.....	43
4.5 Conclusion.....	45

5.	APPLICATION OF SOLUTION-BLOWN 20-50 nm NANOFIBERS IN FILTRATION OF NANOPARTICLES: THE EFFICIENT van der WAALS COLLECTORS.....	47
5.1	Introduction.....	47
5.2	Experiments.....	47
5.2.1	Materials	47
5.2.2	Electrospinning.....	48
5.2.3	Supersonic solution blowing.....	49
5.2.4	Filtration procedure.....	50
5.3	Results and discussions.....	55
5.3.1	Method (a).....	55
5.3.2	Method (b).....	66
5.4	Theoretical.....	77
5.6	Conclusions.....	92
 6.	 POOL BOILING OF NOVEC 7300 AND DI WATER ON NANO- TEXTURED HEATER COVERED WITH SUPERSONICALLY BLOWN OR ELECTROSPUN METALIZED AND PURE POLYMER NANOFIBERS.....	 95
6.1	Introduction.....	95
6.2	Experiments.....	98
6.2.1	Materials.....	98
6.2.2	Electrospinning and supersonic solution blowing.....	98
6.2.3	Electroplating.....	99
6.2.4	Characterization.....	100
6.2.5	Pool boiling set up.....	100
6.2.6	Pool boiling experiments.....	103
6.2.6.1	Copper plated nanofiber nanotextured surface.....	103
6.2.6.2	Pure polymer nanofiber nanotextured surface....	103
6.3	Results and discussion.....	104
6.3.1	General definitions.....	104
6.3.2	Copper plated nanofiber nanotexture.....	106
6.3.3	Pure polymer nanofiber nanotexture.....	110
6.3.3.1	Pool boiling of Novec 7300 fluid.....	110
6.3.3.2	Pool boiling of DI water.....	118
6.4	Conclusion.....	121
 7.	 FLOW OF SUSPENSIONS OF CARBON NANOTUBES CARRYING PHASE CHANGE MATERIALS THROUGH MICROCHANNELS AND HEAT TRANSFER ENHANCEMENT.....	 123
7.1	Introduction.....	123
7.2	Background formulae.....	124
7.3	Experiments.....	125

7.3.1	Materials and suspension preparation	125
7.3.2	Experimental set up.....	127
7.4	Results and discussion	130
7.4.1	Water and aqueous solution of surfactant flows through Microchannels.....	130
7.4.2	Intercalation of wax in CNTs.....	135
7.4.3	Intercalation of erythritol in CNTs.....	137
7.4.4	Flow rates of aqueous suspensions of wax-intercalated CNTs.....	138
7.4.5	Heat removal with wax-intercalated CNT suspension flows.....	139
7.4.6	Heat removal with erythritol-intercalated CNT suspension flows.....	150
7.5	Conclusion.....	155
8.	THEORETICAL AND EXPERIMENTAL INVESTIGATION OF PHYSICAL MECHANISMS RESPONSIBLE FOR POLYMER NANOFIBER FORMATION IN SOLUTION BLOWING.....	157
8.1	Introduction.....	157
8.2	Theoretical	158
8.2.1	Straight part of the jet	158
8.2.2	Perturbed part of the jet.....	162
8.3	Experiments.....	171
8.4	Result and discussion.....	172
8.4.1	Unperturbed straight part of polymer jet.....	173
8.4.2	Perturbed straight part of polymer jet.....	178
8.5	Conclusion	190
9.	CONCLUSION.....	191
10.	CITED LITERATURE.....	194
11.	APPENDIX.....	209
12.	CURRICULUM VITAE.....	217

LIST OF TABLES

<u>TABLE</u>	<u>PAGE</u>
4.1 Spinning conditions for different polymers.....	29
5.1 Filtration efficiency of modified filters with nylon 6 electrospun and solution-blown nanofibers.....	65
7.1 Temperature drop due to the erythritol melting at different flow rates.....	152

LIST OF FIGURES

<u>FIGURE</u>	<u>PAGE</u>
4.1 Graphical representation of experimental schemes employed for supersonic solution blowing: (a) indicates to Method (a) and (b) indicates to Method (b).....	28
4.2 SEM images of Nylon 6 nanofibers with (a) overall view (b) individual nanofiber and (c) nanofiber size distribution.....	31
4.3 SEM image of the 12 wt% solution blown PVDF nanofiber membrane....	33
4.4 SEM images of the PVDF nanofibers along with their fiber size distributions.....	35
4.5 SEM images of the PAN nanofibers along with their fiber size distributions.....	37
4.6 SEM image of the 3.5 wt% PAN nanofibers with beads and broken nanofibers.	38
4.7 SEM images of the PVA nanofibers along with their fiber size distributions.....	40
4.8 Flow-induced crystallization visible in the over-stretched bands as observed in PVA nanofibers, marked by red arrows : (a) 4 wt% PVA in water and (b) 3.5 wt% PVA in formic acid	42
4.9 SEM images of the PEO nanofibers along with their fiber size distributions.....	44
4.10 Flow-induced crystallization and beads on nanofibers as observed in PEO nanofibers from 4 wt% solution in water.....	45
5.1 Schematic of the electrospinning setup and deposition of electrospun fibers on the filter samples.....	49
5.2 Schematic of the electrically-assisted supersonic solution blowing and deposition of fibers on top of the filters.....	50
5.3 Schematic of the experimental setups employed for the filtration experiments.....	54

5.4	The initial particle-size distribution of nanoparticles in an aqueous suspension after 6 min of sonication observed using Dynamic Light Scattering (DLS).....	55
5.5	SEM images of glass filter with (a) supersonically blown nanofiber mat (nylon 6) deposited on it, and (b) electrospun nanofiber mat (PAN) with supersonically blown nanofibers (nylon 6) on top of it.....	56
5.6	SEM images of glass filters after filtration by method (a).....	58
5.7	SEM image of a dual-coated filter sample.....	60
5.8	Efficiencies of the base and modified filters measured at different nanoparticle concentrations [the experiment conducted by method (a)]....	61
5.9	SEM images of dual coated glass filters after the experiment with 2 ppm polystyrene nanoparticles of 100 nm.....	64
5.10	Base and modified glass filters for three different concentrations [the experiment conducted by method (b)]: (a) 2 ppm, (b) 1 ppm, (c) 0.5 ppm.....	67
5.11	SEM images of glass filters after the experiment with the 2 ppm suspension of Cu nanoparticle conducted by method (b).....	70
5.12	Base and modified cellulose a filters for three different concentrations [the experiment conducted by method (b)]: (a) 2 ppm, (b) 1 ppm, (c) 0.5 ppm.....	73
5.13	SEM images of cellulose a filters after the experiment with the 2 ppm suspension of Cu nanoparticle conducted by method (b).....	74
5.14	Base and modified cellulose b filters for three different concentrations [the experiment conducted by method (b)]: (a) 2 ppm, (b) 1 ppm, (c) 0.5 ppm.....	76
5.15	Flow field in the Oseen viscous flow about a cylinder (fiber).....	79
5.16	The van der Waals attraction of a spherical particle to one of the spherical particles aligned along the X-axis.....	80
5.17	The numerically predicted clusters of the 50 nm nanoparticles (shown by thin-line circles in color) collected by a nanofiber (the cross-section of the latter is shows as a bold black circle in each panel) at the oncoming flow velocity of 100 cm/s.....	85

5.18	The numerically predicted clusters of the 50 nm nanoparticles (shown by thin-line circles in color) collected by a nanofiber (the cross-section of the latter is shown as a bold black circle in each panel) at the oncoming flow velocity of 10 cm/s.....	86
5.19	The borderline for the van der Waals attraction of nanoparticles for different nanofiber sizes.....	90
5.20	SEM images of glass filter with dual nanofiber coating: the larger electrospun PAN nanofibers first and then the smaller supersonically blown nylon 6 nanofibers on top of them.....	91
5.21	SEM images of glass filter with dual nanofiber coating: supersonically blown nylon 6 nanofibers first and then the larger PAN electrospun nanofibers on top of them	92
6.1	Sketch of cross-sectional view of the assembled experimental setup used for the pool boiling experiments.....	102
6.2	Pool boiling data for Novec 7300 fluid on bare copper surface (Bare) and copper surface with thin layer of metal plated nanofiber nanotexture (NT).....	107
6.3	Optical microscope images of the metal plated nanofiber nanotextured surface (a-b) and SEM image of the same (c-d).....	108
6.4	Pool boiling data for DI water on bare copper surface (Bare) and copper surface with thin layer of metal plated nanofiber nanotexture (NT).....	109
6.5	Pool boiling curves for Novec 7300 fluid on Bare, Bare+SB and Bare+E surfaces.....	111
6.6	Surface images of the same samples prior (panels with numerals 1) and post boiling (panels with numerals 2) of Novec 7300 fluid for 7.5 h.....	112
6.7	SEM images of the nano-textured surfaces prior and after a prolonged boiling of Novec 7300 for 7.5 h.....	114
6.8	High speed images of vapor bubble nucleation and departure from the heater surface in Novec 7300 fluid.....	116
6.9	Pool boiling curves for DI water on Bare+SB, Bare, and Bare+E surfaces.....	118

6.10	Macroscopic images of the sample surfaces after boiling for 8 hours in DI water.....	120
6.11	SEM images of the supersonically blown polymer nanofibers on copper substrate after prolonged boiling for 8 h in DI water.....	120
7.1	Schematic of the first experimental setup with piston pushing water or aqueous solutions of surfactants and CNT suspensions.....	127
7.2	Schematic of the second experimental setup employed to study heat removal using microchannel flows of wax-intercalated CNTs.....	129
7.3	Volumetric flow rate versus pressure drop.....	130
7.4	Volumetric flow rate of CNT suspensions versus pressure drop with CNT concentrations.....	132
7.5	Enhanced flow rate in 0.5 wt% NADDBS surfactant solution.....	134
7.6	The average slip length versus CNT concentration.....	135
7.7	TEM images of CNTs intercalated with wax.....	137
7.8	DSC Thermogram of wax-intercalated CNT.....	137
7.9	TEM images of CNTs intercalated with erythritol.....	138
7.10	Flow rate versus pressure drop for aqueous suspensions of CNTs intercalated with wax.....	139
7.11	Temperature of the copper block versus time in the case of flows of water, surfactant solution, 1 wt% suspension of the empty CNTs, and 1 wt% of wax-intercalated CNTs in 603 μm channel.....	142
7.12	Temperature of the copper block versus time in the case of flows of water, surfactant solution, 2 wt% suspension of the empty CNTs, and 2 wt% of wax-intercalated CNTs in 1803 μm channel.....	144
7.13	Temperature of the copper block versus time in the case of flows of water, surfactant solution, 3 wt% suspension of the empty CNTs, and 3 wt% of wax-intercalated CNTs in 1803 μm channel.....	147
7.14	Temperature of the copper block versus time in the case of flows of water, surfactant solution, 1.5 wt% suspension of the empty CNTs, and 1.5 wt% of erythritol-intercalated CNTs in 1803 μm channel.....	153

8.1	Experimental setup for high-speed recording of the solution blowing process.....	172
8.2	Several snapshots from a high-speed imaging of solution blowing process where the polymer solution is being issued at the flow rate of 10 ml/h into a parallel high speed air jet.....	175
8.3	Simulation results for a straight part of polymer jet. (a) Cross-sectional radius, (b) velocity, and (c) longitudinal deviatoric stress.....	177
8.4	Axisymmetric velocity field in the air jet.....	178
8.5	Snapshot of the observed jet configuration at the beginning of the bending part.....	181
8.6	Numerically predicted snapshot for $t=39$ (the dimensional time of 0.052 s) and the screen velocity of 0.05 (the dimensional velocity of 7.5 m/s). (a) The three-dimensional view, and (b) and (c) two two-dimensional views.....	182
8.7	Numerically predicted fiber-size distributions for the screen velocity of 0.05 (the dimensional velocity of 7.5 m/s).....	184
8.8	Numerically predicted snapshot for $t=39$ (the dimensional time of 0.052 s) and the screen velocity of 0.15 (the dimensional velocity of 22.5 m/s). (a) The three-dimensional view, and (b) and (c) two two-dimensional views.....	186
8.9	Numerically predicted fiber-size distributions for the screen velocity of 0.15 (the dimensional velocity of 22.5 m/s).....	188
8.10	(a) SEM image of solution-blown nanofiber mat of nylon 6. (b) Fiber-size distribution	189

SUMMARY

The goal of this work is to explore and understand the effect of nanotexture in enhancement of heat and mass transfer in macroscopic objects. Nanoscale objects have enormous surface area compared to the bulk material. This affects different properties and functions of materials like electrical, thermal, separation, catalytic, absorption, etc. In this work nanoscale objects like carbon nanotubes and ultrafine polymer nanofibers were used in the heat and mass transfer applications, mainly focusing upon thermal management of microelectronics and filtration of hazardous nanoparticle, particularly water-borne.

Safe drinkable water is a major concern globally. Global warming, rapid industrialization, deforestation, etc. have already caused a global water crisis. In addition, clean water is another major issue to be dealt with. Water gets polluted either naturally or by human waste. Most importantly, with the sharp increase in nanoparticle-based companies, namely- semiconductor, food industry, packaging, cosmetics, etc. the amount of water-borne nanoparticles has also increased, and often this situation is beyond control. Water filters mostly lack the precision to capture ~100 nm sized particles. Otherwise, they have to be really dense which slows down the outflow dramatically. The 100-300 nm nanoparticles are often called most penetrating particles and most filtration and separation industries should aim to capture them and rate their filters' efficiency accordingly. It is very important to develop a new class of materials which can be inexpensive and can also be efficient to capture those particles. Polymer nanofibers are often used as filtering medium and growing number of researches is being conducted in this field.

Thermal management of microelectronics is a grave concern for the semiconductor society. With the ever growing need of faster computation and slim design an impetus was

imposed on having numerous transistors on the chip. Although the number of transistors are almost coming to the saturation, for the sake of enhancing computation power chip features have been reduced to 10 nm scale. This results in increase in the Joule heating in the equipment and leads to failure of the components if proper heat dissipation measures are not taken. Several researches have been conducted and several methods have been tested. Yet the window is still open for further improvement. The concern does not end only at the Earth gravity but also extends to zero or super gravity situations. Given the boom in semiconductor industry, where silicon-based processors are mostly used and will probably be employed for the next 100 years, thermal management of microelectronics is and will be a major research area along with material development. Researches have been conducted on cooling techniques, coolants, surface modifications, auxiliary units, etc. but there is no ultimate solution yet.

The first part of this thesis describes the development of a novel method in nonwovens forming which can be used to produce polymer nanofibers of size ~ 50 nm on mass scale. The method is the electrically-assisted supersonic solution blowing or just supersonic solution blowing. This method was demonstrated using Nylon 6 and a novel crystalline structure was found in the ultrafine nanofibers. It was verified with several other polymers and consistently 50-100 nm sized nanofibers were obtained on-demand from different solvent-polymer combinations.

In the following chapter of this thesis, the 50 nm Nylon 6 nanofibers were used as a filtering medium aimed at 100 nm nanoparticle separation from water. When these ultrafine nanofibers were deposited on the commercial grade filters they enhanced the efficiency of the filters for 100-300 nm nanoparticle separation. The ultrafine nanofibers due to their

increased surface area proved to be very efficient for surface filtration keeping the depth of the filters clean. Also, an increased flow rate through such filters due to the diminished depth fouling is possible. The nanofibers due to their miniscule size displace fluid less and can entrap more nanoparticles in close proximity by van der Waals forces. A theoretical model is also proposed in this work to account of a single nanofiber-multiple nanoparticles interaction to elucidate how these nanofibers can result in the enhancement of 100 nm nanoparticle separation.

The next section of this work deals with the thermal management of high-power microelectronics. Pool boiling of several coolants like Novec 7300 engineered fluid and DI water was attempted on nanofiber-covered heater surfaces. Two distinctive methods are discussed in this section. In the first approach, metal-plated ultrafine nanofibers are deposited on the heater surface and pool boiling study of the above-mentioned coolants is conducted in comparison with the other bare and textured surface. It is shown that metal-plated nanofiber texture facilitates nucleation boiling more than that of the bare surface. In the second approach, only pure polymer nanofibers (~100 nm) are deposited on the surface, and again pool boiling study is conducted and similar comparisons are discussed. In addition, larger electrospun nanofibers are also deposited as a texturing method to study the effect of electrospun pure polymer nanofibers. This allows one to eliminate the additional metal-plating step of the first approach and to verify the nano-texture viability in enhancing nucleate boiling at the surfaces.

The following section of thesis deals with the thermal crisis of microelectronics in a different way. It involves the passive cooling of microelectronic component using a suspension of carbon nanotubes (CNT) with phase change materials (PCM), like wax or

meso-erythritol, being encapsulated inside the CNTs. PCMs are lucrative heat storage materials for their broad melting domains, chemical inertness, etc., albeit limited by low thermal diffusivity and tendency to stick to walls. However, nanoencapsulation renders the thermal response time of PCM practically negligible in compared to the residence time and can also solve the segregation issue. In this work a comprehensive method of passive convective cooling with nanoencapsulated PCM-filled CNT-water suspension through microchannels is employed to study the mechanism of heat removal based on the latent heat of PCMs.

In the last section of this work a comprehensive quasi-one dimensional model of solution blowing process is proposed. Solution blowing is an alternative method to meltblowing in nonwovens that allows polymer solutions, even bio-polymers, to be used in nanofiber formation. In this method a polymer jet is issued into a coaxial subsonic gas jet which stretches the polymer thread and after going through vigorous bending and flapping and rapid solvent evaporation, the polymer jet thins down to ~500 nm sized nanofibers. The present results include prediction of the polymer jet configurations in flight, as well as reveal the detailed information on the patterns in which the oncoming polymer jets are deposited on the moving screen (the so-called laydown). The laydown characteristics, in particular, the fiber-size distributions obtained under different conditions are predicted. The work also compares and corroborates the experimental and numerical findings. This study serves as a building block for further studies related to solution blown nonwoven mat architecture, porosity, and their filtration/absorption/desorption capabilities.

CHAPTER 1

INTRODUCTION

Nanoscale materials of dimension 1-100 nm attracted significant attentions over the last 20 years. The American physicist Richard Feynman once said “There is plenty of room at the bottom” (1959), which expressed the basic of motivation for research directed at nano-scale materials. However, only after 1974, when the word *Nanotechnology* was first coined as a means of improvement in semiconductors by Dr. Norio Taniguchi, and a more deterministic approach, explicitly expressed by Dr. Drexler during the 1980s, a new research domain under the name Nanotechnology was born about the 1990s. Nanoscale materials possess the greatest advantage of enhanced surface area compared to the bulky material that provides them an enhanced interaction with the surrounding medium, either liquid or gas. For such enhanced-surface-area material such properties as thermal, electrical, ionic, catalytic, etc. properties can be exploited more efficiently as more molecules are present on the surface than in the bulk. Accordingly, over the last 20 years nanomaterials were explored aiming surface transfer enhancement in biological to semiconductor applications, from food packaging to medicine, from energy to environmentally-friendly applications. Nanomaterials like nanoparticles, graphene flakes, carbon nanotubes, polymer nanofibers have found themselves amidst sea of opportunities. Nanoparticles like titanium oxide or zinc oxide are used in food packaging or as pigments. Graphene, theoretically being one of the strongest material and the most electrically and thermally conductive is also widely researched for semiconductor and solar cell applications, Carbon nanotubes were widely used in electronic processes and catalytic applications. Polymer

nanofibers, on the other hand, are not just limited to textiles but find unexpected novel applications.

1.1 Polymer Nanofibers in Heat and Mass Transfer

Potential applications involving polymer nanofibers are vast and numerous like – tissue engineering scaffolds, wound dressing, drug delivery, protective clothing, filtration, sensors, optical, absorbents, etc. Electrospinning became a popular method of production of polymer nanofibers of ~100 nm from polymer solutions from the early 1990s. Numerous researches have been conducted in the fields of pollutant removal from air or water using different filter media [Barhate et al. (2007); Gopal et al. (2007)]. Polymer nanofibers possess an extremely large surface area to volume ratio and high porosity. Hence, for filtration of nanoparticles, like metallic nanoparticles, virus/bacteria, soot, etc. such nanofibers provide a great promise for surface or depth filtration. Also, polymer nanofibers have recently found applications in heat removal from high-power sources, especially in microelectronics. Polymer and metal-plated nanofiber nano-texture has been revealed as an effective tool to eliminate the Leidenfrost effect [Weickgenannt et al. (2011)], or to intensify spray cooling [Srikar et al. (2010), Sinha-Ray, Suman et al. (2011a)].

1.2 Carbon Nanotubes for Thermal Management

With the discovery of multi-walled carbon nanotubes by Ijima (1991), they found applications in several fields like, electronics, optics, electrochemistry, etc. because of their excellent thermal, electrical and mechanical properties. A number of researches have been conducted to enhance thermal conductivity [Berber et al.(2000)], electrical [Bandaru (2007)] and

electronic properties [Fischer et al. (1999)] using CNTs. They also were used to prepare nanofluids [Ding et al. (2006)] aimed as a coolant for heat transfer applications. As a coolant in thermal management applications CNTs have found potential usage as thermal interface materials in electronic packaging [Fabris et al. (2011)]. Although CNTs have been used quite efficiently in packaging, transport and other applications, their very high thermal conductivity in the axial direction ~ 6600 W/m-K implies their benefits for thermal management applications [Berber et al. (2000)].

1.3 Thesis objectives

Although CNTs and polymer nanofibers were already used in several areas, thermal management and pollutant removal application are still open areas of research aiming applications of carbon nanotubes and ultrafine polymer nanofibers. In the present thesis both subjects are tackled to reveal how CNTs and ultrafine nanofibers could facilitate enhancement of heat removal from high-power microelectronics and the efficiency of water filters in the submicron particle range. The present work employs the experimental and theoretical approach to develop subsonic and supersonic solution blowing aiming polymer nanofiber formation from polymer solutions. Chapter 2 is dedicated to the literature survey, whereas chapter 3 outlines the research approach. Chapter 4 aims at development of the electrically-assisted supersonic solution blowing for production of ~ 50 nm nanofibers from different polymer solutions. The effect of addition of the 50 nm Nylon 6 polymer nanofibers to the industrial filter on removal of 100 nm nanoparticles from water flow is described in chapter 5. Pool boiling study aiming thermal management of high-power microelectronics using supersonically blown nanofiber-coated nano-textured surface is discussed in chapter 6. This topic is sub-divided into two major parts

involving both metallized nanofiber and pure polymer nanofibers. Chapter 7 describes the study of suspensions of CNTs with phase change material used for passive cooling of high-power microelectronics. In chapter 8 theoretical and experimental study of nanofiber formation by subsonic solution blowing is discussed based on the fundamental physical principles. Conclusions are drawn in chapter 9.

CHAPTER 2

BACKGROUND AND LITERATURE SURVEY

2.1 Electrically Assisted Supersonic Solution Blowing

(Part of this section has been partially published in Sinha-Ray, Suman, Lee, M.W., Sinha-Ray, Sumit, An, S., Pourdeyhimi, B., Yoon, S.S. and Yarin, A.L. (2013), Supersonic nanoblowing: a new ultra-stiff phase of nylon 6 in 20–50 nm confinement, 1, 3491-3498).

Polymer nanofiber hold great potential in several fields like textiles [Deitezel et al. (2001); Dees and Spuirrel (1974); Gibson et al. (1999); Schreuder-Gibson et al. (2002)], wound dressing [Xu et al. (2004); Verreck et al. (2003); Khil et al. (2003)], tissue engineering [Mathews et al. (2002); Yoshimoto et al. (2003); Maa et al. (2005); Min et al. (2004); Shin et al. (2004)], drug delivery [Abidian et al. (2006); Biondi et al. (2008); Papkov et al. (2007)], and filtration [Grafe et al. (2001); Kosmider and Scott (2002); Shin et al. (2006); Podgórski et al. (2006); Ahn et al. (2006)] especially because of their high surface area, high porosity and small pore sizes. Processes like meltblowing, wet spinning, etc. are traditionally used to produce polymer fibers in the range of ~1-100 μm . Over the years, electrospinning [Reneker and Yarin (2008); Yarin et al. (2014)] has become a popular method for production of nanofibers in micron to sub-micron size range. A relatively new method in nonwovens processes was introduced under the name of solution blowing. In this method a polymer solution is fed through a coaxial nozzle surrounded by a high-speed subsonic gas jet. The polymer thread thins being pulled by the gas jet, thins additionally due to the bending instability, while solvent evaporation and polymer solidification transform the thread into a nanofiber [Sinha-Ray, Suman et al. (2010); Sinha-Ray, Suman et al. (2011b)]. An additional electric field can also be applied between the nozzle and the collector for

additional jet stretching [Sinha-Ray, Suman et al. (2011b)]. However, electrospinning or subsonic solution blowing cannot produce ultrafine nanofibers in the ~50 nm range on demand. Such ultrafine nanofibers could find immense applications in various fields due to their small sizes and large surface area, especially in bio-separation and bio-medical applications, in the fields of sensors, energy storage, battery separators, etc. Also, protecting of portable electronic media from dirt and contaminants was aimed using small-scale nanofibers [Yang et al. (2011); Wang et al. (2013); Filatov et al. (2007)].

Over the last century several polymers were studied in detail and introduced into multiple fields of applications. In particular, Nylon-6 has been studied quite extensively, especially because of its polyamide structure. This particular polyamide is important in the load-bearing applications like in ropes, cords, belts or airbag, as well as reinforcement in composites. Detailed studies of this polymer revealed two most important crystalline structure of Nylon 6, namely- α - and γ - phase, where α - is its most stable phase. However, under the conditions of rapid crystallization, like in meltspinning, γ - phase is predominant. [Liu et al. (2008)]. It has been also noticed that depending upon different takeup speeds, different crystalline phases can be formed. None of the available processes could form nanofiber of the order of 50 nm on mass scale on demand. In the present work a novel method of nonwovens fabrication, the supersonic solution blowing was introduced to form such ultrafine polymer nanofibers. Not only Nylon 6, but such polymers as polyacrylonitrile (PAN), polyvinylidene fluoride (PVDF), polyvinyl alcohol (PVA), polyethylene oxide (PEO) etc. have multiple applications and were studied quite extensively. PVA-based nanofibers have been used for tissue scaffolds, bio-filtration, sensor applications, drug release, etc. [Peresin et al. (2010)]. PEO is considered as one of the easily spinnable polymer which is often used as a host polymer for biological applications. PVDF has been

widely investigated mostly for its pyro- and piezo- electric properties [Laceros-Mendez et al. (2002)] in electrochemical applications, oil separation, etc. PAN has been used mostly as a precursor for making carbon nanofibers and also possesses high chemical inertness, thermal resistivity and sufficient hydrophobicity. Recently researchers from the UIC group have introduced metal-plated PAN nanofibers on Cu substrates for efficient heat removal [Sinha-Ray, Suman et al. (2011a)]. In the present work it is shown that supersonic solution blowing can be applied to many polymers to produce polymer nanofiber in the 50-80 nm range. This opens a new venue for various applications involving polymer nanofibers, particularly when small nanofibers are required. Their orientation, high porosity, extremely large surface area to volume ratio could facilitate such applications as filtration, semi-conductors, electrochemistry, wound dressing, cell culture, efficient heat removal, etc.

2.2 Application of Nanofibers in Filtration of Nanoparticles

(This section has been previously published in Sinha-Ray, Sumit, Sinha-Ray, Suman, Yarin, A.L. and Pourdeyhimi, B. (2015a), Application of solution-blown 20–50 nm nanofibers in filtration of nanoparticles: The efficient van der Waals collectors, Journal of Membrane Science, 482, 132-150).

Possibly the most important breakthrough that can be achieved using 20-50 nm fibers is in the area of filtration of micron- and submicron-sized particles. Over thousands of industries namely bio-medical, cosmetics, food processing, semiconductor, etc. use nanoparticles in their different processing units [Barhate and Ramakrishna (2007)]. They require a high-level control over processes to eliminate the hazardous effects of nanoparticles, but still leach out nanoparticles from their units to the environment (air or water) [Baron (2003)]. In particular,

these nanoparticles aerosolize in air. Often nanoparticles in the range 10-50 nm form clusters and make submicron-sized particles of ~500 nm, which are very hard to break [Barhate and Ramakrishna (2007); Baron (2003)] owing to strong van der Waals interactions between them. Combustion products often aggregate to form such agglomerates. Sub-micron-sized soot particles are considered very hazardous to breathe as they are detrimental for proper functioning of alveoli in lungs when entering above a certain limit [Wang and Pui (2013)]. Not only airborne, but also waterborne or surface-borne nanoparticles are potential hazards. Manufactured nanoparticles have their detrimental effects on aquatic organisms [Handy et al. (2008); Chalew et al. (2013)]. Different nanoparticles like silver or Ti which are often used as antibacterial or antifouling agents remain in the water stream [Benn and Westerhoff (2008)], and above a certain limit of 10 µgm/L these nanoparticles are potential threats to swallow. The ceramic membranes employed for water filtration leach out these nanoparticles. Then, the nanoparticles enter human body via drinking water. All these nanoparticles, which are either washed from industrial units or generated by other sub-processes, end up accumulating in living organisms. Even the most efficient HEPA filters have the maximum efficiency for particles larger than 0.3µm [Barhate and Ramakrishna (2007)]. Surprisingly, there is almost no information or regulations on specific nanoparticle sizes in filtration of drinking water, and focus has been mostly on micron-sized particles, whereas in reality submicron-sized particles and pathogens (microbes, bacteria, virus, etc.) are frequent among harmful waterborne particles.

For the last two decades electrospinning has gained immense popularity in producing filter media for capturing micron and submicron particles [Gopal et al. (2006); Groitzsch and Fahrback (1986); Grafe and Graham (2003)]. Electrospun membranes have been used mostly as pre-filters, especially after asbestos fibers were proven to be detrimental and were replaced by the polymeric

fiber membranes [Porter (1990)]. However, the strength issues related to those fibers are one of the main concerns when liquid is pressurized for separation [Barhate and Ramakrishna (2007)]. For different grades of filtration, for example, for ultra-filtration or micro-filtration, the usage of electrospun membranes has thus been limited to a sandwiched layer [Wang et al. (2005)]. Donaldson Inc. is one of the forerunners in using nanofibrous media in filtration, and currently there are several other industries which use them for filtering application [Barhate and Ramakrishna (2007)]. Nanofibrous media have multiple applications in transportation air filtration [Grafe et al. (2001)], dust collection [Kosmider and Scott (2002)], liquid filtration, smoke filtration, and coalescence filters [Shin et al. (2005)]. Research has been also conducted on commercial HEPA filters with electrospun layers. It was shown that these are better performing filters than the previously used ones [Ahn et al. (2006)] mostly due to the modified porosity with a larger surface area. However, nanofibers in a filter also increase pressure drop, especially in coalescence filters [Shin et al. (2005)]. Even in air filtration nanofibers rapidly result in a cake-like structure formation and block the flux. With air particulate filtering, flow reversal (pulsing) to brush off the collected particles and to regain filter's efficiency is quite natural, albeit it is uneasy in regards to filtration of waterborne particles.

Though different filter media remove particles from the stream differently, there all involve such common mechanisms as the inertial impaction, direct interception or Brownian motion [Gopal et al. (2006)]. The smallest particles, in the range ~ 10 nm, are commonly caught due to Brownian motion (diffusion) [Podgórski (2006)], particles in the range of microns are commonly captured by sieving or inertial impacts. The particles in the mid-range are regularly intercepted by big fibers, if not by impact then just by brushing along the fiber surface. The most penetrating particle size for air filtration has been found as $0.3 \mu\text{m}$. However, as mentioned earlier, water

filtration still lacks such precise data on the most penetrating particle size. Also, for particle separation from liquid, the scenario is far worse, since particle diffusion is much slower in liquid and inertial impacts are not as helpful as normal sieving mechanism [Lee et al. (1993)]. There are several other mechanisms important in filters, like electrostatic double-layer interaction, etc. Note also that one of the frequently used options to intercept the smallest nanoparticles is an increase in the filter media thickness, which, however, in also results in higher pressure drop to sustain a given flow rate, which is undesirable.

The van der Waals interactions between nanofibers and nanoparticles represent another mechanism which is responsible for particle agglomeration in the filter media [Cheremisinoff (1998)]. Nanofibrous pre-filter media can be a potential area where the van der Waals interactions can become effective due to a tremendous surface area to volume ratio. Though the van der Waals interactions are weaker in comparison to those responsible for the common mechanisms of direct impact or interception, this mechanism can be useful when the particle-to-fiber diameter ratio is close to 1, and indeed in such cases the smallest fibers (~50 nm) can act as potential “magnets” in the fibrous media, as demonstrated in sections 3-5 below. A number of numerical and analytical studies dealt with the effect of the van der Waals forces on the interception of particles of the sizes ~100 nm [Hallez (2012); Kirsch (2000); Parsegian and Ninham (1971); Chen (2012); Bhattacharjee et al. (2000); Martines et al. (2008)]. It was also shown theoretically that as the fiber size would diminish to the 20-50 nm range, the capture efficiency of nanoparticles of the size 10-100 nm would increase by an order of magnitude [Kirsch (2000)]. It should be emphasized that electrospinning can produce fibers in the range of 100-300 nm, however, fibers in the range of 20-50 nm cannot be normally produced by electrospinning [Yarin et al. (2005)]. In the previous work of this group [Sinha-Ray, Suman et al.

(2103)] it was shown that supersonic solution blowing is capable of routinely producing nanofibers in the 20-50 nm range. To the best of our knowledge, no other methods are available for modifying filter media with such nanofibers. Accordingly, it is expected that a single-layered mat of 20-50 nm nanofibers deposited by supersonic solution blowing on a commercially available filter can be sufficient to raise the efficiency from a moderate one without increasing the pressure drop. This can scavenge the midsize ($\sim 0.3 \mu\text{m}$) or smaller nanoparticles and make clusters of them, still without fouling the filter. The present work aims at this goal.

2.3 Pool Boiling of Coolant on Superheated Microelectronic Surface

(Part of this section have been previously published in Sahu, R.P., Sinha-Ray, Sumit, Sinha-Ray, Suman and Yarin, A.L., Pool Boiling of Novec 7300 and Self-Rewetting Fluids on Electrically-Assisted Supersonically Solution-Blown, Copper-Plated Nanofibers (2016), International Journal of Heat and Mass Transfer, 95, 83-93 and Sinha-Ray, Sumit, Zhang, W., Sinha-Ray, Suman, Sahu, R.P. and Yarin A.L. (2017), Pool boiling of Novec 7300 and DI water on nano-textured heater covered with supersonically blown or electrospun polymer nanofibers, International Journal of Heat and Mass Transfer, <http://dx.doi.org/10.1016/j.ijheatmasstransfer.2016.08.101>).

Ever growing need of miniaturization of transistors in microelectronic components aimed to increase computational speed, facilitate automation, data processing, etc., has posed severe challenges in terms of heat dissipation and an effective heat removal. For smaller transistors, densely crowded in integrated circuits, thermal management becomes critical to avoid thermal failure due to differential thermal expansion of components and extend their operational lifetime [Guo et al. (1993); Miner and Ghosal (2006)]. Several approaches to cooling microelectronics

were explored in the past, such as single-phase liquid cooling [Zhang et al. (2005); Peng et al. (1994a); Peng et al. (1994b)], flow boiling [Yarin et al. (2009); Leão (2014)], jet impingement cooling [Beratlis and Smith (2003); Wang et al. (2004); An et al. (2014)], spray cooling [Cotler et al. 2014)], heat pipes [Kim and Golliher (2002)], liquid metal cooling [Silverman et al. (2004); Miner and Ghosal (2004)], indirect cooling with phase change materials [Sinha-Ray et al. (2014)], and pool boiling [Anderson and Mudawar (1989); Webb and Kim (2005)]. Pool boiling is one of the most promising methods of thermal management problem, which stems from high latent heat of evaporation of liquids. Pool boiling is relevant for thermal management of nuclear power plants, refrigeration, metallurgical quenching processes, petrochemical processes, and air conditioning. In the latter, different refrigerants are used which release heat at the evaporators in refrigeration system in the so-called flooded regime with pool or flow boiling at solid surfaces. Heat removal in pool boiling steeply rises when nucleate boiling sets in due to convective heat transfer by buoyant bubbles, albeit it begins to decrease steeply as the Critical Heat Flux (CHF) is reached and a subsequent film boiling sets in [Kutateladze (1963)].

Surface modification can significantly enhance the bubble nucleation process and thus facilitate pool boiling [Tien (1962)]. The macroscopic shape and features of the heater surface, e.g. a wire or a plane surface, rough or smooth surface, an intact or porous one, a wettable or a non-wettable surface also matter [Nukiyama (1966); Rioboo et al. (2009a); Dong et al. (2014); Li and Peterson (2010); Rainey and You (2000); McHale et al. (2011); Chang and You (1997); Kim et al. (2007); Li et al. (2015); Bourdon et al. (2013); Rioboo et al. (2009b)].

Heat removal in pool boiling significantly depends on the coolants used, and such coolants as DI water, alcohols, Fluorinert fluids and fluid mixtures were explored [Calus and Leonidopoulos (1974); Jensen and Jackman (1984); Sun et al. (2004); McGillis and Carey

(1996); Sathyanarayana et al. (2012); Forrest et al. (2013); Amaya et al. (2013); Kim and Kim (2009)]. Suspensions of nanoparticles [Wen and Dong (2005); Das et al. (2003); You et al. (2003)] or surfactant solutions [Quinn and Cetegan (2010)] were also used as coolants aiming to shift the CHF to a higher value.

Electrospun polymer nanofiber mats deposited on a heater surface create a nano-textured porous interface which facilitates pinning of the impacting coolant drops on the surface, which dramatically enhances heat removal rate and even eliminates the Leidenfrost effect [Weickgenannt (2011)]. Nano-textured surfaces formed using metal-plated electrospun nanofiber mats were used to enhance heat removal rate in spray cooling [Sinha-Ray, Suman et al. (2010a); Sinha-Ray, Suman and Yarin (2014); Sinha-Ray, Suman et al. (2014)] and pool boiling [Jun et al. (2014)]. These inexpensive nano-textured surfaces allowed achieving heat removal rates close to 1 kW/cm² in drop impact cooling [Sinha-Ray, Suman et al. (2010a)]. In the case of pool boiling the rough metal-plated nanofibers act as nucleation sites, as well as a hot “cage” for growing bubbles, i.e. simultaneously increase the number of bubbles and their growth rate [Jun et al. (2014)].

Nanofibers, even smaller than the electrospun ones, can be developed by supersonic solution blowing [Sinha-Ray, Suman et al. (2013)] as it has been mentioned in previous chapter. These nanofibers revealed a much better robustness than their electrospun counterparts. Supersonically-blown nanofibers can be used for the enhancement of heat transfer in pool boiling both in metal-plated and in pure polymer form. Although metal-plating of fibers on heater surface is not only an extra fabrication step but also might be dangerous for certain microelectronics substrates, it can provide lot of nucleation sites for enhanced nucleate boiling. However it would be also attractive to eliminate metal-plating, if it would be possible to sustain a

certain level of heat enhancement. It was recently shown that supersonically-blown polymer nanofibers not only enhance heat transfer and lower surface superheat in mini-channel flows with Taylor bubbles but also sustain adhesion to the heater surface for a long time [Freystein et al. (2016)]. Therefore, in the present work pool boiling of Novec 7300 fluid and DI water are studied on bare copper surface and nano-textured surface covered with polymer, non-metallized electrospun and supersonically-blown nanofibers and also on metalized nanofibers. The result of metalized nanofiber in pool boiling of several coolants represents a published work by Dr. Sahu et al. (2016).

2.4 Microelectronic Cooling and Phase Change Materials

(This section has been previously published in Sinha-Ray, Sumit, Sinha-Ray, Suman, Sriram, H. and Yarin, A.L. (2014), Flow of suspensions of carbon nanotubes carrying phase change materials through microchannels and heat transfer enhancement, 14, 494-508).

Thermal management of microelectronics has become a grave concern for the semiconductor industry. According to Moore's law, the number of chips per circuit is expected to increase exponentially every year, which results in a dramatic increase of heat released per unit volume. Bulky fans and the other traditional mean have their own severe limitations (e.g. bulky space, thermal inertia, etc.) and can hardly resolve the emerging cooling problems. The usage of liquid coolants for cooling microelectronics attracts a wider attention. Along with pool boiling as mentioned in *section 2.3* different other liquid cooling techniques like liquid metals [Miner and Ghosal (2004)] and dielectric coolants [Arik and Bar-Cohen (1998)] have already been explored in the context of microelectronics cooling. The use of phase change materials (PCMs) holds great promise for the cooling enhancement. PCMs absorb heat as the latent heat of

fusion, and release this heat when solidifying elsewhere [Kandasamy et al. (2008)]. Several different kinds of PCMs are available, such as fatty acids [Feldman et al. (1989)], hydrated salts, paraffin waxes, and eutectic compositions [Farid et al (2004); Wang et al. (2007); Faraji et al. (2009)], and numerical investigations of potential single-phase or multi-phase PCM effect on microelectronics cooling reveal their benefits [Kuravi et al. (2009); Gong and Mujumdar (1996); Goel et al. (1994); Sabbaha (2009)]. Paraffin waxes are attractive PCMs due to their relatively high latent heat of fusion (~ 200 J/g); chemical inertness, and minor phase segregation, albeit their drawback is in low thermal conductivity and diffusivity [Zalba (2003)]. Low thermal conductivity of wax extends its melting time to the level inappropriate for such flow-through systems as microchannels. The efforts to enhance the effective thermal conductivity of wax involve the addition of metallic fillers of a much higher thermal conductivity and diffusivity [Velraj et al. (1999); Hasnain (1998); Wu et al. (2010)]. The melting time of wax diminishes as a square of the PCM particle size, which led to development of nano-encapsulated wax particles inside carbon nanotubes [Sinha-Ray, Suman et al. (2011)]. In this case the characteristic melting time becomes very short ($\sim 10^{-7}$ s). Nano-encapsulation inside CNTs is also helpful, since it can diminish sticking to the channel walls, and also allows for adjusting the operational temperature range by mixing different kind of waxes with different fusion temperatures [Sinha-Ray, Suman et al. (2011c)]. Potentially the melting temperature band could reach 40°C - 80°C . Therefore, aqueous suspensions of CNTs with nano-encapsulated waxes hold great potential as an effective coolant for microelectronics devices. Similarly to the other of methods of microelectronics cooling, heat is removed from the channel section where PCM nanoparticles solidify.

The present work aims at the experimental investigation of heat removal with aqueous suspensions of CNTs with encapsulated wax. The coolants flow through straight

microcapillaries of circular cross-section embedded in a heated copper block which acts as a prototype of a heated microelectronics device.

2.5 Solution Blowing

(This section has been previously published in Sinha-Ray, Sumit, Sinha-Ray, Suman, Yarin, A.L. and Pourdeyhimi, B. (2015b), Theoretical and experimental investigation of physical mechanisms responsible for polymer nanofiber formation in solution blowing, *Polymer*, 56, 452-463).

Solution blowing is kindred to meltblowing. In solution blowing polymer solution is issued as a slow jet into a co-flowing sub- or supersonic gas jet which stretches the polymer jet directly, as well as via a vigorous bending instability, thus leading to formation of polymer nanofibers. In meltblowing molten polymer jet undergoes similar transformations in co-flowing subsonic gas jet, which results in formation of polymer microfibers. For several decades meltblowing, a process much more mature than solution blowing, gained immense popularity in nonwoven industry, which uses several thermoplastic polymers to form nonwoven mats of polymer microfibers in the size range of 1-100 μm [Fedorova and Pourdeyhimi (2007); Pinchuk et al. (2002); Grafe and Graham (2003); Zhao and Wadsworth (2003)]. In distinction to meltblowing which results in microfibers, solution blowing results in nanofibers. It does it with the production rate superior to electrospinning and with much less restrictions on the electrical parameters of polymer solutions [Medeiros et al. (2009); Sinha-Ray, Suman et al. (2010b); Yarin et al. (2014)]. Solution blowing has been used to form polymer nanofibers mats for different applications, such as nanotubes [Sinha-Ray, Suman et al. (2010b); Yarin et al. (2014); Oliveira et al. (2012)], microfiltration [Zhuang et al. (2012)], and biomedical applications [Behrens et al. (2014);

Khansari et al. (2013a)]. Successful applications of solution blowing in forming nanofibers from various biopolymers were recently demonstrated [Khansari et al. (2013a); Sinha-Ray et al (2011b); Khansari et al (2013b); Zhang et al. (2013)]

Recent theoretical/numerical and experimental results shed light on the physical mechanisms responsible for microfiber formation in meltblowing and provided their detailed description [Sinha-Ray et al. (2010c); Yarin et al. (2010); Yarin et al. (2011)]. The situation with solution blowing is different: until now it has been lacking a theoretical description. Since solution blowing is related to meltblowing, and in general, to free liquid jets moving relative surrounding gas with high speed, it is worth of mentioning some of these works as an appropriate context for the present work [Yarin et al. (2014); Yarin et al. (1993)]. Highly viscous liquid jets moving with a high speed relative to the surrounding gas experience lateral distributed force which tends to increase bending perturbations, as was revealed in the seminal work [Weber (1931)]. A general theory of thin liquid jets moving in air applicable to both Newtonian and non-Newtonian liquids, including viscoelastic polymer solutions and melts, was given in Refs. Yarin et al.(1993) and Entov and Yarin (1984). It was already applied to describe electrospinning [Renekar et al. (2000) and Yarin et al. (2001)] and meltblowing [Sinha-Ray, Suman et al. (2010b); Yarin et al. (2010); Yarin et al. (2011)]. This approach is extended in the preset work to incorporate solution blowing.

CHAPTER 3

RESEARCH OUTLINE

3.1 Electrically Assisted Supersonic Solution Blowing

(Part of this section has been partially published in Sinha-Ray, Suman, Lee, M.W., Sinha-Ray, Sumit, An, S., Pourdeyhimi, B., Yoon, S.S. and Yarin, A.L. (2013), Supersonic nanoblowing: a new ultra-stiff phase of nylon 6 in 20–50 nm confinement, 1, 3491-3498).

Ultrafine polymer nanofibers are important for various applications involving wound dressing, filtration, cell culture, bio-sensing, semiconductor, and electrodes. However, none of the processes in use could produce polymer nanofibers of the order of 50 nm on a mass scale. Although such processes as meltblowing, electrospinning, meltspinning etc., or such recent techniques like subsonic solution blowing are capable of production of polymer nanofibers of the order of 100 -5000 nm, they are yet inadequate to produce of 50 nm nanofibers en masse. The present work addresses this problem and presents a solution as a novel supersonic solution blowing.

The primary goal of the present work is to develop the electrically-assisted supersonic solution blowing, which involves a combination of electrospinning and gas blowing, where the gas is issued from a Laval nozzle at a speed of ~564 m/s. During this process, polymer solution is fed through a needle using a syringe pump and the needle is placed normally to the Laval nozzle axis. This needle is the cathode as in the conventional electrospinning, albeit the nozzle is grounded. The polymer jet issued from needle is attracted to the Laval nozzle and thus to the core of the supersonic gas flow. There the polymer jet makes a sharp kink since it is swept by the gas flow. The polymer jet is experiencing a tremendous stretching of the order of 10^7 1/s and

vigorous flapping and bending sets in. This process was realized with different polymers like Nylon 6, Polyvinylidene fluoride, Polyacrylonitrile, etc. Nylon 6 was the first polymer processed by this method. The collected Nylon 6 nanofibers were thoroughly studied to reveal their crystal structure. That resulted in discovery of a novel crystal phase of Nylon 6, namely the χ - phase. An individual nanofiber of this type is stiff strong and a mat of such nanofibers is strongly adherent to a substrate surface with a milky appearance on them. Furthermore, this process was demonstrated using the other polymers, like PVDF, PEO, PVA etc. A thorough statistical study on these nanofibers revealed that in most cases more than 60% of the nanofibers belong to the 50 nm range and in some cases more than 70% belong to the less than 50 nm range. These nanofibers can be useful in applications requiring large surface area and high porosity and in sensor applications. PAN formed nanofibers in the below 100 nm range, which is beneficial for thermal management discussed below in this thesis.

3.2 Application of Solution-blown 20-50 nm Nanofibers in Filtration of Nanoparticles

(This section has been previously published in Sinha-Ray, Sumit, Sinha-Ray, Suman, Yarin, A.L. and Pourdeyhimi, B. (2015a), Application of solution-blown 20–50 nm nanofibers in filtration of nanoparticles: The efficient van der Waals collectors, Journal of Membrane Science, 482, 132-150).

An important application of the supersonically blown 50 nm nanofibers is related to filtration of nanoparticles, particularly in the 100-300 nm range, either air or water-borne. Such nanoparticles are considered as the most penetrating nanoparticles. In this work filtration efficiency of commercially available filter media like glass fiber filter and cellulose filter with fiber/pore sizes of the scale of 10 μ m is dramatically increased by not only adding electrospun nanofibers, as is usually done, but also a layer of ultrafine supersonically-blown 20-50 nm

nanofibers. Three different commercially available base filters were modified with (i) electrospun nanofibers alone, (ii) solution-blown 20-50 nm alone, and (iii) the dual coating with electrospun nanofibers deposited first and the solution-blown 20-50 nm deposited on top of them. Detailed observations of nanoparticle removal by these base and the above-mentioned modified filters revealed that the dual electrospun nanofibers (deposited first) and the solution-blown 20-50 nm deposited on top of them are the most effective in removing the below-200 nm Cu nanoparticles/clusters from aqueous suspensions. Experiments were conducted in two different time ranges: (a) for 8-15 s, and (b) for 8 min. It was found that the efficiency of the dual-coated filters containing 20-50 nm fibers was significantly higher than those of the others at the lowest nanoparticle concentrations of 0.2-0.5 ppm in suspension. The experiments conducted for longer time revealed that the nanofibers were as efficient in particle retention as in the shorter-time experiments, and there was no visible breakage pattern of these nanofibers. The theory developed in the present work explains and describes how the smallest solution-blown nanofibers introduce a novel physical mechanism of nanoparticle interception (the attractive van der Waals forces) and become significantly more efficient collectors compared to the larger electrospun nanofibers. The theory predicts the domain of nanoparticle collection due to the van der Waals forces. The theory also elucidates the morphology of the nanoparticle clusters being accumulated at the smallest nanofiber surfaces, including the clusters growing at the windward side, or in some cases also on the leeward side of a nanofiber.

3.3 Pool Boiling of Coolant on Nano-textured Heater Covered with Ultrafine Metalized and Pure Polymer Nanofibers

(Part of this section have been previously published in Sahu, R.P., Sinha-Ray, Sumit, Sinha-Ray, Suman and Yarin, A.L., Pool Boiling of Novec 7300 and Self-Rewetting Fluids on

Electrically-Assisted Supersonically Solution-Blown, Copper-Plated Nanofibers (2016), International Journal of Heat and Mass Transfer, 95, 83-93 and Sinha-Ray, Sumit, Zhang, W., Sinha-Ray, Suman, Sahu, R.P. and Yarin A.L. (2017), Pool boiling of Novec 7300 and DI water on nano-textured heater covered with supersonically blown or electrospun polymer nanofibers, International Journal of Heat and Mass Transfer, <http://dx.doi.org/10.1016/j.ijheatmasstransfer.2016.08.101>). The main aim of this work was to study the effect of polymer nanofiber nanotexture on the heater surface on pool boiling above it. This study was mainly focused on heat removal from high-power microelectronic components using pool boiling of different coolants, like Novec 7300 and DI water. Earlier, electrospun polymer nanofibers were used in microchannels to prevent dry out over high-power microelectronics elements. Metal-plated nanofiber nanotextured surfaces were also used for spray cooling. However, under microgravity conditions the system sometimes was in the pool boiling regime. Also, mechanical stability of electrospun nanofibers was a problem in pool boiling. The present work deals with the 100 nm polymer nanofibers (PAN), both metalized and non-metalized in pool boiling over high-power heater surface. The 100 nm PAN nanofibers, after Cu plating, proved to be excellent candidate for this task. After a prolonged pool boiling, the nanofiber layer remained intact and facilitated the enhancement of nucleation at much lower surface superheat than the corresponding bare Cu surface. Such nanofibers also helped to delay the Critical Heat Flux. Nucleate boiling could be achieved at $\sim 5^{\circ}\text{C}$ less surface superheat than on the bare Cu surface using Novec 7300 fluid as a coolant. An additional study using pure non-metallized ultrafine polymer nanofibers revealed that their performance in pool boiling can approach that of the metallized ones. Even though pure polymer nanofibers possess less nucleation sites than the Cu-plated ones, they still could significantly enhance bubble nucleation

and detachment. In addition, the supersonically-blown ultrafine polymer non-metalized nanofiber architecture remained intact after prolonged and vigorous boiling in all coolants. The elimination of the electroplating post-processing makes nano-texturing extremely simple and straightforward and applicable to a wide variety of surfaces. On the other hand, it comes with a price of a lower heat removal rate compared to that on metal-plated nanofibers, albeit the present experiments revealed that the reduction is not that drastic as it would be expected. It is also demonstrated that the supersonically-blown polymer nanofibers outperformed the electrospun nanofibers. Supersonically-blown nanofibers provide a larger number of nucleation sites than electrospun nanofibers or a bare copper surface, and thus, facilitate nucleate boiling much stronger. The ultrafine supersonically-blown polymer nanofibers are very robust and did not delaminate from the heater surface either in Novec 7300 or DI water after prolonged vigorous boiling process. Overall, the enhancement of heat removal due to the ultrafine supersonically-blown polymer nanofibers on the heater surface in Novec 7300 is more significant than in DI water, which is associated with the smaller bubble size in the former case.

3.4 Flow of Suspensions of Carbon Nanotubes Carrying Phase Change Materials for Passive Cooling of Microelectronics

(This section has been previously published in Sinha-Ray, Sumit, Sinha-Ray, Suman, Sriram, H. and Yarin, A.L. (2014), Flow of suspensions of carbon nanotubes carrying phase change materials through microchannels and heat transfer enhancement, 14, 494-508).

This work explores the potential of nano-encapsulated phase change materials (PCMs) in the applications related to microelectronic cooling. More than 50% of the portable digital electronics fail due to thermal reasons. Bulky fans are often design-unfriendly and direct liquid

cooling is also not always desirable. Indirect cooling with PCMs is an excellent alternative for cooling of high-power electronics. Different PCMs offer a variety of melting points, high latent heat of fusion, and chemical inertness, albeit they suffer from poor thermal conductivity and diffusivity and tendency to segregation at the walls. Present work aims at a realistic solution of the above-mentioned problems and a design of a throughflow system to tackle the microelectronics overheating issue. PCMs (wax or meso-erythritol) were encapsulated in carbon nanotubes (CNTs) by the method of self-sustained diffusion at room temperature and pressure.

(i) Such nano-encapsulated wax nanoparticles alone allow for heat removal in a relatively wide range of temperature (different waxes have melting temperatures in the 40-80 °C range). On the other hand, such nano-encapsulated meso-erythritol nanoparticles allow for heat removal in the 118-120 °C range. The combination of the two PCMs (wax and meso-erythritol) would extend the temperature range to 40-120 °C, when both types of nanoparticles (wax and meso-erythritol intercalated) would be suspended in the same carrier fluid (an oil). (ii) The nanoparticles possess a short response time of the order of 10^{-7} s. (iii) Such nano-encapsulation can also prevent PCM from sticking to the wall. In the experiments of this work with the wax-intercalated CNTs, stable aqueous suspensions of CNTs with concentrations up to 3 wt% with and without nano-encapsulated wax were prepared using a surfactant Sodium Dodecyl Benzene Sulfonate (NaDDBS). These suspensions were pumped through two channels of 603 μm or 1803 μm in diameter subjected to a constant heat flux at the wall. It was found that the presence of the surfactant in CNT suspensions results in a pseudo-slip at the channel wall which enhances flow rate at a fixed pressure drop. When aqueous solutions of the surfactant are employed (with no CNTs added), the enhanced convection alone is responsible for ~ 2 °C reduction in temperature in comparison with pure water flows. When CNTs with nano-encapsulated wax are added, an

additional ~ 1.90 °C reduction in temperature due to the PCM fusion was observed when using 3 wt% CNT suspensions. In addition, suspensions of meso-erythritol-intercalated CNTs in alpha-olefin oil were used as coolants in flows through the 1803 μm -diameter microchannel. These suspensions (1.5 wt% CNT) revealed a temperature reduction due to the PCM fusion up to 3.2 °C, and the fusion temperature in the 118-120 °C range.

3.5 Theoretical and Experimental Investigation of Solution Blowing

(This section has been previously published in Sinha-Ray, Sumit, Sinha-Ray, Suman, Yarin, A.L. and Pourdeyhimi, B. (2015b), Theoretical and experimental investigation of physical mechanisms responsible for polymer nanofiber formation in solution blowing, *Polymer*, 56, 452-463).

This work describes a comprehensive numerical model of solution blowing process of multiple three-dimensional polymer jets issued from a die nosepiece into a high-speed air flow and deposited onto a moving screen. The model solves the quasi-one-dimensional equations of the mechanics of free liquid jets with the jet axis configuration being three-dimensional. It accounts for the polymer solution viscoelasticity, jet interaction with the surrounding high-speed air flow, and solvent evaporation and jet solidification. The results include the polymer jet configurations in flight as well the detailed information on the pattern in which the oncoming polymer jets are deposited on the moving screen (the so-called lay-down), and its characteristics, in particular, the fiber-size distributions obtained under different conditions. The work also describes experiments on solution blowing and comparison of the numerical and experimental data.

CHAPTER 4

SUPERSONIC SOLUTION BLOWING FOR PRODUCTION OF 50 nm NANOFIBERS

Part of this chapter has been partially published in Sinha-Ray, Suman et al. (2013)

Reprinted with permission from [Sinha-Ray, Suman, Lee, M. W., Sinha-Ray, Sumit, An, S., Pourdeyhimi, B., Yoon, S. S., Yarin, A. L. (2013), Supersonic nanoblowing: a new ultra-stiff phase of nylon 6 in 20–50 nm confinement, Journal of Material Chemistry C, 21 (1), 3491-3498]. Copyright 2013 Royal Society of Chemistry.

4.1 Introduction

This work aims at the development of a novel method of formation of nanofibers of the order of 50 nm en masse from different polymer solutions. Not only production of the nanofibers but also complete characterization of these nanofibers is tackled. The proposed method is a combination of electrospinning and supersonic gas blowing where the electrified polymer jet issued from an electrospinning needle, is attracted to the supersonic gas stream and is swept by it. The supersonic nozzle is a Laval nozzle is grounded. The experimental process is described in section 2. Fiber-forming from Nylon 6 and the complete characterization details are provided in section 3. Section 4 details the results involving the other polymers. Conclusions are drawn in section 5.

4.2 Experiments

4.2.1 Materials

In this work five different polymers were used- Nylon 6 (molecular weight of repeat unit 104.83 Da), Polyacrylonitrile (PAN, molecular weight 130 KDa), Polyvinyl alcohol (PVA,

molecular weight 146 KDa, 99%+ hydrolyzed), Polyethylene oxide (PEO, molecular weight 600 KDa), Polyvinylidene fluoride (PVDF, molecular weight 180 KDa). The polymers were purchased from Sigma-Aldrich. The solvents for the required polymers namely-N,N-dimethylformamide (DMF), Formic acid, Acetone, were all purchased from Sigma-Aldrich as well.

4.2.2 Solution Preparation

The 15 wt% Nylon solution was prepared in formic acid. For this method 1.5 g of Nylon-6 pellets were dissolved in 8.5 g of formic acid to make in total 10 g of solution, which was stirred for 24 h on a magnetic stirrer at 60 °C. Further the solutions for different polymers were also prepared. Namely, three different PAN solutions were used in this experiment: 4, 5 and 6 wt% in DMF to produce (10 g of solution for each weight percentage was prepared). The solutions were kept on a hotplate with a magnetic stirrer at 60 °C for 4-6 h depending on the concentration. Four different concentrations of PVA were prepared using formic acid as a solvent. The concentrations were 3.5, 4, 5 and 6 wt%, (all as 10 g of solutions). The solutions were placed on a hotplate at 80 °C for 6-8 h, depending on concentration with a magnetic stirrer for proper dissolution. Four different concentrations of PVDF solutions were also prepared – 12, 14, 16 and 18 wt%. The solvent was a mixture of acetone and DMF in a 2:3 weight ratio. The solution preparation time, as stated above, was 4-6 h at 60 °C. Three different PEO solutions were also used, namely- 3, 4 and 5 wt% in formic acid. The solution preparation time was 24 h at 30 °C using a magnetic stirrer.

4.2.3 Supersonic Solution Blowing

Polymer solution was fed through a 25/32 g needle using a syringe pump (New Era Pump system, Inc.). Electric connection was set up between the needle and the Silvent de Laval nozzle (voltage varied for different polymers), where the ground was the nozzle, so that the electrified polymer jet can be attracted to the nozzle. The Laval nozzle operated at 70 Psi and issued air at a speed of 564 m/s. As the electrospun polymer thread approaches the core of the supersonic air jet, the thread immediately is swept by the air flow and undergoes vigorous bending and flapping, which causes additional stretching of the polymer thread. The collector, an aluminum foil, was placed at a distance of 30 cm from the Laval nozzle, mounted on a plate, rotating at 50 rpm. The humidity in the chamber was kept at $40 \pm 5\%$ using dehumidifier tube connected to the airline for pre-drying air, and the temperature of the chamber was kept at $32^\circ \pm 2^\circ \text{C}$. Two different configurations of the supersonic blowing was employed, denoted as *Method (a)* and *(b)*. In *Method (a)* the electrospinning needle was placed vertically with respect to the Laval nozzle. The horizontal (d1) and vertical distances (d2) were kept at 2 cm and 2.5 cm. In *Method (b)* the electrospinning needle was placed normally to the nozzle in the same horizontal plane. The distances (d1 and d2) were maintained at 2 cm and 2.5 cm as well. *Method (b)* was used for the polymer solutions prone to dripping inside the high-speed air jet. Polymer solutions like PEO 3-5 wt% and PVA 3.5-5 wt% were used in *Method (b)*. The experimental schemes are illustrated in Fig. 4.1. Different conditions of supersonic blowing for different polymers are listed in Table 4.1.

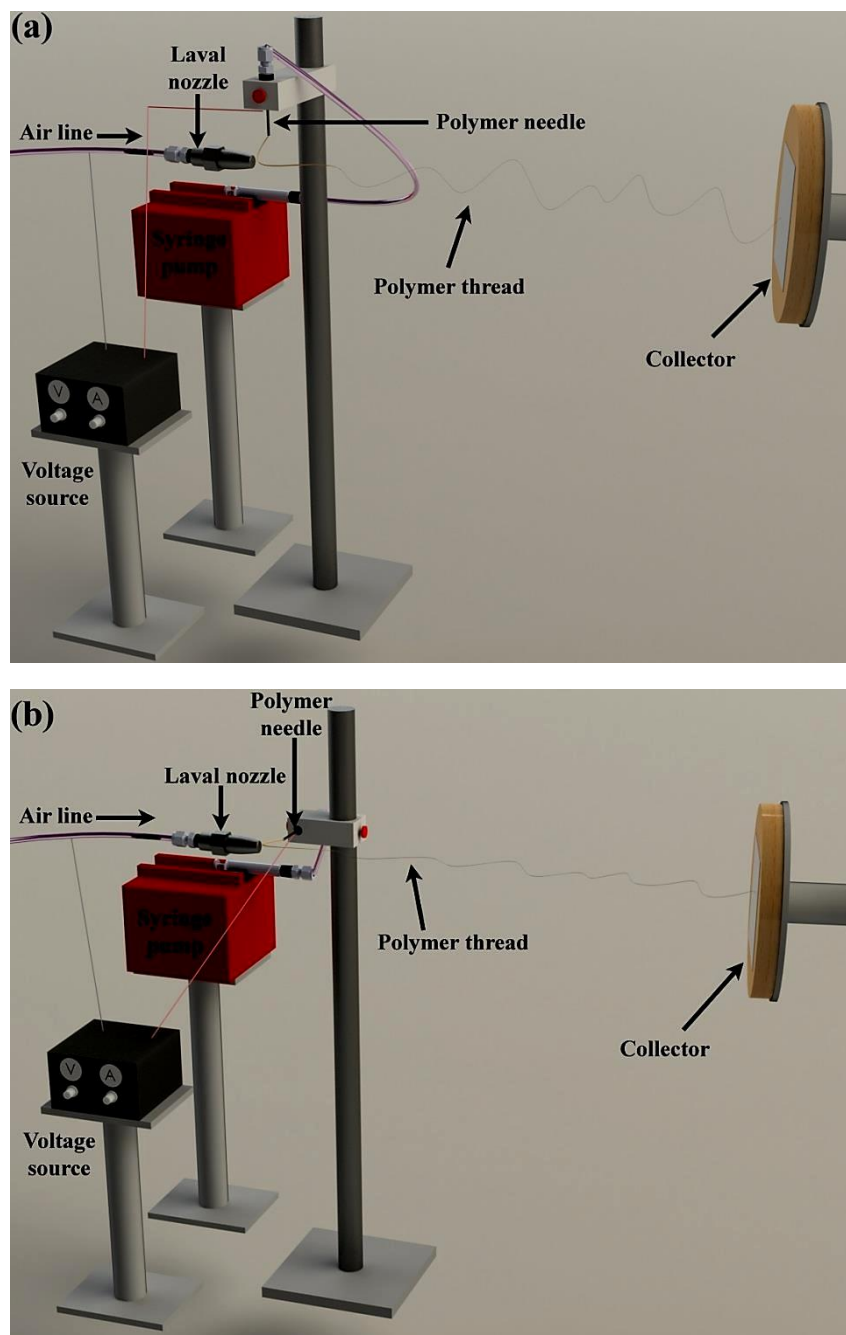


Figure 4.1: Schematic of the experiments employing supersonic solution blowing: (a) corresponds to *Method (a)* and (b) corresponds to *Method (b)*.

Table 4.1: Experimental conditions for different polymers. Different flow rate and voltages were applied according to different concentrations. All polymers were delivered through a 25 gauge needle.

Polymer	Concentration (wt%)	Flow rate (ml/hr)	Voltage (KV)
Nylon	15	0.1	5.6
PAN	4	0.3	5.6
	5	0.3	6.2
	6	0.5	6.8
PVDF	12	0.2	5.2
	14	0.3	5.8
	16	0.5	6.1
	18	0.5	6.2
PEO	3	0.05	4.8
	4	0.1	5.2
	5	0.2	5.6
PVA	3.5	0.1	6.8
	4	0.2	6.6
	5	0.4	7
	6	0.5	7.2

4.2.4 Characterization

This work made use of a field emission SEM, JEOL JSM 6320F, a high resolution SEM with cold field emission source, to observe the polymer nanofiber samples in Electron Microscopy Service (Research Resources Center, UIC).

4.3 Supersonic Solution Blowing of Nylon 6

Results of this section are reproduced from ref. Sinha-Ray, Suman et al. (2013)

The method was first established using Nylon 6 where the 15 wt% solution was delivered using either a 25 gauge or 32 gauge needle. The SEM images of the nanofiber mats and individual nanofibers and their corresponding nanofiber sizes are listed in Fig. 4.2. During measurement of individual nanofibers, Photoshop was used for measuring the fiber diameter and more than 30 nanofibers were measured from different parts of the nanofiber mat in SEM images. In Fig. 4.2 the left hand side column shows an overall view of the nanofiber mat and the middle column shows individual nanofibers. It should be emphasized that an individual nanofiber was used for nanofiber size measurement to avoid any astigmatism error in the zoomed out view. The nanofiber size distribution is shown in the right hand side column in Fig. 4.3. In the same figure the rows (a) and (b) used 25 gauge needle for solution supply and column (c) used 32 gauge needle. It can be seen clearly that with reduction in the needle size the mean fiber size was reduced from 54 nm to 42 nm, indicating a stronger polymer jet stretching. A conservative estimate of polymer stretching indicates that in supersonic blowing a polymer thread experiences the stretching ratio of the order 10^7 , given by the following formula $\left(\text{polymer mass fraction} \times \left(\frac{d_{\text{initial}}}{d_{\text{final}}} \right)^2 \right)$, where $d_{\text{initial}} \approx 250 \mu\text{m}$ and $d_{\text{final}} \approx 50 \text{ nm}$. This stretching happens in a time interval of 1 ms [Sinha-Ray et al.(2011c), Sinha-Ray et al. (2010), Yarin et al.

(2010)] which indicates the strain rate of the order of 10^7 10^{10} 1/s. This enormous stretching can potentially slide and/or reorganize the macromolecules and pack them in a narrow confinement and freeze them into an energetically unfavorable phase from a more favorable α - phase.

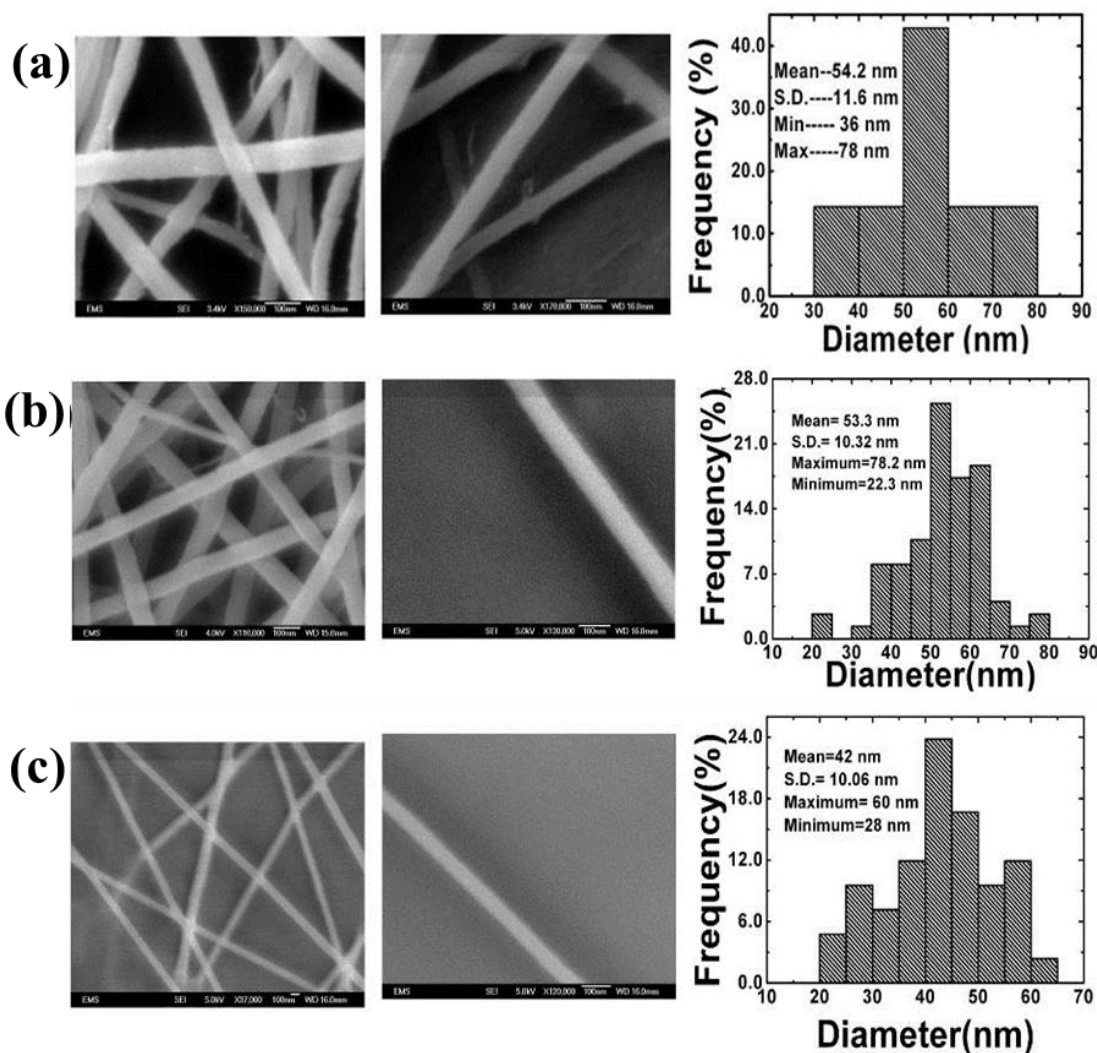


Figure 4.2: SEM images of Nylon 6 nanofibers with (a) overall view (b) individual nanofiber and (c) nanofiber size distribution. 25 g needle was used for (a) and (b) and 32 g needle was used for (c).

Detailed characterization study on these supersonically-blown 20-50 nm nanofibers was conducted via Transmission Electron Microscopy (TEM), Small Area Electron Diffraction (SAED), Raman Spectroscopy, Atomic Force Microscopy (AFM) and Differential Scanning Calorimetry (DSC). From TEM and SAED a novel crystalline phase was discovered, distinct from the known α - and γ - phases in terms of the d-spacing between parallel macromolecules. The Raman spectroscopy also provided evidence of a decrease in the O-H bond distance, which in turn leads to stiffer nanofibers, which was corroborated with AFM study. Finally, a different melting behavior of these nanofibers according to the DSC thermogram compared to the known α - phase and metastable β - phase in Nylon 6 proved the existence of a novel χ -phase in supersonically-blown Nylon 6 nanofibers. The above-mentioned study of the χ -phase was published in Sinha-Ray, Suman et al. (2013), and conducted by my coauthors.

4.4 Supersonic Solution Blowing of Different Polymers

4.4.1 Polyvinylidene Fluoride (PVDF)

As mentioned in Table 4.1, four different concentrations of PVDF were used in solvent Acetone:DMF (2:3). The SEM images of the nanofibers and their fibers size distributions are shown in Fig. 4.4. It can be clearly seen that as the polymer concentration increased from 14 to 18 wt%, the mean nanofiber size also increased from 40.1 nm to 71.6 nm. This stems from the fact that as the concentration of the polymer in the solvent increases, the tangling of polymer macromolecule also increases. This increases the viscoelasticity of the polymer solution and evidently the stretching capability of the solution reduces. A conservative estimate of polymer stretching was provided in section 4.3 which reveals the strain rate of the order of 10^7 - 10^{10} s⁻¹. This enormous stretching rate can potentially slide and/or reorganize the macromolecules and pack them in a narrow confinement and solidify them into an energetically unfavorable phase

from a more favorable α - phase, which is often observed in PVDF, albeit the study of phase structure in the supersonically-blown PVDF requires a further investigation . However, it was seen that it is impossible to form intact or uniform PVDF nanofibers below the concentration of 14 wt% with such solvent system. Especially in case of 12 wt% a variety of sizes of nanofibers with large beads were observed. A representative SEM image of nanofibers formed from 12 wt% PVDF polymer solution is shown in Fig. 4.3. Beading and broken nanofibers reveal a low spinnability of such polymer solution resulting in capillary breakup of the polymer jet. Also, it is seen from the image that the solvent did not dry completely and the nanofibers merged. At 14 wt% a minor effect of such incomplete evaporation of solvents can be observed, resulting in a few cases of nanofiber merging. For 16 wt% (Fig. 4.4 b) such effects were eliminated. However, at a lower concentration sharper size distributions of nanofibers can be obtained, whereas at higher concentrations a larger standard deviation of the fiber sizes was found.

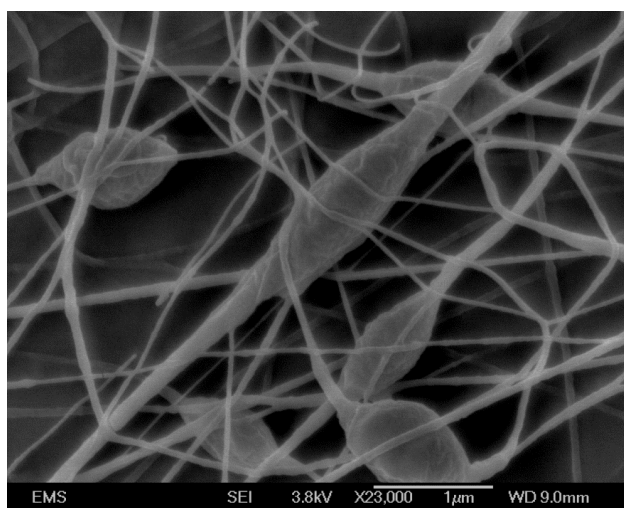


Figure 4.3: SEM image of the 12 wt% supersonically solution-blown PVDF nanofiber membrane with different sizes of nanofibers along with beads.

PVDF solutions in Acetone: DMF solvent system were not used at polymer concentrations beyond 18 wt%. At 18 wt% the mean fiber size already reaches ~70 nm, while the minimal size is 40.6 nm. The aim of the present work was to produce polymer nanofibers ~ 50 nm, therefore, the more concentrated solutions were excluded.

A detailed statistical analysis was employed to elucidate the obtained fiber size distributions using SEM images. One can find the ratio of nanofibers in the 20-50 nm range to the entire nanofiber size range using the data on the right-hand side panels in Figs. 4.4(a)-4.4(c), which can be fitted using the log-normal distribution

$$f(x|M, \sigma) = \frac{1}{x\sigma\sqrt{2\pi}} \exp\left(\frac{-(\ln x - M)^2}{2\sigma^2}\right) \quad (4.1)$$

where the parameters, M and σ , are related to the mean value m and the variance v through the following expressions

$$M = \ln\left(\frac{m^2}{\sqrt{v + m^2}}\right), \quad \sigma = \sqrt{\ln\left(\frac{v}{m^2 + 1}\right)} \quad (4.2)$$

Using Eq. (4.1) one can find that for the 14 wt% PVDF solution, 83.3% of the nanofibers belong to the 20-50 nm range, which proves that supersonic solution blowing is capable of producing the below - 50 nm PVDF nanofibers in large quantities. As the concentration becomes higher, i.e. for 16 and 18 wt%, the 20-50 nm range includes 54.31% and 7.9% of fibers, respectively. This is a clear manifestation of the effect of polymer concentration and macromolecular entanglement in the solvent which leads to poorer stretching at 18 wt% compared to 14 wt%. Note also, that in the 50-80 nm range 64.2% of nanofibers formed from the 18 % PVDF solution can be found.

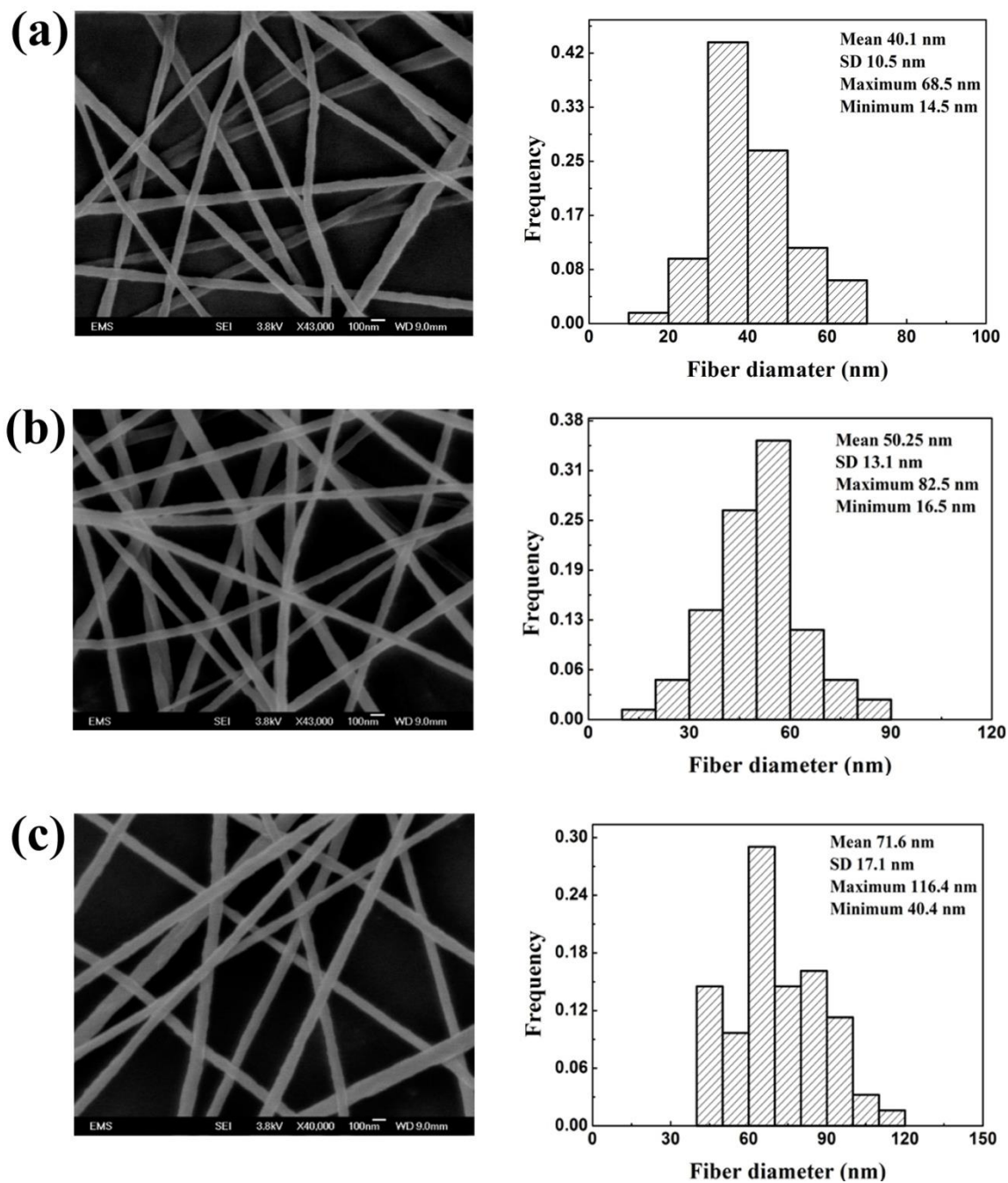


Figure 4.4: SEM images of the PVDF nanofibers and their fiber size distributions, where different panels correspond to different polymer concentrations: (a) 14wt%, (b) 16 wt%, (c) 18 wt%.

4.4.2 Polyacrylonitrile (PAN)

Three different concentrations of PAN were tested using DMF as a solvent, namely- 4, 5 and 6 wt%. SEM images of the nanofibers and their corresponding size distributions are shown in Fig. 4.5. As is seen in the SEM images, the mean nanofiber sizes increase from 63.9 nm to 97.6 nm as the polymer concentration changes from 4 to 6 wt% (cf. Fig. 4.5). Previous researches have shown that solubility of PAN in DMF changes in subtle way. It was found that [Iovleva et al. (2001)] beyond 5 wt% concentration PAN solubility in DMF reduces in distinction from the other organic aprotic solvents like DMAA, DMSO, etc. Again, PAN also possesses an extremely stiff structure. Detailed X-ray analysis suggests that [Bohn et al. (1961)] PAN macromolecules reveal a chain- to- chain lateral order which leads to a stiffening effect in them. This forces the backbone chain to configure into a “twisted and kinked” conformation. Such configuration is one of the main reasons which leads to poor solubility and high melting point of PAN. In this conformation stretching of polymer may lead to larger nanofiber formation even under strong stretching. This effect of macromolecule alignment leads to rather poor stretching especially for concentration ~5 wt%, when the macromolecules remain unassociated.

Using the same statistical analysis, as in section 4.4.2, a wide spectrum of 50-80 nm nanofibers in the nanofiber mats was revealed. Their relative ratio is 72.81%, 20.18% and 20.04% for 4, 5 and 6 wt% solutions, respectively. The mean nanofiber sizes practically remain unaltered from 5 to 6 wt% solutions, which stems from the fact that DMF becomes a weaker solvent at critical 5 wt% concentration and can trigger macromolecular entanglement effects under such conditions. Also it is worth mentioning that it is intuitively clear that with an increase in polymer concentration, the viscosity of the polymer increases and especially for PAN/DMF system it increases exponentially. The increase became more drastic starting from 5 wt% [Lin et

al. (2005), Wang et al. (2007)]. A research was conducted to study the electrospinning behavior of 6 wt% PAN at high temperature and the 80-100 nm nanofibers were observed. They were mostly amorphous [Wang et al. (2007)].

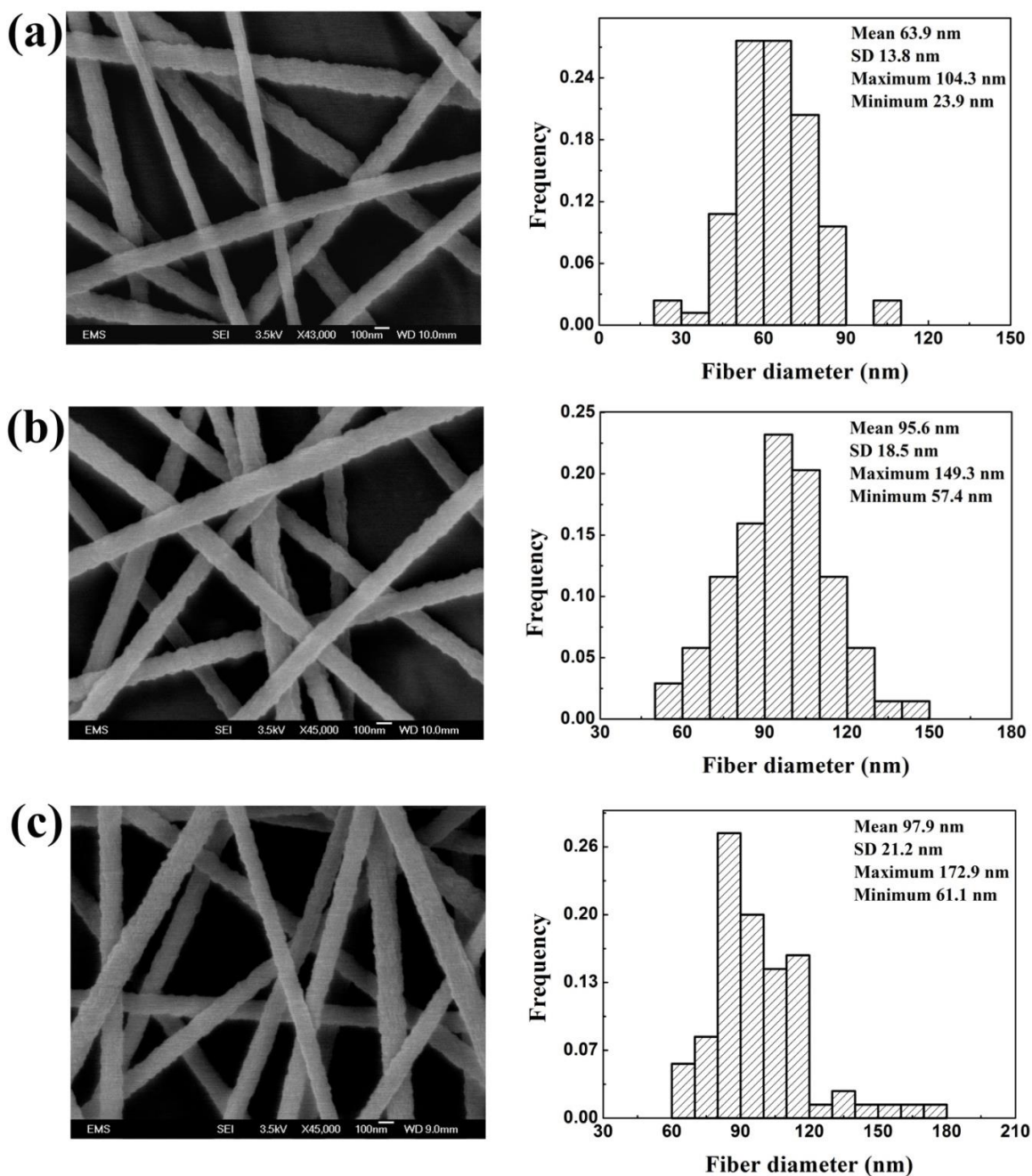


Figure 4.5: SEM images of the PAN nanofibers and their fiber size distributions, where different panels correspond to different polymer concentrations: (a) 4 wt%, (b) 5 wt%, (c) 6 wt%.

At polymer concentration less than 4 wt% highly beaded fiber structures were found. The beading was mostly because of a reduced polymer content, which results in a weaker viscoelasticity and henceforth facilitates capillary breakup and formation of multiple broken fibers as well. The capillary breakup in PAN/DMF solutions at such low concentrations was also mentioned in several previous researches. A representative image of the beaded nanofiber formed from 3.5 wt% PAN solution is shown in Fig. 4.6.

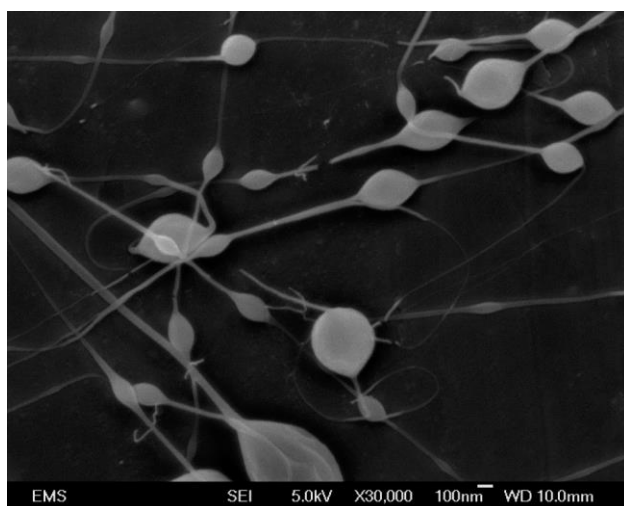


Figure 4.6: SEM image of the 3.5 wt% PAN nanofibers with beads and broken nanofibers.

4.4.3. Polyvinyl Alcohol (PVA)

Electrospinning of PVA has been mostly attempted using water as a solvent [Park et al. (2010)]. In the present work formic acid was used as a solvent for low concentration of PVA like 3.5 to 6 wt%. The representative SEM images of PVA nanofibers and the corresponding fiber size distributions are presented in Fig. 4.7. As can be seen, the mean nanofiber size increased from 47.8 nm for 3.5 wt% to 62.4 nm for 6 wt% solution. Surprisingly, the mean fiber size did

not change dramatically in the 4-6 wt% range, and was close to ~60 nm. Also, the majority of these nanofibers belong to the ~50 nm range. Using the same statistical analysis as the one in section 4.3, we can also calculate the ratio of nanofibers in the ~20-50 nm range to the entire nanofiber mat. The corresponding results were the following- 61.83%, 31.77%, 16.75%, 28.02% for 3.5, 4, 5, 6 wt%, respectively.

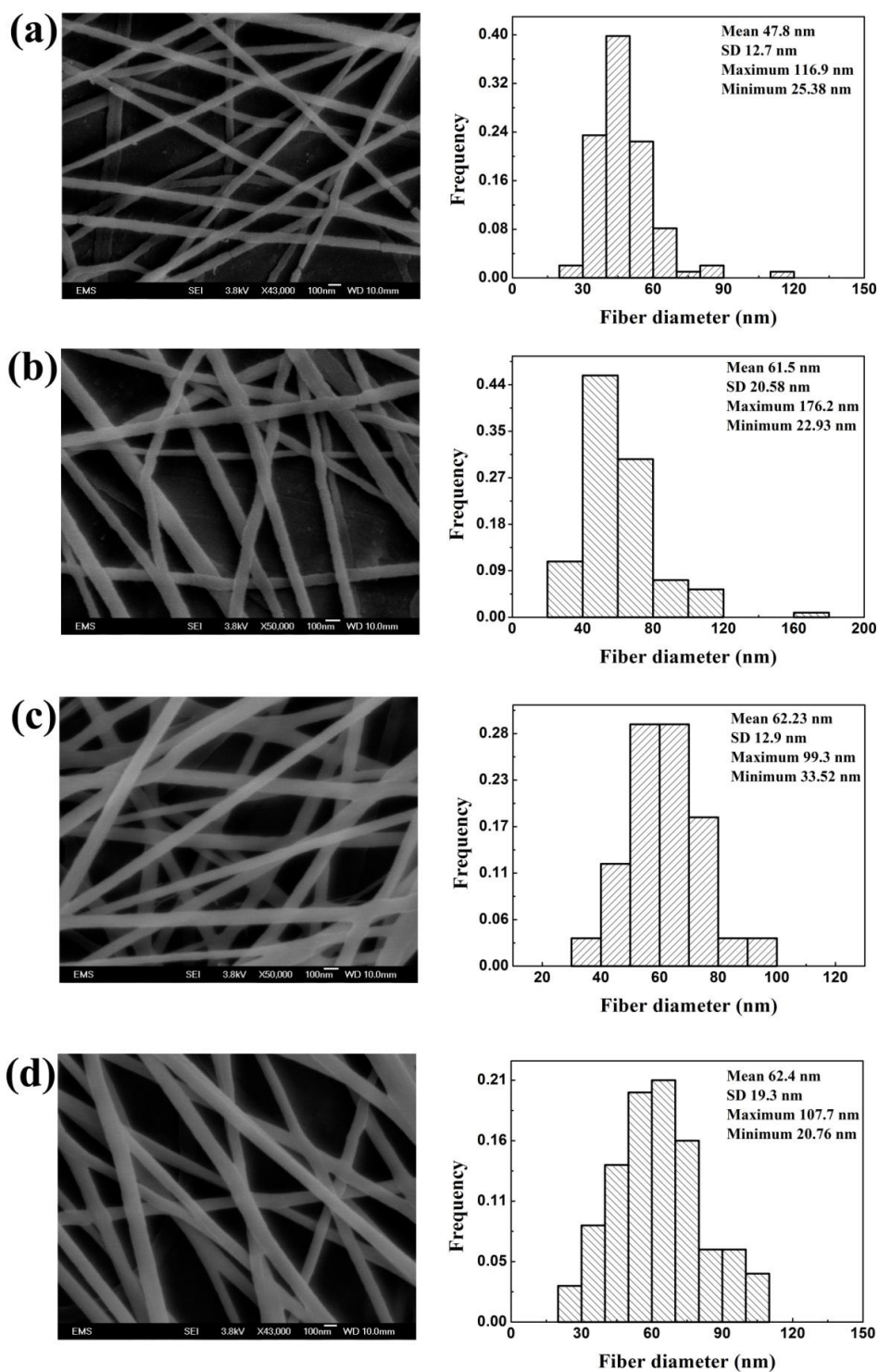


Figure 4.7: SEM images of the PVA nanofibers and their fiber size distributions where different panels correspond to different polymer concentrations: (a) 3.5 wt%, (b) 4 wt%, (c) 5 wt%, (d) 6 wt%.

Although the percentages of nanofibers below 50 nm reduced at the higher concentrations of PVA, the resulting nanofiber mats exhibited a much narrower fiber size distribution close to 50 nm than in the other cases. On the other hand, a lower molecular weight PVA yielded a much wider distribution of nanofibers [Park et al. (2010)]. It was found that with water as a solvent the fiber sizes were close to ~200 nm for 8 wt% polymer concentration and any concentration below that resulted in bead formation. Also use of surfactant has been reported for higher degree of hydrolysis (DH) of PVA to prevent gel formation and reduce surface tension [Park et al. (2010)]. Both water and formic acid used as solvents in the present work are polar solvents with almost the same boiling point and the same order of dipole moment (1.85D for water and 1.41D for formic acid). Solutions with concentrations as low as 3.5 wt% could be easily solution blown. Albeit for low concentrations (3.5 wt% in formic acid and 4 wt% in water) PVA nanofibers exhibited flow-induced crystallization where a shish-kebab type structure could be seen (cf. Fig. 4.8) [Zussman et al. (2003)]. In such a structure central fibrillary part crystallizes while being fully stretched.

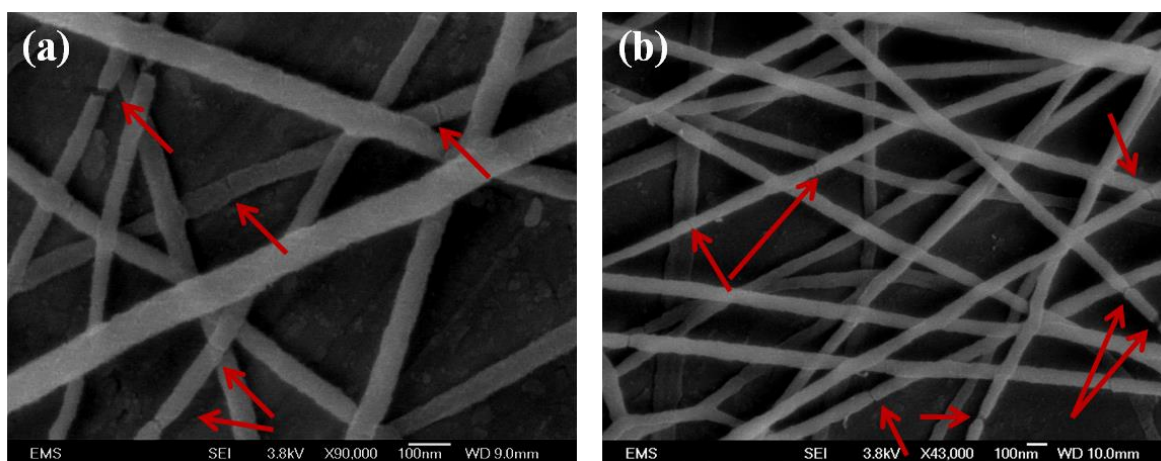


Figure 4.8: Flow-induced crystallization (marked by red arrows) visible in the over-stretched bands observed in PVA nanofibers: (a) 4 wt% PVA in water and (b) 3.5 wt% PVA in formic acid.

Small nanofibers from lower PVA concentration in water, such as 4 wt%, could be obtained, as seen in Fig. 4.8. However, these nanofibers possess a wider range of sizes. Therefore, water was not used as a solvent further. PVA solutions with more than 6 wt% in formic acid were considerably more viscous and difficult to pump through a 25 gauge needle using the current experimental setup and thus they were excluded from further experimentation. It should be emphasized that in both solvents polymer concentrations higher than the lowest amount resulted in a negligible flow-induced crystallization. Due to rapid solvent evaporation and solidification in electrospinning, the degree of crystallinity may be reduced [Srikanth et al. (2009), Yarin et al. (2014)] in polymer nanofibers. However, it should be emphasized that in supersonic solution blowing the local temperature drops down at the nozzle exit which may lower the solvent evaporation rate. A polymer thread close to nozzle exit experiences the most rapid stretching. This coupling can help in generating more flow-induced crystallization in nanofibers for lower concentration polymer solutions. For higher polymer concentrations it may

not happen due to a higher degree of entanglement of polymer macromolecules and thus lesser tendency to formation of shish-kebabs in polymers.

4.4.4 Polyethylene Oxide (PEO)

Three different concentrations of PEO in formic acid were used to form ultrafine nanofibers by supersonic blowing, namely 3, 4 and 5 wt%. The SEM images of the nanofibers and their fiber size distributions are shown in Fig. 4.9. It can be seen from Fig. 4.9 that the mean nanofiber sizes varied from 44.7 nm to 67.6 nm for 3 to 5 wt% solutions. Using the statistical analysis described above, one can also evaluate reproducibility of the process of forming nanofibers in the 20-50 nm range. This range comprises 75.83%, 64.46% and 6.2% of nanofibers formed from the 3, 4 and 5 wt% solutions. The part of PEO nanofibers below 50 nm is lower for the 5 wt% PEO solution. It should be emphasized that that for such molecular weight and concentration the solution becomes relatively viscous. The 50-80 nm range then, however, comprises 78% of the total nanofibers. For PEO the horizontal setup was employed to prevent dripping of solution at lower concentrations.

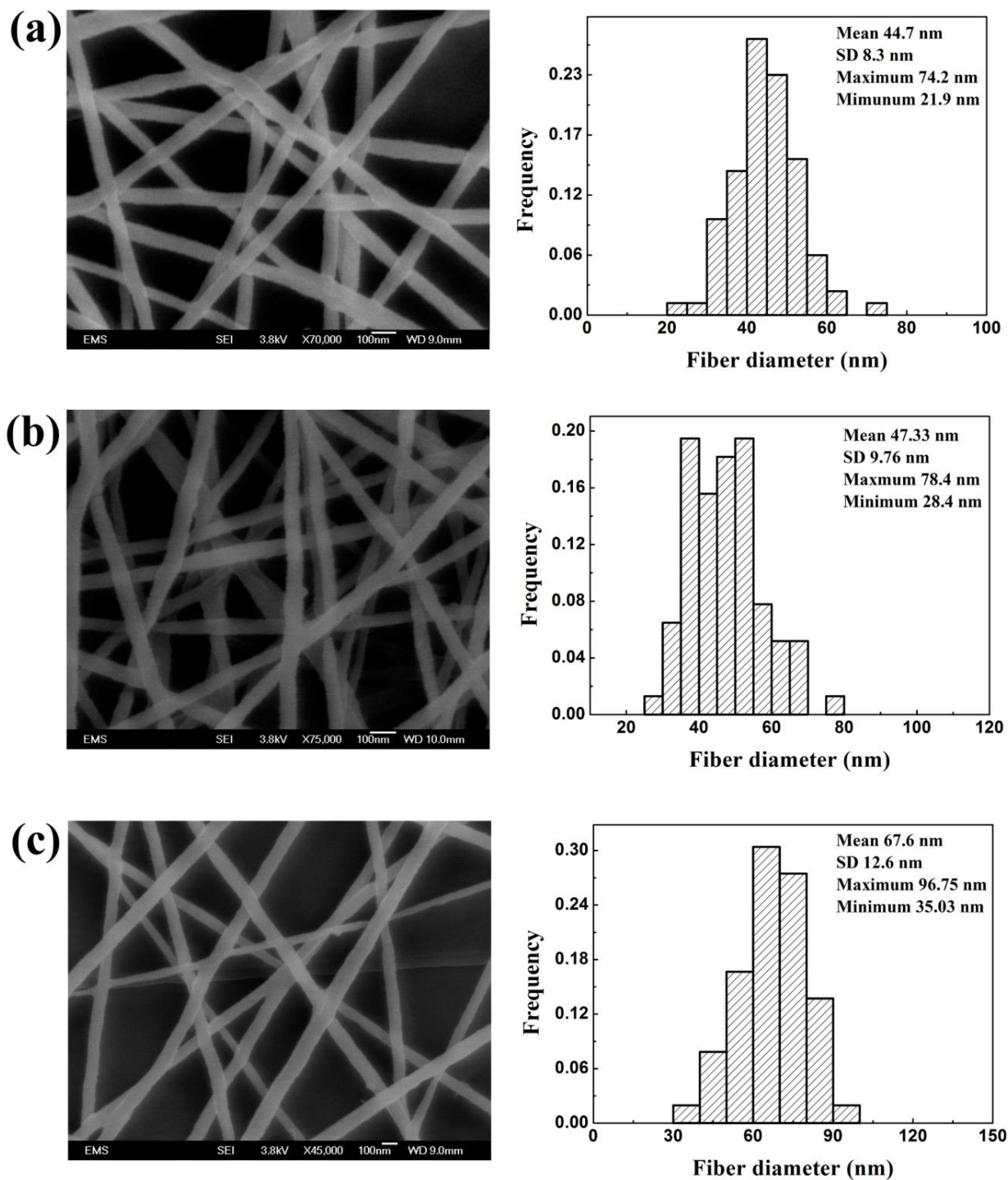


Figure 4.9: SEM images of the PEO nanofibers and their fiber size distributions where different panels correspond to different polymer concentrations: (a) 3 wt%, (b) 4 wt%, (c) 5 wt%.

Along with PVA, flow-induced crystallization was also observed with PEO, especially for low concentrations. The 4 wt% PEO solution was prepared in water and supersonically blown. Shish-kebab structures [Yarin et al. (2014), Zussman et al. (2003)] were observed in those fibers along with beads. These beads, may result from capillary instability and uneven drying.

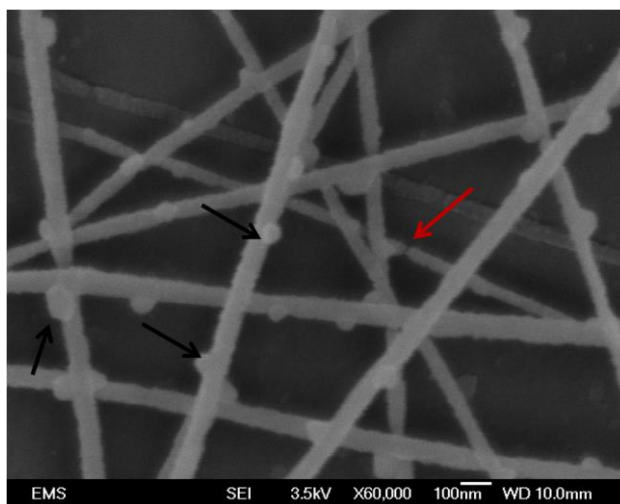


Figure 4.10: Flow-induced crystallization and beads on nanofibers observed in PEO nanofibers formed from 4 wt% solution in water: crystallized area marked by red arrow and beads marked by black arrows.

4.5 Conclusion

The results obtained in this chapter demonstrate the applicability of the electrically-assisted supersonic solution blowing to several polymers like Nylon 6, PVDF, PAN, PEO and PVA in different solvents to form the extremely thin nanofibers, in most cases close to the ~50 nm range. It was shown that at an appropriate concentration of Nylon 6 in formic acid (15 wt%) 20-50 nm nanofibers could be formed in significant quantity which is impossible with electrospinning. In

those supersonically- blown nanofibers a novel crystal phase, the so called χ -phase was discovered with a much smaller d-spacing than in the other stable phases of Nylon 6. Also the individual nanofibers were extremely stiff. This method was applicable to other polymers as well. Acetone:DMF (2:3) blend was found to be a suitable solvent for PVDF and it has been shown that more than 70% of nanofibers in a mat formed from 14 wt% PVDF solution are below 50 nm. For higher PVDF concentrations this number decreases, but still a majority of the nanofibers belong to the ~50 nm range. For PAN, 4 wt% solution in DMF was found to be the most suitable one for forming nanofibers below 50 nm. The fiber size practically remained unchanged from 5 to 6 wt% PAN concentration in DMF, which is an indication of macromolecular entanglement in the solution in a critical domain around 5 wt%. PVA and PEO were the other two polymers which formed nanofibers below 50 nm quite easily at low concentrations. However, for PVA, the fiber sizes were very close to 50 nm, which revealed a narrow fiber-size distribution. These ultrafine nanofibers can be used for various applications, particularly in filtration, sensors, virus entrapment, separation, cell culture, etc. because of their extremely small size, 1D shape, an increased porosity and a large surface area. Later in this thesis ultrafine nanofibers will be used for filtration and for thermal management applications where the supersonic solution blowing will play a critical role to produce ultrafine nanofibers.

CHAPTER 5

APPLICATION OF SOLUTION-BLOWN 20-50 nm NANOFIBERS IN FILTRATION OF NANOPARTICLES: THE EFFICIENT van der WAALS COLLECTORS

This chapter has been previously published in Sinha-Ray, Sumit et al. (2015a).

Reprinted with permission from [Sinha-Ray, Sumit, Sinha-Ray, Suman, Yarin, A. L. and Pourdeyhimi, B. (2015a), Application of Solution-blown 20-50 nm Nanofibers in Filtration of Nanoparticles: The Efficient van der Waals Collectors, Journal of Membrane Science, 485, 132-150]. Copyright 2015 ELSEVIER.

5.1 Introduction

This work aims enhancement of filtration capability of commercially available filters by applying a thin layer of supersonically blown 50 nm nanofiber in conjunction with single layer of electrospun nanofiber layer. The next section describes the materials and the experimental setup, followed by a section on results and discussion. This is followed by theoretical development and finally conclusions are drawn.

5.2 Experiments

5.2.1 Materials

The experiments were conducted using three different grades of commercial filters: (1) glass filter-GC90 of 90 mm diameter, and mean pore size 2.7 μm and thickness 1 mm, and (2) cellulose filters of mean pore size 17 μm , thickness 0.6 mm (referred to as *cellulose a* later), and (3) of mean pore size 2.5 μm , thickness 0.61 mm (referred to as *cellulose b* later). Polyacrylonitrile (PAN) (molecular weight 130 kDa) solution in N,N-dimethylformamide (DMF)

was used to form polymer nanofibers by electrospinning and deposit them on top of the above-mentioned filters. Both PAN and DMF were obtained from Sigma-Aldrich. Nylon 6 (molecular weight of repeat unit 104.8 Da) was used as a polymer to form nanofibers by means of the electrically-assisted supersonic blowing [Sinha-Ray, Suman et al. (2013)]. These nanofibers were deposited on top of the filters as well, either directly, or on top of the electrospun PAN nanofibers. Nylon 6 was also used for electrospinning in additional experiments to produce filters with both solution-blown and electrospun nylon 6 nanofibers deposited on the base filter medium. Nylon 6, along with its solvent formic acid, was obtained from Sigma-Aldrich. Polypropylene filter holder (47 mm), obtained from Cole-Parmer was used in filtration experiments. Aqueous suspensions of copper nanoparticles, obtained from Skyspring Nanomaterials (~40-60 nm, as per manufacturer), at different concentrations were used as the suspensions to be filtered. Also, aqueous suspensions of polystyrene 100 nm nanoparticles, from Microspheres-Nanospheres were used.

5.2.2 Electrospinning

Electrospinning of 12 wt% PAN, dissolved in DMF and mixed for 24 h using a magnetic stirrer, was conducted using a syringe pump (obtained from New Era Pump System) pushing the polymer solution through an 18 gauge needle at a flow rate of 0.5 ml/h. The distance between the collector and the needle was kept at 12 cm and the electric field strength was sustained at 1.2 kV/cm. The collector was mainly an aluminum foil. The above mentioned filters, cut in 47 mm circles, were placed carefully on the foil so that the electrospun fibers can be collected on the filters as well (cf. Fig. 5.1). Electrospinning was conducted for 45 s on each of the filter samples,

which resulted in a very thin layer of nanofibers on the filters. After electrospinning was finished, the samples were carefully removed without damaging the fiber layers.

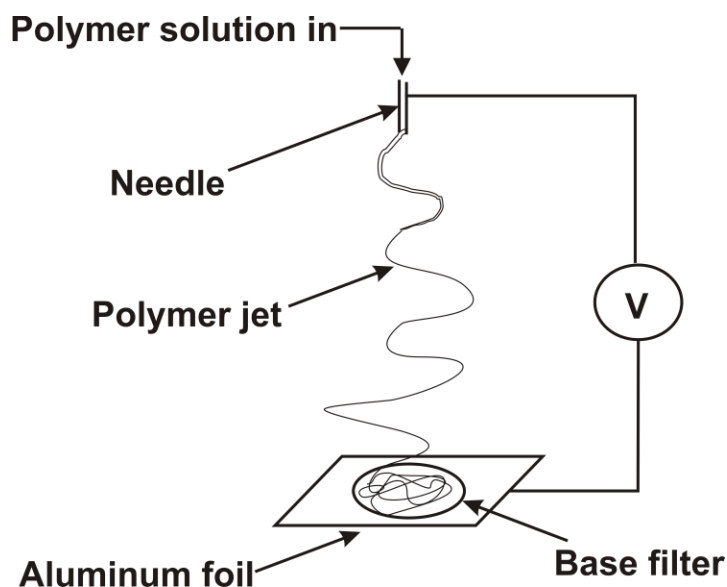


Figure 5.1: Schematic of the electrospinning setup and deposition of electrospun fibers on the filter samples.

5.2.3 Supersonic Solution Blowing

The electrically-assisted supersonic solution blowing was conducted as in referred in Chapter 4. The 15 wt% nylon 6 solution in formic acid, mixed for 8 h on a magnetic stirrer, was used in the electrically-assisted solution blowing experiments (nanofibers formed by this method will be denoted as supersonically solution-blown nanofibers). The pump was operated at 0.1 ml/h flow rate to pump the polymer solution through a 25 gauge needle, while the supersonic nozzle (209 L, obtained from Silvent) was operated at pressure of 5.5 bar to blow air at supersonic speed of 564 m/s. The electric potential was set up between the needle and the nozzle,

with the nozzle being grounded and the voltage was sustained at 7.5 kV. The electrically-driven polymer jet issued from the needle was attracted to the core of the supersonic nozzle and then got swept away by the high-speed air flow [Sinha-Ray, Suman et al. (2013)] and collected on the filters for 4 min at a distance of 22 cm from the tip of the nozzle (cf. Fig. 5.2).

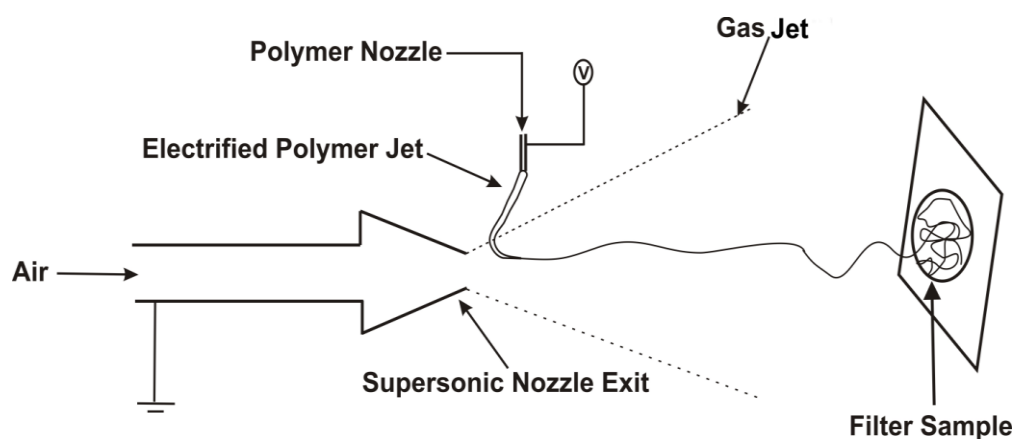


Figure 5.2. Schematic of the electrically-assisted supersonic solution blowing and deposition of fibers on top of the filters.

5.2.4 Filtration Procedure

Filtration experiments were conducted in two time frames: in *method (a)* a small volume of liquid (200 ml) was filtered for a short time (8-15 s), and in *method (b)* a larger volume of liquid (~4.5 liters) was filtered for a longer time (8 min).

For *methods (a) and (b)* 4 different filters were used for comparison: (i) base filters (i.e. glass or cellulose filters), (ii) base filters with electrospun PAN fibers on top of them, (iii) base filters with supersonically blown nylon-6 fibers on top of them, and (iv) base filters with electrospun PAN fiber layer first and then supersonically blown nylon-6 fibers on top of them

(referred to as dual-coated filters). The layers were deposited on the base filters as described in sections 5.2.2 and 4.2.3. Fig. 5.3a depicts the experimental procedure of *method (a)*. A 200 ml jar containing a certain concentration (e.g. 2 ppm, 1 ppm, etc.) of Cu nanoparticle suspension in water was attached to an air line to provide an external over-pressure of 150 mbar, measured by the pressure gauge (HHP2023, obtained from Omega) connected with the airline in parallel. The hydrostatic pressure was negligibly small compared to the applied over-pressure. The pressurized suspension then passed through the filter assembly. The modified filters were placed in the filter assembly in such a way that the suspension passed through the nanofiber layers first and then through the base filter. In particular, if the solution-blown layer was deposited over electrospun nanofibers, then the flow entered the filter medium first through the solution-blown layer, then the electrospun layer, and finally through the base layer. The pressure monitor showed practically no change in pressure in time. Three different concentrations, 2 ppm, 1 ppm, and 0.5 ppm of Cu nanoparticle suspensions in water were used for filtration with glass filters and *cellulose b* filters, whereas *cellulose a* filters were used to filter suspensions of 1 ppm, 0.5 ppm and 0.2 ppm. For a proper distribution of nanoparticles, a certain (e.g. 0.4 mg) mass of nanoparticles was suspended in 20 ml of water by means of sonication using a probe sonicator (Qsonica, 500 Hz). After 6 min of sonication the suspension was diluted with a pre-set (e.g. 180 mL) volume of water to obtain the required concentration, say 2 ppm. Particle-size distribution resulting from this preparation method is shown in Fig. 5.4a. The distribution was observed by the Dynamic Light Scattering (DLS) technique and was considered as the initial size-range of particles that reaches the filter along with the water. It is seen that even though the particle sizes were 40-60 nm, in reality they remain as agglomerates of different sizes ranging from 30 nm to 1500 nm. The most prominent intensity was observed for the mid-range particles ~200 nm (cf.

Fig. 5.4a). The duration of process (a) mostly varied in the range 8-15 s for all filters. Water samples were collected before and after the filtration experiment. The concentrations of metal nanoparticles in these samples were measured using Atomic Absorption Spectroscopy (AAS) [the device AAnalyst200 obtained from Perkin Elmer]. To measure concentrations of pristine and filtered nanoparticle suspensions denoted as C_{in} and C_{out} , respectively, AAS was used as follows. Metal nanoparticles in these solutions were dissolved by adding acid. Then, samples of such acidic solutions were subjected to the acetylene flame in AAnalyst200 device, which employs the classical spectroanalytical method to quantify the presence of metals. In addition, filters after the experiment were observed using Scanning Electron Microscopy (SEM, JEOL-JSM 6320F). The particle-size distributions in the upper layer of deposits on the filters were recovered from the micrographs of the very top layer.

Similar experiments were also conducted for aqueous suspensions of polystyrene nanoparticles of 100 nm. The measured particle-size distribution confirms that all the polystyrene particles were in the range sufficiently close to 100 nm (Fig. 5.4b). The experiments conducted using polystyrene nanoparticles were used for observation purposes only, and no efficiency study was associated with them, as these particles were non-metallic and the AAS instrument was inapplicable to such particles.

Fig. 5.3b illustrates the *method (b)* employed in the filtration experiments. The smaller jar was replaced by a bigger jar. The same process of displacing water with pressurized air was used, where the air pressure was kept at 120 mbar. The latter was measured during the entire experiment by a pressure gauge, and the hydrostatic pressure head was 30 mbar (the hydrostatic pressure head $P_{hydrostatic} = \rho_w g h$, where ρ_w is the water density, g is the gravity acceleration, and h is the height of water column). In the present case $h=30.48$ cm, which is equivalent to 30 mbar.

Therefore, the total pressure head of 150 mbar corresponded to the average face velocity of 0.6 cm/s, or to the average flow rate of 10 ml/s. An initial suspension sample was taken before the experiment to measure the concentration C_{in} using AAS. Samples were also collected to measure the concentration C_{fin} at the very beginning of the filtration process at 0 ml of water displaced and then after every 750 ml of water displaced. Sampling continued up to 4.5 liters of water have been displaced. All concentrations of Cu nanoparticles in the samples were measured using AAS. The pressure was constant for the entire experiment duration and flow rates were measured every 20 s using a stopwatch. The sampling continued until 4.5 liters of water have been displaced, and the duration of the experiments when the flow rate was measured was 8 min. The suspensions have been replenished from the backup reservoir during the entire experiment.

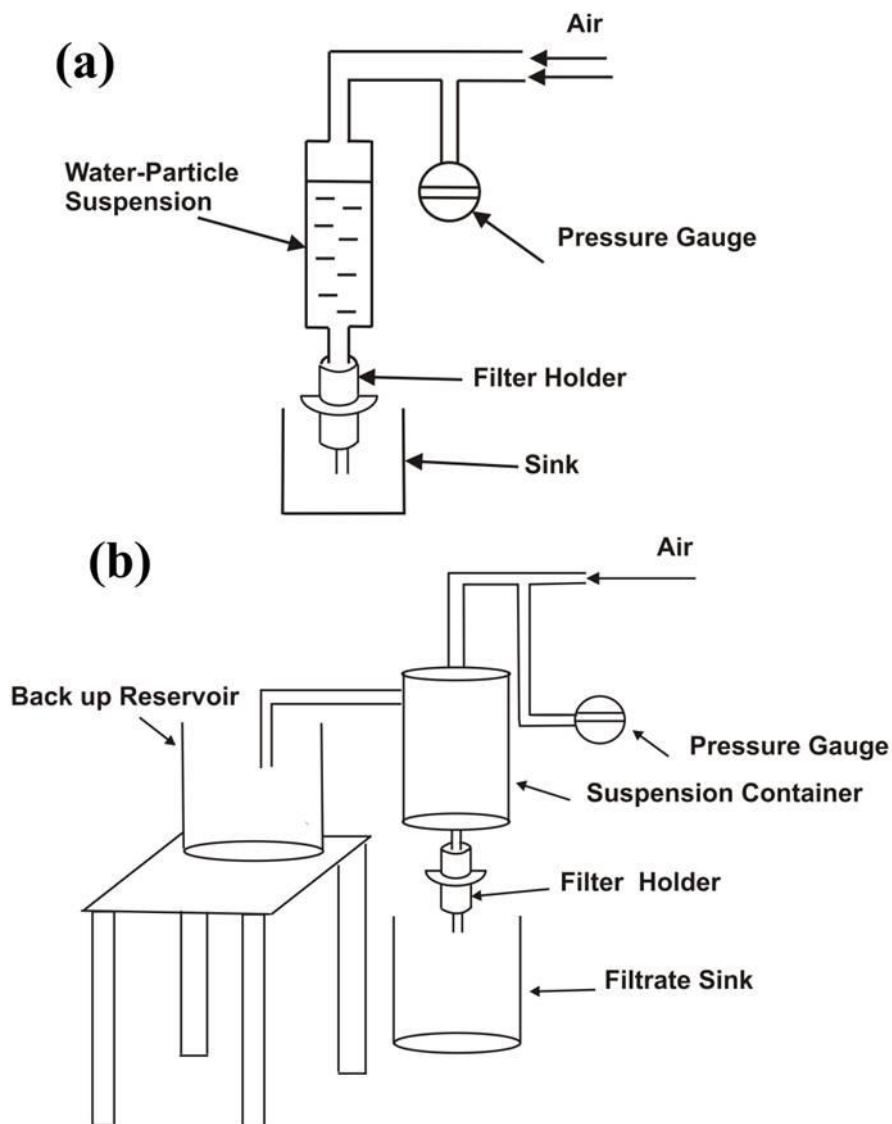


Figure 5.3. Schematic of the experimental setups employed for the filtration experiments. Panel (a) depicts the short-time experimental setup corresponding to method (a). Panel (b) shows the longer-range experimental setup corresponding to method (b).

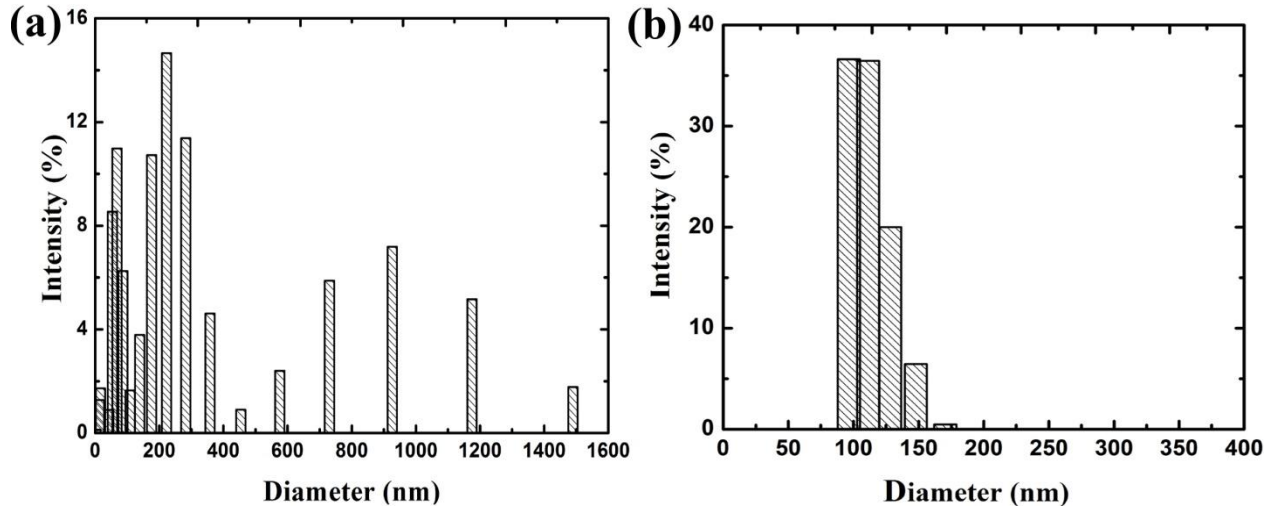


Figure 5.4. The initial particle-size distribution of nanoparticles in an aqueous suspension after 6 min of sonication observed using Dynamic Light Scattering (DLS): panel (a) for Cu nanoparticles, and panel (b) for polystyrene nanoparticles.

5.3. Results and Discussion

5.3.1 Method (a)

To elucidate the effect of nanofibers on nanoparticle interception, short-time experiments were conducted using several filters media. According to Darcy's law $\dot{Q} = kA|\Delta P / \Delta L| / \mu$ [Whitaker (1986)], where \dot{Q} is the volumetric flow rate, k is the filter media permeability, A is the cross-sectional area, μ is the liquid viscosity, ΔP is the pressure drop across the filter, and ΔL is the depth of the filter. The focus in this experiment was solely on the thin filter samples, minimizing the depth effect, showing the effect of the smallest nanofibers in capturing particles to elucidate the corresponding filter efficiency changes, especially in regards to the most penetrating particle sizes close to 300-400 nm [Barhate and Ramakrishna (2007), Gopal et al.

(2006)]. The experiments conducted using glass filters employed three different concentrations of Cu nanoparticles, namely, 2 ppm, 1 ppm, and 0.5 ppm. Care was taken to avoid any considerable change in the filters thickness while depositing nanofibers on them, and so the electrospun and supersonically blown nanofiber mats were deposited as thin as possible (cf. Fig. 5.5a with the supersonically blown nanofiber mat alone and Fig. 5.5b with the supersonically blown nanofiber mat above electrospun nanofiber mat). From the SEM images (Figs. 5.6, 5.7 and 5.9) it is seen that there were only a few electrospun nanofiber layers and a very few supersonically blown nanofiber layers. Even though the glass filters have a relatively high basic efficiency (cf. the green line in Fig. 5.8a), the nanofibers were able to increase further the performance of these filters.

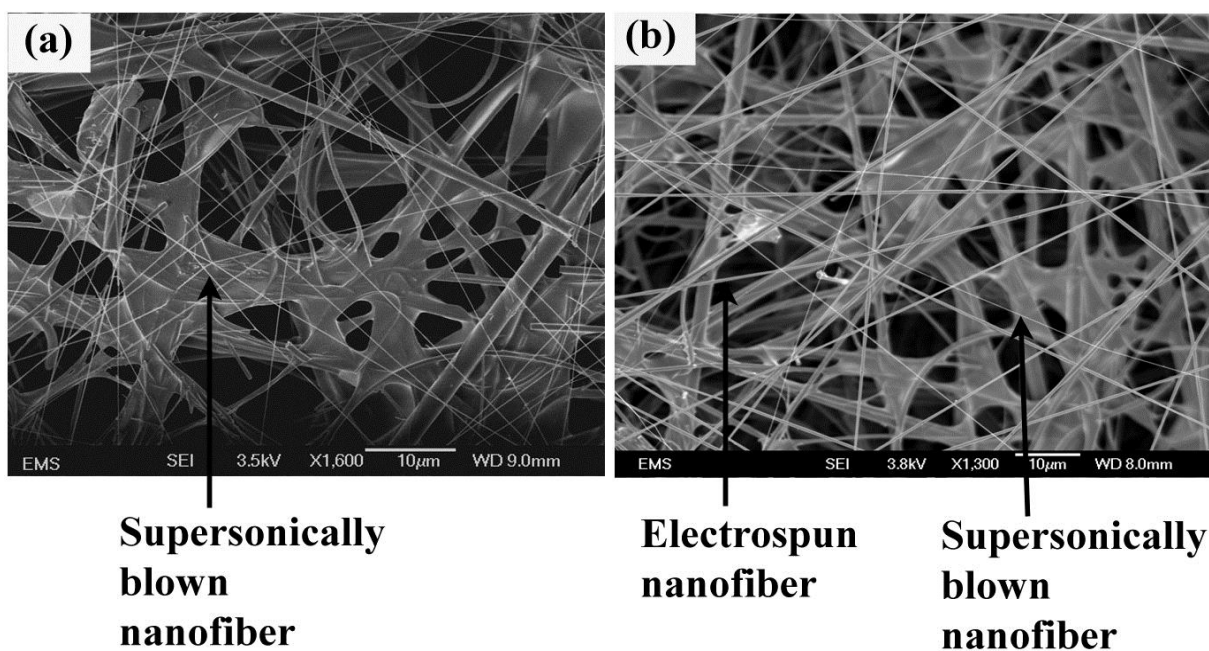


Figure 5.5. SEM images of glass filter with (a) supersonically blown nanofiber mat (nylon 6) deposited on it, and (b) electrospun nanofiber mat (PAN) with supersonically blown nanofibers (nylon 6) on top of it. The nanofiber mats are very thin (only a few layers).

Fig. 5.6 illustrates the effect of nanofibers on nanoparticle removal during filtration, and in addition, the particle-size distribution in the layer of the deposited nanoparticles.

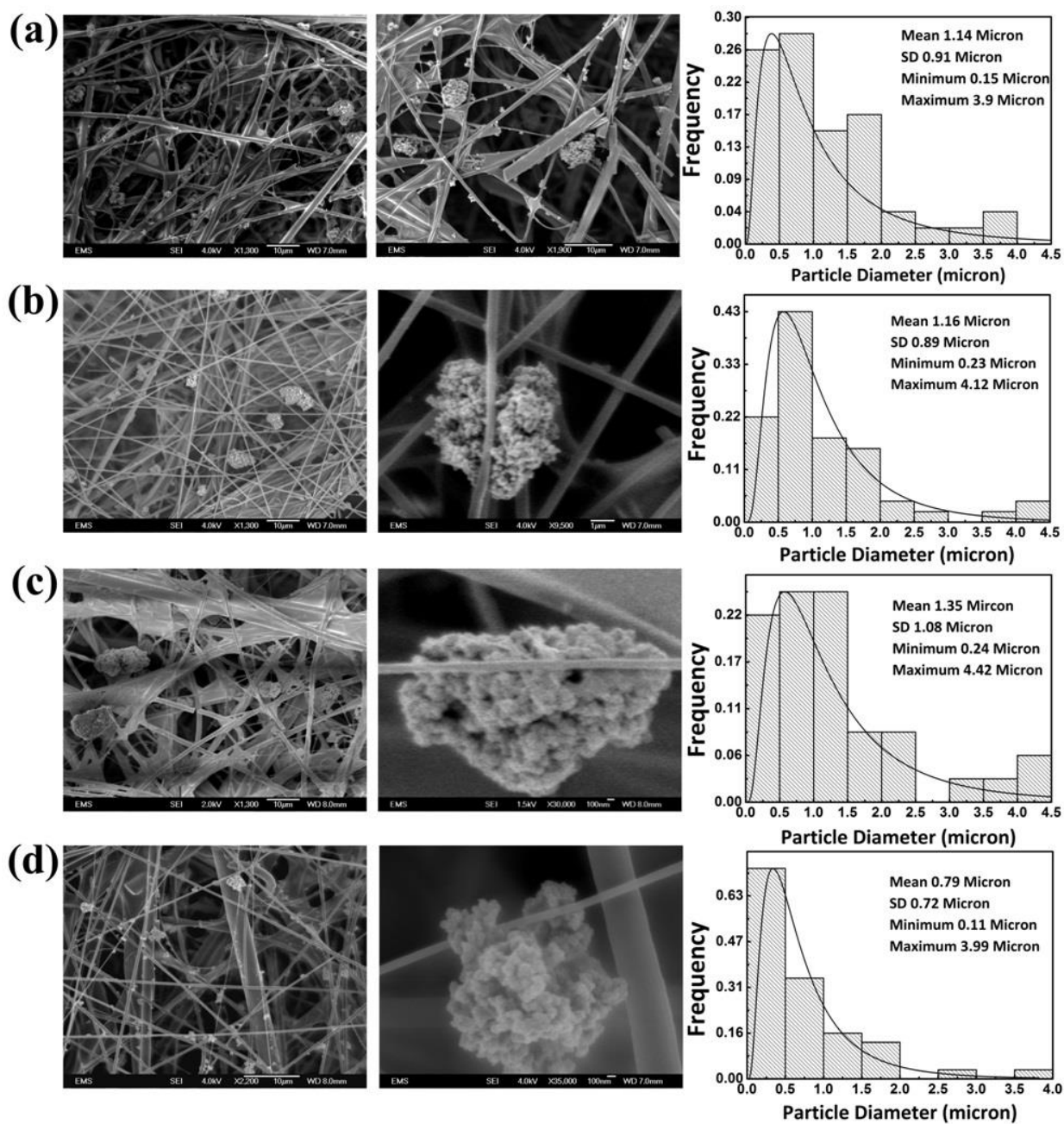


Figure 5.6. SEM images of glass filters after filtration by *method (a)*- as a whole (the left-hand side images); of the particle-capturing mode on the nanofibers (in the middle); and the particle (cluster)-size distributions (the right-hand side panels) for the initial concentration of 2 ppm. Note that what is seen are mostly particle clusters accumulated in the filters. Panels (a), (b), (c), and (d) correspond to the base filter, the base filter with deposited electrospun PAN nanofibers, to the base filter with supersonically blown nylon 6 nanofibers, and to the dual coated filter, respectively. Particle size distributions were measured by using particle areas seen in the SEM images to evaluate their radii, and then to calculate their volumes.

Figs. 5.6a-d illustrate the mode of capturing nanoparticles from the aqueous suspensions by different filters. In Fig. 5.6a it is seen that bigger particles are being captured by the filter pore, i.e. by sieving. In the case of glass filters with electrospun nanofibers, a mixed mode of particle removal by pore capturing and impact interception is seen in Fig. 5.6b. It is worth mentioning that particles are also seemed to be entrapped predominantly in the nanofiber layers, which is illustrated in the SEM image [the middle panel of Fig. 5.6b]. Figs. 4.6c and 4.6d show that the particles are not only being captured by the big pores between the fibers of the basic filter, but are also deposited onto the smallest nanofibers, namely onto the 20-50 nm solution-blown nanofibers. In fact, the majority of the particles are being deposited on the smallest nanofibers. It is also seen that particles, even 300-1500 nm in diameter, are “hanging upside down” from the smallest nanofibers (~50 nm nanofibers), yet no breakage of these fibers is visible. The collected particles are much larger than the fibers. They are hardly intercepted by a simple impact and seemingly “embrace” the nanofibers, as seen in Figs. 4.6c and 4.6d (in the middle).

Having a dual layer of electropun and supersonically blown nanofibers [cf. Fig. 5.6d] allowed capturing 42.1% of the smaller particles in the range 200-500 nm. These smaller particles formed clusters embracing the nanofibers. Fig. 5.6d also shows that the electropun and solution-blown nanofiber layers do not block significantly the bigger pores and thus do not increase significantly the pressure drop required to sustain a given volumetric flow rate.

The particle-size distribution of the captured particles seen in the SEM image in Fig. 5.6d shows that in the case of electropun and supersonically blown nanofibers jointly deposited on the filter, the percentage of the particles in the range below 500 nm is 42.1%, as mentioned above, as compared to the cases of the basic filter, 20.53%, in Fig. 5.6a, the base filter with electropun nanofibers alone, 18.49%, in Fig. 5.6b, and the base filter with solution-blown nanofibers alone, 14.44%, in Fig. 5.6c. It should be emphasized that the above percentages of the intercepted particles were calculated following [Hayter (1996)]. The experimental data in the right-hand side panels in Figs. 4.6a-4.6d were approximated by the log-normal distribution as provided in previous chapter (repeated here for better understanding)

$$f(x|M, \sigma) = \frac{1}{x\sigma\sqrt{2\pi}} \exp\left(-\frac{(\ln x - M)^2}{2\sigma^2}\right) \quad (5.1)$$

where the parameters M and σ are related to the mean value m and the variance v through the following expressions.

$$M = \ln\left(\frac{m^2}{\sqrt{v + m^2}}\right), \quad \sigma = \sqrt{\ln\left(\frac{v}{m^2 + 1}\right)} \quad (5.2)$$

As mentioned in the Introduction, in the case of water filtration diffusion capturing cannot be a significant nanoparticle removal mechanism [Lee et al. (1993)]. The results shown in Fig.

5.6 suggest that the van der Waal (vdW) interactions [Gregory(1981), Kirsch (2003), Rosenfield and Wasan (1974), Zhang et al. (2006), Hamaker (1937). Israelachvili (1997)] cannot be neglected in the small scales introduced by the 20-50 nm solution-blown nanofibers. This conclusion is facilitated by the theoretical findings discussed below in section 5.4.

In Fig. 5.7 it is seen that the nanometer-sized particles are caught by the smallest fiber, on which they tend to conglomerate and grow along the surface.

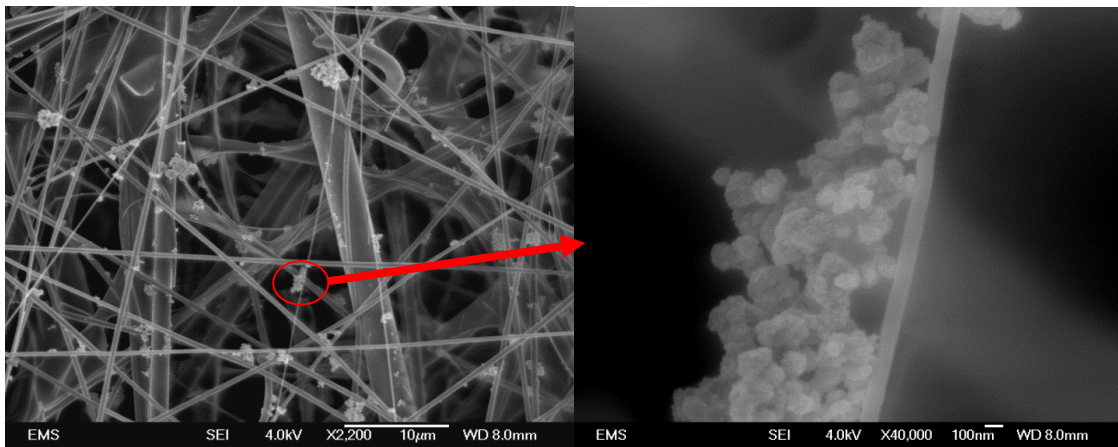


Figure 5.7. SEM image of a dual-coated filter sample: the overall view is on the left-hand side, and the zoomed-in view of a single smallest nanofiber (supersonically blown nylon 6 nanofiber) with nanoparticles being clustering on it is shown on the right-hand side.

The filtration efficiencies were calculated using the following equation [Gopal et al. (2006)]

$$\text{Efficiency(\%)} = \left(1 - \frac{C_{\text{out}}}{C_{\text{in}}} \right) \times 100 \quad (5.3)$$

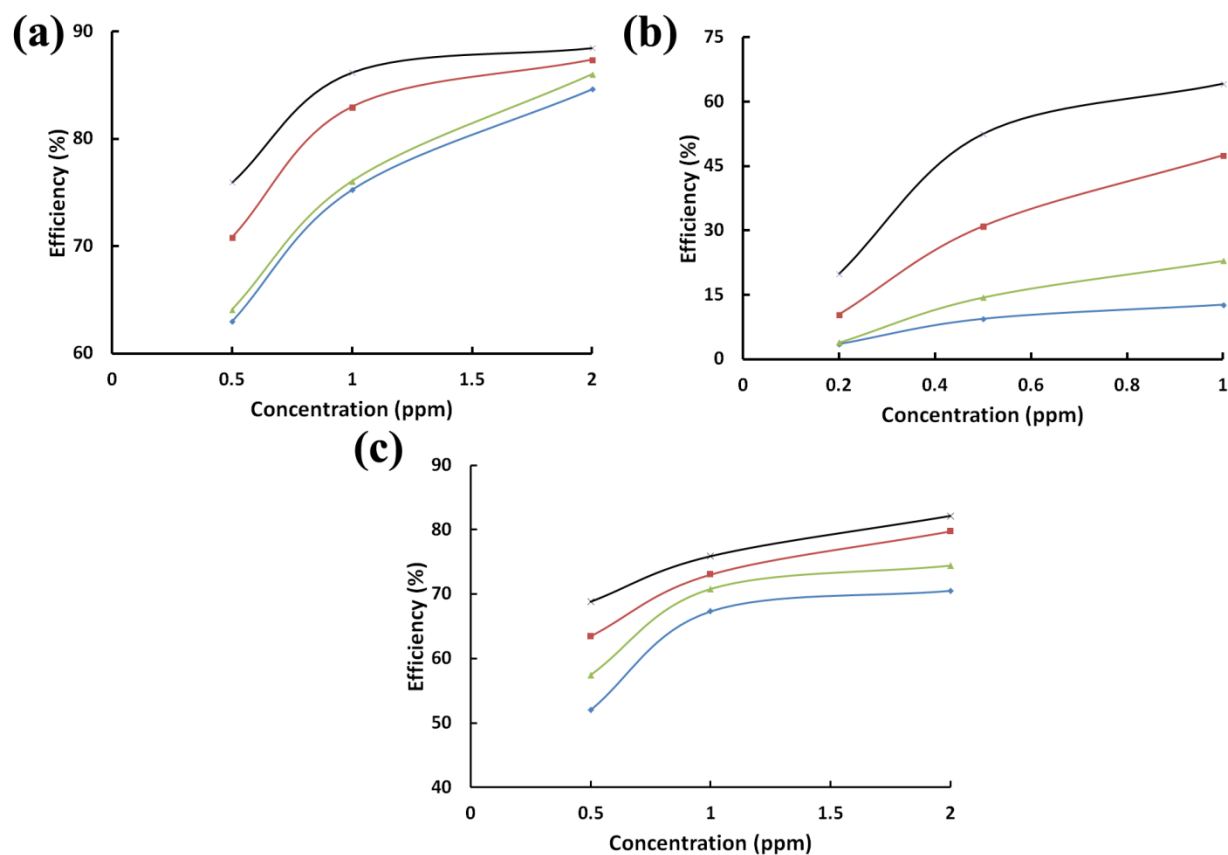


Figure 5.8. Efficiencies of the base and modified filters measured at different nanoparticle concentrations [the experiment conducted by *method (a)*]. Panel (a) corresponds to glass filter, panel (b) to *cellulose a*, and panel (c) to *cellulose b* filters. The blue, green, red and black lines correspond to the base filter, the base filter with electrospun PAN nanofibers, the base filter with supersonically blown nylon 6 nanofibers, and the dual-coated filter, respectively. The nanoparticle size range is provided in Fig. 5.4.

It should be emphasized that in this equation the initial concentration C_{in} is always known very accurately due to suspension preparation (and also verified with the AAS results), and the after-filter concentration C_{out} is also measured very accurately using AAS. The corresponding

results are shown in Fig. 5.8. It is seen that the originally low filtration efficiency of the glass filters can be significantly increased by a very thin layer of ultrafine nanofibers obtained by supersonic solution blowing, especially when very low concentration suspensions are filtered. The latter are practically important and would be difficult to achieve without increasing the filter thickness, and thus, the pressure drop, if nanofibers would not be used.

Similar results were obtained for *cellulose a* and *b* filters. As mentioned in the section 5.2.1, *cellulose a* filters have larger pore sizes compared to the glass filters, which inevitably results in their lower efficiency, especially in the range of submicron particles. For those filters, the experiments were conducted with 1 ppm, 0.5 ppm and 0.2 ppm of Cu nanoparticle suspensions. In such cases the base filters capture practically nothing (as the SEM images show). The effective efficiency increase in these filter samples was dramatic. The increase in the efficiency of the dual-coated filters compared to the corresponding base filters was 52%, 43% and 24% for 1 ppm, 0.5 ppm, and 0.2 ppm, respectively. *Cellulose b* filter samples had pore size comparable to the glass filter and their performance was similar to that of the glass filters when they were subjected to the flows of the 2 ppm, 1 ppm and 0.5 ppm Cu-nanoparticle suspensions through the base and modified filters.

Note that at higher concentrations the efficiency increase of the modified glass filters in comparison to the base filters may not be as high as at lower concentrations (cf. Fig. 5.8). Nevertheless using the dual coating with electrospun and solution-blown nanofibers results in a more than two-fold removal of the below-500 nm nanoparticles when modified filters are used. It means that in spite of a highly permeable base membrane, it is still possible to capture a significant percentage of such nanoparticles. The dual nanofiber coating becomes especially efficient for the nanoparticle size ~300 nm.

It should be emphasized that in the short-time experiments the efficiencies of all filter media increased with nanoparticle concentration in original suspension according to Fig. 5.8. The SEM images clearly show that in such experiments the pores are not clogged. Therefore, nucleation of new clusters in the porous media is enhanced as the nanoparticle concentration increases, as well as each nanoparticle cluster adds an additional surface area for the oncoming nanoparticle aggregation.

The experiments with modified glass filters were also conducted with polystyrene nanoparticles at 2 ppm concentration. This was done to elucidate the effect of the smallest nanofibers and to observe the nanofiber/nanoparticle interactions. It should be emphasized that the experiments with polystyrene nanoparticles were conducted only for the observation purposes and not to measure the filtration efficiency via AAS (which is impossible with polystyrene). Namely, (a) to observe whether the capture pattern depends on the choice of material, and (b) to observe whether the modified filters can intercept particles with a narrow size distribution (the polystyrene nanoparticles had sizes sharply-centered about 100 nm, whereas the copper nanoparticles had had a wider size distribution). The SEM images show that irrespective of the type of nanoparticles (Cu nanoparticles in Figs. 4.6 and 4.7, or polystyrene nanoparticles in Fig. 5.9) the smallest nanofibers remove them similarly well. The polystyrene nanoparticles were not clustered originally (cf. Fig. 5.4b). Therefore, their clusters in the SEM images in Fig. 5.9 reveal the aggregation on the nanofibers and suggest once more the van der Waals attraction as the mechanism.

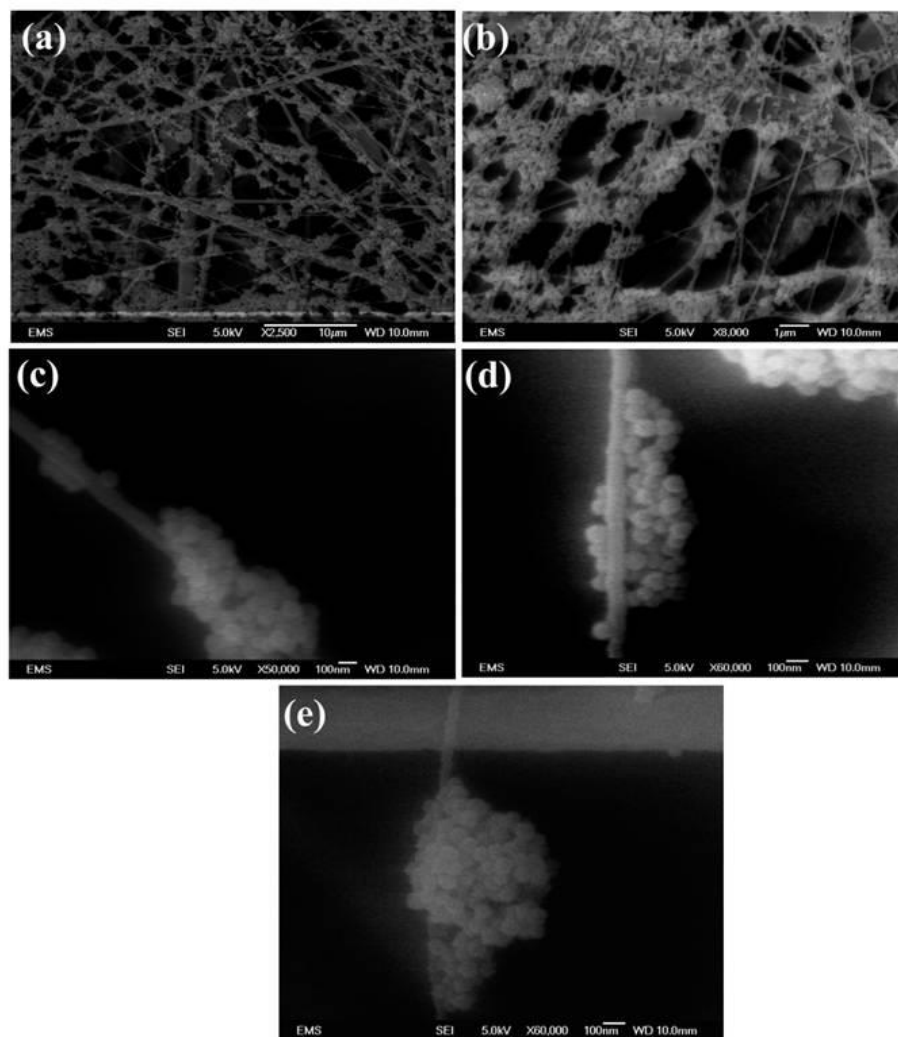


Figure 5.9. SEM images of dual coated glass filters after the experiment with 2 ppm polystyrene nanoparticles of 100 nm. Panels (a) and (b) shows two different overall views of the dual-coated filters capturing nanoparticles. Panels (c), (d) and (e) reveal the effect of individual supersonically blown nylon 6 nanofibers in catching and clustering the nanoparticles.

Electrospinning of PAN produces 300-500 nm sized nanofibers, which is the fiber size sufficiently separated from the size of the nylon 6 solution-blown nanofibers ~20-50 nm important for the van der Waals force-related nanoparticle interception. Electrospinning of nylon

6 results in nanofibers close to 100 nm. A joint SEM observation and discrimination of such nanofibers from 20-50 nm fibers is not an easy task. However, it is instructive to verify that the addition of the 20-50 nm solution-blown nylon 6 nanofibers to electrospun 100 nm nanofibers formed from the same material nylon 6 still significantly enhances filtration efficiency. This was demonstrated in a series of additional short-time experiments, with the results listed in Table 5.1.

Table 5.1. Filtration efficiency of modified filters with nylon 6 electrospun and solution-blown nanofibers.

Modified filter type	Initial concentration (ppm)	Final concentration (ppm)	Efficiency (%)
Base filter with electrospun nanofibers alone (nylon 6)	2	0.34	83
	1	0.22	78
Base filter with dual coating (nylon 6 electrospun and solution-blown nanofibers)	2	0.19	90.5
	1	0.16	84

The results shown in Table 5.1 clearly corroborate the fact that the dual-coated filters outperform the filters with electrospun nanofibers alone not because nylon 6 outperforms PAN, but because 20-50 nm nanofibers, which introduce the van der Waals forces as an effective interception physical mechanism, outperform any larger electrospun fibers (either nylon 6 or PAN).

5.3.2 Method (b)

As mentioned above, the short-time experiments of *method (a)* were conducted to elucidate the interception of nanoparticles by nanofibers (especially by the smallest nanofibers) before any cake formation happens. In addition, since the nanofiber layer is the first layer that encounters the oncoming flow, it is also necessary to observe its performance in a long-time experiment, in particular, to verify the absence of any structural damage to the smallest nanofibers caused by nanoparticle clusters and viscous drag imposed by the flow. Therefore, all the filters were tested in a longer-time experiment, which was termed as *method (b)*. The main aim of this experiment was to observe the modified filter performances during a longer exposure to the test suspensions and to observe the nanoparticle deposition patterns. As was mentioned before, during these experiments the pressure was kept constant and the volumetric flow rate was measured. According to Darcy's law, volumetric flow rate is related to filter permeability. The filters were modified as described before in section 5.2.1 and the nanofiber layers were very thin, not to affect the pressure drop. The experiments were carried out using the 2 ppm, 1 ppm and 0.5 ppm Cu nanoparticle suspensions. The results are shown in Figs. 4.10-4.14.

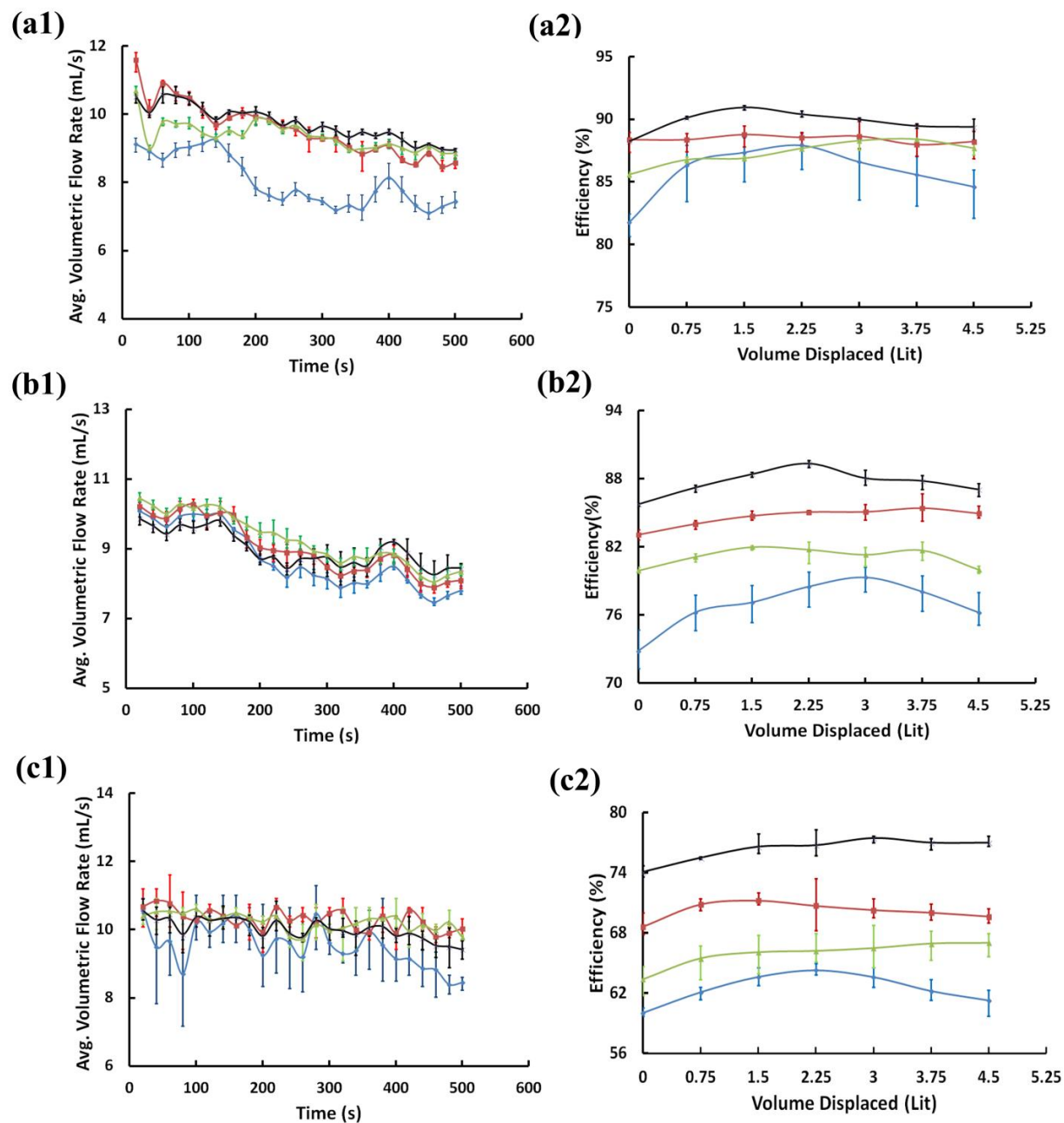


Figure 5.10. Base and modified glass filters for three different concentrations [the experiment conducted by *method (b)*]: (a) 2 ppm, (b) 1 ppm, (c) 0.5 ppm. Numeral 1 of each graph corresponds to the average flow rates for different concentrations, and numeral 2 to the data on the efficiencies of different samples at the concentrations tested. Blue, green, red and black curves correspond to the base filter, base filter with electrospun PAN nanofibers, base filter with nanofibers and nanofibers.

supersonically blown nylon 6 nanofibers, and base filter with electrospun PAN and supersonically blown nylon 6 nanofibers (i.e. the dual-coated filters), respectively. The average values were found based on three trials and the error bars show the maximum and minimum deviations from the average values.

According to Fig. 5.10, for the 2 ppm suspension the average flow rate through the base glass filter decreases within the first 50 s, and later rises up again followed by a period of a relatively steady flow rate. The corresponding filtration efficiency shows a reverse pattern. Initially the filter efficiency increases in time, and then a decrease in the efficiency is observed. The filter efficiency at the later time becomes steady on the background of a relatively steady flow rate. The drop in the volumetric flow rate and the accompanying increase in the filtration efficiency correspond to the cake formation inside the filter. The higher the content of the smaller particle in fluid, the faster the filter is clogged. Since in the test suspensions the nanoparticle sizes were mostly in the range of ~200-300 nm, the particles began to clog the pores relatively fast. A further increase in the flow rate with a corresponding decrease in the filter efficiency is indicative of dislodging of the nanoparticles from the filter. The observed slightly 'zigzag' pattern of the dependence of the flow rate on time is thus indicative of the clogging-dislodging process occurring inside the filter in time. For the glass filters with supersonically blown nanofibers (corresponding to the green lines in Fig. 5.10) the increase in the efficiency was greater than that for the base one, though by a small margin. However, the flow and the efficiency trends were completely different. The flow rate became steady within 100 s from the beginning of the experiment, which suggests that no clogging occurred in this case. Accordingly, the efficiency increased in time. The steady average flow rate was higher in the case of the filter

with the supersonically blown nanofibers than that for the base filter. As explained in regards to *method (a)*, the smallest nanofibers capture the nanoparticles ~200-300 nm by presumably van der Waals attractive forces. In time, the nanoparticle clusters grow on these nanofibers. This helps the 200-300 nm nanoparticles to be removed from water flow, accumulates them on rarely spaced smallest nanofibers and prevents the overall pore clogging.

Figs. 4.10 a2, 4.10b2 and 4.10c2 show that there are two distinctly different trends in the efficiency variation with volume displaced. Namely, (i) as the nanoparticle concentration in suspension decreases, the efficiency of the dual-coated filter becomes significantly higher than that of the base filter, and (ii) the efficiency of the dual-coated filter remains almost constant irrespective of the volume displaced, while the efficiency of the base filter decreases significantly. The latter points at the cake formation in the base filter contrary to the dislodging of collected nanoparticle clusters in the dual-coated filter. These results are statistically significant, as the error bars in Fig. 5.10 reveal. Note in addition, that in filtration the challenge is to remove nanoparticles at very low concentrations, where the conventional base filter does not work properly, as Fig. 5.10c2 shows. On the contrary, the dual-coated filter outperforms the base filter by about 14% at 0.5 ppm, according to Fig. 5.10c2.

The SEM images illustrating the nanofiber performance, as seen on the filter surface, are shown in Fig. 5.11. Since the electrospun fibers were of the sizes of 300-500 nm (cf. Fig. 5.5), these nanofibers captured particles predominantly via simple interception and in some cases by sieving, as is seen in Fig. 5.11. The average flow rate in this case was higher than that for the base filter. It shows a decreasing pattern with similar ‘zigzags’, albeit less prominent than that for the base filter. Accordingly, the efficiency pattern is mostly steady and plateaued and distinctively higher than that of the un-modified base filter. The dual-coated filter revealed the

best results in terms of the efficiency and flow rates. This filter effectively removes the ~200-300 nm particles and retains them at the filter surface, which results in a significant increase in the efficiency, as compared to the filters modified with only electrospun or only the supersonically blown nanofibers. The dual-coated filter avoids an intact cake formation characteristic of the base filter and also keeps the permeability relatively high (Fig. 5.11).

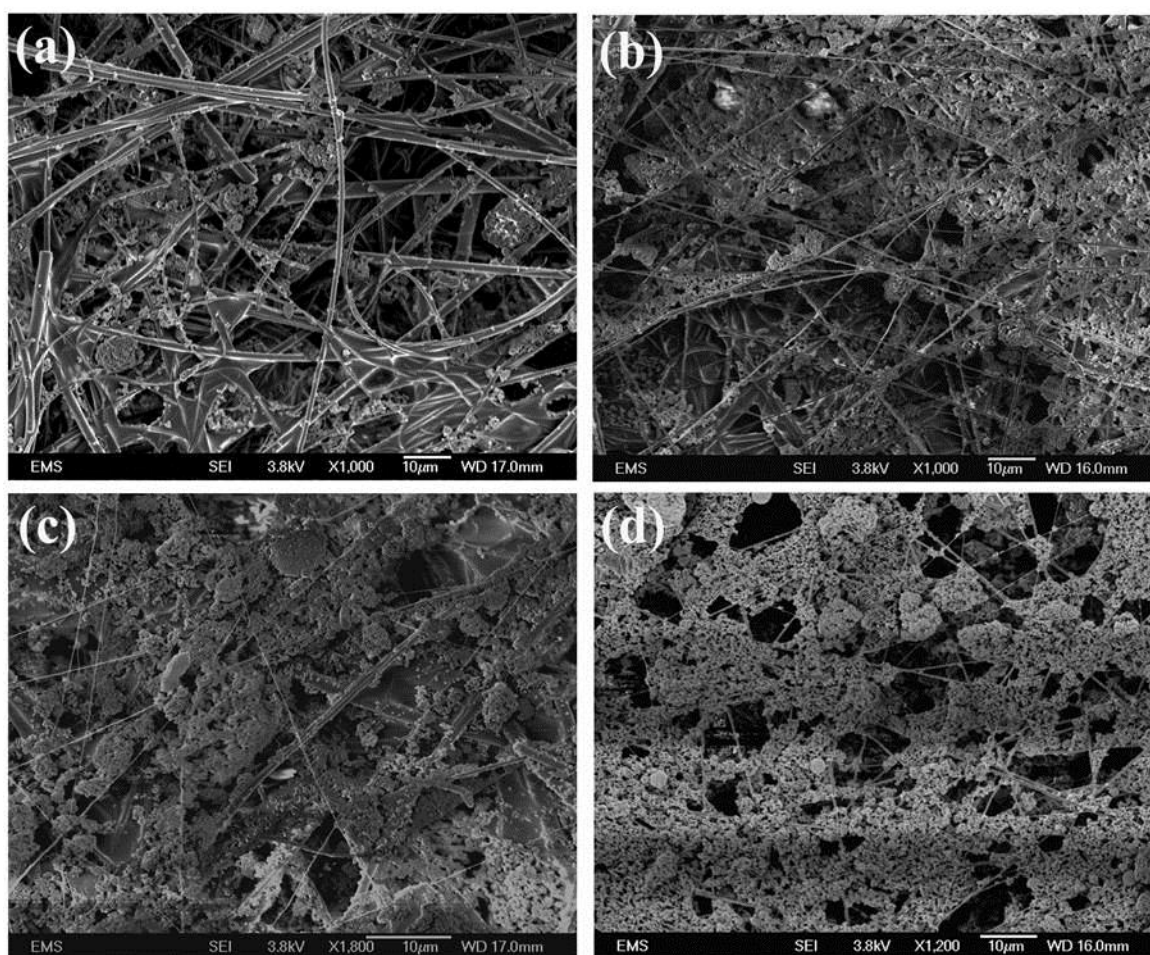


Figure 5.11. SEM images of glass filters after the experiment with the 2 ppm suspension of Cu nanoparticle conducted by *method (b)*. Panels (a), (b), (c) and (d) correspond to the base filter, base filter with electrospun PAN nanofibers, base filter with supersonically blown nylon 6 nanofibers, and the dual-coated filter, respectively.

A significant enhancement of the efficiency was observed in the modified glass filters with nanofibers compared to the base case in the experiments with 1 ppm and 0.5 ppm suspensions [cf. Figs. 4.10b2 and 4.10c2]. Also a relatively steady average flow across the filters can be seen for the modified filters, since cake formation is delayed. This sustains a high efficiency for a longer time compared to the base glass filter. The performance of the dual-coated filters (with electrospun and supersonically blown nanofibers) shows great promise at such nanoparticle concentrations which is also corroborated by Fig. 5.8. For the lowest nanoparticle concentration, an increase of 25% in the efficiency was observed. For the suspension concentration of 1 ppm nanoparticles tend to form clusters on the nanofibers more than on the base filter itself. This phenomenon is more prominent for the dual-coated filters, which is indicative of the van der Waals attraction of the smallest nanoparticles to the smallest fibers, with a subsequent clustering on them. At the nanoparticle concentration of 0.5 ppm, the average flow rate in the filters is higher than in the two cases considered above, because of the lower concentration. However, for the base glass filter, the flow rate fluctuated during the entire experiment, which can be attributed to the fact that the samples may vary from batch to batch. Nevertheless, for such a low concentration the flow rates were almost steady during the beginning of the experiment, but later on decreased, which indicates a delayed filter clogging. On the other hand, clogging was not observed in the modified filters. The difference in the efficiencies between filter samples was much more pronounced. Even at such a low concentration (0.5 ppm) the efficiency of the dual-coated filters was the highest.

The effect of nanofibers on the *cellulose a* filters was much more pronounced which is manifested by the corresponding efficiencies. Since these filters possess a relatively larger pore

size, the average volumetric flow rates were relatively higher than for the glass filters. In this case the base filter efficiencies were poor and were as high as 20% for 2 ppm suspensions and as low as 9% for 0.5 ppm suspensions. This means that the filters were relatively unclogged and there was practically no build-up of nanoparticles inside, whereas for the dual-coated filters the efficiency ranged from 70% to 50% for 2 ppm to 0.5 ppm suspensions, respectively. However, it can be seen in Figs. 4.12 [(a1), (b1) and (c1)] that the volumetric flow rates through the dual-coated filters (shown by black curves) in all the cases are close to those of the base filters. This indicates the fact that most of the nanoparticles are being retained by nanofibers at the filter surface. The build-up pattern of nanoparticles on supersonically blown nanofibers is also visible in both Figs. 4.13c. It is clearly seen how the smallest supersonically blown nanofibers facilitate the electrospun nanofibers and allow retention and clustering of nanoparticles. On the contrary, the base filters with only supersonically blown nanofibers do not reveal an enhanced efficiency. The experiments conducted for 8 min for all three different concentrations exhibit the same pattern of steady flow rate reached within the first 100 s of the experiment. The efficiencies of these filters also reached a steady value, with a small change in time, albeit their differences were much more pronounced.

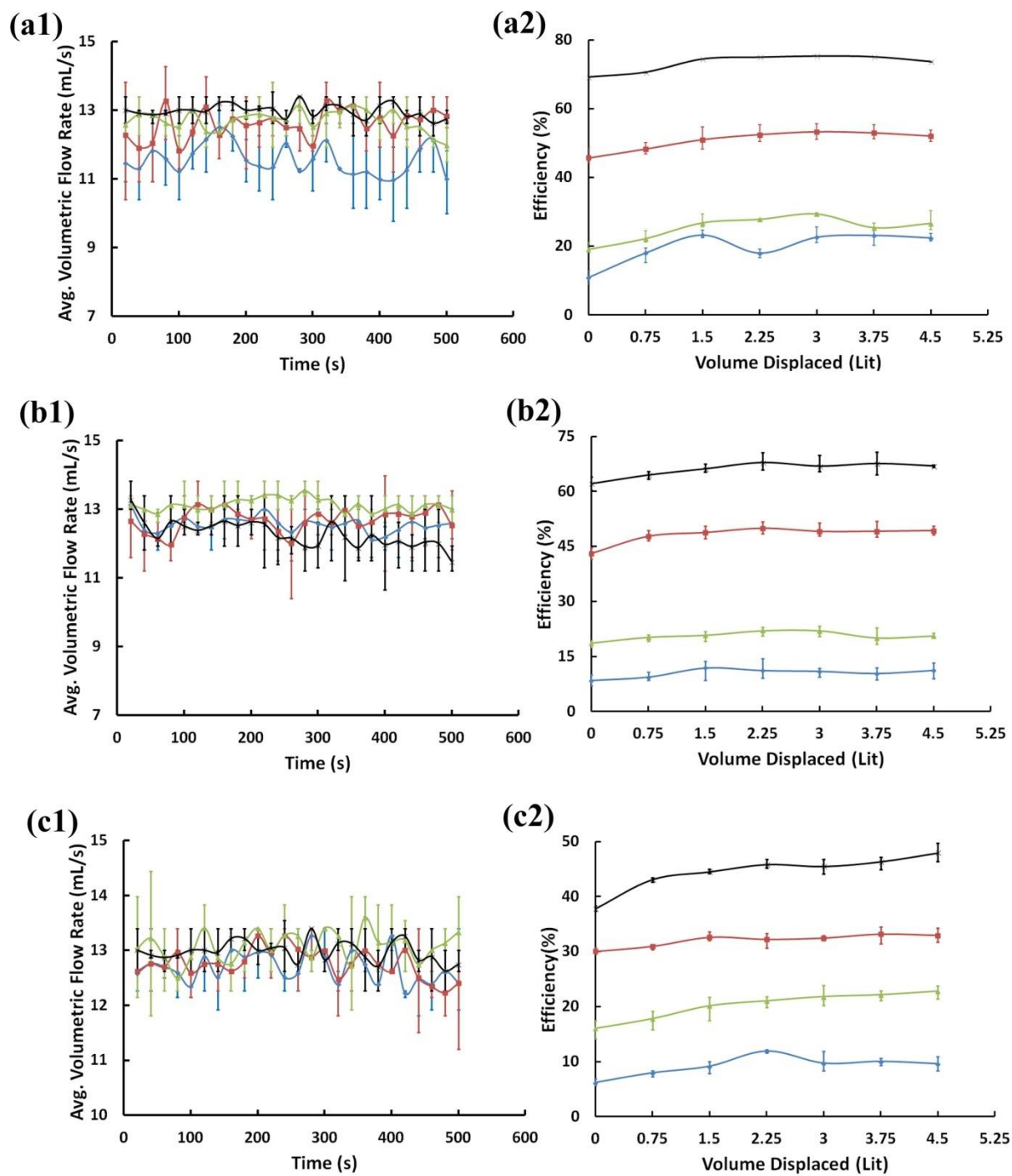


Figure 5.12. Base and modified *cellulose a* for three different concentrations [the experiment conducted by *method (b)*]: (a) 2 ppm, (b) 1 ppm, (c) 0.5 ppm. Numeral 1 of each graph corresponds to the average flow rates for different concentrations, and numeral 2 - to the data on

the efficiencies of different samples at the concentrations tested. Blue, green, red and black curves correspond to the base filter, base filter with electrospun PAN nanofibers, base filter with supersonically blown nylon 6 nanofibers, and base filter with electrospun PAN and supersonically blown nylon 6 nanofibers (i.e. the dual-coated filters), respectively. The average values were found based on three trials and the error bars show the maximum and minimum deviations from the average values.

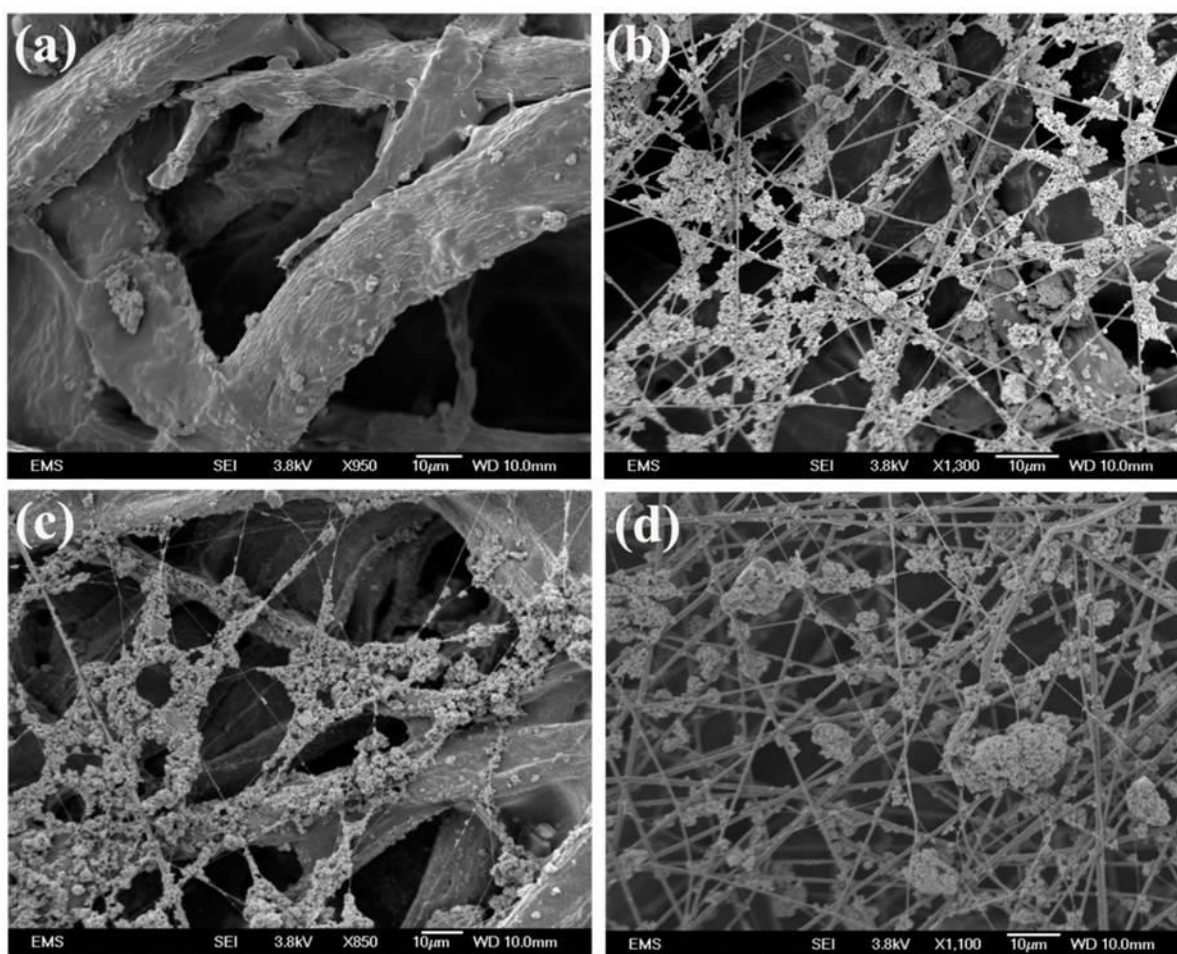


Figure 5.13. SEM images of *cellulose a* filters after the experiment with filtration of 2 ppm suspension of Cu nanoparticles [the experiment conducted by *method (b)*]. Panels (a), (b), (c)

and (d) correspond to base filter, base filter with electrospun PAN nanofibers alone, base filter with supersonically blown nylon 6 nanofibers alone, and the dual-coated filter.

The SEM images of the *cellulose a* filters show that the base filter does not remove anything. The modified filters catch nanoparticles mostly at the surface, and especially interesting is to see how the nanoparticles tend to cluster around such fibers and stick to them, albeit surfaces of the other fibers are available around.

The experiments conducted with *cellulose b* filters revealed results similar to those of the glass filters, as their pore sizes were almost in the same range (see section 5.2.1). At all three different nanoparticle concentrations, the average volumetric flow rates of the base filters were the least compared to those of the modified filters, and so were their efficiencies. The initial drop in the flow rate accompanied by an increase in the efficiency, similarly to those observed with glass filters, can be also seen in Fig. 5.14 for *cellulose b* filters. Nanofibers had similar effects in terms of increasing the efficiency in all the cases.

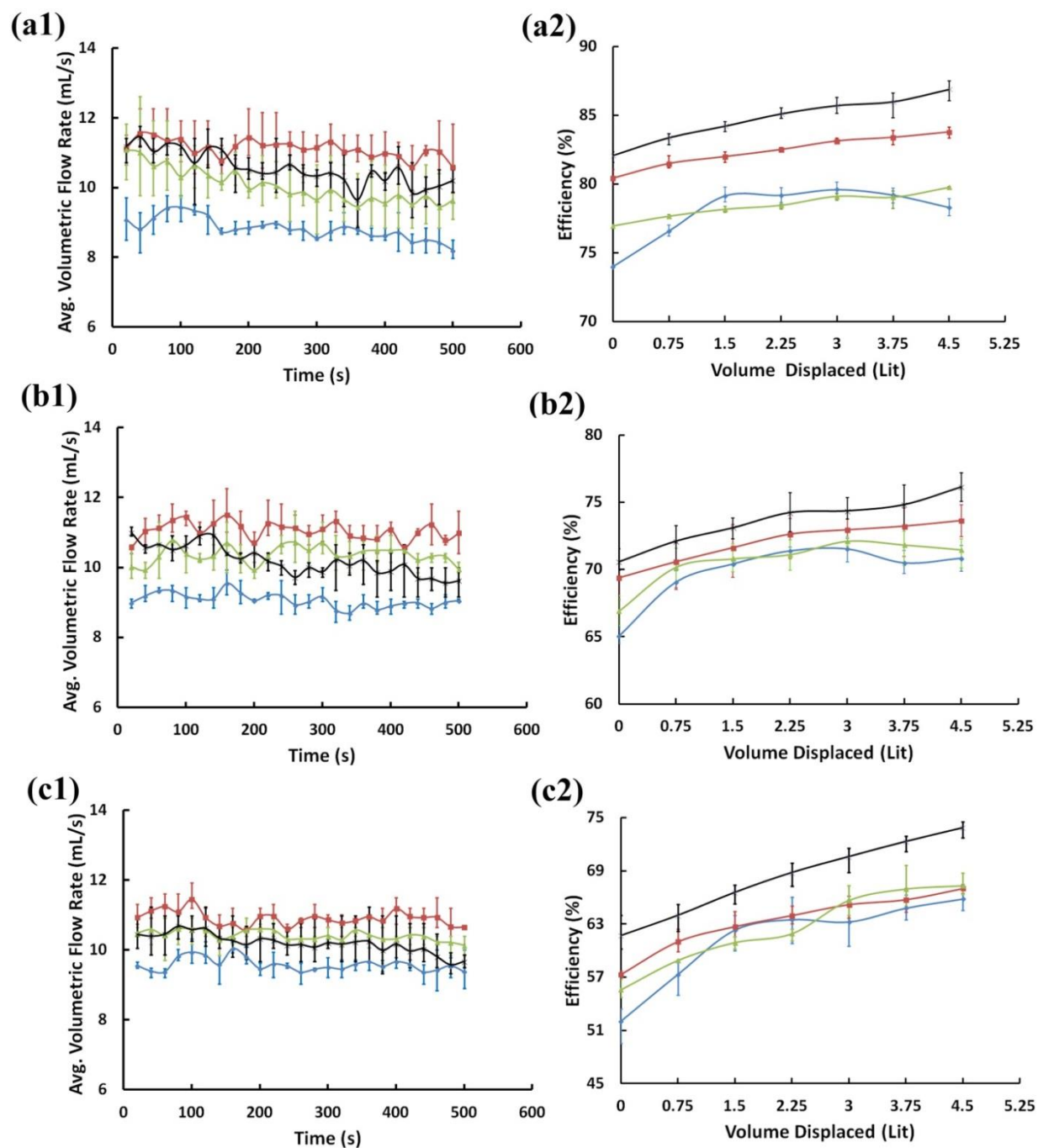


Figure 5.14. Base and modified *cellulose b* for three different concentrations: (a) 2 ppm, (b) 1 ppm, (c) 0.5 ppm. Numeral 1 of each graph corresponds to the average flow rates for different concentrations, and numeral 2 - to the data on the efficiencies of different samples at the concentrations tested. Blue, green, red and black curves correspond to the base filter, base filter

with electrospun PAN nanofibers, base filter with supersonically blown nylon 6 nanofibers, and base filter with electrospun PAN and supersonically blown nylon 6 nanofibers (i.e. the dual-coated filters), respectively. The average values were found based on three trials and the error bars show the maximum and minimum deviations from the average values.

Note also that a single layer of solution-blown nanofibers does not increase the overall thickness, since they are deposited onto a surface with depressions much larger than their diameter, and they do not even affect the pressure drop. Moreover, as Figs. 5.8, 5.10, 5.12 and 5.14 show, a single layer of the 20-50 nm solution-blown nanofibers outperforms a layer of electrospun 300-500 nm nanofibers.

5.4 Theoretical

The theory proposed in this section aims at the incorporation of the van der Waals attractive interactions between spherical nanoparticles in fluid flow and an individual cylindrical collector (a nanofiber) oriented normally to the flow. The planar fluid flow is treated in the Oseen approximation accounting for both viscous and inertial forces acting in the carrier fluid. The steady near-field flow past a circular cylinder in polar coordinates (the radial coordinate r and the angular coordinate θ) in the Oseen approximation is given by the following expressions [Oseen (1910), Kochin et al. (1963)]

$$v_r = \frac{U \cos \theta}{1 - 2 \ln(\gamma \kappa a_f / 2)} \left[-1 + \frac{a_f^2}{r^2} + 2 \ln \left(\frac{r}{a_f} \right) \right] \quad (5.4)$$

$$v_{\theta} = -\frac{U \sin \theta}{1 - 2 \ln(\gamma \kappa a_f / 2)} \left[1 - \frac{a_f^2}{r^2} + 2 \ln \left(\frac{r}{a_f} \right) \right] \quad (5.5)$$

$$\psi = -\frac{U a_f \sin \theta}{1 - 2 \ln(\gamma \kappa a_f / 2)} \left[-\frac{r}{a_f} + \frac{a_f}{r} + 2 \frac{r}{a_f} \ln \left(\frac{r}{a_f} \right) \right] \quad (5.6)$$

In Eqs. (5.4)-(5.6) the radial and azimuthal velocity components are denoted as v_r and v_{θ} , respectively; the corresponding stream function is denoted as ψ ; U is the oncoming flow velocity at infinity; a_f is the cylinder (fiber) cross-sectional radius; γ is related to the Euler-Mascheroni constant $\gamma_{EM}=0.577215$ as $\gamma = \exp(\gamma_{EM})=1.7811$; also, the dimensionless $\kappa a_f = Re/4$, where the Reynolds number based on the fiber diameter $Re = U 2a_f / \nu$, with ν being the kinematic viscosity of fluid.

It should be emphasized that the asymptotic form of Eqs. (5.4)-(5.6) is valid only near the cylinder (in the near field), whereas far away from it another asymptotic is valid, which is discussed below. The streamlines of the near-flow field (5.6) are shown in Fig. 5.15 where an additional Cartesian coordinate system associated with the fiber center x,y is introduced ($x = r \cos \theta$ and $y = r \sin \theta$).

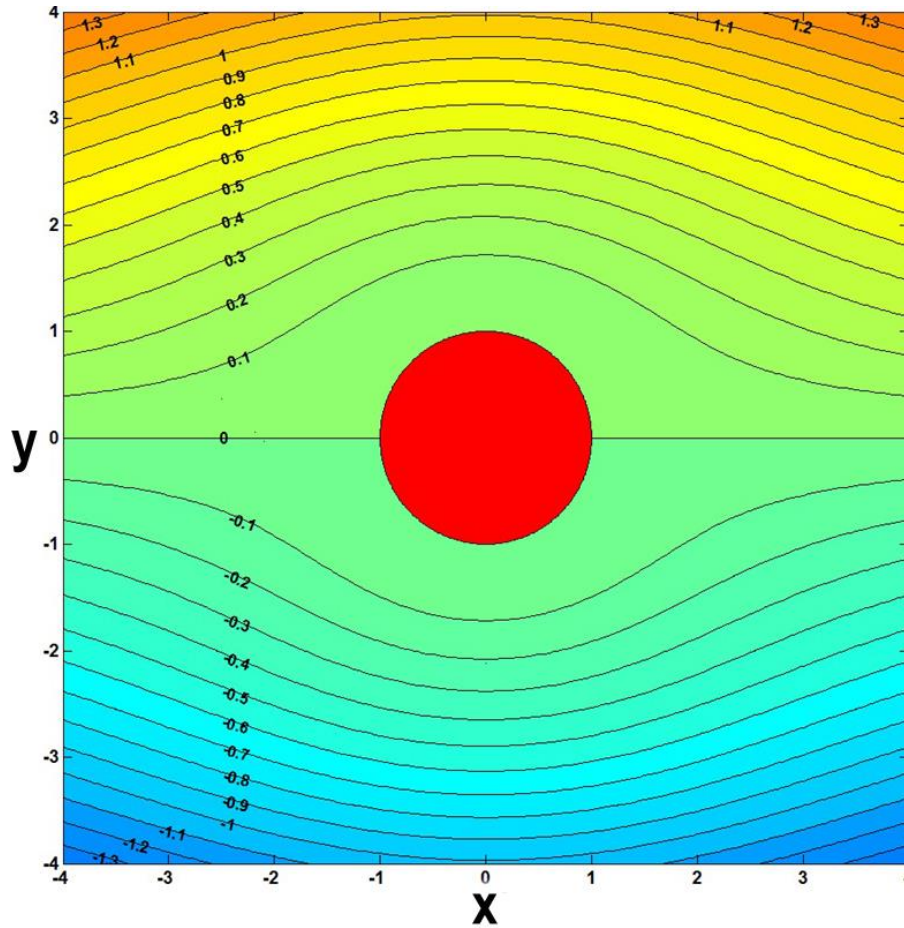


Figure 5.15. Flow field in the Oseen viscous flow about a cylinder (fiber). The stream function ψ is rendered dimensionless by Ua_f and the Reynolds number $Re=5 \times 10^{-2}$ for $2a_f=50$ nm and $U=100$ cm/s for water.

The flow velocity components u and v in projections to the Cartesian coordinates are $u = v_r \cos \theta - v_\theta \sin \theta$ and $v = v_r \sin \theta + v_\theta \cos \theta$, respectively.

Being swept by the Oseen flow described above, nanoparticles also experience the van der Waals attraction toward the cylindrical collector (nanofiber) and diffusion. It should be emphasized that direct numerical simulations of the van der Waals attraction force of a sphere to

a cylinder is prohibitively time-consuming, and different approximations were proposed for several limiting cases [Hallez (2012), Chen (2012), Bhattacharjee et al. (2000), Martinez et al. (2008)]. In particular, the sphere packing approach was proposed for calculations of the van der Waals force [Zhang et al. (2006)]. A similar approximation, which we employ below, allows for an accurate prediction of the long-range van der Waals attraction force, which is the most important element of the particle interception process. A detailed description of nanoparticle “docking” at a collector is secondary in this sense, and moreover, is impractical, since in reality neither nanoparticles are perfect spheres nor the collectors perfect cylinders.

To calculate the van der Waals force attracting a spherical nanoparticle to a cylindrical (nanofiber) collector, we will start from the van der Waals force attracting a spherical particle of radius a_p to one of the spherical particles of radius a_f aligned along the X-axis, as shown in Fig. 5.16. In this case, account for the fact that the distance between these particles is equal to $R - (a_p + a_f)$, where R is the distance between the centers of these particles (see Fig. 5.16). Then, the van der Waals force between

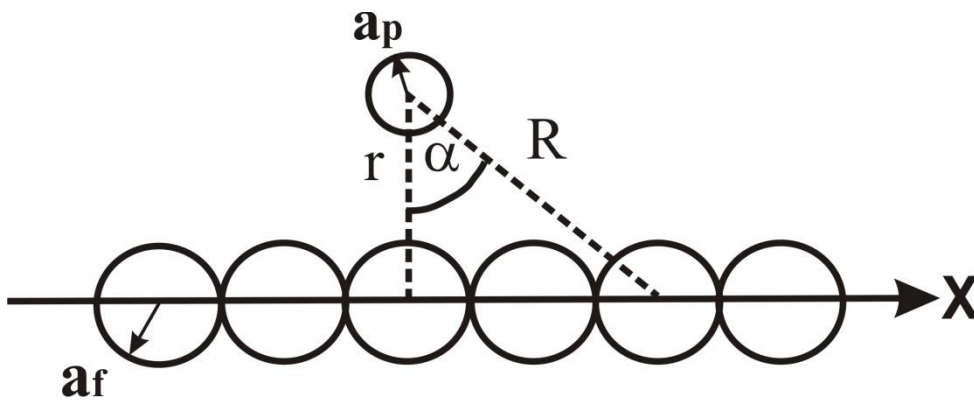


Figure 5.16. The van der Waals attraction of a spherical particle to one of the spherical particles aligned along the X-axis.

these two particles is [Hamaker (1937), Israelachvili (1997)]

$$f'_{vdW} = -\frac{A}{6[R - (a_p + a_f)]^2} \left(\frac{a_p a_f}{a_p + a_f} \right) \quad (5.7)$$

where $A > 0$ is the Hamaker constant, and the force is attractive. It should be emphasized that this force acts along the center line connecting these two particles, while its component directed toward the X-axis in Fig. 5.16 is equal to

$$f_{vdW} = f'_{vdW} \cos \alpha = f'_{vdW} \frac{r}{R} \approx -\frac{Ar}{6R^3} \left(\frac{a_p a_f}{a_p + a_f} \right) \quad (5.8)$$

where we imply that $R \gg a_p + a_f$.

Since according to Fig. 5.16 $R = (X^2 + r^2)^{1/2}$, using Eq. (5.8) one can introduce the “density” of the attractive van der Waals force along the X-axis as

$$\frac{f_{vdW}}{2a_f} = -\frac{Ar}{12} \frac{a_p}{(a_p + a_f)} \frac{1}{(X^2 + r^2)^{3/2}} \quad (5.9)$$

Then, the van der Waals force attracting the chosen nanoparticle to the entire array of the particles aligned along the X-axis is equal to

$$F_{vdW} = -\frac{Ar}{12} \frac{a_p}{(a_p + a_f)} \int_{-\infty}^{\infty} \frac{dX}{(X^2 + r^2)^{3/2}} = -\frac{Aa_p}{6(a_p + a_f)} \frac{1}{r} \quad (4.10)$$

and this force can be considered approximately as the van der Waals force attracting a spherical nanoparticle of radius a_p to a cylindrical nanofiber with the axis at the X-axis.

Denote the Oseen flow field $\mathbf{v} = u(x_p, y_p)\mathbf{i} + v(x_p, y_p)\mathbf{j}$ determined by Eqs. (4.4) and (4.5), with \mathbf{i} and \mathbf{j} being the unit vectors of the Cartesian x and y -axes (cf. Fig. 5.151), and x_p and y_p being current coordinates of a nanoparticle. Then, accounting for the van-der Waals force (4.10), the second law of Newton for an individual nanoparticle reads

$$\left(m_p + \frac{m_\ell}{2}\right) \frac{d\mathbf{v}_p}{dt} = -\frac{Aa_p}{6(a_p + a_f)} \frac{1}{(x_p^2 + y_p^2)^{1/2}} (\mathbf{i}\cos\theta + \mathbf{j}\sin\theta) - 6\pi\mu a_p (\mathbf{v}_p - \mathbf{v}) \quad (5.11)$$

In Eq. (4.11) \mathbf{v}_p is the nanoparticle velocity, m_p is its mass, m_ℓ is the mass of liquid displaced by the nanoparticle (and thus, $m_\ell / 2$ is the added mass), and the last term of the right-hand side is the Stokes drag force, with μ being the liquid viscosity. Note also, that in Eq. (5.11) $\cos\theta = x_p / (x_p^2 + y_p^2)^{1/2}$ and $\sin\theta = y_p / (x_p^2 + y_p^2)^{1/2}$.

The momentum balance equation (4.8) is supplemented by the kinematic equation

$$\frac{d\mathbf{R}_p}{dt} = \mathbf{v}_p \quad (5.12)$$

for the position vector of the nanoparticle $\mathbf{R}_p = \mathbf{i}x_p + \mathbf{j}y_p$.

Equations (5.11) and (5.12) can be integrated numerically to determine the motion and locations of the nanoparticle in time. However, nanoparticle diffusion is not accounted for yet. It can be “admixed” to the results produced by Eqs. (5.11) and (5.12) by adding diffusion after each time step as following. Numerical diffusion of an individual nanoparticle is realized as a random walk [Yarin et al. (2014), Cussler (1997)], in which the Cartesian coordinates x_p and y_p of this particle change during a short time interval Δt as

$$x_{p,i+1} = x_{p,i} + \Delta\zeta_i \cos \Delta\vartheta_i, \quad y_{p,i+1} = y_{p,i} + \Delta\zeta_i \sin \Delta\vartheta_i \quad (5.13)$$

with

$$\Delta\zeta_i = \sqrt{D \ln\left(\frac{1}{P_i}\right) \Delta t}, \quad \Delta\vartheta_i = 2\pi Q_i \quad (5.14)$$

where for every nanoparticle at any time step the values of P_i and Q_i are two independent random numbers from the interval $[0,1]$, and D is the diffusion coefficient. It should be emphasized that the latter two equations correspond to the physical diffusion process (the Brownian motion), in which the probability of a Brownian leap $\Delta\zeta$ during time Δt is equal to $P = \exp\left[-(\Delta\zeta)^2 / (D\Delta t)\right]$.

In addition, note that when a nanoparticle first touches a nanofiber, or another nanoparticle already attached to the nanofiber (practically, as the distance between them being less than 2 nm), it is considered to be intercepted, and stops moving.

It should be emphasized that the theoretical approach outlined above is only the first approximation in the description of an extremely complicated process of formation of nanoparticle clusters. It does not account for the particle-particle interaction in fluid, while they are swept toward the collector, as well as for the potential cluster nucleation in flow (albeit expected to be a minor effect at low nanoparticle concentrations of interest here). The first approximation also does not account for the collector shape change due to the growing cluster, which is plausible as long as the inequality $r \gg a_p + a_f$ holds, i.e. the particle-collector distance is much larger than their combined size. The effect of the Oseen flow modification due to the collector shape change is also not considered due to the long-range attraction being of the primary interest here, as well as the multiple-collector interactions are not accounted for. All

these phenomena can affect a detailed morphology of growing clusters and definitely deserve a thorough elucidation in future, even though they are not expected to significantly affect the main theoretical result - the domain of nanoparticle collection due to the van der Waals forces established below [cf. Eq. (5.20) and Fig. 5.19].

The numerical simulations to solve Eqs. (5.11) and (5.12) were conducted using the Kutta-Merson method with the automatically chosen variable time step determined by the pre-set accuracy. The calculations were carried for two nanofiber sizes: (i) 50 nm diameter nanofiber, corresponding to the supersonically blown nanofibers, and (ii) 300 nm diameter nanofiber, corresponding to electrospun nanofibers. In both cases we considered 50 nm nanoparticles oncoming onto an individual nanofiber with fluid velocities of either 100 cm/s or 10 cm/s. In the simulations 20 nanoparticles were issued one-by-one from a randomly chosen y-coordinate in the range of 240 nm from a distance $x=8a_f$ upstream from the nanofiber center. Figs. 5.17 and 5.18 corresponding to 100 cm/s and 10 cm/s, respectively, show the predicted patterns of nanoparticle clusters captured by both types of nanofibers. The nanoparticle clusters attached to the nanofibers visible in these figures were grown due to the consecutive interception of more and more nanoparticles brought by the flow. In Figs. 5.17 and 5.18 the best performance of each of the nanofibers is shown in the left-hand-side panels, while the worst one is illustrated in the right-hand-side panels. It can be seen that the smaller (50 nm) nanofibers are more efficient in capturing nanoparticles than the larger (300 nm) nanofibers. It was found that for the oncoming velocity of 100 cm/s, the 50 nm nanofiber captured in average $30 \pm 8.2\%$ of the nanoparticles, whereas the 300 nm nanofibers captured in average $16.8 \pm 8\%$. For the oncoming velocity of 10 cm/s the 50 nm nanofiber captured in average $25 \pm 5\%$ of the nanoparticles, whereas the 300 nm nanofibers captured in average $12.9 \pm 6.3\%$. The results revealed that the efficiency of single-

fiber collectors described here reduces as the flow velocity reduces. This counter-intuitive result stems from the fact that at a lower velocity it takes more time for an individual nanoparticle to approach a collector. Then, the longer-time diffusion can take it away from the collector in the y -direction to a too large distance for an effective capture by any physical mechanism.

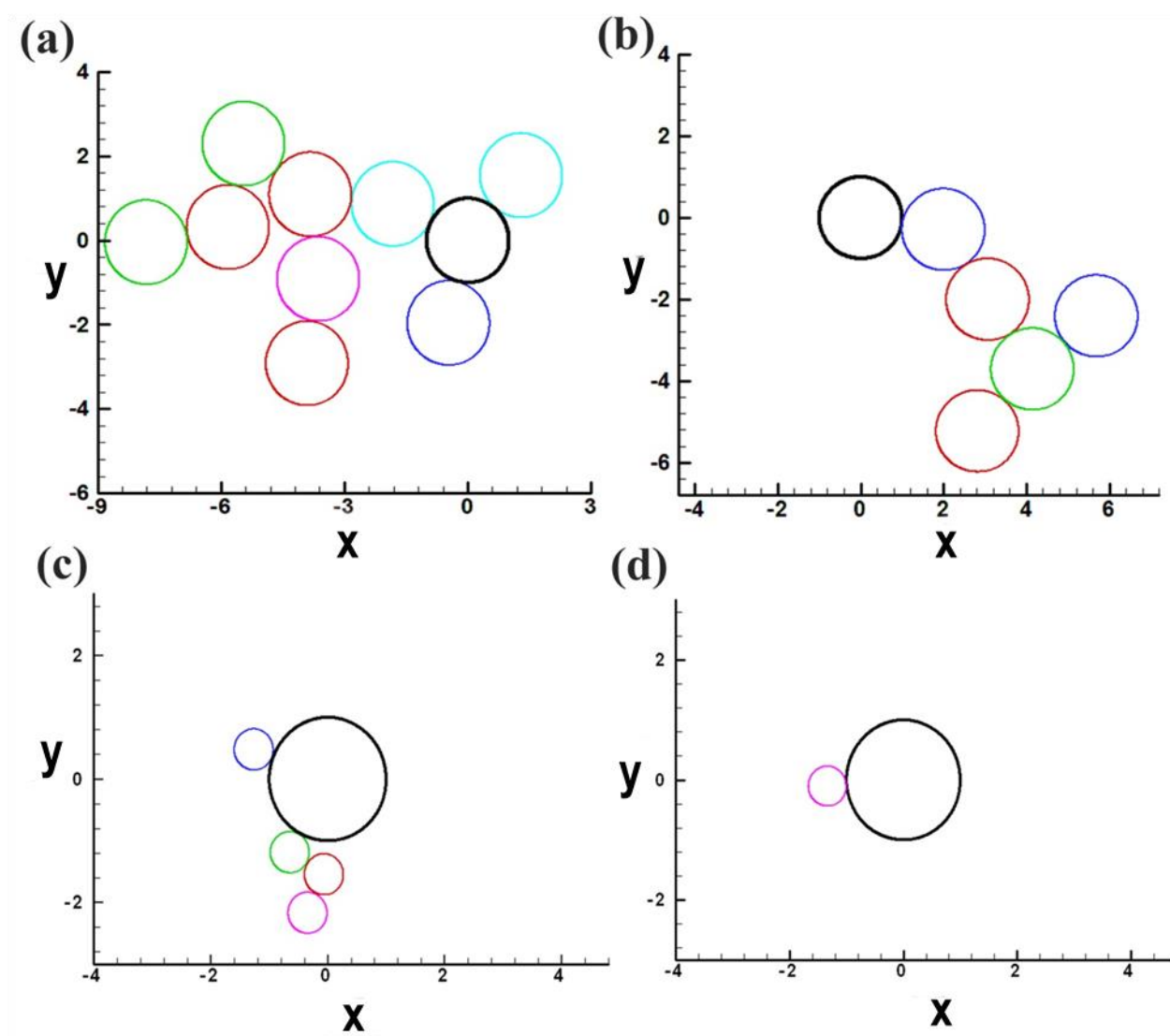


Figure 5.17. The numerically predicted clusters of the 50 nm nanoparticles (shown by thin-line circles in color) collected by a nanofiber (the cross-section of the latter is shown as a bold black circle in each panel) at the oncoming flow velocity of 100 cm/s. Panels (a) and (b) correspond to

the 50 nm nanofibers and show the best and worst deposition patterns, respectively. Panels (c) and (d) correspond to the 300 nm nanofibers and show the best and worst deposition patterns, respectively.

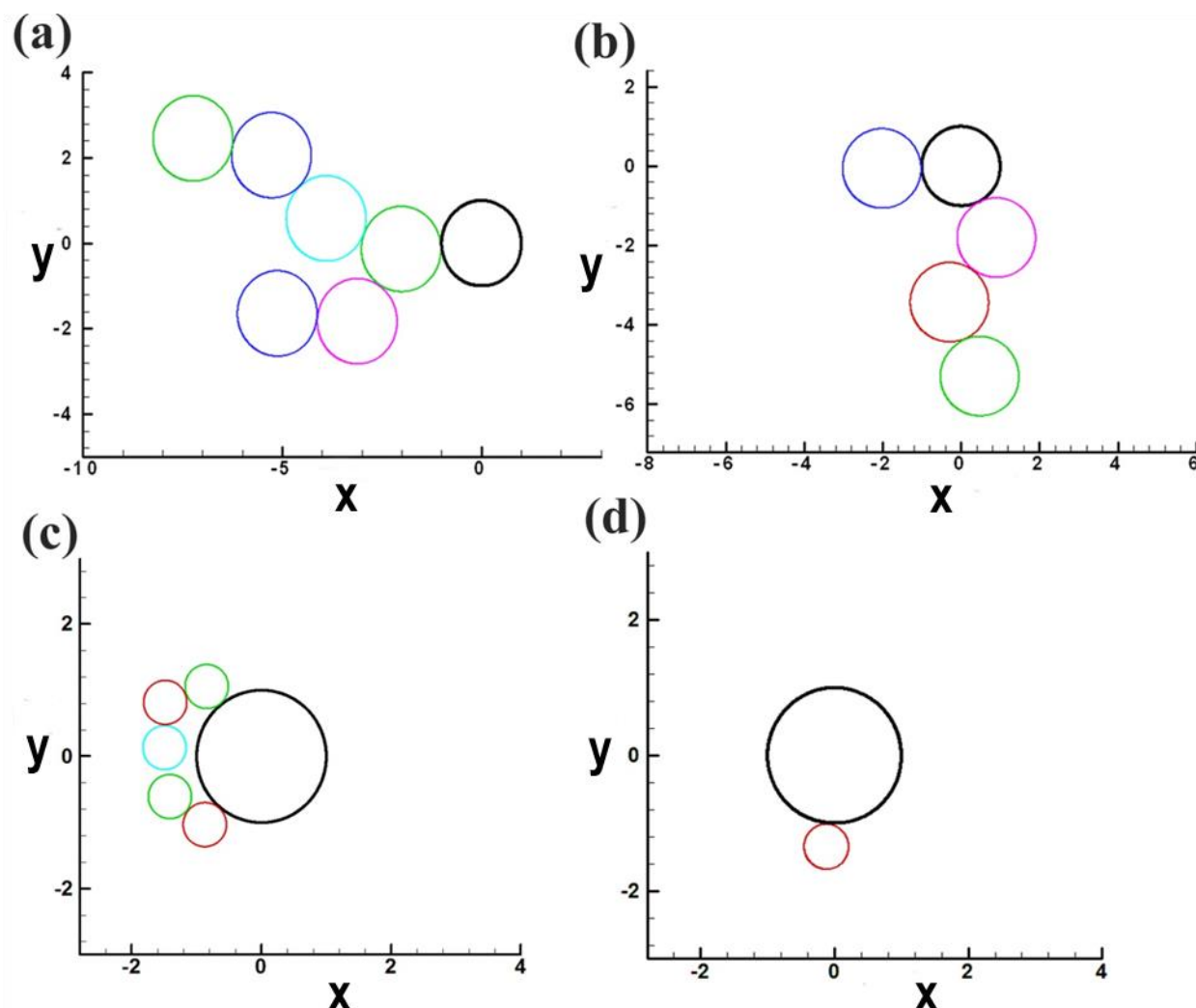


Figure 5.18. The numerically predicted clusters of the 50 nm nanoparticles (shown by thin-line circles in color) collected by a nanofiber (the cross-section of the latter is shown as a bold black circle in each panel) at the oncoming flow velocity of 10 cm/s. Panels (a) and (b) correspond to the 50 nm nanofibers and show the best and worst deposition patterns, respectively. Panels (c)

and (d) correspond to the 300 nm nanofibers and show the best and worst deposition patterns, respectively.

The numerical predictions in Figs. 4.17 and 4.18 clearly show that as the nanofiber size increases, the 50 nm nanoparticles tend to pass by the nanofiber without being intercepted, thus making the 50 nm nanofiber a more efficient individual collector than the 300 nm nanofiber. This stems from the fact that fluid streamlines are displaced by the smaller nanofiber to smaller distances where the van der Waals forces are still felt and capable of attracting nanoparticles to the nanofiber. The numerical results imply that most of the smaller nanoparticles would tend to agglomerate on the smaller nanofibers rather than on the larger ones. This conclusion is supported by the experimental observations, as revealed by Figs. 5.20 and 5.21 in. Indeed, it can be seen there that nanoparticles tend to be intercepted much more on the smaller supersonically blown nanofibers than on the larger electrospun fibers. It should be emphasized that irrespective of the position of larger electrospun PAN nanofibers, either underneath the smaller solution-blown nylon 6 nanofibers (Fig. 5.20) or on top of them (Fig. 5.21), the nanoparticles are collected predominantly by the smaller 20-50 nm solution-blown nanofibers. Even though there are large pores available for the nanoparticles to sip through, they still accumulate on the smaller nanofibers. This phenomenon is a clear manifestation of a strong attraction of nanoparticles to the 20-50 nm solution-blown nanofibers due to the van der Waals forces.

It should be emphasized that the results of the simulations in Figs. 5.17 and 5.18 reveal that nanoparticle clusters on solution-blown nanofibers can grow not only at the frontal side where the oncoming flow impinges onto the fibers, but also (and counter-intuitively) on the rear side.

The predicted cluster growth on the windward side of the 50 nm nanofiber (cf. Figs. 5.17a and 5.18a) corresponds to the experimental observation in Fig. 5.7, whereas the predicted cluster growth on the leeward side of the nanofiber (cf. Figs. 4.17b and 5.18b) corresponds to the experimental observation in Fig. 5.6d.

It is instructive to calculate which part of the oncoming flow is displaced by nanofibers of different sizes to such distances that the van der Waals attraction effective only at distances below ~ 100 nm would be precluded for that body of fluid and the nanoparticles would be swept by it from the collector. In distinction from Eqs. (5.4)-(5.6) for the near field, the far field of the flow is described by the following asymptotic expressions valid at distances $r \gg a_f$ [Oseen (1910), Kochin et al. (1963)]

$$u = U + \frac{2U}{\kappa[1 - 2\ln(\gamma\kappa a_f / 2)]} \frac{x}{(x^2 + y^2)} \quad (5.15)$$

$$v = \frac{2U}{\kappa[1 - 2\ln(\gamma\kappa a_f / 2)]} \frac{y}{(x^2 + y^2)} \quad (5.16)$$

$$\psi = Uy + \frac{2U}{\kappa[1 - 2\ln(\gamma\kappa a_f / 2)]} \arctan\left(\frac{y}{x}\right) \quad (5.17)$$

According to the near-field Eq. (4.6), the fluid body (and nanoparticles inside it) encompassed by the streamline ψ_{vdw} passing through the point $r = \ell = a_f + 100$ nm at $\theta = \pi/2$ (cf. Fig. 5.15) will be affected by the attractive van der Waals forces; a_f here and hereinafter is expressed in nm. Therefore,

$$\psi_{vdw} = \frac{Ua_f}{1 - 2\ln(\gamma\kappa a_f / 2)} \left[-\bar{\ell} + \frac{1}{\bar{\ell}} + 2\bar{\ell} \ln(\bar{\ell}) \right] \quad (5.18)$$

where $\bar{\ell} = \ell / a_f$. It should be emphasized that Eq. (5.18) completely determines the value of ψ_{vdW} .

The streamline of the near field is matched with the corresponding streamline in the far field. The exact matching location is immaterial, since in any case, the stream function value should be continuous, i.e. the same at the same streamline in the near and far field. Then, from Eqs. (4.17) and (5.18) one arrives at the following equation determining the borderline (for the van der Waals attraction) streamline $y_{100}(x)$ in the far field

$$Uy_{100} + \frac{2U}{\kappa[1 - 2\ln(\gamma\kappa a_f / 2)]} \arctan\left(\frac{y_{100}}{x}\right) = \frac{Ua_f}{1 - 2\ln(\gamma\kappa a_f / 2)} \left[-\bar{\ell} + \frac{1}{\bar{\ell}} + 2\bar{\ell} \ln(\bar{\ell}) \right] \quad (5.19)$$

We are interested in finding the value of $Y_{100} = y_{100}|_{x \rightarrow -\infty}$, when the second term on the left in Eq. (5.19) vanishes. Then,

$$Y_{100} = \frac{a_f}{[1 - 2\ln(\gamma\kappa a_f / 2)]} \left[-\left(\frac{a_f + 100 \text{ nm}}{a_f}\right) + \left(\frac{a_f}{a_f + 100 \text{ nm}}\right) + 2\left(\frac{a_f + 100 \text{ nm}}{a_f}\right) \ln\left(\frac{a_f + 100 \text{ nm}}{a_f}\right) \right] \quad (4.20)$$

The dependence described by Eq. (5.20) is illustrated in Fig. 5.19. It is seen that for the smaller nanofiber radii, the fluid domain $y \leq Y_{100}$ (with the nanoparticles inside, which would be affected by the attractive van der Waals forces) is wider than for the larger nanofibers, since the values of Y_{100} are higher at the lower values of a_f . This proves theoretically, in full agreement with the experimental observations, that the smaller supersonically solution-blown nanofibers are more effective “van der Waals collectors” than the electrospun nanofibers.

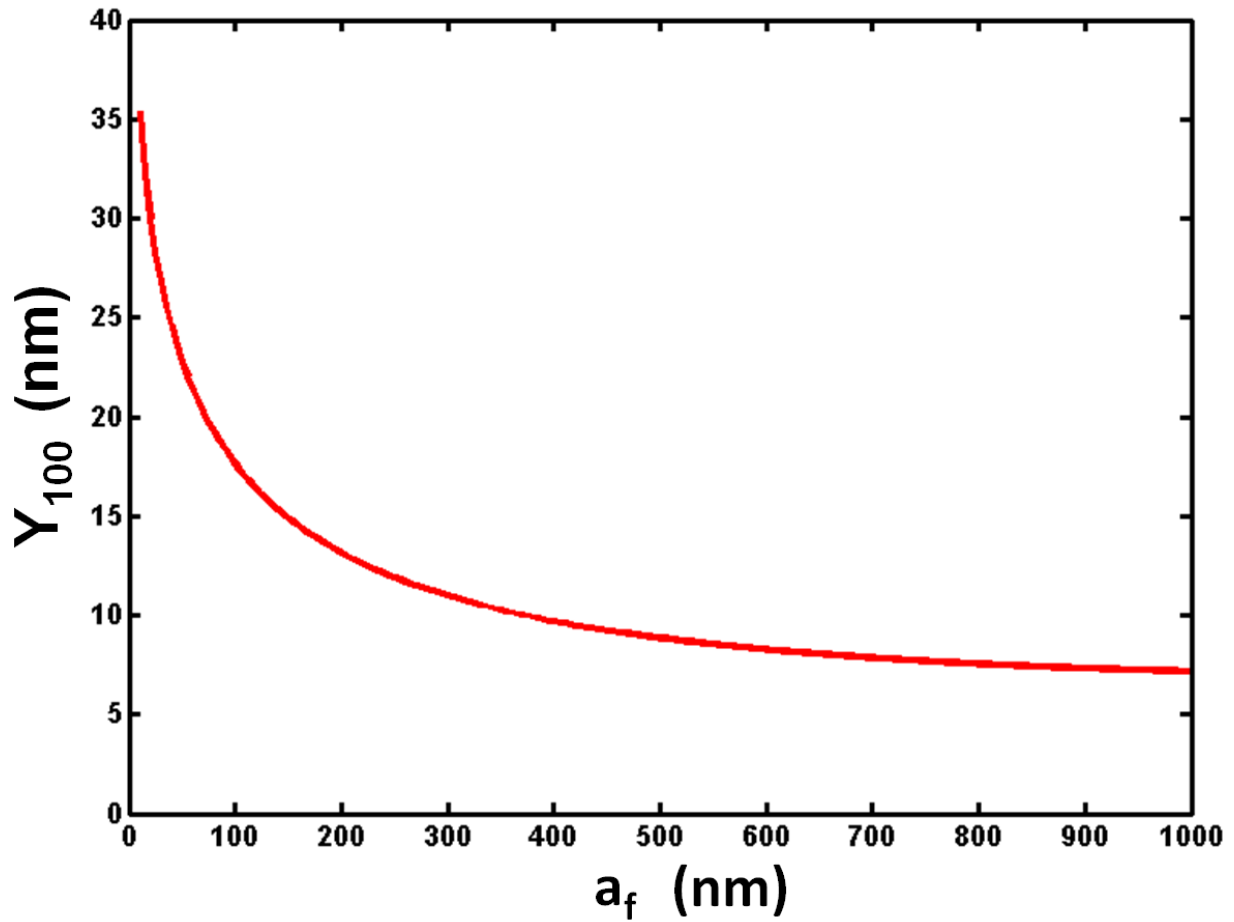


Figure 5.19. The borderline for the van der Waals attraction of nanoparticles for different nanofiber sizes.

Note also that according to Eq. (4.20), the dimensionless borderline of the collection domain of a single van der Waals attractor Y_{100}/a_f depends on the Reynolds number (since $\kappa a_f = \text{Re}/4$, while $\text{Re} = U 2a_f / \nu$), and the dimensionless group $(A / \mu a_p a_f U) \omega(a_p / a_f)$, since the

ratio ($100 \text{ nm}/a_f$) is proportional to it, with $\omega(a_p/a_f)$ being a dimensionless function of the ratio a_p/a_f .

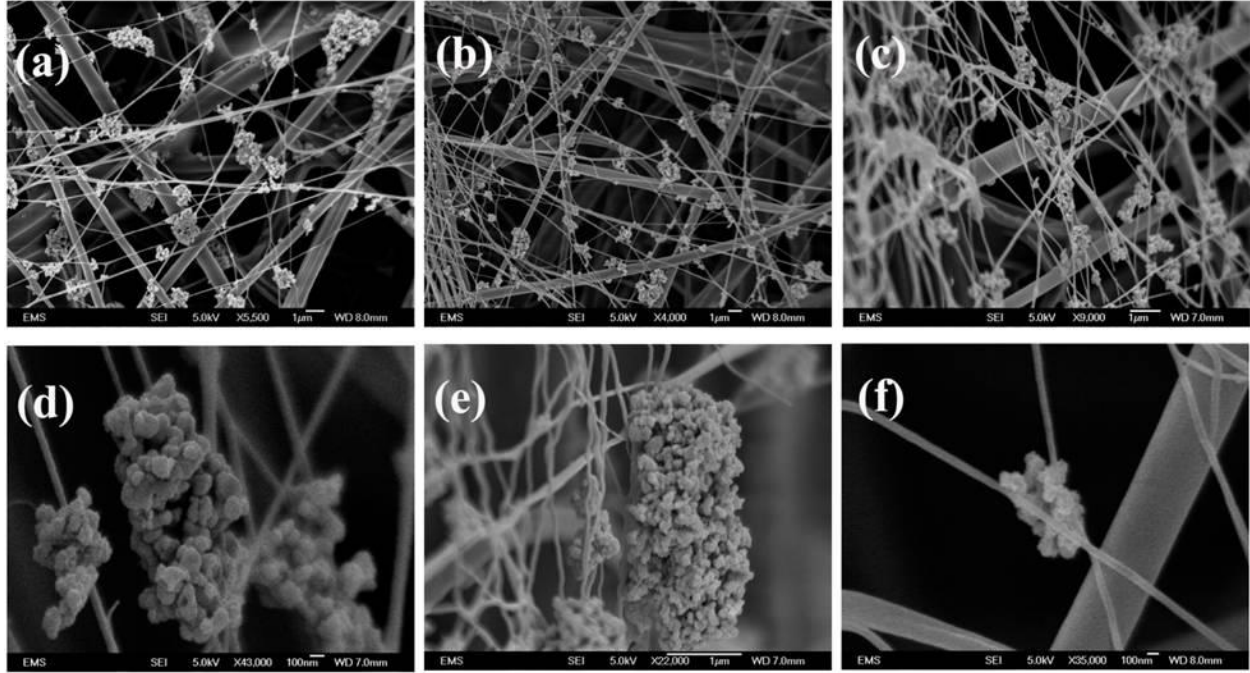


Figure 5.20. SEM images of glass filter with dual nanofiber coating: the larger electrospun PAN nanofibers first and then the smaller supersonically blown nylon 6 nanofibers on top of them. Panels: (a-b) Top views of the nanofiber layers; (c) Nanofiber layer seen at 45°; (d-f) An individual nanofiber collecting nanoparticles/clusters seen at different angles. The images clearly show minimal deposition of nanoparticles on electrospun PAN nanofibers (300-500 nm), while predominant nanoparticle cluster growth on the supersonically blown smaller nanofibers.

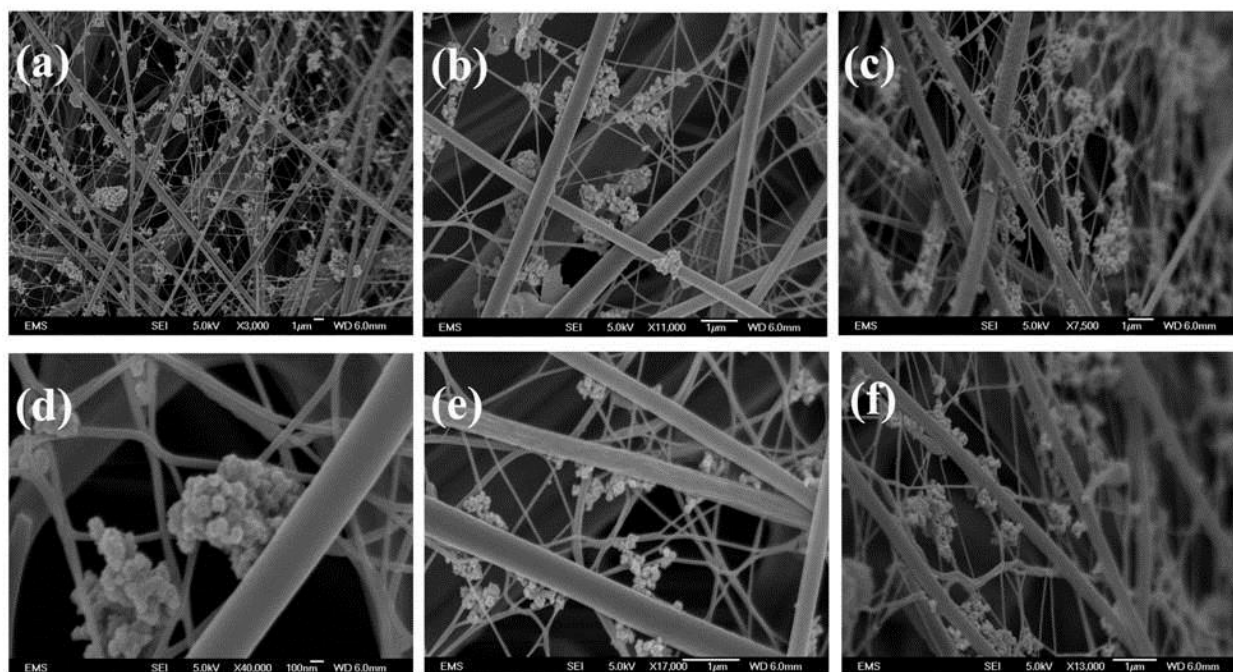


Figure 5.21. SEM images of glass filter with dual nanofiber coating: supersonically blown nylon 6 nanofibers first and then the larger PAN electrospun nanofibers on top of them. Panels (a-b) top view of the nanofiber layers; (c) Nanofiber layer seen at 45° angle; (d-f) Zoomed-in view of nanofibers collecting nanoparticles/clusters seen at different angles. The images clearly show minimal deposition of nanoparticles on electrospun nanofibers (300-500 nm) and predominant nanoparticle deposition on the supersonically blown smallest fibers.

5.5 Conclusion

Formation of ultrafine nanofibers in the range 20 to 50 nm by the supersonic solution blowing process, introduces the attractive van der Waals forces as an effective mechanism of nanoparticle interception, which holds great promise in filtration. A few layers of such nanofibers deposited on the filter medium or sandwiched in it can significantly improve water filtration efficiency without any need to increase filter thickness and thus pressure drop. In

particular, our results reveal how the efficiencies of three types of commercial filters were increased significantly in filtration of the 0.2-2 ppm aqueous suspensions of 100-300 nm nanoparticles. Two types of the experiments were conducted using the base and modified filters. First, a short time experiment was conducted to elucidate the particle capturing mechanism by the smallest nanofibers, and then, a longer time experiment was conducted to test the modified filters capabilities under the long-loading conditions. In both types of the experiments it was found that the dual-coated filters (with the supersonically blown 20-50 nm fibers superimposed on the 300 nm electrospun fibers on top of the base filters) performed best in terms of the efficiency and sustainability of the downstream flow rate in time. No visible breakage pattern of the 20-50 nm nanofibers could be seen in the SEM images even after the long-time experiments. The theory developed in the present work accounts for the convective transport of nanoparticles by flow about a single nanofiber collector, nanoparticle diffusion and attraction to the collector by the van der Waals forces. The theoretical predictions demonstrated how the oncoming nanoparticles are intercepted by the nanofiber and cluster attached to its surface or to the previously attached nanoparticles. In agreement with the experiment, the theory revealed that the smaller nanofibers (the 20-50 nm supersonically solution-blown nanofibers) are more efficient collectors of nanoparticles than the larger electrospun nanofibers. Also, in agreement with the experimental observations the theory predicted that the nanoparticle clusters on solution-blown nanofibers can grow either on the frontal side of an individual collector, where the oncoming flow impinges onto the fibers, or on the rear leeward side. One of the main theoretical results of the present work is the prediction of the domain of nanoparticle collection due to the van der Waals forces. The present theory is the first approximation valid for an individual cylindrical van der Waals collector of nanoparticles. The collector-collector interactions deserve a future study

to address the effect of flow directionality (from the solution-blown 20-50 nm nanofibers toward the base filter or vice versa) on the cluster morphology.

Summarizing, note that it is shown experimentally and theoretically that only the 20-50 nm solution-blown nanofibers reveal an enhanced filter efficiency (due to the van der Waals forces making such collectors extremely effective). The presence of electrospun fibers is useful, albeit to a lesser extent, since they displace flow too much for an effective van der Waals interception, and if added as a thicker layer, also significantly increase pressure drop. Adding electrospun nanofibers to increase filter efficiency is a standard practice today. The present work demonstrates that the efficiency can be enhanced well beyond that, especially in the case of filtration of the smallest nanoparticles from dilute aqueous suspensions.

CHAPTER 6

POOL BOILING OF NOVEC 7300 AND DI WATER ON NANO-TEXTURED HEATER COVERED WITH SUPERSONICALLY BLOWN OR ELECTROSPUN METALIZED AND PURE POLYMER NANOFIBERS

This chapter has been partially published in Sinha-Ray, Sumit et al. (2017) and partially in Sahu et al. (2016). Reprinted with permission from [Sinha-Ray, Sumit, Zhang, W., Sinha-Ray, Suman, Sahu, R.P. and Yarin A.L. (2017), Pool boiling of Novec 7300 and DI water on nano-textured heater covered with supersonically blown or electrospun polymer nanofibers, International Journal of Heat and Mass Transfer, <http://dx.doi.org/10.1016/j.ijheatmasstransfer.2016.08.101>] and [Sahu, R.P., Sinha-Ray, Sumit, Sinha-Ray, Suman, and Yarin, A.L. (2016), Pool boiling of novac 7300 and self-rewetting fluids on electrically-assisted supersonically solution-blown, copper-plated nanofibers, International Journal of Heat and Mass Transfer, 95, 83-93] . Copyright 2016-17 Elsevier.

6.1 Introduction

This work aims at the enhancement of the heat removal in microelectronics component under pool boiling conditions. Nearly 55% of the microelectronics components suffer failure due to a poor or inadequate heat removal from the circuit. With the ever growing need of miniaturized and compact, yet powerful electronic components, the number of transistors in an integrated circuit has grown exponentially over the last 40 years. This has resulted in an increased heating due to the Joule effect and left the microelectronics industry in a dire need of an effective cooling of such components. Several approaches to cooling microelectronics were explored in the past, such as single-phase liquid cooling [Zhang et al. (2005), Peng et al. (1994a),

Peng et al. (1994b)], jet impingement cooling [Beratlis and Smith (2003), Wang et al. (2004), An et al. (2014)], spray cooling [Cotler et al. 2014)], heat pipes [Kim and Golliher (2002)], indirect cooling with phase change materials [Sinha-Ray, Sumit et al. (2014)], and pool boiling [Anderson and Mudawar (1989), Webb and Kim (2005)]. Pool boiling is one of the most promising methods of thermal management problem, which stems from high latent heat of evaporation of liquids and is important in nuclear power plants and refrigeration, petrochemical processing, etc.

However, pool boiling suffers one critical drawback, namely the Critical Heat Flux (CHF) [Kutateladze (1963)], when boiling stops being nucleate boiling and forms a vapor film. Several modifications of the boiling surfaces have been attempted to facilitate nucleate boiling and delay CHF in works of Nukiyama (1966), Rioboo et al. (2009a), Dong et al. (2014), Li and Peterson (2010), Rainey and You (2000), McHale et al. (2011) etc. Different liquids were also tested/modified, like water, fluorinert fluids, or fluid mixtures were reported in works of Calus and Leonidopoulos (1974), Jensen and Jackman (1984), Sun et al. (2004), McGillis and Carey (1996), Sathyanarayana et al. (2012), Forrest et al. (2013), Amaya et al. (2013), Kim and Kim (2009) etc. Different nanofluids were explored in researches conducted by Wen and Dong (2005), Das et al. (2003), You et al. (2003), etc.

Electrospun polymer nanofiber mats deposited on a heater surface which create a nano-textured porous interface have recently been explored as a means of surface modification for spray cooling and enhancement of flow boiling and pool boiling. Electrospun nanofibers facilitate pinning of the impacting coolant drops at the surface, enhancing heat removal rate and even eliminating the Leidenfrost effect [Weickgenannt et al. (2011)]. It was recently shown that electrospun polymer nanofibers enhance heat transfer and diminish surface superheat in mini-

channel flows with Taylor bubbles [Freystein et al. (2016)]. Nano-textured surfaces formed using metal-plated electrospun nanofiber mats were used to enhance heat removal rate in spray cooling [Sinha-Ray, Suman et al. (2010a), Sinha-Ray, Suman and Yarin (2014), Sinha-Ray, Suman et al. (2014a)] and pool boiling [Jun et al. (2014)]. These inexpensive nano-textured surfaces allowed achieving heat removal rates close to 1 kW/cm^2 in drop impact cooling [Sinha-Ray, Suman et al. (2010a)]. Also, these metal-plated nano-textured surfaces allowed $\sim 100 \text{ W/cm}^2$ heat removal at microgravity. In the case of pool boiling the rough metal-plated nanofiber act as nucleation sites, as well as a hot “cage” for growing bubbles, i.e. simultaneously increase the number of bubbles and their growth rate [Jun et al. (2014)].

Nanofibers, even smaller than the electrospun ones, can be developed by supersonic solution blowing [Sinha-Ray, Suman et al. (2013)] as it has been described in Chapter 4. These nanofibers revealed a higher robustness than their electrospun counterparts. Supersonically blown nanofibers can be used for the enhancement of heat transfer in pool boiling both in metal-plated and in pure polymer form since they provide additional nucleation sites, a large surface area and an enhanced porosity. In spite of the fact that metal-plating of nanofibers on heater surface is an extra fabrication step which might be dangerous for certain microelectronics substrates, it can provide multiple additional nucleation sites for enhanced nucleate boiling. However, it would be also attractive to eliminate metal-plating, if it would be possible to sustain a certain level of heat removal enhancement. Therefore, in the present Chapter pool boiling of Novec 7300 fluid and DI water are studied on bare copper surface and nano-textured surfaces covered with polymer, non-metalized electrospun and supersonically-blown nanofibers, and also by metalized nanofibers for comparison. The results for metalized nanofibers in pool boiling of several coolants appeared in the published work by Sahu et al. (2016). In the next section the

experimental aspects will be discussed, followed by the results and discussion for supersonically blown metalized polymer nanofibers and pure polymer (non-metalized) nanofiber nano-textured surfaces. Conclusions are drawn at the latter section.

6.2 Experiments

6.2.1 Materials

Polymer, polyacrylonitrile (PAN; molecular weight $M_w=200$ kDa) was obtained from Polymer Inc. Solvent for PAN, N,N-Dimethyl formamide (DMF) anhydrous-99.8%, was obtained from Sigma-Aldrich. Novec 7300 engineered fluid was purchased from 3M. Also, DI water was used. Oxygen-free high-conductive (OFHC) 101 grade copper rods purchased from McMaster-Carr were used as a heated substrate. These copper rods were cut into cylindrical pieces as disks of 1.9 cm in diameter and 1.9 cm in height. The surfaces of these substrates were smoothened using 3M 2000 Grit sandpaper and are denoted hereinafter as bare copper surfaces. In addition, smoothened copper surfaces with deposited polymer nanofibers were also used as heaters and are denoted hereinafter as nano-textured heater surfaces. For copper-plating, sulfuric acid, hydrochloric acid, copper sulfate-pentahydrate, and formaldehyde, all obtained from Sigma-Aldrich, were used. Oxygen-free high-conductive (OFHC) 101 grade copper rod was used as anode for electroplating.

6.2.2 Electrospinning and Supersonic Solution Blowing

Electrospinning of PAN was carried out in the following order. First, 9 wt% PAN solution in DMF was pumped through a 5 mL syringe with a 20G needle connected to it. A syringe pump, purchased from New Era Pump Systems, was employed for pumping the solution at 0.6 mL/h.

The Cu substrate was grounded, while the needle was the positive electrode. Electrospinning was carried out at 9 kV with the tip-to-collector distance being 25 cm. Electrospun fibers were collected for 45 s. The electrically-assisted supersonic solution blowing was carried out using 6 wt% PAN solution as described in Chapter 3 and in Sahu et al. (2015, 2016) and Sinha-Ray, Sumit et al. (2015a). Copper cylinders were used as the substrates located at a distance of 37.5 cm from the supersonic nozzle. Nanofibers were collected for 4 min on the Cu substrates.

The total amount of nanofibers deposited on the samples is difficult to accurately measure directly, since the nanofiber mass is significantly smaller than that of the substrate. However, the nanofiber mass can be controlled by controlling the total deposition time, which was kept constant. Electrospun nanofibers were collected for 45 s and the supersonically blown nanofibers were collected for 4 min. For electrospinning, the PAN solution concentration was 9 wt%, while the flow rate was maintained at 0.6 mL/h, which means that approximately 0.68 mg of polymer nanofibers were deposited (taking the polymer solution density of 1 g/cm³). Similarly, for supersonic blowing the mass of the deposited polymer nanofibers was approximately 0.4 mg. Accordingly, the mass of the deposited polymer nanofibers was similar in both the processes. However, it should be emphasized that due to the fact that the area of the sample covered by nanofibers was small in comparison to the overall area over which the nanofibers are normally deposited, only a small fraction of the above mentioned mass was deposited onto the samples used in the boiling experiments. Still, it was almost the same for both processes and samples.

6.2.3 Electroplating

Electroplating of polymer nanofiber was carried out following the same method as in Sinha-Ray, Suman et al. (2010). An electroplating bath was prepared for Cu plating on the

supersonically blown nanofibers using the chemical mixture of sulfuric acid (5 g), hydrochloric acid (0.5 g), copper sulfate-pentahydrate (16 g) and formaldehyde (10 g) in 100 mL of deionized (DI) water. Before copper plating on the polymer nanofibers, the nanofiber mat was coated with Pt-Pd layer of 7.5 nm using Cressington Sputter Coated. Such a thin metal layer on the surface allows an electrical path between the Cu^{2+} ions in the solution and the polymer nanofiber, since polymer itself is an electric insulator. Such masking allows successful metal plating. The nanofiber-coated surface was connected as cathode and the copper plate was connected to anode. Both surfaces were dipped into the plating bath and the electric current density was kept similar to that of Sinha-Ray, Suman et al. (2010). After 15 s, the nanofibers were plated yielding a thorny-devil type structure. Further these samples were washed in DI water and dried in nitrogen for further testing.

6.2.4 Characterization

Scanning electron microscopy (SEM) of copper-plated nanofiber mats was done using JEOL JSM-6320F with a cold emission source. The high-speed imaging was done using a Phantom V210 camera.

6.2.5 Pool Boiling Setup

The experimental setup employed in the present investigation is described below- It consists of (i) two layers of teflon casing for proper thermal insulation; (ii) the main copper cylinder with five cartridge heaters (200 W), purchased from Omega, inserted into it for uniform heat supply to the Cu substrate separately screwed on it; (iii) the glass chamber containing the working liquid; (iv) the recuperation unit to facilitate vapor condensation and returning back to

the liquid pool. The schematic of the experimental setup is shown in Fig. 6.1. The main Cu substrate, to be tested, was of 1.9 cm of diameter and 1.9 cm in height. It was screwed to the primary copper rod of length 7.6 cm. Before screwing the substrate to the main cylinder, a thin layer of thermally conductive silver paste (obtained from MG Chemicals Inc.) was applied between the substrate and the cylinder. The main cylinder was machined from a diameter of 4.44 cm to 1.9 cm for proper intensification of the heat flux supplied from the above-mentioned heaters inserted into it. The primary teflon case containing the Cu cylinder had an insulating air gap of 0.6 cm between teflon and the Cu cylinder. Using teflon as a casing for the entire heating chamber was appropriate for the outer thermal insulation. Two holes were drilled laterally within the copper substrate at a distance of 0.625 cm between them. The holes were drilled to the center of the copper substrate to allow thermocouples to be put through them. A small amount of silver paste was also applied on the thermocouples for proper contact with the copper substrate and accurate temperature reading. These two T-type thermocouples were plugged to a HH806AW thermometer (Omega). The secondary teflon casing was attached to the glass chamber, the outer casing of which was made of aluminum. The boiling chamber was of the sizes 3.81 cm 3.81 cm 8.26 cm. The teflon assembly was then placed surrounding the Cu substrate and exposing the substrate to the liquid that would fill the boiling chamber. An O-ring was used inside teflon to seal the gap between the copper substrate and the secondary teflon casing. The vapor recuperation unit made of Aluminum was then placed on top of the boiling chamber. The unit contained multiple channels drilled through it to circulate cold DI water and to keep the temperature of the unit below room temperature and facilitate vapor condensation. This allowed sufficient cooling at the top of the chamber and kept a steady vertical temperature gradient during the boiling experiments. A small hole of 0.1 cm in diameter was drilled at the top of the

recuperation unit which allowed the excess vapor formed inside the chamber to escape out to avoid any pressure rise inside the chamber. A 100 W immersion heater (obtained from Watlow) was inserted into the boiling chamber to keep the temperature of the liquid close to the saturation conditions during the entire experiment and also to degasify the liquid as much as possible. Both the immersion heater and the cartridge heater assembly were then connected to two separate variable transformers for controlling the heat input.

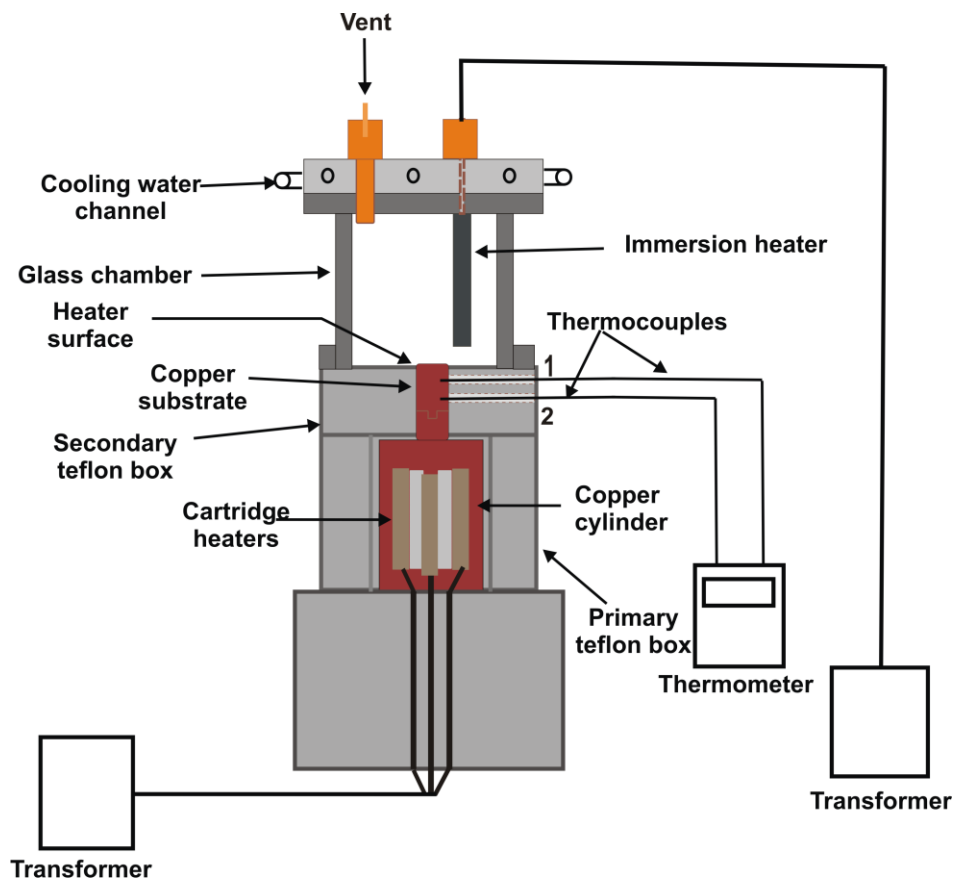


Figure 6.1. Sketch of cross-sectional view of the assembled experimental setup used for the pool boiling experiments.

6.2.6 Pool Boiling Experiments

6.2.6.1 Copper-plated Nanofiber Nanotextured Surface

During pool boiling experiment on the Cu- plated nanofiber nano-textured surfaces, they were compared to the pool boiling experiments on the corresponding bare copper surface. For imental both surfaces the experimental procedure was similar. The substrate was screwed over the top of the primary Cu cylinder and then two thermocouples were inserted in the substrate through the slot in the teflon chamber for the proper acquisition of temperatures. Additional themrocouples were attached to the heater. All the heaters were controlled using a transformer. Test liquid (90 ml) was poured into the boiling chamber during each experiment which lasted for several cycles. The initial setting in the transformer was at 16% of the maximal power. An additional immersion heater (120 V) operated at 100%. The immersion heater was kept at this setting during the entire experiment keeping the liquid temperature at saturation. This procedure allowed maximal degassification of the liquid inside the chamber. Accordingly, after 50 min, the input of the variable transformer was steadily increased by 4%. That setting was kept for 10 min, after which the thermocouple reading did not show any temperature fluctuation. This was considered as a steady state regime. The temperature values at the thermocouple locations were then recorded. The experiments with Novec 7300 fluid were conducted up to 34% of the maximal transformer input, while for DI water it was up to 60%.

6.2.6.2 Pure Polymer Nanofiber Nanotextured Surface

Three types of the heater surfaces were used in these experiments: bare Cu surface (denoted as Bare), Cu surface with electrospun polymer nanofibers on top of it (denoted as

Bare+E), and Cu surface with supersonically blown polymer nanofibers on top of it (denoted as Bare+SB). During each experiment, 90 mL of liquid was used. The immersion heater was operated at 120 V of transformer output (100%) the entire duration of any experiment. The cartridge heater assembly was, however, operated differently in different experiments. For DI water, initially the cartridge heaters were operated at 18% of transformer output and kept at this output for approximately 50 min until the two thermocouples would record a steady-state temperature; after that the transformer was turned to 20% output. After 10 min at this setting as the two temperature records would become steady again, the temperatures were recorded. After that, the output was raised by 4% and kept for 10 min until steady-state temperatures would be recorded. At the end of this ramp, the final transformer output was kept at 60% for all the experiments with DI water, since beyond that the heat flux would have reached CHF and a vigorous temperature rise began.

For Novec 7300 fluid, in all the cases the initial transformer output was at 16%. The further rise in transformer output was kept by 2% after 10-12 min until the temperature records become steady again, while the final output at the end of this ramp was limited to 34% before CHF could be reached. During the entire boiling experiments with NOVEC 7300 fluid, the immersion heater was used to keep liquid at saturation temperature and to achieve as much degasification as possible prior to the boiling onset (for 50 min).

6.3. Results and Discussion

6.3.1 General Definitions

Pool boiling experiments on copper substrate, with or without polymer nanofibers, were conducted using two different liquids, DI water and Novec 7300 fluid, as two limiting cases.

Though their boiling points are close (98 °C for Novec 7300 fluid and 100 °C for DI water) they differ markedly in terms of their specific heat capacity, 1.14 kJ/kg-K for Novec 7300 fluid and 4.2 kJ/kg-K for DI water, their surface tension, 15 mN/m for Novec 7300 fluid and 72 mN/m for DI water, and their latent heat of evaporation 102 kJ/kg for Novec 7300 and 2257 kJ/kg for DI water. In this works it is shown that copper-plated and pure supersonically blown nanofibers significantly enhance heat removal rate in nucleation boiling regime at low surface superheat for both Novec 7300 and DI water, and also for such low surface tension liquids as, for example, ethanol (20 mN/m) [Sahu et al. (2015, 2016)]. Along with metal plating the present work aims to explore to what extent the positive effect of copper-plated nanofibers could be retained with pure polymer nanofibers, even though the surface textures of individual nanofibers of these two types are drastically different and the thermal conductivity of the former is significantly higher than for the latter ($k_{Cu} = 401 \text{ W/m-K}$ versus $k_{PAN} = 0.26 \text{ W/m-K}$, respectively). The main aim of the subsequent experiments with pure polymer nanofiber is to explore the structural integrity (robustness) in nucleate boiling and their capability to enhance heat removal rates. Also the effectiveness of supersonically blown metal plated nanofibers as a robust counterpart of electrospun metal plated nanofiber nanotexture will be explained before briefly which has been shown in Sahu et al. (2015, 2016)

The thermocouples 1 and 2 in Fig. 6.1 measured, respectively, temperatures T_1 and T_2 which were used to determine the surface temperature of the substrate T_s as

$$T_s = T_1 - \left(\frac{T_2 - T_1}{\Delta x_{12}} \right) \Delta x_{1s} \quad (6.1)$$

where Δx_{12} is the distance between the locations of thermocouples 1 and 2, and Δx_{1s} is the distance between the location of thermocouple 1 and the top surface exposed to liquid. Equation

(6.1) is determined by the linearity of the practically one-dimensional temperature distribution along the copper substrate.

Accordingly, the degree of superheat $\Delta T = T_s - T_f$, where T_f is the saturation temperature of the boiling liquid. The heat transfer to the boiling liquid from the substrate surface is found using the Fourier law as

$$q'' = k_{Cu} \left(\frac{T_2 - T_1}{\Delta x_{12}} \right) \quad (6.2)$$

6.3.2 Copper Plated Nanofiber Nano-texture

Pool boiling of Novec 7300 fluid on the copper-plated nanofibers revealed a remarkable enhancement in nucleate boiling and a higher heat removal at lower surface superheat. The results are shown in Fig. 6.2 [Sahu et al. (2015b)]. The heat transfer coefficient is higher on the copper-plated nanofiber surface than on the bare copper surface, as is also evident from Fig. 6.2 where the heat transfer coefficient h is found by the following equation $h = q'' / \Delta T$. For metal-plated nanofiber surface the surface superheat at the beginning of nucleate boiling was sufficiently lower than at the bare surface and was as low as 6 °C. The two consecutive trials that were conducted, both on the bare and nanofiber-covered surface, showed insignificant difference; hence, the repeatability was established as well. More importantly, the nanofiber surface was intact and no further delamination or deterioration was observed on it, neither visually nor in the microscope as is seen in Fig. 6.3. It shows the optical microscope and SEM images both prior and post pool boiling experiments. Surface texture seen in Fig. 6.3 c-d, from the prior boiling to the post boiling images, reveals practically no difference and henceforth the robustness of the nano-texture was well established. The steep rising pool boiling curve on

metal-plated nanofiber nano-textured surface also established the benefit of such surfaces in prolonged boiling experiment.

Nanofiber nano-textured surface showed a remarkable increase in CHF by 33% in comparison with the bare surface at 10 °C lower surface superheat for Novec 7300.

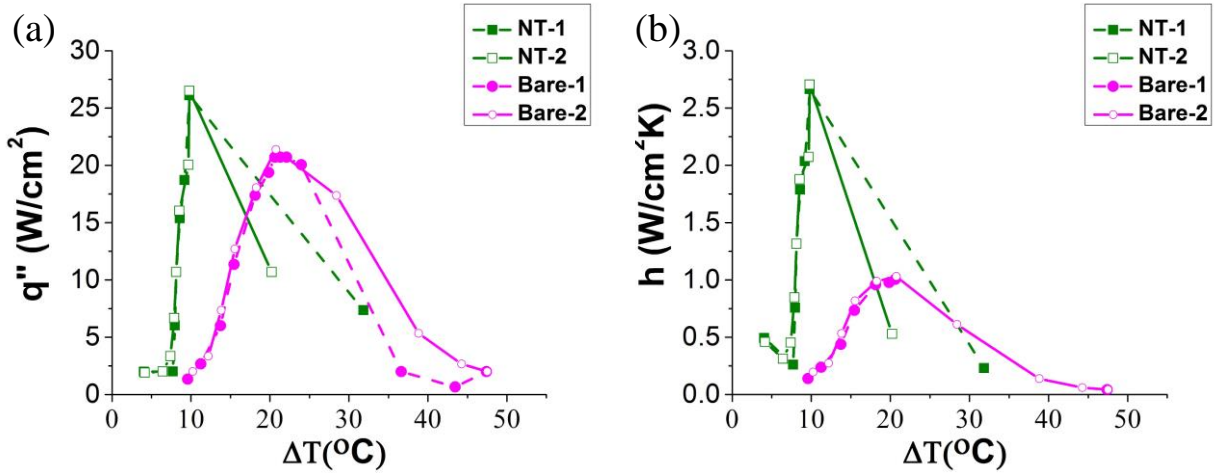


Figure 6.2. Pool boiling data for Novec 7300 fluid on bare copper surface (Bare) and copper surface with thin layer of metal-plated nanofiber nano-texture (NT). The experiments were repeated twice on the same surface and data is shown with numerals 1 and 2 for these trials. (a) Heat flux versus surface superheat, and (b) the corresponding heat transfer coefficient versus surface superheat.

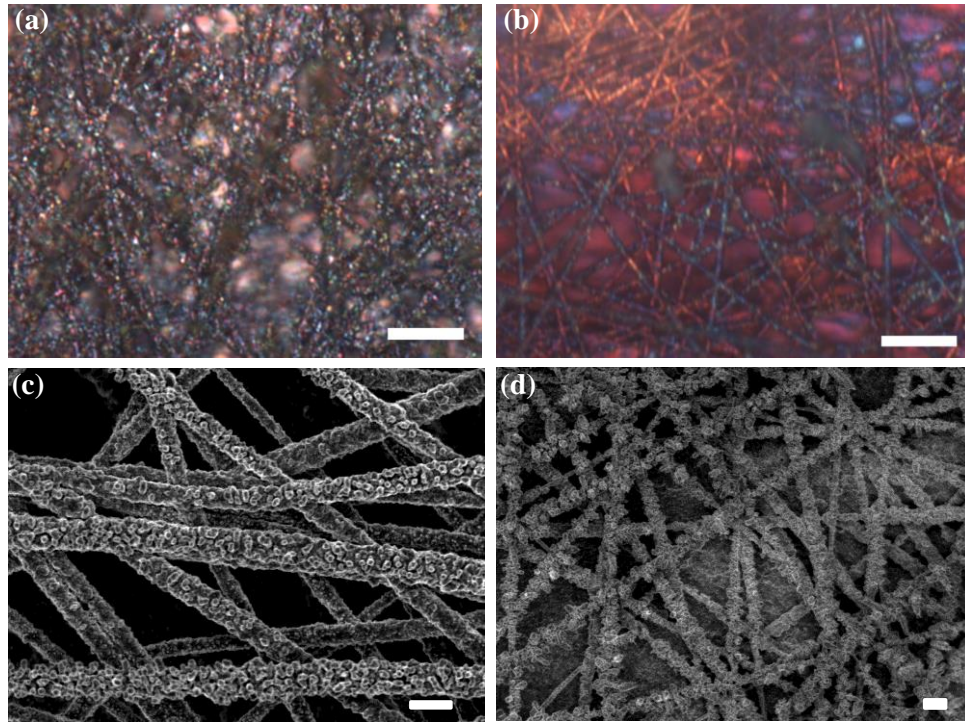


Fig. 6.3. Optical microscope images of the metal- plated nanofiber nano-textured surface (a-b) and SEM image of the same surfaces (c-d), where (a,c) correspond to the prior boiling images and (b,d) –to the post boiling ones. Scale bars are 10 μm in panels (a, b) and 1 μm in panels (c, d).

The results for the pool boiling experiment conducted with DI water are shown in Fig. 6.4. The metal- plated nanofiber surface revealed a better heat removal than the bare surface both in terms of the inception of nucleate boiling and in delaying CHF. However, the effect was not as pronounced as with Novec 7300 fluid. Still, the nucleation began at 1.5 $^{\circ}\text{C}$ lower surface superheat for metal- plated nanofiber surface than for the bare surface and at the highest heat flux surface superheat was as low as $\sim 5^{\circ}\text{C}$ in the former case compared to the later one.

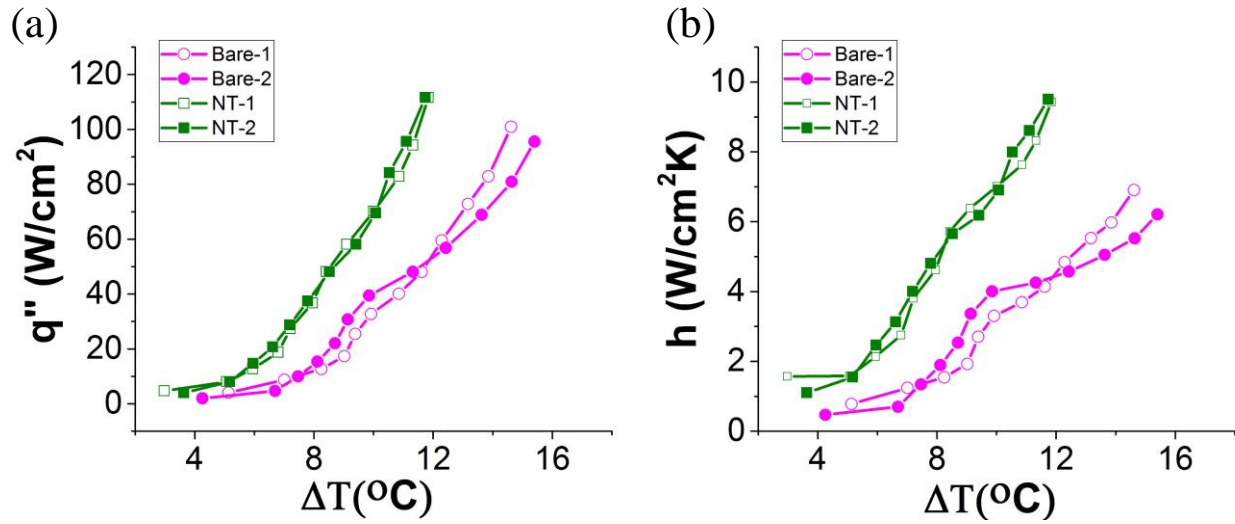


Figure 6.4. Pool boiling data for DI water on bare copper surface (Bare) and copper surface with thin layer of metal-plated nanofiber nano-texture (NT). The experiments were repeated twice on the same surface and data is shown with numeral 1 and 2 for these trials. (a) Heat flux versus surface superheat, and (b) the corresponding heat transfer coefficient versus surface superheat.

After several hours of boiling, Cu surface or the copper nano-texture were converted into Cu-oxide as seen in the X-ray diffraction pattern. However, the repeatability of the boiling pattern was unchanged. This indicates that the nano-texture is mainly responsible for the enhanced nucleation and heat removal and henceforth in the consequent section nano-texture associated with pure polymer nanofibers was tested, which eliminates the extra post-processing step.

6.3.3 Pure Polymer Nanofiber Nanotexture

6.3.3.1 Pool Boiling of Novec 7300 Fluid

All experiments were conducted thrice for the same sample. For Novec 7300 fluid nucleation of vapor bubbles was observed at the Bare+SB surface at ΔT lower by 1 °C than on Bare or Bare+E surfaces. Accordingly, the pool boiling curve is shifted toward lower surface superheat on Bare+SB surface than on either Bare or Bare+E surfaces, cf. Fig. 6.5a. The corresponding heat transfer coefficient $h=q''/\Delta T$ is shown in Fig. 6.5b.

Not only supersonically-blown polymer nanofibers revealed higher heat removal rates at the same surface superheat and thus outperformed the bare surface and the surface covered with electrospun polymer nanofibers, they also revealed the pool boiling enhancement quite comparable to that of copper-plated supersonically-blown nanofibers in [Sahu et al. (2016)]; cf. Fig. 6.5c. The latter is quite amazing, since copper plating not only introduces additional nucleation sites (the copper-plated thorny-devil nanofibers of [Sahu et al. (2016)] are very rough compared to the relatively smooth polymer nanofibers of the present work) but also increases thermal conductivity of the nanofiber mat. Still, copper-plated supersonically solution-blown nanofibers outperform the non-plated ones, as Fig. 6.5c shows. Namely, the difference in the heat fluxes between them at the same surface superheats is quite significant. After the surface superheat of about 7.5 °C copper-plated nanofiber mat outperforms the non-plated nanofiber mat. At the surface superheat of about 10 °C copper-plated thorny devil nanofibers remove about 44% more heat in comparison to the non-plated ones. In fact, Fig. 6.5c clearly shows that an additional nano-texture associated with metal nucleation sites created by copper-plating are beneficial for heat removal. Still the non-plated supersonically-blown pure polymer nanofibers

yield significant benefits too compared to the bare surface or to the larger electrospun nanofibers, which is ascertained by the results shown in Figs. 6.5a and c.

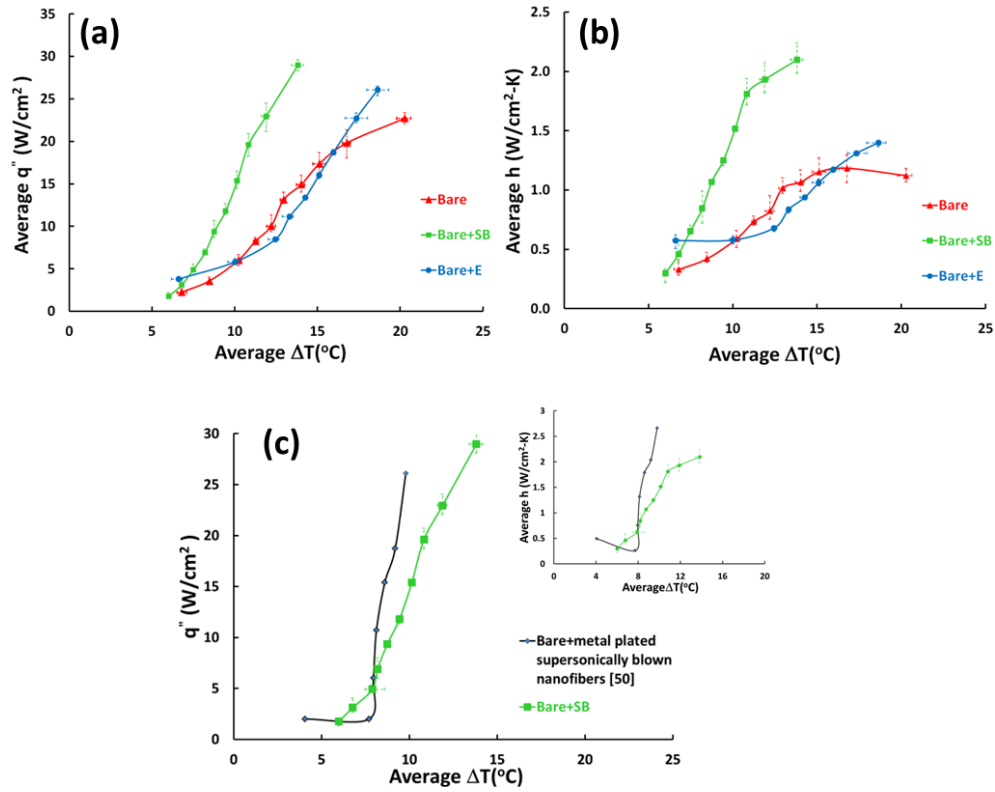


Figure 6.5. Pool boiling curves for Novec 7300 fluid on Bare, Bare+SB and Bare+E surfaces. The experiments were repeated thrice on the same surface and the average values of q'' , h and ΔT are used in these graphs. (a) Heat flux versus surface superheat, and (b) the corresponding heat transfer coefficient versus surface superheat. (c) Boiling curves on Bare+SB surface with polymer nanofibers (from panel a) versus Bare+SB surface with copper-plated nanofibers from [Sahu et al. (2015b).], with the corresponding heat transfer coefficient versus surface superheat in the inset. The error bars show the maximum and minimum deviations from the average values.

Fig. 6.6 shows the overall view of the heater surfaces prior and after prolonged boiling. There is no macroscopically visible deterioration of either supersonically blown nanofibers (Fig. 6.6b) (which are very thin and look like a milky mat, similarly to [Sinha-Ray, Suman et al. (2013)]), or electrospun nanofibers (Fig. 6.6c) which are clearly seen. There is also no significant oxidation of the copper surface which would be recognizable by color change.

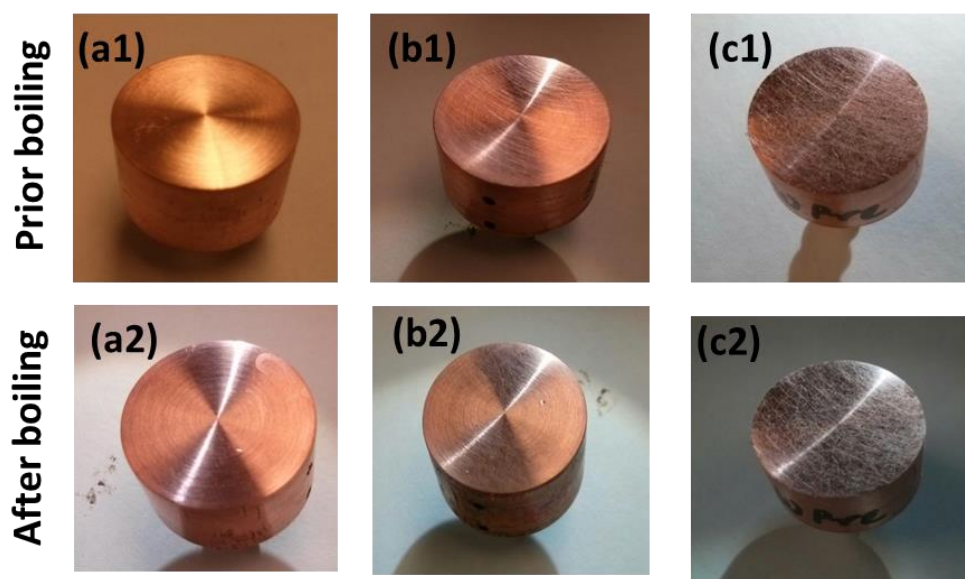


Figure 6.6. Surface images of the same samples prior (panels with numerals 1) and post boiling (panels with numerals 2) of Novec 7300 fluid for 7.5 h. (a) Bare, (b) Bare+SB surfaces, (c) Bare+E surfaces. Nanofiber mats are seen as fine white lines on the surfaces, practically invisible on Bare+SB and clearly visible on Bare+E surfaces. The surfaces are 1.9 cm in diameter.

However, the macroscopic images of Fig. 6.6b-c are insufficient for definite determination of the nanofiber state after prolonged boiling. Therefore, in addition to the macroscopic images of Fig. 6.6b-c, SEM images of the Bare+SB and Bare+E surfaces are shown in Fig. 6.7. The latter images reveal that electrospun nanofibers deteriorated in several places and the intact

coating ceased to exist after 7.5 h of boiling of Novec 7300. On the other hand, the supersonically blown nanofibers remained intact after 7.5 h of boiling of Novec 7300.

It should be emphasized that nanofiber adhesion is critical because it results in a better thermal contact of supersonically-blown nanofibers with the heater compared to the electrospun ones. A better thermal contact results in a higher rate of vapor bubble nucleation and removal, and thus intensifies the heat removal process. Additionally, the supersonically-blown nanofibers do not delaminate from the heater due to their stronger adhesion and samples could be used for long multi-hour boiling. The stronger adhesion of the supersonically-blown nanofibers is caused by the van der Waals attraction effective on the scale about 100 nm [Sinha-Ray, Sumit et al. (2015a)], which is the case of these nanofibers in distinction from the electrospun ones. Accordingly, the superior heat-removal performance of the supersonically-blown nanofiber in comparison with larger electrospun nanofibers stems from a combination stronger adhesion and faster bubble nucleation on abundant nucleation sites provided by the smaller size nanofibers.

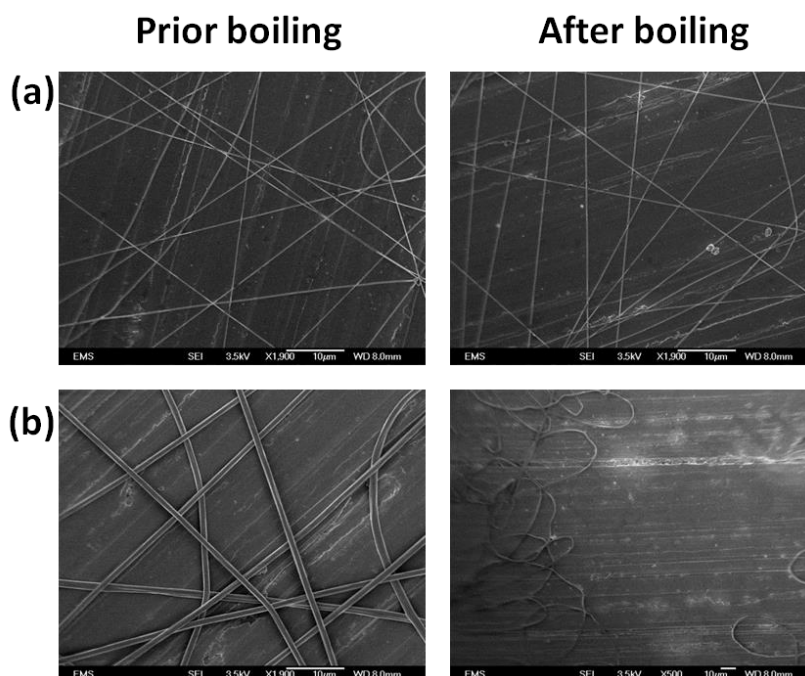


Figure 6.7. SEM images of the nano-textured surfaces prior and after a prolonged boiling of Novec 7300 for 7.5 h. (a) Bare+SB surface, and (b) Bare+E surface. All scale bars are 10 μm .

The comparison of Figs. 6.7a and 6.7b also shows that being observed at the same magnification, supersonically blown polymer nanofiber mats prior boiling are thinner in comparison to the electrospun ones. Accordingly, the supersonically blown nanofibers provide much more nucleation sites per unit area than the electrospun ones. The much smaller supersonically blown polymer nanofibers adhere to the copper substrate much stronger than the electrospun nanofibers.

According to [Tien (1962)], on a surface where active nucleation sites are distributed randomly, the center-to-center distance between the bubbles $S \sim n^{-1/2}$, where n is the surface density of the active nucleation sites. For bare copper surfaces only a few bubbles nucleated from

the heater surface itself but rather from its periphery in contact with Teflon [Sahu et al. (2015b)]. On the other hand, on the copper-plated nanofiber surfaces the entire heater surface contains multiple nucleation sites and generates multiple bubbles [Sahu et al. (2015b)]. The same phenomenon was observed in the present work (Fig. 6.8), and since the value of n for solution-blown nanofibers is larger than for the electrospun or bare ones, the former result in a higher heat removal rate. All the surfaces, Bare, Bare+SB and Bare+E, have been compared at same surface superheat of 3.65°C with only the main cartridge heater supplying heat from the bottom and the immersion heater being off for improved visualization. For the sake of comparison, 114 ms after the onset of boiling of Novec 7300 snapshots of boiling on all the surfaces are shown in Fig. 5 (taken from high-speed videos using Phantom V210 at 2200 fps). It is seen that for Bare+SB surface the bubble density is much higher compared to the bubble density for Bare and Bare+E surfaces.

Careful examination of 80 bubbles on several images using Photoshop revealed the following average bubble radii at the moment of departure from the surface: 0.125 ± 0.032 mm for Bare+SB surface, 0.20 ± 0.044 mm for Bare+E surface and 0.301 ± 0.07 mm for Bare copper surface. In case of the Bare surface the bubble radius r at the departure moment is determined by buoyancy and surface tension, and can be estimated as $r = [\sigma / (\rho g)]^{1/2}$, with ρ and σ being the density and surface tension of liquid and g being gravity acceleration. Taking for the estimate $\rho \sim 1.48 \text{ g/cm}^3$ and $\sigma \sim 10 \text{ g/s}^2$, from the manufacturer, this expression yields $r \sim 0.8$ mm, which overestimates the observed value mentioned above. On the other hand, on nano-textured surfaces, the bubble growth is arrested by the surrounding nanofibers. Fig. 6.7 shows that the average inter-fiber pore areas on the Bare+SB and the Bare+E surfaces are $\sim 30 \mu\text{m}^2$ and $33 \mu\text{m}^2$ with the corresponding porosity of 86% and 78% (Measured using ImageJ software).

Accordingly, the pore sizes are of the order of $3\ \mu\text{m}$, which are significantly smaller than the above-mentioned measured bubble sizes. This corresponds to the observations in [Sahu et al. (2015a)], where it was argued that vapor jets are squeezed from such pores and undergo the Rayleigh capillary instability which results in bigger bubble formation. Some occasional big bubbles on the Bare+SB surfaces could also be seen; however, most of them originated from the periphery in contact with teflon and were pushed inward.

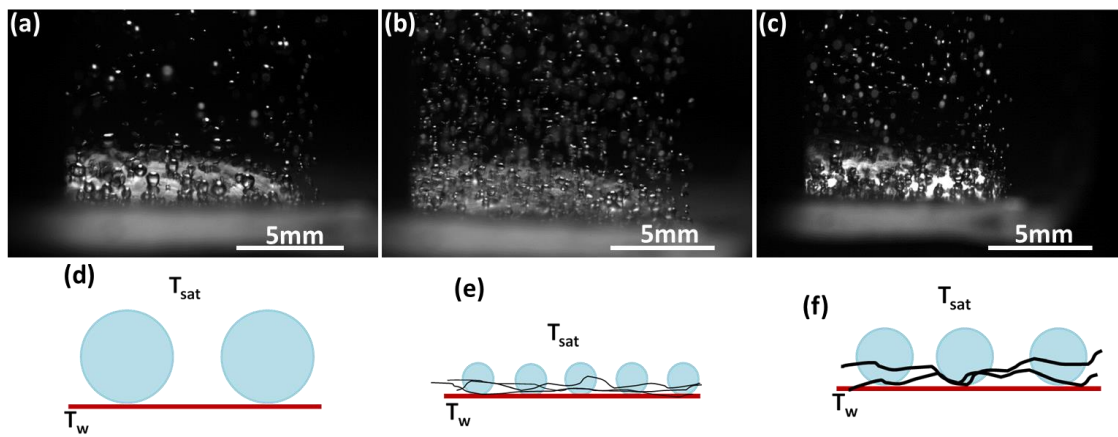


Fig. 6.8. High speed images of vapor bubble nucleation and departure from the heater surface in Novec 7300 fluid. (a) Bare, (b) Bare+SB and (c) Bare+E surfaces. Panels (d), (e) and (f) sketch the phenomena observed in panels (a), (b) and (c), respectively.

Fewer bubbles nucleating and departing from Bare copper surface generate a weaker convective flow and thus, a diminished heat transfer process compared to that on Bare+SB surface where multiple bubbles appear due to the effect of nanofibers. Correlations for heat flux q'' in nucleate pool boiling on bare on horizontal surfaces read [Tien (1962), Nishikawa and Yamagata (1960)]

$$q'' = c \cdot \text{Pr}^{0.33} \cdot k \cdot n^{1/2} \cdot \Delta T \quad (6.3)$$

where, q'' is the average heat flux (W/cm^2), Pr is the Prandtl number, c is a dimensionless constant, k is the thermal conductivity of liquid ($\text{W}/\text{cm}\cdot\text{K}$), n is the surface density of active nucleation sites (cm^{-2}), and ΔT is the surface superheat (K).

Accordingly, the heat transfer coefficient h ($\text{W}/\text{cm}^2\cdot\text{K}$) is

$$h = c \cdot \text{Pr}^{0.33} \cdot k \cdot n^{1/2} \quad (6.4)$$

The latter equations show that both q'' and h increase with the surface density of bubble as $n^{1/2}$ [Tien (1962), Gaertner and Westwater (1960)]. This conclusion can be extrapolated to the present case of surfaces covered with nanofibers. Also, when the convective flow driven by rising bubbles becomes turbulent [Tien (1962), Zuber (1961)], the dependence of both q'' and h on the Prandtl switches from $\text{Pr}^{0.33}$ to $\text{Pr}^{0.6}$. For Novec 7300 fluid $\text{Pr}=21.3$, whereas, for DI water $\text{Pr}=6.41$. Therefore, the combined effect of the higher nucleation rate, more frequent bubble departure and faster transition to turbulence in the bubble-driven flow results in the fact that at the same surface superheat both q'' and h on the Bare+SB surfaces are larger than those on the Bare+E surfaces, while the latter are larger than the q'' and h values for the Bare copper surface.

It should be emphasized that the supersonically blown PAN nanofibers are very small, of the order of 100 nm in diameter (cf. Fig. 6.7a), and thus their surface curvature is extremely high. Therefore, they are very effective heat transfer elements to the surrounding medium (liquid in the present case) [Zeldovich (1985)], and thus additionally facilitate nucleate boiling.

6.3.3.2 Pool Boiling of DI Water

Experiments conducted with DI water on different substrates were limited to maximum of 60% of the transformer output to avoid reaching CHF. The results are shown in Fig. 6.9. It is seen that the enhancement of the heat removal rate due to nanofibers at any surface superheat is less pronounced compared to the case of Novec 7300 fluid (Fig. 6.5), even though the trend stays the same, i.e. the heat transfer is the highest on the Bare+SB surface. The surface superheat of the Bare+SB surface was almost 1.7°C lower in comparison to that of the bare surface and 1.5°C lower than that of the Bare+E surface at 60% (the maximum value used) of the total input of the transformer driving the cartridge heater.

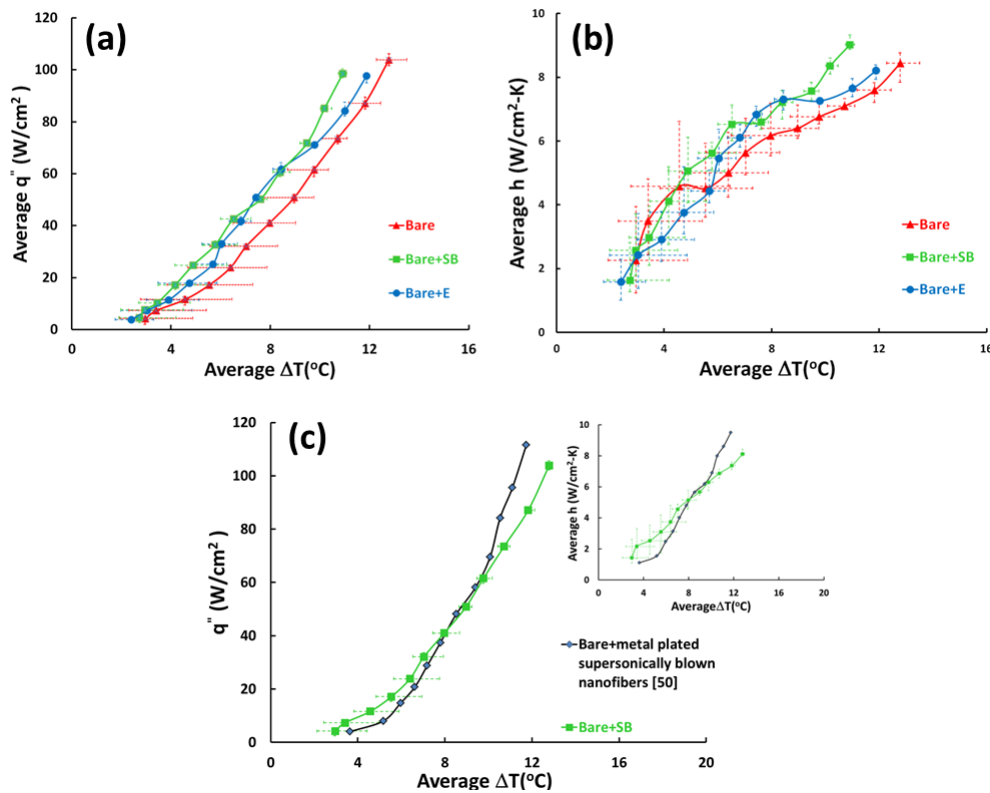


Fig. 6.9. Pool boiling curves for DI water on Bare+SB, Bare, and Bare+E surfaces. The experiments were repeated thrice on the same surface and the average values of q'' , h and ΔT are

used in these graphs. (a) Heat flux versus surface superheat, and (b) the corresponding heat transfer coefficient versus surface superheat. (c) Boiling curves on Bare+SB surface with polymer nanofibers (from panel a) versus Bare+SB surface with copper-plated nanofibers from [50], with the corresponding data for the heat transfer coefficient in the inset. The error bars show the maximum and minimum deviations from the average values.

Macroscopic images of test surfaces reveal that boiling of water for several hours on bare Cu surface leads to formation of copper oxide (cf. Fig. 6.10a), as in [Moliere (1990)]. The oxide layer is manifested by green color of the surface. In the case of the Bare copper surface this oxide formation can prevent nucleation and can affect the superheat values in the further trials. The change in the copper surface characteristics due to the formation of the oxide layer is the main reason of the larger data scatter in the case of DI water boiling in comparison to Novec 7300 fluid boiling. In addition, after boiling in DI water on the Bare+E surface the nanofiber layer was completely ripped off (cf. Figs. 6.10b and 6.6c2), similarly to some cases reported in [Jun et al. (2013)] for copper-plated nanofibers. This happens mainly due to the growth of vapor bubbles which pull the fibers with forces associated with surface tension, which is high for DI water compared to Novec 7300 fluid. On the contrary, supersonically blown polymer nanofibers on the Bare+SB samples stayed attached to the substrate surface and mostly retained the architecture of the nanofiber mat. Fig. 6.10b reveals the presence of a thin white transparent fiber layer on the surface characteristic of the supersonically blown nanofiber mats, which is confirmed by SEM images in Fig. 6.11. Fig. 6.11 shows that the supersonically blown polymer nanofibers retained their structures and no delamination from the copper substrate happened.

Moreover, these nanofibers seem to be bonded to the copper surface and with each other (cf. Fig. 6.11b).

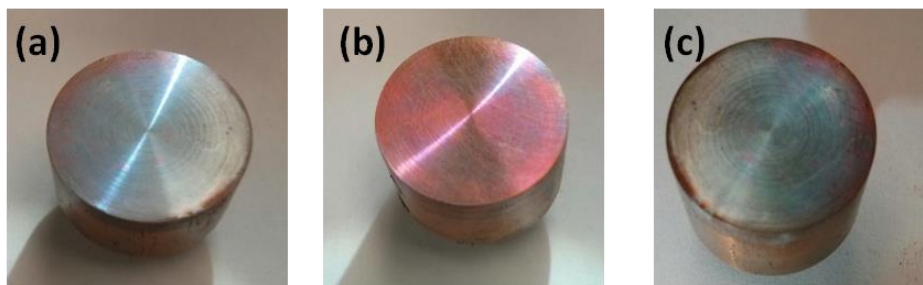


Fig. 6.10. Macroscopic images of the sample surfaces after boiling for 8 hours in DI water. (a) Bare, (b) Bare+SB, and (c) Bare+E surfaces. The green copper oxidized layer on the surfaces is visible. Sample surfaces are of 1.9 cm in diameter.

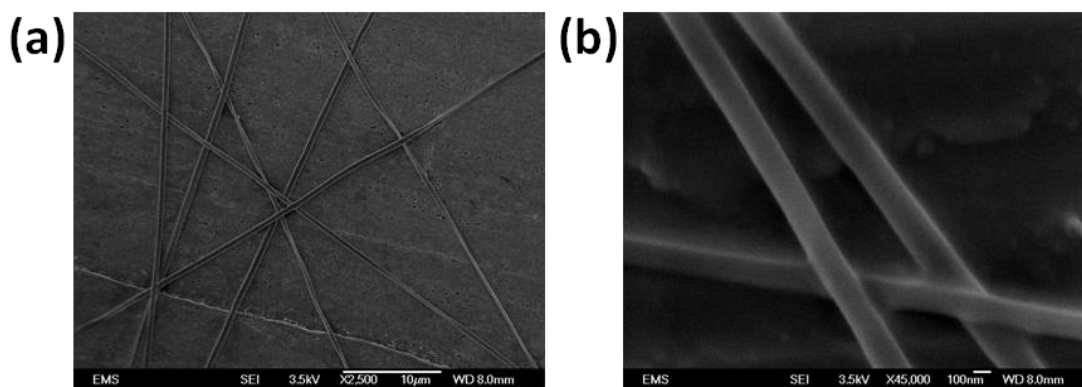


Fig. 6.11. SEM images of the supersonically blown polymer nanofibers on copper substrate after prolonged boiling for 8 h in DI water. Nanofiber bonding to the surface and to each other is also visible. Scale bar in panel (a) is 10 μm and in panel (b) is 100 nm.

Figs. 6.5 to 6.10 show that the effect of supersonically blown polymer nanofibers on heat transfer to boiling water is less dramatic than for Novec 7300 fluid. Figs. 6.7, 6.10 and 6.11 also

show that supersonically solution-blown nanofibers slightly changed morphology after boiling in water being sintered to each other, whereas boiling in Novec 7300 fluid no morphology changes have been observed. Smaller bubbles in Novec 7300 fluid intensify the heat removal rate in it in comparison to the bare surface more effectively than in water boiling in comparison to bare surface was not drastic. That is probably the reason of the inter-polymer fiber bonding in boiling water, given the fact that PAN nanofibers have the glass transition temperature around 100 °C (the boiling point of water), which should not be confused with melting, since melting point of PAN is nearly 320 °C. Note also that up to $\Delta T \sim 9$ °C the supersonically blown polymer nanofiber mat performed better than the supersonically blown metal-plated nanofiber mat (cf. Fig. 6.10c).

6.4. Conclusion

Pool boiling experiments with Novec 7300 fluid and DI water conducted on bare Cu surface, and copper surface coated with either electrospun or supersonically blown pure polymer nanofibers and supersonically blown Cu-plated nanofibers revealed significant benefits of the supersonically-blown nanofiber nano-textured. For Cu-plated nanofibers the effect of the additional nucleation sites was more pronounced than on the bare surface leading to an enhanced nucleation boiling. For Novec 7300 fluid, nucleate boiling was observed at nearly 6 °C lower surface superheat than on the bare surface and accordingly, nucleate boiling was more favored. CHF was also delayed by 33%, while no deterioration of the metal-plated nanofiber nano-texture was observed. Significant improvement in DI water boiling was also observed on nanofiber surface in comparison with the bare surface, and the inception of nucleate boiling was also hastened. Without metal-plating, when using pure polymer nanofiber coatings, a significant

improvement in nucleate boiling could be achieved, especially with supersonically- blown ultrafine nanofibers, which were much more effective than electrospun nanofibers. The supersonically blown polymer nanofibers significantly enhanced the heat removal rate from the heater surface, especially in the case of Novec 7300 fluid where the maximum surface superheat was reduced by at least 7 °C versus 5 °C for the electrospun surface. The supersonically blown 100 nm polymer nanofibers facilitated bubble nucleation serving as active nucleation sites. Such nanofiber mats also possess a larger number of small pores than electrospun nanofibers, which cut and release the growing bubbles. Supersonically blown nanofibers revealed the best adhesion to the copper substrate and retained their architecture after prolonged 7.5 h of boiling. The experiments conducted with DI water did not show as strong enhancement of the heat removal rate, as the experiments with Novec 7300 fluid did, even though compared to the bare copper surface, the surface superheat was reduced on supersonically blown nanofibers by ~1.7 °C at the maximum heat flux after 8 h of boiling. On the other hand, after boiling in DI water, electrospun nanofibers were completely delaminated from the copper substrate, unlike the supersonically blown nanofibers which retained their adhesion and architecture. The inexpensive surfaces coated with supersonically blown nanofibers can remove heat at the rate of ~30 W/cm² in Novec 7300 fluid.

CHAPTER 7

**FLOW OF SUSPENSIONS OF CARBON NANOTUBES CARRYING PHASE
CHANGE MATERIALS THROUGH MICROCHANNELS AND HEAT TRANSFER
ENHANCEMENT**

This chapter has been previously published in Sinha-Ray, Sumit et al. (2014). Reprinted with permission from [Sinha-Ray, Sumit, Sinha-Ray, Suman, Sriram, H., Yarin, A. L., Flow of Suspensions of Carbon Nanotubes Carrying Phase Change Materials Through Microchannels and Heat Transfer Enhancement (2014), Lab Chip, 14, 494-508]. Copyright 2014 Royal Society of Chemistry.

7.1 Introduction

The present work aims at passive cooling of microelectronics using nano-encapsulated phase change materials. Passive/indirect cooling of microelectronics is one of the attractive methods because of high heat removal capacity when the coolant does not come in direct contact with the heated system and henceforth there is no chance of contamination. Phase change materials like wax, sugar alcohol, fatty acids and metal hydrides, etc. [Kuravi et al. (2009); Gong and Mujumdar (1996); Goel et al. (1994); Sabbah et al. (2009)] have many benefits, namely, a relatively high latent of fusion (~ 200 J/g), a wide melting-point temperature domain for different mixtures of PCMs, chemical inertness; although they suffer from the problems related to low thermal conductivity and diffusivity and potential segregation at the channel walls [Zalba et al. (2003)]. Both disadvantages could be avoided using nano-encapsulation in carbon nanotubes (CNT) via self-sustained diffusion [Sinha-Ray, Suman et al. (2011c)] which can lower the thermal response time to the level of 10^{-7} s. Such PCM-filled CNT suspensions can be

potentially useful in passive cooling of high-power microelectronics when a convective flow through microchannels attached to the heat-releasing system is employed. In the present Chapter such a cooling method has been developed, with a PCM-filled CNT suspension in water being flowing through microchannels embedded in a heated block mimicking a microelectronics device. The theory is detailed in section 2. Experiments are discussed in section 3, while the results and discussion are described in section 4. Conclusions are drawn in section 5.

7.2 Background Formulae

In pressure-driven flows of pure liquids through straight channels of circular cross-section of radius a with no-slip boundary conditions at the wall, the velocity profile is parabolic [Loitsyanskii (1966)]

$$v = -\frac{1}{4\mu} \frac{dp}{dz} a^2 \left(1 - \frac{r^2}{a^2} \right) \quad (7.1)$$

and the corresponding volumetric flow rate is given by the Poiseuille law

$$\dot{Q} = \frac{\pi a^4}{8\mu} \left| \frac{dp}{dz} \right| \quad (7.2)$$

In Eqs. (7.1) and (7.2) v is the longitudinal velocity in the direction of the channel axis Oz , \dot{Q} is the volumetric flow rate, μ is the fluid viscosity, and $dp/dz < 0$ is a constant pressure drop. Equations (7.1) and (7.2) imply fully developed laminar flows [Bazilevsky et al (2008b); Loitsyanskii (1966)]

In the case of a given constant heat flux at the channel wall, the temperature profile is given by [Holman (1986)]

$$T - T_c = \frac{1}{\alpha} \frac{dT}{dz} \frac{v_c a^2}{4} \left[\left(\frac{r}{a} \right)^2 - \frac{1}{4} \left(\frac{r}{a} \right)^4 \right] \quad (7.3)$$

where α is the fluid thermal diffusivity, v_c and T_c are the axial velocity and temperature in the channel, and dT/dz is the temperature gradient along the channel which is a given constant. Equation (7.3) implies laminar flow which is fully developed hydro-dynamically and thermally.

To evaluate the expected temperature reduction ΔT due to the presence of PCM-containing CNTs, the following thermal balance is used

$$\rho c_p V \Delta T = L \rho \phi V \quad (7.4)$$

where ρ and c_p are the fluid density and specific heat, respectively, V is the total volume of the suspension, ϕ is the PCM volume fraction, and L is the latent heat of fusion. Then,

$$\Delta T = \frac{L}{c_p} \phi \quad (7.5)$$

It is emphasized that the PCM volume fraction ϕ can be affected by flow. In particular, CNT alignment by flow in microchannels can effectively increase the local value of ϕ compared to that in the solution bulk, and thus enhance the temperature reduction ΔT , as the experimental results discussed below reveal.

7.3 Experiments

7.3.1 Materials and Preparation of Suspension

Carbon nanotubes PR24XT-LHT-AM of small aspect ratio $r \sim 142$ were acquired from Pyrograf Products. Surfactant NaDDBS (Sodium Dodecyl Benzene Sulfonate) was supplied by

Sigma. Mustard oil of viscosity 76.5 cP was purchased in a grocery store. Carbon nanotube suspensions were prepared as follows: 1.5 g of a previously prepared 1 wt% aqueous solution of NADDBS was blended with 18.5 g of 0.1 wt% aqueous suspension of empty CNTs. Similarly, 2 wt% solution of NADDBS was added to 0.2 wt% CNT suspension, etc. for the other wt% values for the empty CNT suspensions. The blends were sonicated in an ultrasonic bath sonicator of 55 W. Benzene and wax [Sinha-Ray, Suman et al. (2011c)] (the melting point in the range 45-47 °C) were obtained from Sigma Aldrich.

For preparing wax-intercalated CNT suspensions, the method of self-sustained diffusion [Sinha-Ray, Suman et al. (2011c); Brazilevski et al. (2007); Brazilevski et al. (2008a)] was used. First, wax solution in benzene was prepared by dissolving 0.3 g of wax in 19.7 g of benzene. The solution was sonicated for 30 min. After that, 60 mg of empty CNTs were added to the wax solution and sonicated for 2-3 min. Then, the CNT suspension in wax solution was left to evaporate in chemical hood. As benzene was evaporating, wax diffused into CNTs. Since the wax concentration in the solution was permanently increasing during evaporation, the concentration gradient was self-sustained and wax continued to diffuse into CNTs which were intercalated with wax significantly. After the evaporation was finished, the dry CNTs intercalated with wax were additionally rinsed in benzene to remove wax deposited outside and sonicated for 2 min more. After that, the suspensions of CNTs in benzene were filtered. The resulting wax-intercalated CNTs were used to prepare their suspension in water.

To prepare aqueous suspensions of wax-intercalated CNTs, a probe sonicator of 500 W [20 KHz (Qsonica)] was employed along with the bath sonicator. Prior to the bath sonicator, the probe sonicator was used for 5 min at 40% power. That helped in removing the residual chunks as wax can increase the tendency to CNT clustering. The pre-sonication with the probe sonicator

allowed a reduction in duration of bath sonication to 5 h. The 1 g surfactant solution was handled similarly to the above-mentioned 19 g suspension. Namely, 0.5 g of surfactant solution was added prior to probe sonication, the rest of surfactant solution was added during the bath sonication in steps. Namely, 0.1 g of surfactant solution was added to the suspension after every hour of sonication.

7.3.2 Experimental Setup

In the setup used to study pure water or the aqueous surfactant solutions flows, two 10 ml syringes were coupled and glued with epoxy to make an oil chamber (Fig. 7.1). For every new experimental run, mustard oil in the chamber was changed. The sketch of the experimental setup in Fig. 7.1 also incorporates

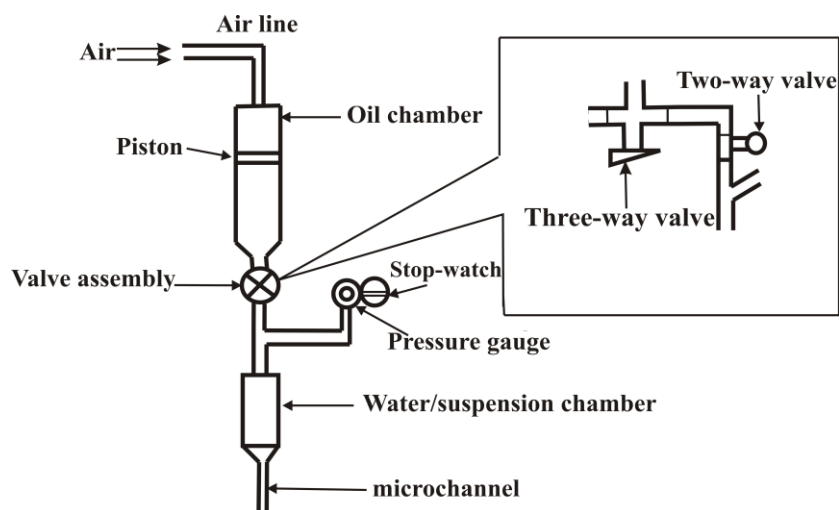


Figure 7.1. Schematic of the first experimental setup with piston pushing water or aqueous solutions of surfactants and CNT suspensions.

the air-driven piston which pushes oil inside the oil chamber. The oil, in turn, pushes pure water or aqueous solutions of surfactants in the lower chamber. Direct air-driven piston pushing of water or aqueous solutions of surfactants without an intermediate mustard oil layer was found to be unstable.

The microchannel used in the setup of Fig. 7.1 was a 25G stainless steel needle with an ID of 260 μm . The air pressure was monitored from the primary air-line, and the pressure maintained at the top of the oil chamber could be measured with the help of the pressure gauge. Two DSLR cameras were employed to take images. One of the cameras recorded the pressure and time readings, and the other one recorded the volume change in the water/suspension chamber. The imaging was done simultaneously using a wired trigger in every 30 s. The recorded time, pressure and volume were used to evaluate the corresponding flow rate. The data were averaged over two consecutive trials.

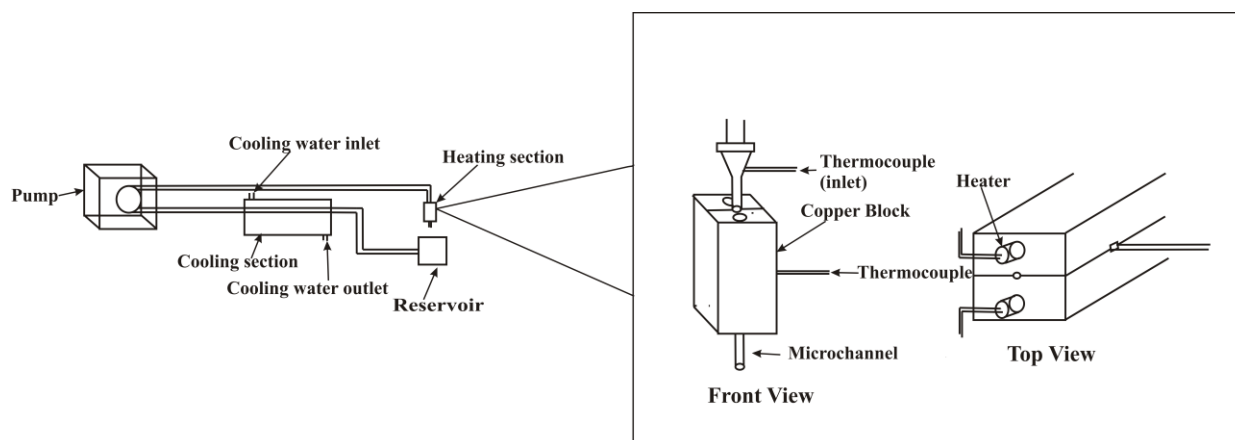


Figure 7.2. Schematic of the second experimental setup employed to study heat removal using microchannel flows of wax-intercalated CNTs.

In the experiments on cooling using aqueous suspensions of CNTs intercalated with wax, a peristaltic pump was included in the system instead of the air pressure driven system to sustain the flow for a long time (Fig. 7.2). The peristaltic pump was purchased from New Era Pump Systems Inc. In this case 20G or 13G needles (603 and 1803 μm ID, respectively) were used as microchannels. The aqueous suspensions of CNTs were re-circulating through the microchannels by means of the peristaltic pump. The suspensions were pumped from the reservoir at a specific flow rate through the microchannel embedded in the heated copper block. The returning suspension was then passed through a cooling section which was kept at 12 °C in cooling water re-circulating in the cooling water section surrounding the microchannel with flowing suspension. The experiments were conducted at different flow rates ranging from 5 ml/min to 55 ml/min preset at the pump.

Two 50 W heaters received from Omega were used for heating the copper block of the lateral dimensions 1.5 cm \times 1.5 cm with the length of 3.175 cm which was a prototype of a heated integrated microelectronic system. The heating was sustained at a constant level of 9 W maintained with the help of a transformer. The microchannel was put inside the copper block and properly tightened with screws. Silver paste was used in the gap between the microchannel and copper block to ensure proper contact and guarantee an unperturbed heat transfer from the block to the suspension. Two thermocouples purchased from Omega were used to measure the temperature distributions along the heating section. The thermocouples were embedded in the copper block (Fig. 7.2). One thermocouple was embedded at the very entrance of the needle to measure the inlet temperature, and the other one was embedded in the middle of the copper block to measure the microchannel temperature there. The latter was considered as the average

temperature of the channel. All temperature measurements were done using Omega H8065W thermometer.

7.4 Results and Discussions

7.4.1 Water and Aqueous Solution of Surfactant Flows Through Microchannels

In the experiments pressure drop was the governing parameter, while volumetric flow rate was measured. The experimental results for pure water flows are plotted in Fig. 7.3 together with the Poiseuille law given by Eq. (7.2). Fig. 7.3 shows that the agreement of the theory and the experimental results is very good, which verifies the accuracy of the measurements. It is emphasized that the extra pressure drop between the pressure gauge and the microchannel entrance is practically negligible. So, it can be safely assumed that the pressure at the microchannel entrance is the same as the one on the pressure gauge.

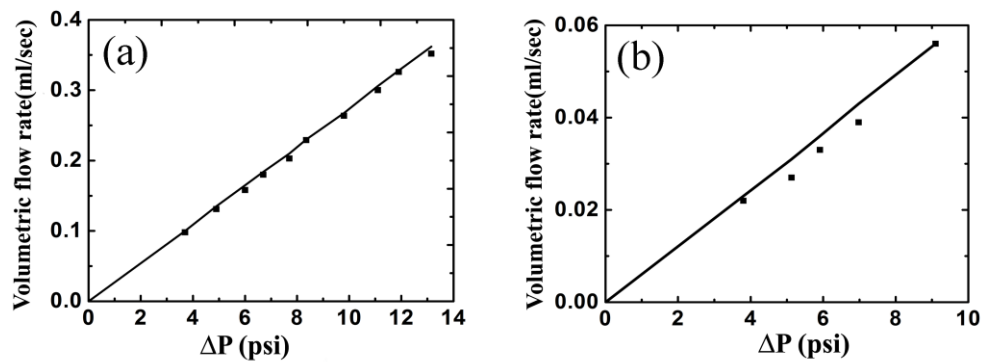


Figure 7.3. Volumetric flow rate versus pressure drop. (a) Circular glass microchannel (260 μm in diameter), and (b) circular metal microchannel (260 μm in diameter). Symbols show the experimental data, straight lines are the theoretical results.

The flow is definitely laminar since the Reynolds number $Re=9.774$, say, at the flow rate which corresponds to the pressure drop of 6 psi (the Reynolds number $Re = \rho VD / \mu$ where ρ is the fluid density, V is the average velocity and D is the channel cross-sectional diameter.)

The entrance length ℓ_e at which a fully developed flow in a microchannel will be formed is found as [Nguyen and Wereley (2007)]

$$\frac{\ell_e}{D} = \frac{0.6}{1 + 0.035Re} + 0.56Re \quad (7.6)$$

In the present case $\ell_e = 0.15$ cm which is much less than the microchannel length $\ell = 5$ cm. Therefore, there is practically a fully developed flow from the very beginning of all microchannels used in the present work.

The CNT suspensions were stabilized with different surfactants, which were also beneficial to diminish the tendency to microchannel clogging. The CNTs are apparently hydrophobic which does not allow them to disperse in water properly. This can enhance the viscous losses during pumping the suspension even when a moderate concentration of CNTs is used. The apparent hydrophobicity of the CNTs in polar solvents like water stems from the fact that they have sufficiently high aspect ratios and flexibilities. Therefore, strong van der Waal attraction between them results in formation of a tightly entangled (rope-like) structure with dense packing [Vaisman et al. (2006)]. Dispersion of CNTs can be facilitated by ultra-sonication or shear mixing, by means of functionalization with acids, or by using surfactants to modify surface characteristics in favor of tube hydration and prevention from agglomeration. However, ultra-sonication or shear mixing, as well as the acid treatment often lead to surface fracture [Vaisman et al. (2006)]. Surfactants are a better way to disperse CNTs in water. There have been

reports on the application of different surfactants, e.g. Sodium Dodecyl Sulphate (SDS) or Sodium Dodecyl Benzene Sulfonate (NaDDBS) which are claimed to be better than some organic surfactants [Islam et al. (2003); Rakov (2006)]. NaDDBS is superior, since it has benzene ring attached to it, which adsorbs on the CNTs with the help of the π - interactions [Vaisman et al. (2006)]. Sonication allows the entangled CNT bundles to disperse and thereby enhances surfactant molecules adsorption on individual CNTs [Strano et al. (2003)]. With NaDDBS added, it was found that the maximum concentration of CNTs at which clogging does not happen in the 260 μm microchannel is 1 wt%. Beyond that limit, CNT aggregates clog the entrance of the microchannel. Volumetric flow rates of CNT suspensions with added surfactant were measured at different pressure drops and the results are shown in Fig. 7.4.

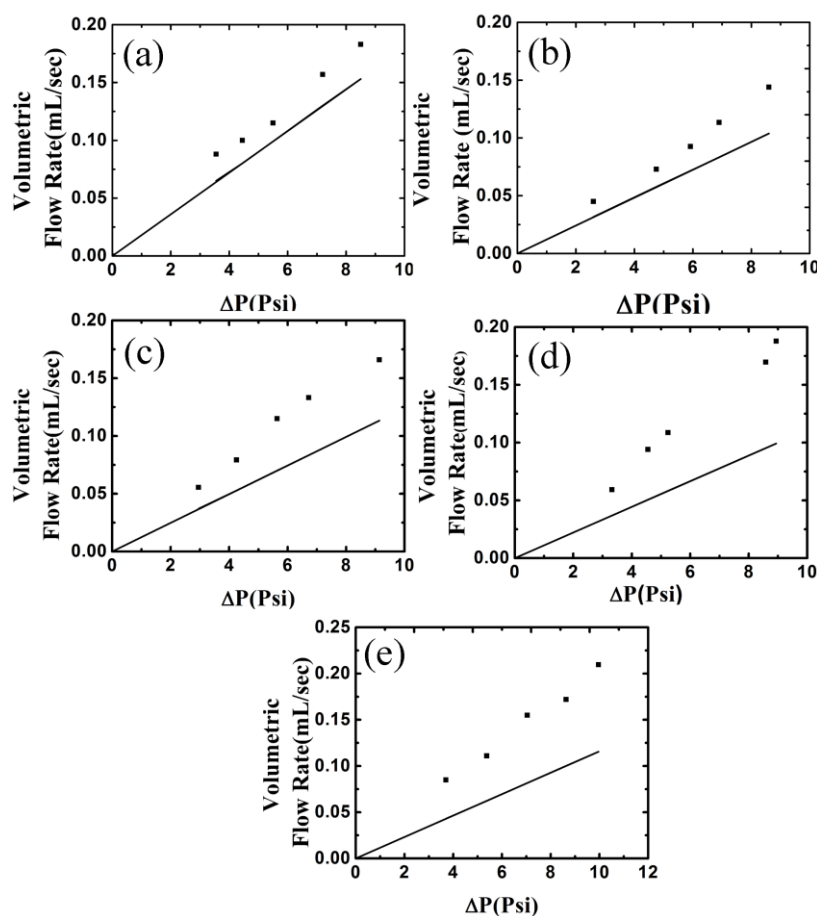


Figure 7.4. Volumetric flow rate of CNT suspensions versus pressure drop with CNT concentrations: (a) 0.1 wt%, (b) 0.2 wt%, (c) 0.6 wt%, (d) 0.9 wt%, and (e) 1 wt%. The experimental data are shown by symbols. Straight lines show the predictions of the Poiseuille law, Eq. (2).

Fig. 7.4 shows that the CNT suspensions with the added surfactant demonstrate much larger volumetric flow rates than the pure solvent at the same pressure drop (the flows of the pure solvent correspond to the Poiseuille law), even though the presence of particles should increase the effective viscosity. The reason for the observed flow enhancement might be associated with the presence of the surfactant. To verify this hypothesis, experiments were conducted with the aqueous 0.5 wt% solution of surfactant without CNTs. The results are depicted in Fig. 7.5. The flow rate of the surfactant solution was significantly higher than that of pure water at the same pressure drop, which confirms that the observed flow enhancement is due to the surfactant. Note, that the shear viscosity of the surfactant solution, measured using LV-II+ cone and plate Brookfield viscometer was found to be 1 cP, is the same as that of water. Surfactant molecules can be tethered at the microchannel and effectively displace water from the wall, resulting in a pseudo-slip. The surfactant “forest” at the wall can also trigger degassing and formation of nanobubbles near the wall which also facilitate slip [Zhu and Granick (2001); de Gennes (2002), Zhang and Yarin (2010)]. To diminish the presence of the entrapped gas in solutions, they were left for 30 min after sonication to let bigger bubbles be removed by buoyancy. As pressure drops down in the flow along the microchannel, degassing (according to Henry’s law) can also result in formation of nanobubbles. The latter is corroborated by the fact

that the flow enhancement at higher pressure drops was more significant than at that at the lower ones (cf. Figs. 7.4 and 7.5).

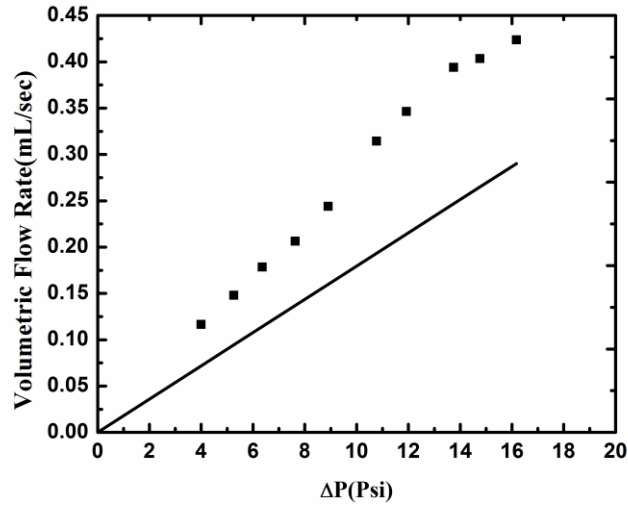


Figure 7.5. Enhanced flow rate in 0.5 wt% NADDBS surfactant solution. The experimental data are shown by symbols. The straight line shows the predictions of the Poiseuille law, Eq. (2).

According to [Lauga (2007)], volumetric flow rate increases due to a slip at the microchannel wall according to the following expression

$$\frac{\dot{Q}_S}{\dot{Q}_{NS}} = 1 + 4 \frac{\lambda}{a} \quad (7.7)$$

where \dot{Q}_S is the flow rate with a slip, \dot{Q}_{NS} is the flow rate without slip which is given by Eq. (7.2), and λ is the slip length.

The data in Fig. 7.4 was used to determine the effective slip lengths corresponding to the flows of the CNT suspensions with surfactant. The results are shown in Fig. 7.6. The slip length of the order of tens of microns is a clear manifestation of the liquid displacement from the wall, in particular due to the formation of gas pockets triggered by tethered surfactant molecules. The slip length increases with the CNT concentration, since the surfactant presence increases proportionally. As a result, a denser “forest” of surfactant molecules is tethered at the wall with more entrapped gas, and water displacement from the wall becomes more severe.

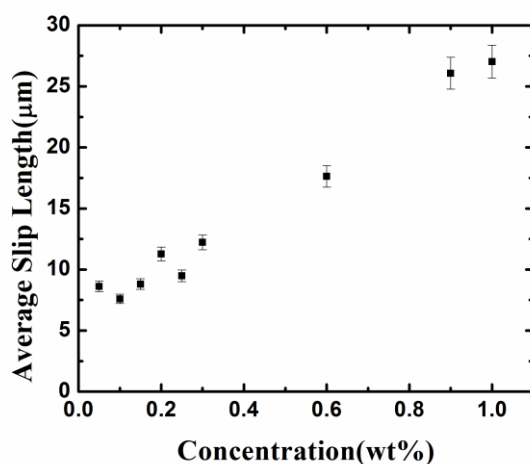


Figure 7.6. The average slip length versus CNT concentration.

7.4.2 Intercalation of wax in CNTs

As the next step, CNT suspensions intercalated with wax were prepared. Wax intercalation into CNTs was conducted using the method of self-sustained diffusion as in [Sinha-Ray, Suman et al. (2011c)]. The observations of the wax-intercalated CNTs were done using JEOL JEM 3010 Transmission Electron Microscopy (TEM). The images shown in Fig. 7.7 clearly reveal the presence of wax in the CNT bore with no wax deposits on the outside walls.

In addition to the TEM observation, DSC measurements were also conducted to quantify the amount of the intercalated wax. For that, 2.07 mg of wax-intercalated CNT sample (see Fig. 7.7) was heated at 5°C/min in N₂ atmosphere up to 75°C. A representative thermogram is shown in Fig. 7.8. According to the manufacturer's specification, the CNTs used in this work have the ID~35 nm, the OD ~55-90 nm and the length ~10-30 µm. These data were used to evaluate the amount of wax encapsulated in the sample and responsible for its heat removal due to the heat of fusion. The heat absorbed during DSC measurement due to wax melting (corresponding to the endothermic peak in Fig. 7.8) was 51.75 mJ for 2.07 mg sample mass. Using the CNTs volume, the wax density of 0.9 g/cm³ and the CNT density of 1.6 g/cm³, the mass fraction m_w of wax in the sample is found as 0.1578. Then, the total mass of wax in the sample was 0.327 mg. The total heat of fusion of wax is then $H = m_w L$, which has the measured value of 51.75 mJ. Correspondingly, the specific heat of fusion L is equal to 158 J/g. This result is commensurate with the value of 141 J/g reported for the bulk samples of the same wax (melting point 45-47°C) [Sinha-Ray, Suman et al. (2011c)]. The small difference in the values of L stems from the fact that the mass of wax intercalated in CNTs, has been calculated here using the average aspect ratio and the inner diameter of CNTs. Our result for L shows that the CNTs were completely intercalated with wax with no deposits on the outside walls. This corroborates the direct observations in Fig. 7.7.

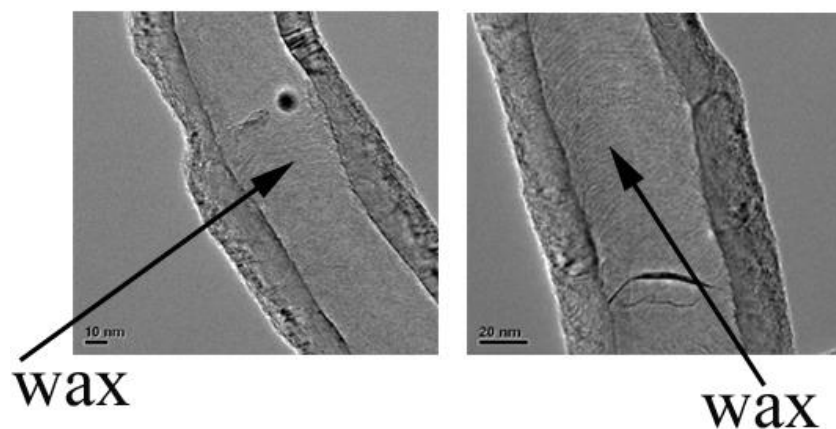


Figure 7.7. TEM images of CNTs intercalated with wax.

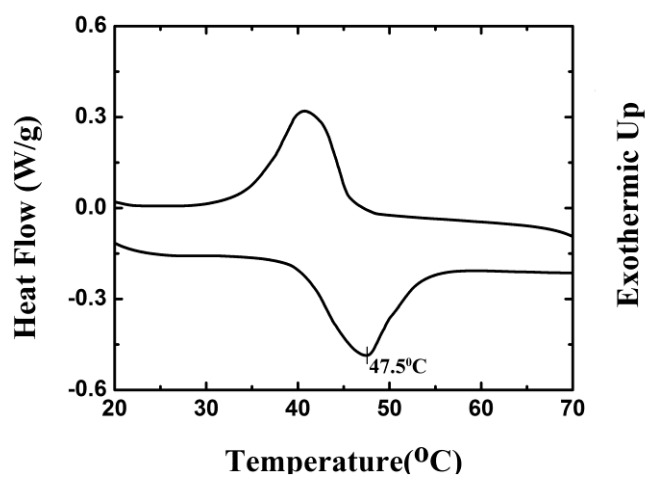


Figure 7.8. DSC Thermogram of wax-intercalated CNT.

7.4.3 Intercalation of Erythritol in CNTs

Erythritol intercalation into CNTs was conducted using the method of self-sustained diffusion. The observations of the erythritol-intercalated CNTs were done using JEOL JEM 3010

Transmission Electron Microscopy (TEM). The images shown in Fig. 7.9 reveal the presence of erythritol encapsulated in the CNT bore with practically no PCM deposits on the outside walls.

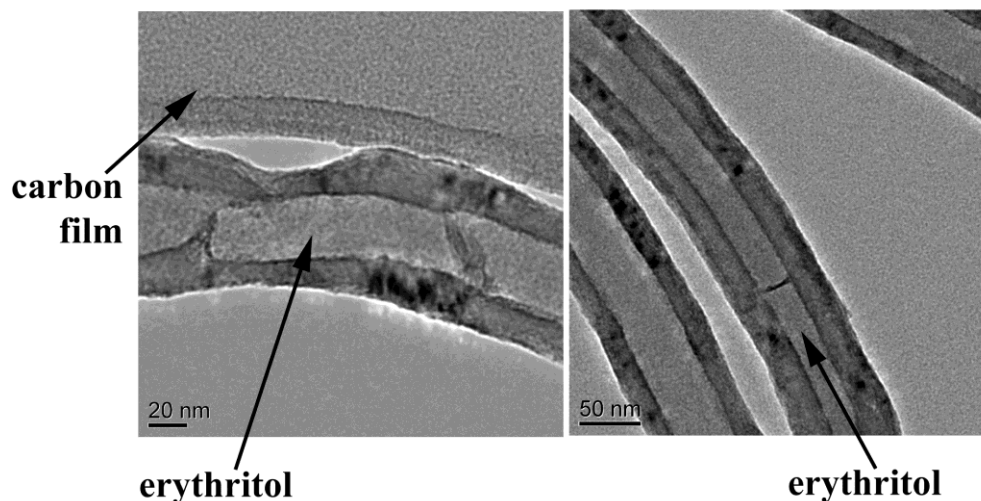


Figure 7.9. TEM images of CNTs intercalated with erythritol.

7.4.4 Flow Rates of Aqueous Suspensions of Wax-intercalated CNTs

Flow rates of different aqueous suspensions of CNTs intercalated with wax measured at different pressure drops are depicted in Fig. 7.10. Similarly to the results for the aqueous suspensions of empty CNTs in Fig. 7.4, the results in Fig. 10 demonstrate a higher flow rate of suspensions than that of pure water at the same pressure drop. As before, this effect is attributed to the presence of surfactant. In distinction from the empty CNTs, clogging takes place at a lower CNT concentration, namely suspensions of 1 wt% were clogging with CNTs intercalated with wax but not with the empty CNTs in Fig. 7.4 where the 260 μm channel was used.

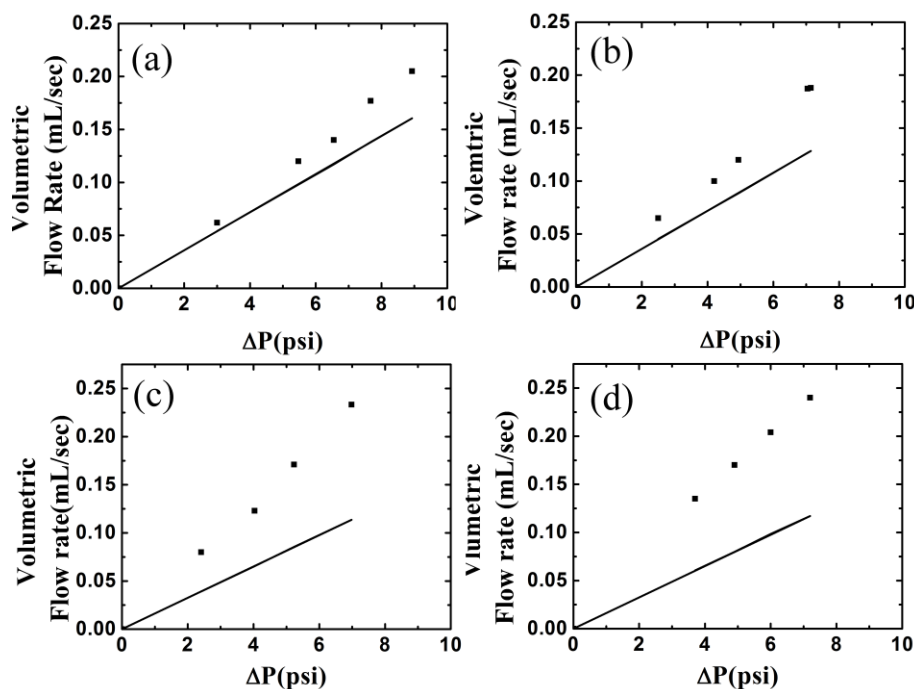


Figure 7.10. Flow rate versus pressure drop for aqueous suspensions of CNTs intercalated with wax. Panels correspond to the following surfactant concentrations: (a) 0.15 wt%, (b) 0.2 wt%, (c) 0.5 wt% and (d) 0.7 wt%. The experimental data are shown by symbols. Straight lines show the predictions of the Poiseuille law, Eq. (7.2).

7.4.5 Heat Removal with Wax-intercalated CNT Suspension Flows

Four different types of coolants were used for comparison in the heat removal experiments in the present sub-section: pure water, the aqueous solutions of surfactant NaDDBS, the aqueous suspension of the empty CNTs, and the aqueous suspension of the wax-intercalated CNTs. All the measurements were started from the average temperature of the copper block of 60 °C at a constant heat flux of heating of 9 W. Figs. 7.11-7.13 depict all the recorded temperature histories

of the copper block as coolants were flowing through the microchannel embedded in it. Fig. 7.11 shows the plots of the temperature/time dependences in the case of 1 wt% suspensions flowing through a 603 μm channel. Figs. 7.12 and 7.13 were plotted for 2 wt% and 3 wt% suspensions flowing through the 1803 μm channel, respectively. The panels on the right hand side in Fig. 7.11 show that in the range of flow rates from 5 to 35 ml/min, the most effective cooling (and thus, the lowest steady-state temperature T_s) is achieved by the aqueous suspension of wax-intercalated CNTs. At the higher flow rates than this range, the residence time of coolant material elements in the microchannel becomes too small (of the order of 1 s), the solvent carrying CNTs does not reach the high enough temperature, and thus, the wax intercalated in the CNTs does not undergo melting and removes no latent heat of fusion. The characteristic thermal transient time in the present case would be of the order of 1 s. Figs. 7.11 shows the lowest values of the temperature plateaus in the case of the CNT suspension compared to that of pure water at the flow rates of 5 and 25 ml/min. This might imply that the temperature reduction is caused by the presence of CNTs. However, to prepare a stable suspension of CNTs, the surfactant was added. It was shown above that the surfactant presence of results in nano-scale bubbles which cause slip in the shear flow near the channel wall (cf. Fig. 7.5). That enhances the flow rate in the channel. To verify that, a similar series of tests were conducted with the aqueous solution of the surfactant prepared similarly to the CNT suspension. These tests were conducted with the same flow rates as those with the CNT suspensions. The results of these tests revealed a similar temperature reduction for the same range of the flow rates (cf. Fig. 7.11). This clearly indicates that the temperature reduction does not stem only from the presence of the CNTs but partially originates from the higher flow rates due to the presence of the surfactant, which facilitates the enhanced convective heat transfer.

Fig. 7.11 shows that the steady-state temperatures achieved with the aqueous suspensions of the wax-intercalated CNTs are by 0.6-1.3 °C lower than those with the aqueous suspensions of the empty CNTs, whereas the later reduced the temperature by 1 °C compared to pure water at the lowest and moderate flow rate of 5 and 25 ml/min due to the presence of surfactant. At 5 ml/min the maximum effect of the temperature drop (1.3 °C) solely due to the PCM melting was observed, whereas at 25 ml/min an optimum combination of both convective heat removal and PCM fusion was recorded.

In addition, careful examination of Fig. 7.11 shows that at the higher flow rate (55 ml/min) the temperature reduction in water flow is larger than that in the CNT suspension flows at these flow rates. The probable reasons are the following. (i) At the high flow rates the CNT residence time in the hot section is too short for wax melting, so no latent heat of wax fusion is involved, while the heat capacity of the CNTs is less than that of water they replaced. (ii) At the higher flow rates more bubbles are shed from the wall covered by surfactant layer and tethered on the CNTs which also prevents wax melting.

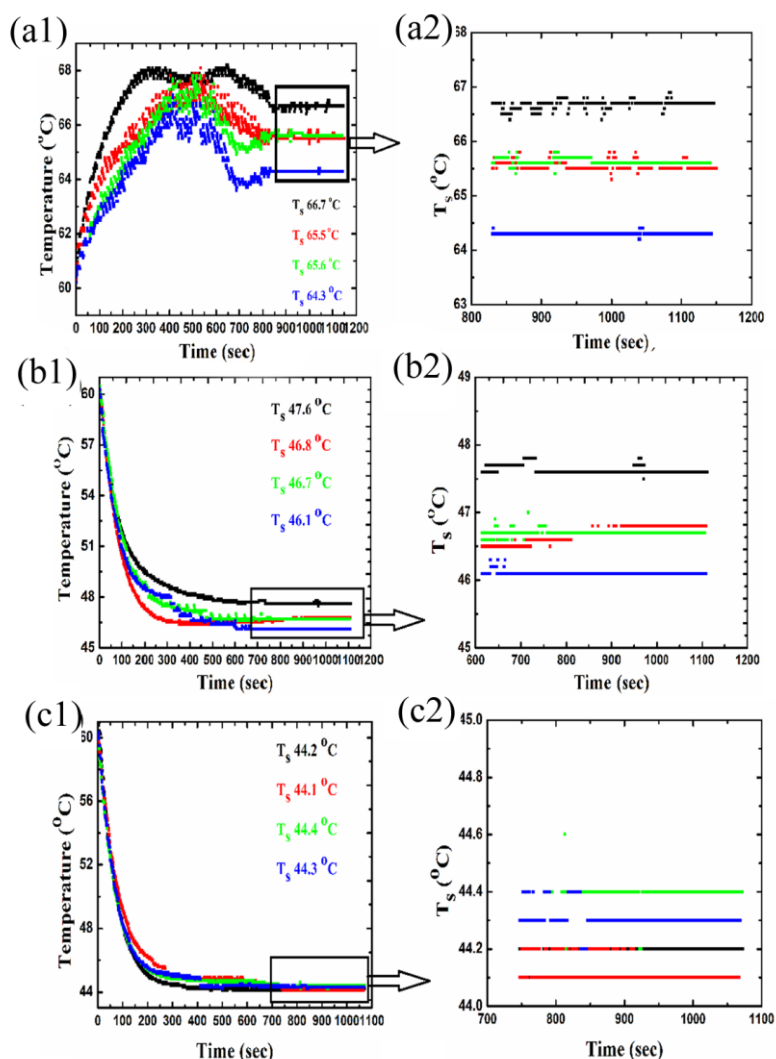


Figure 7.11. Temperature of the copper block versus time in the case of flows of water, surfactant solution, 1 wt% suspension of the empty CNTs, and 1 wt% of wax-intercalated CNTs in 603 μm channel. The panels show the temperature histories corresponding to the following rates of the coolant flow: (a1) and (a2) correspond to the flow rate of 5 ml/min, (b1) and (b2) – to 25 ml/min, (c1) and (c2) – to 55 ml/min. The panels marked with numeral 1 reveal the transient phase, whereas those marked with numeral 2 – the subsequent steady-state stage. Black symbols correspond to pure water, red symbols - to the aqueous surfactant solution, green symbols - to the aqueous suspension of the empty CNTs, and blue symbols - to the aqueous solution of the wax-

intercalated CNTs. The values of the steady-state temperature T_s achieved are shown by the corresponding colors. For the experiments with the 5 ml/min flow rates the inlet coolant temperature was 25.6 °C, whereas for the other experiments it was 23.2 °C. The rectangular domains in the left hand side panels corresponding to the steady-state regimes are shown in detail in the right hand side panels.

The experiments conducted with the higher concentrations (2 wt% and 3 wt %) of the wax-intercalated CNT suspensions flowing through the 1803 μm microchannel showed (cf. Figs. 7.12 and 7.13) a larger cooling effect compared to that of the 1 wt% suspension in Fig. 7.11. In the case of the 2 wt% wax-intercalated CNT suspension, a maximum temperature reduction of 2.2 °C was found due to the wax fusion at 5 ml/min flow rate (compare with 1.3 °C in Fig. 7.11). At this low flow rate the low flow velocity of 1 cm/s results in a longer residence time of the PCM-intercalated CNTs in the channel (~ 3 s). This is longer than the characteristic thermal transient time in the channel which is of the order of 1 s, and definitely much longer than the characteristic time scale for wax melting inside a CNT which is of the order of $\sim 10^{-7}$ s. Note that a lower flow rate also diminishes the convective cooling component. It is also emphasized that even for the 2 wt% wax-intercalated CNT suspension the viscous dissipation was still negligibly small, since the measured shear viscosity was very close to that of water, namely 1.08 cP.

The maximum effect of the 2 wt% wax-intercalated CNT suspension in cooling was found at 25 ml/min where the total wall temperature reduction was 3.4 °C, of which 1.4 °C was due to the wax melting (Fig. 7.12). At the flow rate of 45 ml/min a considerable temperature reduction was still visible with the 2 wt% wax-intercalated CNT suspension, since in the bigger channel

the flow velocity was smaller and the residence time longer as compared to the smaller channel in Fig. 7.11. Only at the flow rate of 55 ml/min the effect of cooling due to the wax fusion was diminished to the level of the 1 wt% wax-intercalated CNT suspension in the smaller channel.

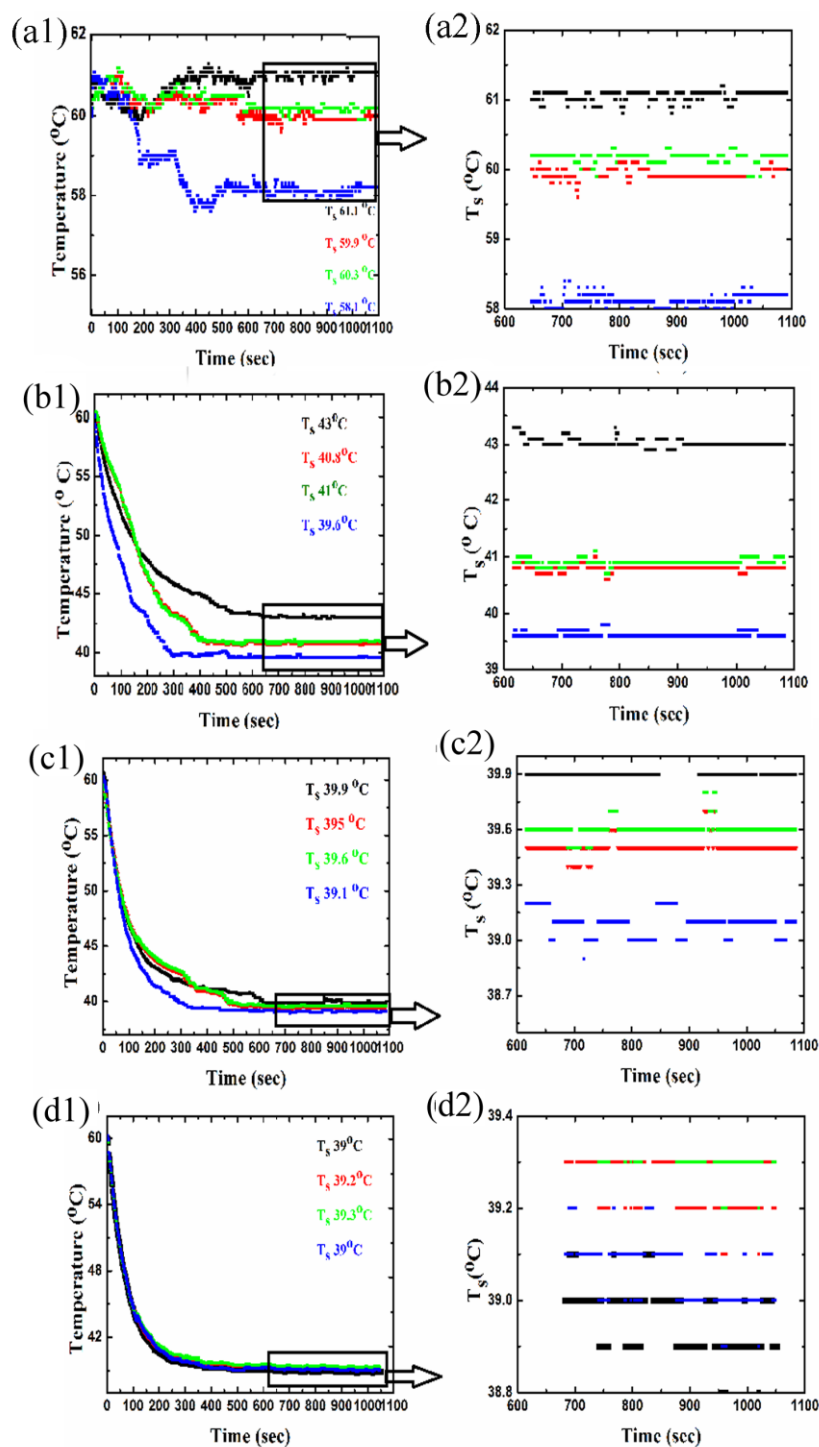


Figure 7.12. Temperature of the copper block versus time in the case of flows of water, surfactant solution, 2 wt% suspension of the empty CNTs, and 2 wt% of wax-intercalated CNTs in 1803 μm channel. The panels show the temperature histories corresponding to the following rates of the coolant flow: (a1) and (a2) correspond to the flow rate of 5 ml/min, (b1) and (b2) – to 25 ml/min, (c1) and (c2) – to 45 ml/min, (d1) and (d2) – to 55 ml/min. The panels marked with numeral 1 reveal the transient phase, whereas those marked with numeral 2 – to the subsequent steady-state stage. Black symbols correspond to pure water, red symbols - to the aqueous surfactant solution, green symbols - to the aqueous suspension of the empty CNTs, and blue symbols - to the aqueous solution of the wax-intercalated CNTs. The values of the steady-state temperature T_s reached are shown by the corresponding colors. For the experiments at the flow rate of the 5 ml/min the inlet coolant temperature was 23.6 °C, whereas for the other experiments it was 20.2 °C. The rectangular domains on the left hand side panels corresponding to the steady-state regimes are shown in detail in the right hand side panels.

The experiments with the 3 wt% wax-intercalated CNT suspension were conducted next. The results are plotted in Fig. 7.13. They show that at the lower flow rate of 5 ml/min a significant temperature reduction due to wax melting was observed (up to 3.9 °C reduction). At the intermediate flow rate of 25 ml/min, the suspension was not better than the surfactant solution as a coolant. Two probable reasons of this phenomenon could be mentioned. First, a lower specific heat material (wax in the CNT and the CNTs themselves) replaced a higher specific heat material (water). Second, the presence of a significant amount of CNTs increases the effective viscosity of suspension, which reduces the flow rate at a given pressure drop, and thus diminishes convective transfer. The measured shear viscosity of the 3 wt% CNT suspension

was 1.38 cP compared to 1 cP of water, which enhances the viscous losses and diminishes cooling. The cooling effect (both, due to the wax melting in the CNTs and the convective component) was enhanced at the flow rates of 45 ml/min. At 55 ml/min PCM fusion was responsible for a 2 °C reduction in the steady-state temperature compared to the corresponding case of suspension of the empty CNTs.

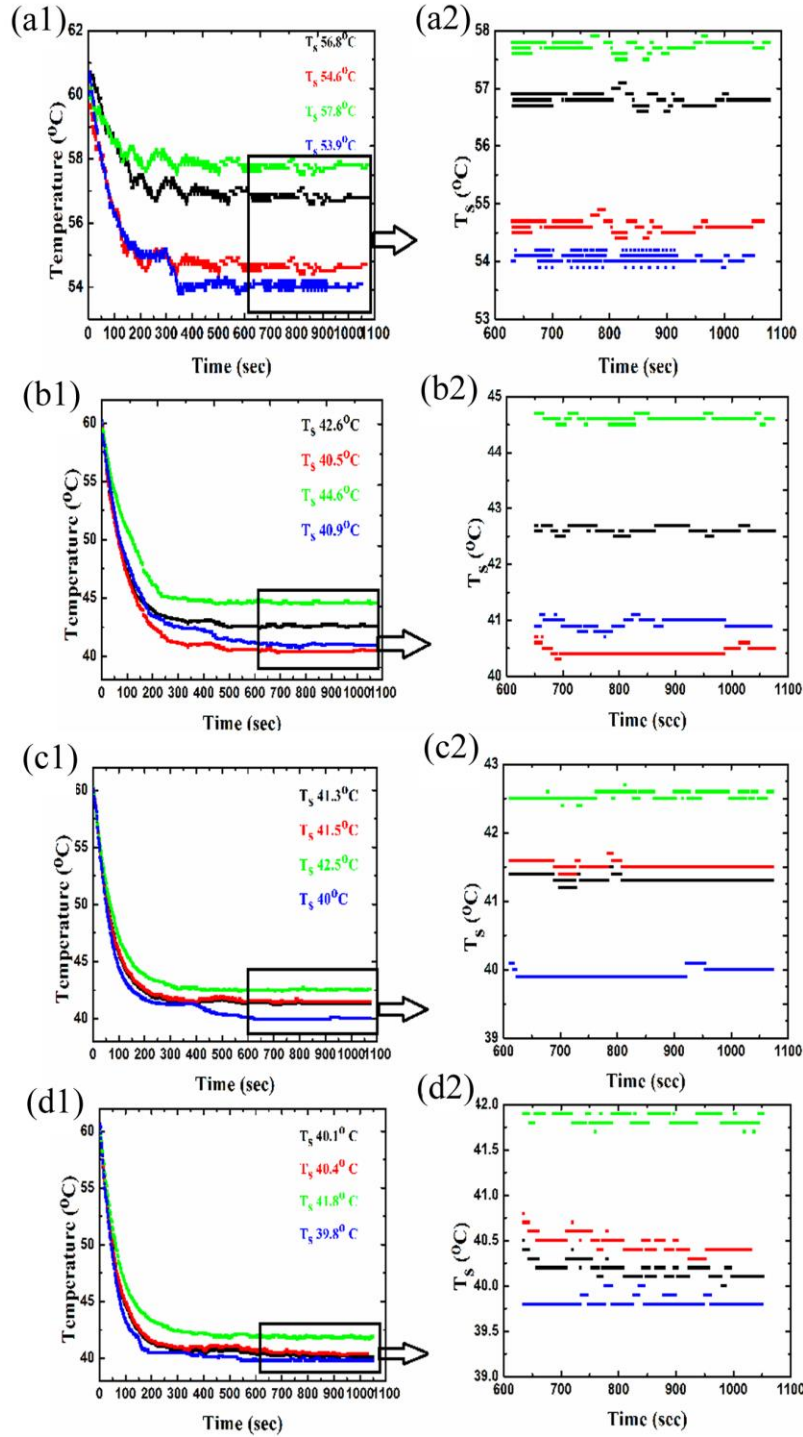


Figure 7.13. Temperature of the copper block versus time in the case of flows of water, surfactant solution, 3 wt% suspension of the empty CNTs, and 3 wt% of wax-intercalated CNTs in 1803 μm channel. The panels show the temperature histories corresponding to the following

rates of the coolant flow: (a1) and (a2) correspond to the flow rate of 5 ml/min, (b1) and (b2) – to 25 ml/min, (c1) and (c2) – to 45 ml/min, (d1) and (d2) – to 55 ml/min. The panels marked with numeral 1 correspond to the transient phase, whereas those marked with numeral 2 – to the subsequent steady-state stage. Black symbols correspond to pure water, red symbols - to the aqueous surfactant solution, green symbols - to the aqueous suspension of the empty CNTs, and blue symbols - to the aqueous solution of wax-intercalated CNTs. The values of the steady-state temperature T_s reached are shown by the corresponding colors. For the experiments at the flow rate of the 5 ml/min the inlet coolant temperature was 23.6 °C, whereas for the other experiments it was 20.2 °C. The rectangular domains in the left hand side panels corresponding to the steady-state regimes are shown in detail in the right hand side panels.

These experiments with the 3 wt% suspension of the wax-intercalated CNTs were repeated at all flow rates for longer times. The repeatability of the results was fully verified with the error bars being negligibly small. The repeatability of the results irrespective the experiment duration also sheds light onto the origin of air bubbles resulting in the observed slip. One could assume the following two possibilities for the air bubbles to emerge. (i) When a suspension enters a dry microchannel, air can be entrapped in the emerging forest of the tethered surfactant molecules at the microchannel wall. (ii) The dissolved air is being released from the suspension according to Henry's law (since it flows toward the lower pressure end), the bubbles migrate to the wall and are anchored there. If the mechanism (i) would be important, then the slip effect would be transient, and disappear in long experiments over time, because the trapped air would be washed away or dissolved. On the other hand, if the mechanism (ii) is relevant, there should be no fading of the slip effect. The latter, in fact, happens, which confirms that the anchored bubbles responsible for the slip are sustained due to Henry's law. Since liquids inevitably contain some

air, either due to diffusion from the surrounding atmosphere, or a prior processing, pressurization followed by de-pressurization in microchannel flows inevitably leads to bubble formation due to Henry's law and a sustainable slip effect.

The value of ΔT predicted by Eq. (5) using the parameters $L=158$ J/g, $c_{p,suspension}=4.08$ J/(g \times K), and the volume fraction $\phi=5.26\times 10^{-3}$ is 0.204 °C for 3 wt% of suspension. The specific heat of suspension was calculated using the following expression: $c_{p,suspension}=(m_{water}c_{p,water}+m_{wax}c_{p,wax}+m_{CNT}c_{p,CNT})/M_{total}$, where $c_{p,wax}=2.2$ J/(g \times K), $c_{p,CNT}=c_{p,carbon(graphite)}=0.71$ J/(g \times K) and $c_{p,water}=4.18$ J/(g \times K). The masses of water, wax and CNTs were calculated as discussed before. The calculated value of ΔT is significantly lower than the maximum temperature reduction of 1.9 °C measured in the experiments. It means that the CNT alignment by flow in microchannels can effectively increase the local value of ϕ compared to that in the solution bulk, and thus enhance the temperature reduction ΔT .

It is worth mentioning that it was impossible to work with more concentrated suspensions of CNTs (with the concentrations above 3 wt%). This is related to the high aspect ratio of CNTs. The aspect ratio of carbon nanotubes plays a very important role beginning from the suspension preparation. For a fixed weight percentage the aspect ratio of CNTs determines whether a suspension is or semi-dilute, and thus the flow regimes. In particular, in semi-dilute suspensions hydrodynamic particle-particle interactions can become so significant that a microchannel flow cannot be sustained. Suspensions of elongated particles (e.g. CNTs) are dilute if $\phi \ll \kappa^{-2}$, where ϕ is the volume fraction and κ is the particle aspect ratio. For a 3 wt% CNT suspension ϕ is about 0.03 and $\kappa^{-2}=5\times 10^{-5}$, i.e. the suspension is already semi-dilute ($\kappa^{-2} < \phi \ll 1$) and significant

hydrodynamic particle/particle interactions are present and increase resistance to flow. In particular, CNTs tend to orient along the channel and form aggregates effectively clogging it.

Note also that the effect of the thermal resistance associated with the nanotube wall can be estimated as follows. Consider, for example, a CNT suspension at a flow rate of 25 ml/min (which is 0.42 ml/s) subjected to 9 W of thermal energy transferred through the microchannel wall (as measured in the present case). In 0.42 ml which passes through the microchannel per 1 second the number of particles is of the order 10^{11} (estimated using the known CNT content, 2 wt%, and mass of an individual CNT, 8.6×10^{-14} g). Accounting for the heat received by wax, we find that each individual nanotube is subjected to $Q = 3.7 \times 10^{-10}$ W. The thermal resistance of a cylindrical shell (CNT) is $R_{tr} = (2\pi k \ell_{CNT})^{-1} \ln(r_o / r_i)$ where r_o and r_i are the outer and inner cross-sectional radii, respectively, with $r_o/r_i \approx 2$, and k being the thermal conductivity of CNT [10^3 W/m \times K (as per manufacturer)]. Also, $\ell_{CNT} \approx 10 \mu\text{m}$ is the CNT length. Since the temperature difference at the CNT wall $\Delta T_{tr} = QR_{tr}$, we find that $\Delta T_{tr} \sim 10^{-9}$ K, which is negligibly small. In addition, the thermal response time of CNT wall of the thickness $h = r_o - r_i$ is of the order of $\tau = h^2 / \alpha$ where α is the thermal diffusivity of CNT. This estimate yields $\tau \sim 10^{-11}$ s which is also negligible. The estimate is obtained under the assumption that in a good suspension stabilized with surfactants, there is no air layer at the outer CNT wall and it is in direct contact with the carrying liquid.

7.4.6 Heat Removal with Flows of Oil-based Erythritol-intercalated CNT Suspensions

In the heat-removal experiments with the oil-based erythritol-intercalated CNT suspensions, four different types of coolants were compared: pure alpha-olefin oil, the solution of surfactant NaDDBS in oil, the oil-based suspension of the empty CNTs, and the oil-based

suspension of the erythritol-intercalated CNTs. The need for the oil-based suspensions is due to the fact that the melting point of erythritol is in the 118-120 °C range, above the boiling temperature of water, which excludes the latter as a carrier fluid. All the measurements were started from the average initial block temperature of ~145 °C and were conducted at a constant heat flux of 20 W. Fig 7.14 shows the recorded temperatures of the copper block as the oil-based coolants were flowing through the microchannel (13 gauge needle, 1803 μm in diameter) embedded in it. Fig. 7.14 corresponds to the 1.5 wt% suspension flows. All the results on the right-hand side in Fig. 7.14 show that in lower flow rates range from 25 to 45 ml/min the most effective cooling, and correspondingly, the lowest steady-state temperature T_s of the copper block was achieved in the experiments with the oil-based suspension of erythritol-intercalated CNTs. At the higher flow rates, i.e., 55ml/min and 65ml/min, the residence time of the coolant material elements in the microchannel is already very small (of the order of 1 s). As a result, the oil-based CNT suspension could not reach the high enough temperature in the channel needed for the erythritol melting. Therefore, the erythritol intercalated in the CNTs could not undergo complete melting and utilize its latent heat of fusion. Fig. 7.14 also show the lowest values of the temperature plateaus for the oil-based surfactant solution compared to that of the pure oil at almost all flow rates. This might be interpreted as a decrease of viscosity of the surfactant solution compared to the original oil, which would result in an increased flow rate. Measurements of the shear viscosity were conducted for both pure oil and the oil-based surfactant solution at 25 °C using LV-II+ cone and plate Brookfield viscometer, at a shear rate of 112 s^{-1} . For both liquids the viscosity of 6.8 cP was measured disproving the above-mentioned interpretation. However, it was found that when the surfactant was added to oil, it caused production of air bubbles as the solution impinged the reservoir after leaving the channel.

Since the oil has a lower surface tension of 31 dyne/cm than that of water (72 dyne/cm), the bubbles in oil still existed in the re-circulating flow in the channel. These might be even very small nano-sized bubbles. Such nano-sized bubbles could cause pseudo-slip, which can indeed enhance the apparent flow rate and thereby result in an enhanced convective heat transfer compared to the one produced by pure oil. On the other hand, this was not the case with the oil-based CNT suspensions with the surfactant, for which the shear viscosity at room temperature was measured as 9.4 cP, almost 35 % higher than that of the surfactant solution.

Fig. 7.14 shows that the steady-state temperatures achieved with the oil-based suspensions of the erythritol-intercalated CNTs are by 0.5-3.2 °C lower than those achieved with the oil-based suspensions of the empty CNTs. Table 7.1 shows the measured temperature drop (in comparison to the suspension of the empty CNTs) due to the erythritol melting in CNTs in steady-state regimes for different flow rates. In addition note that the oil-based suspensions of the empty CNTs had practically the same cooling effect as the pure oil due to the balancing the effect of the surfactant induced-slip by the increased viscosity due to the CNT presence. The results in Table 7.1 show that the longer residence time in the channel maximized the erythritol melting and its cooling effect.

Table 7.1. Temperature drop due to the erythritol melting at different flow rates.

Flow rate (ml/min)	ΔT
25	3.2 °C
45	1.8 °C
55	1 °C
65	0.5 °C

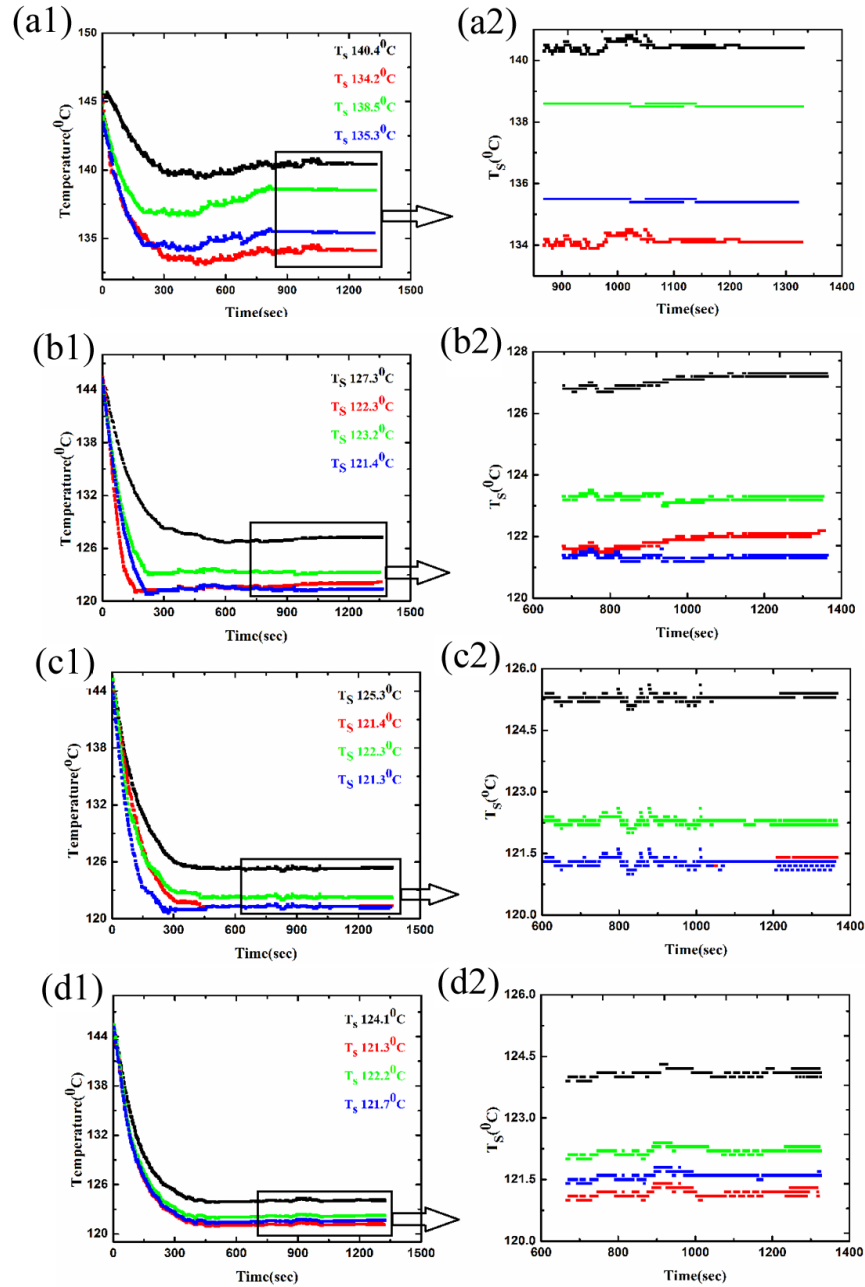


Figure 7.14. Temperature of the copper block versus time in the case of flows of oil, oil-based surfactant solution, 1.5 wt% suspension of the empty CNTs, and 1.5 wt% of erythritol-intercalated CNTs in the 1803 μm channel. The panels show the temperature histories corresponding to the following rates of the coolant flow: (a1) and (a2) correspond to the flow rate of 25 ml/min, (b1) and (b2) – to 45 ml/min, (c1) and (c2) – to 55 ml/min, (d1) and (d2) – to

65 ml/min. The panels marked with numeral 1 reveal the transient phase, whereas those marked with numeral 2 – the subsequent steady-state stage. Black symbols correspond to pure oil, red symbols - to the oil-based surfactant solution, green symbols - to the oil-based suspension of the empty CNTs, and blue symbols - to the oil-based suspension of the erythritol-intercalated CNTs. The values of the steady-state temperature T_s achieved are shown by the corresponding colors. For the experiments the inlet coolant temperature was 24.6 °C. The rectangular domains in the left-hand side panels corresponding to the steady-state regimes are shown in detail in the right-hand side panels.

To evaluate the expected temperature drop ΔT due to melting of the erythritol intercalated in CNTs, Eq. 7.5 is used again. The specific heat capacity value of the suspension in the present case can be evaluated using the following formula

$$c_{p,suspension} = (m_{oil}c_{p,oil} + m_{erythritol}c_{p,erythritol} + m_{CNT}c_{p,CNT}) / M_{total},$$

where $c_{p,erythritol} = 1.4 \text{ J/(g} \times \text{K)}$, $c_{p,CNT} = c_{p,carbon(graphite)} = 0.71 \text{ J/(g} \times \text{K)}$, $c_{p,oil} = 2.63 \text{ J/(g} \times \text{K)}$ (as per manufacturer specification), all the values for the 140-150 °C temperature range. For 20 g of a suspension, 19.7 g is oil, neglecting the presence of surfactant in the 2 g oil-surfactant solution. For the 0.3 g of CNTs with the intercalated erythritol we use the following data: the erythritol density is 1.45 g/cm^3 , the CNT density is 1.6 g/cm^3 (as per manufacturer specification), the average ID of CNTs is $\sim 35 \text{ nm}$, the average OD is $\sim 55\text{-}90 \text{ nm}$, and the length is $10 \text{ }\mu\text{m}$, the erythritol mass is 0.09 g and the CNT mass is 0.21 g. Then, the volume fraction ϕ appears to be 2.06×10^{-3} . Correspondingly, we find $c_{p,suspension}$ as 2.604 J/g. The latent heat of erythritol is 339.8 J/g (Ref. 19). Using Eq 5, we find the expected temperature drop, ΔT as 0.27 °C, which is less than the measured value of 0.5-3.2 °C, as in the case of the aqueous suspensions of the wax-

intercalated CNTs. This means that the CNT alignment by flow in microchannels can effectively increase the local value of ϕ compared to that in the solution bulk, which results in a larger reduction of the copper block temperature.

7.5 Conclusion

The results show that wax-intercalated and erythritol-intercalated carbon nanotubes (CNTs) hold promise as phase change materials (PCM) for cooling microelectronics using coolant suspension flow in microchannels. CNTs were intercalated with wax using the method of self-sustained diffusion. Surfactant-stabilized aqueous suspensions of 1 wt% CNTs did not clog 603 μm channel, whereas in a 1803 μm channel flows of suspensions of up to 3 wt% wax-intercalated CNTs were possible. The flow rates of such suspensions were in the range 5-55 ml/min. It was found that the presence of the surfactant NaDDBS in water led to an apparent slip at the channel walls, which enhanced the convective heat removal from a hot copper block, in which the microchannels with flowing aqueous coolant were embedded. The presence of wax inside CNTs additionally facilitated heat removal through the latent heat of wax fusion. Wax melted in the range 45-47 $^{\circ}\text{C}$ and this effect alone was responsible for the maximum temperature reduction of 1.9 $^{\circ}\text{C}$. The heat removal due to wax melting is diminished at the highest flow rates, since the CNT residence time inside the 3.175 cm-long channel becomes too short for wax melting.

The presence of erythritol inside CNTs additionally facilitated heat removal through the latent heat of its fusion in flows of the oil-based suspensions. The erythritol melted in the 118-120 $^{\circ}\text{C}$ range and this effect alone was responsible for the maximum temperature reduction of 3.2 $^{\circ}\text{C}$ in flows of the oil-based 1.5 wt% suspension of erythritol-intercalated CNTs. The present

approach can be also used in the case of mixtures of different PCMs, e.g. wax and erythritol (separately in different CNTs, or together in the same CNTs) to widen the temperature range in some applications.

CHAPTER 8

THEORETICAL AND EXPERIMENTAL INVESTIGATION OF PHYSICAL MECHANISMS RESPONSIBLE FOR POLYMER NANOFIBER FORMATION IN SOLUTION BLOWING

This chapter has been previously published in Sinha-Ray, Sumit et al. (2015b). Reprinted with permission from [Sinha-Ray, Sumit, Sinha-Ray, Suman, Yarin, A.L. and Pourdeyhimi, B. (2015b), Theoretical and experimental investigation of physical mechanisms responsible for polymer nanofiber formation in solution blowing, *Polymer*, 56, 452-463]. Copyright 2015 ELSEVIER.

8.1 Introduction

The primary aim of this Chapter is to investigate an industrially viable method, sub-sonic solution blowing for the production of polymer nanofibers of diameter ~500 nm. This process has already been scaled-up to the industrial level by Kolbasov et al. (2016) using a bio-friendly polymer (soy-protein). Several polymers which degrade upon heating and are not used for meltblowing can be easily used to form nanofibers by the solution blowing method. In this process a solution of a polymer is fed through a core of a concentric nozzle, where through the outer shell a high speed gas jet is issued [Sinha-Ray, Suman et al. (2010a, 2011b), Khansari et al. (2012)]. The polymer solution jet is then stretched in the gas co-flow and undergoes vigorous bending and flapping and subsequent evaporation of solvent, and finally precipitates and transforms into nanofibers. The applicability of this process to forming bio-friendly polymer nanofibers is immense and henceforth an in-depth investigation of this method is important. Additionally, such a study can also help to predict nonwoven architecture and porosity to

evaluate the filtration and absorption capacities. In general, free viscous liquid jets moving relative to surrounding gas with a high speed, experience lateral distributed force which tends to increase bending perturbations [Weber (1931), Yarin (1993)]. This mechanism is also characteristic of meltblowing [Sinha-Ray et al. (2010c), Yarin et al. (2010), Yarin et al. (2011), Yarin et al. (2014)] as well as of solution blowing. The present Chapter is subdivided in four sections, where section 2 describes the theoretical aspects of this work, and section 3 details the experimental scheme. The theoretical and experimental results are described and discussed in section 4. Conclusions are drawn in section 5.

8.2. Theoretical

8.2.1 Straight Part of the Jet

The experimental data discussed below show that polymer solution jets in solution blowing possess a straight part where the cross-sectional diameter of the jet is still large enough to prevent significant bending perturbations. The jet is straight, pulled in the axial direction by the surrounding high-speed gas flow and attenuating in response. This happens on the background of solvent evaporation. Following Yarin et al. (2001), the mass of an unperturbed element of unit length in the straight part of the jet decreases according to the following equation

$$\frac{d(fV)}{dx} = -h_m [C_{s,eq}(T) - C_{s,\infty}] 2\pi a \quad (8.1)$$

Here x is the axial coordinate reckoned along the straight jet axis, f is the area of a jet cross-section which is assumed to be circular, with a being its radius, V is the absolute axial jet velocity, h_m is the mass transfer coefficient, $C_{s,eq}(T)$ and $C_{s,\infty}$ are the solvent vapor volume

fractions at the jet surface and far away from it, respectively, T is temperature which is the same of polymer solution and the surrounding air in the case of solution blowing, which is assumed to be an isothermal process.

According to Yarin et al. (2001), the mass transfer coefficient is given by the following expression

$$h_m = \frac{D_a}{2a} 0.495 \text{Re}^{1/3} \text{Sc}^{1/2} \quad (8.2)$$

where $\text{Re} = V2a/v_a$ and $\text{Sc} = v_a/D_a$ are the Reynolds and Schmidt numbers, respectively, with v_a being the kinematic viscosity of air and D_a being the solvent vapor diffusion coefficient in air.

The momentum balance in the straight part of the jet reads [Yarin et al. (2014), Yarin (1993)]

$$\rho \frac{d(fV^2)}{dx} = \frac{d(\sigma_{xx}f)}{dx} + q_\tau \quad (8.3)$$

where ρ is the polymer solution density, σ_{xx} is the longitudinal stress in the jet, and q_τ is the aerodynamic drag pulling the jet in the axial direction, which is given by the following expression [Ziabicki (1976), Ziabicki and Kawai (1985)]

$$q_\tau = c\pi a \rho_a (U_a - V)^2 \left[\frac{2(U_a - V)a}{v_a} \right]^{-0.81} \quad (8.4)$$

In Eq. (8.4) c is an empirical constant discussed below, ρ_a is the air density, and U_a is the absolute velocity of air in the axial direction. It should be emphasized that the empirical Kase-Matsuo equation (4) incorporates the dependence of the aerodynamic drag on the Reynolds

number based on the relative velocity, $Re_{\text{relative}} = 2(U_a - V)a / v_a$, as $Re_{\text{relative}}^{-0.81}$, which is characteristic of the turbulent boundary layer (in distinction from the laminar boundary layer where the dependence $Re_{\text{relative}}^{-0.5}$ would be expected [Loitsiyanskii (1966), Groeber et al. (1961), Yarin (1983)]).

In addition, according to [Yarin et al. (2014), Yarin (1993)] , the longitudinal stress σ_{xx} is equal to the difference of the axial and radial deviatoric stresses, τ_{xx} and τ_{yy} , respectively, i.e. can $\sigma_{xx} = \tau_{xx} - \tau_{yy}$. In flows with strong uniaxial elongation, such as in solution blowing, the radial component τ_{yy} is negligibly small compared to the axial one τ_{xx} , and $\sigma_{xx} \approx \tau_{xx}$. In the uniaxial elongation flows, such as the electrospinning and meltblown jets, a plausible description of the rheological behavior of polymer solutions and melts is given by the upper-convected Maxwell model (UCM) [Yarin et al. (2014), Yarin (1993), Sinha-Ray, Suman et al. (2010b). Yarin et al. (2010), Yarin et al. (2011), Yarin et al. (2001), Reeneker et al. (2000)]

$$V \frac{d\tau_{xx}}{dx} = 2 \frac{dV}{dx} + 2 \frac{\mu}{\theta} \frac{dV}{dx} - \frac{\tau_{xx}}{\theta} \quad (8.5)$$

where μ and θ are the viscosity and the relaxation time of polymer solution, respectively.

Equations (8.1), (8.3) and (8.5) can be reduced to the following system of two differential equations for two unknowns V and τ_{xx}

$$\frac{dV}{dx} = \frac{\rho \kappa V - (\tau_{xx} / V)(\kappa + f / \theta) + q_\tau}{\rho_0 f_0 V_0 - \rho \kappa x - (f / V)(\tau_{xx} + 3\mu / \theta)} \quad (8.6)$$

$$\frac{d\tau_{xx}}{dx} = \frac{1}{V} \left[2 \frac{dV}{dx} (\tau_{xx} + \mu / \theta) - \tau_{xx} / \theta \right] \quad (8.7)$$

In these equations the jet cross-section f is given by

$$f = \frac{1}{V}(f_0 V_0 - \kappa x) \quad (8.8)$$

where, as in Eq. (8.8) and hereinafter, subscript 0 denotes the values in the initial cross-section which are given. Also, the constant κ is given by

$$\kappa = \frac{D_a}{2a} 0.495 \text{Re}^{1/3} \text{Sc}^{1/2} [C_{s,\text{eq}}(T) - C_{s,\infty}] 2\pi \quad (8.9)$$

In addition, due to solvent evaporation the viscosity μ and relaxation time θ vary with the polymer volume fraction C_p along the jet as [Yarin et al. (2014), Yarin et al. (2001)]

$$\mu = \mu_0 10^{6(C_p^m - C_{p0}^m)}, \quad \theta = \theta_0 \frac{C_p}{C_{p0}} \quad (8.10)$$

It should be emphasized that the loss of mass from the jet is associated only to the solvent evaporation, and thus similarly to Eq. (8.1) the solvent volume in a unit jet length $M_s = C_s f V$ is subjected to the following equation

$$\frac{d(C_s f V)}{dx} = -h_m [C_{s,\text{eq}}(T) - C_{s,\infty}] 2\pi a \quad (8.11)$$

where C_s is the volume ratio of solvent.

Then, integrating Eq. (8.11), we find C_s as

$$C_s = \frac{C_{s0} f_0 V_0 - \kappa x}{f V} \quad (8.12)$$

Therefore, the polymer volume fraction $C_p = 1 - C_s$ is found using Eqs. (8.12) and (8.8) as

$$C_p = \frac{C_{p0}}{1 - \kappa x / (f_0 V_0)} \quad (8.13)$$

The latter equation provides us with the values of C_p needed to find the viscosity and relaxation times using Eqs. (8.10).

The system of Eqs. (8.6) and (8.7) is solved numerically using the Kutta-Merson method using the boundary conditions

$$x = 0: \quad V = V_0, \quad \tau_{xx} = \tau_{xx0} \quad (8.14)$$

where the values of the polymer feeding velocity V_0 and the longitudinal stress τ_{xx0} at the nozzle exit are determined by the flow in the nozzle and are, in principle known.

8.2.2 Perturbed Part of the Jet

The general quasi-one-dimensional theory of free liquid jets moving in air provides us with two inter-related types of approaches to problems related to jet bending [Yarin et al. (2014), Yarin (1993)]. If the jet is thick enough, its bending stiffness, i.e. the shearing force in jet cross-section and the moment-of-momentum balance equations are accounted for. On the other hand, for very thin liquid jets, the momentless approximation is used in which the bending stiffness is neglected compared to the other internal forces governing bending. This is possible, since the bending stiffness depends on the cross-sectional jet radius as a^4 , while the other forces as a^2 , and $a^2 \gg a^4$ as $a \rightarrow 0$ [Yarin et al. (2014), Yarin (1993)]. In the present work related to solution blowing of very thin jets resulting in polymer nanofibers the momentless approximation can be

used, which allows us to neglect the shearing force in the jet cross-section and the entire moment-of-momentum equation determining it. As a result, the quasi-one-dimensional equations we are dealing with form the following system of the continuity [Eqs. (4.49) and (4.50) in Yarin et al. (2014), or Eqs. (4.18) on p. 48 in Yarin (1993)]

$$\frac{\partial \lambda f}{\partial t} + \frac{\partial f W}{\partial s} = 0 \quad (8.15)$$

$$\frac{\partial \lambda f \mathbf{V}}{\partial t} + \frac{\partial f W \mathbf{V}}{\partial s} = -\frac{1}{\rho} \frac{\partial P \boldsymbol{\tau}}{\partial s} + \lambda f \mathbf{g} + \frac{\lambda}{\rho} \mathbf{q}_{\text{total}} \quad (8.16)$$

In Eqs. (8.15) and (8.16) t is time, s is an arbitrary parameter (coordinate) reckoned along the jet axis, the cross-sectional area $f(s, t) = \pi a^2$ [the cross-section is assumed to be circular even in bending jets, which is a valid approximation according to Refs. [Yarin (1993), Yarin and Entov (1984)]]; the cross-sectional radius is $a(s, t)$, W is the liquid velocity along the jet relative to a cross-section with a certain value of s , the stretching factor $\lambda = |\partial \mathbf{R} / \partial s|$, with $\mathbf{R}(s, t)$ being the position vector of the jet axis, $\mathbf{V}(s, t)$ is the absolute velocity in the jet, ρ is liquid density, $P(s, t)$ is the magnitude of the internal force of viscoelastic origin in the jet cross-section directed along the jet axis, $\boldsymbol{\tau}$ is the unit tangent vector to the jet axis, \mathbf{g} is gravity acceleration and $\mathbf{q}_{\text{total}}$ is the overall aerodynamic force acting on a unit jet length from the surrounding air. Here and hereinafter the boldfaced characters denote vectors.

It is convenient to consider s to be a Lagrangian parameter of liquid elements in the jet (e.g. taking their initial Cartesian coordinate along the blowing direction as their values of s). Then, $W=0$, since the particles always retain their Lagrangian coordinate unchanged, and Eq. (8.15) can be integrated, which yields

$$\lambda a^2 = \lambda_0 a_0^2 \quad (8.17)$$

Here and hereinafter subscript zero denotes the initial values discussed below.

In the case of three-dimensional bending perturbations of the jet, using Eq. (8.17), we obtain the projections of Eq. (8.16) on the directions of accompanying trihedron (the local unit tangent $\boldsymbol{\tau}$, normal \mathbf{n} and binormal \mathbf{b}) of the jet axis in the following form

$$\frac{\partial V_\tau}{\partial t} = V_n \left(\frac{1}{\lambda} \frac{\partial V_n}{\partial s} + k V_\tau \right) + \frac{1}{\rho f \lambda} \frac{\partial P}{\partial s} + g_\tau + \frac{q_{\text{total},\tau}}{\rho f} \quad (8.18)$$

$$\frac{\partial V_n}{\partial t} = -V_\tau \left(\frac{1}{\lambda} \frac{\partial V_n}{\partial s} + k V_\tau \right) + \frac{P k}{\rho f} + g_n + \frac{q_{\text{total},n}}{\rho f} \quad (8.19)$$

$$\frac{\partial V_b}{\partial t} = -V_b \left(\frac{1}{\lambda} \frac{\partial V_n}{\partial s} + k V_\tau \right) + \frac{P k}{\rho f} + g_b + \frac{q_{\text{total},b}}{\rho f} \quad (8.20)$$

where k is the local curvature of the jet axis and subscripts τ , n and b correspond to the vector projections onto the local tangent and normal and binormal to the jet axis.

The position vector of the jet axis is described as

$$\mathbf{R} = \mathbf{i}\xi(s, t) + \mathbf{j}H(s, t) + \mathbf{k}Z(s, t) \quad (8.21)$$

where \mathbf{i} , \mathbf{j} and \mathbf{k} denote the unit vectors of the directions of blowing and two normal to it, respectively, while the geometric parameters, the stretching ratio and curvature, λ and k , are calculated as

$$\lambda = \left(\xi_{,s}^2 + H_{,s}^2 + Z_{,s}^2 \right)^{1/2} \quad (8.22)$$

$$k = \frac{\sqrt{(Z_{,ss}H_{,s} - H_{,ss}Z_{,s})^2 + (\xi_{,ss}Z_{,s} - Z_{,ss}\xi_{,s})^2 + (H_{,ss}\xi_{,s} - \xi_{,ss}H_{,s})^2}}{\lambda^3} \quad (8.23)$$

The total aerodynamic force is comprised of the distributed longitudinal lift force of the potential (Bernoulli-like) origin, the distributed drag force resulting from air flow across the jet and the pulling drag force imposed by the longitudinal air flow. Correspondingly,

$$\begin{aligned} \mathbf{q}_{\text{total}} &= \mathbf{n}q_{\text{total},n} + \boldsymbol{\tau}q_{\text{total},\tau} = \\ &= -\rho_a U_a^2 \mathbf{n} \left[f \frac{\xi_{,s}^2 (H_{,ss}\xi_{,s} - \xi_{,ss}H_{,s})}{(\xi_{,s}^2 + H_{,s}^2)^{5/2}} + a \frac{(H_{,s}/\xi_{,s})^2 \text{sign}(H_{,s}/\xi_{,s})}{1 + (H_{,s}/\xi_{,s})^2} \right] \\ &+ \pi a \rho_a (U_a \tau_\xi - V_\tau)^2 c \left[\frac{2a(U_a \tau_\xi - V_\tau)}{v_a} \right]^{-0.81} \boldsymbol{\tau} \end{aligned} \quad (8.24)$$

where U_a is the magnitude of the absolute local blowing velocity of air, τ_ξ denote the projection of the blowing velocity onto the local direction of the jet axis, and c is a constant value [cf. Eq. (8.4)]. It is easy to see that $q_{\text{total},b} = 0$.

In addition, in Eqs. (8.18)-(8.20) the projections of the gravity acceleration \mathbf{g}_τ , \mathbf{g}_n and \mathbf{g}_b are equal to $\mathbf{g}_\tau = g\boldsymbol{\tau}_\xi$, $\mathbf{g}_n = g\mathbf{n}_\xi$ and $\mathbf{g}_b = g\mathbf{b}_\xi$, with g being its magnitude, and $\boldsymbol{\tau}_\xi$, \mathbf{n}_ξ , and \mathbf{b}_ξ are the local projections of the unit tangent, normal and binormal to the jet axis onto the direction of blowing.

The longitudinal internal force of viscoelastic origin in the jet cross-section [Grafe and Graham (2003)] $P=f(\tau_{\tau\tau}-\tau_{nn})$ with $\tau_{\tau\tau}$ and τ_{nn} being the longitudinal and normal deviatoric stresses in the jet cross-section. As usual in the case of strong stretching (which corresponds to solution blowing), $\tau_{\tau\tau} \gg \tau_{nn}$, and thus the normal deviatoric stress can be neglected.

Correspondingly, the longitudinal internal force $P=f\tau_{\tau\tau}$, while the constitutive equation for $\tau_{\tau\tau}$ is provided by the viscoelastic upper-convected Maxwell model [Yarin et al. (2014, 2010, 2011, 1993)] (UCM) in the form

$$\frac{\partial \tau_{\tau\tau}}{\partial t} = 2\tau_{\tau\tau} \frac{1}{\lambda} \frac{\partial \lambda}{\partial t} + 2 \frac{\mu}{\theta} \frac{1}{\lambda} \frac{\partial \lambda}{\partial t} - \frac{\tau_{\tau\tau}}{\theta} \quad (8.25)$$

Equations (8.18)-(8.20) and (8.22)-(8.25) describe the jet dynamics in the process of solution blowing. They are supplemented by the following kinematic equations describing the shape of the jet axis

$$\frac{\partial \xi}{\partial t} = n_{\xi} V_n + b_{\xi} V_b + \tau_{\xi} V_{\tau} \quad (8.26)$$

$$\frac{\partial H}{\partial t} = n_{\eta} V_n + b_{\eta} V_b + \tau_{\eta} V_{\tau} \quad (8.27)$$

$$\frac{\partial Z}{\partial t} = n_{\zeta} V_n + b_{\zeta} V_b + \tau_{\zeta} V_{\tau} \quad (8.28)$$

The projections of the unit vectors of the accompanying trihedron $\boldsymbol{\tau}$, \mathbf{n} and \mathbf{b} on the directions of the unit vectors \mathbf{i} , \mathbf{j} and \mathbf{k} of the Cartesian coordinate framework associated with the blowing direction, are given by the following expressions

$$\tau_{\xi} = \frac{\xi_s}{\lambda}, \tau_{\eta} = \frac{H_s}{\lambda}, \tau_{\zeta} = \frac{Z_s}{\lambda} \quad (8.29)$$

$$n_{\xi} = \frac{\xi_{ss}(H_s^2 + Z_s^2) - \xi_s(H_{ss}H_s + Z_{ss}Z_s)}{\lambda \sqrt{(Z_{ss}H_s - H_{ss}Z_s)^2 + (\xi_{ss}Z_s - Z_{ss}\xi_s)^2 + (H_{ss}\xi_s - \xi_{ss}H_s)^2}} \quad (8.30)$$

$$n_\eta = \frac{H_{ss}(\xi_s^2 + Z_s^2) - H_s(\xi_{ss}\xi_s + Z_{ss}Z_s)}{\lambda\sqrt{(Z_{ss}H_s - H_{ss}Z_s)^2 + (\xi_{ss}Z_s - Z_{ss}\xi_s)^2 + (H_{ss}\xi_s - \xi_{ss}H_s)^2}} \quad (8.31)$$

$$n_\zeta = \frac{Z_{ss}(\xi_s^2 + H_s^2) - Z_s(\xi_{ss}\xi_s + H_{ss}H_s)}{\lambda\sqrt{(Z_{ss}H_s - H_{ss}Z_s)^2 + (\xi_{ss}Z_s - Z_{ss}\xi_s)^2 + (H_{ss}\xi_s - \xi_{ss}H_s)^2}} \quad (8.32)$$

as well as $b_\xi = \tau_\eta n_\zeta - n_\eta \tau_\zeta$, $b_\eta = \tau_\zeta n_\xi - n_\zeta \tau_\xi$, $b_\zeta = \tau_\xi n_\eta - n_\xi \tau_\eta$.

According to the theory of the axisymmetric turbulent gas jets [Yarin e al. (2007)], the air flow field is found using the following expression

$$U_a(\xi, H) = U_{a0}\varphi(\xi, H) \quad (8.33)$$

where U_{a0} is the air velocity at the nozzle exit, whereas the dimensionless function $\varphi(\xi, H)$ is given by

$$\varphi(\xi, H) = \frac{4.8/\ell}{(\xi + 4.8/\ell)} \frac{1}{(1 + \zeta^2/8)^2}, \quad \zeta = \zeta(\xi, H) = \frac{H}{0.05(\xi + 4.8/\ell)} \quad (8.34)$$

In Eq. (8.34) ξ and H are rendered dimensionless by L , the distance between the current cross-section and the end of the straight part of the polymer jet, with the latter being known from the results of section 3.1. Also, in Eqs. (34) $\ell = L/a_0$.

Neglecting secondary terms, the governing equations of the problem (8.18)-(8.20) and (8.24)-(8.28) in the isothermal case can be reduced to the following system of equations written in the dimensionless form

$$\frac{\partial^2 \xi}{\partial t^2} = \frac{2}{\text{Re}} \Phi \frac{\partial^2 \xi}{\partial s^2} + \frac{1}{\text{Fr}^2} \tau_\xi + \text{J} \ell \frac{q_{\text{total}, \tau}}{f} + \ell \frac{1}{\text{Pe}} \frac{b}{a^2} \frac{\partial \xi}{\partial t} \quad (8.35)$$

$$\begin{aligned} \frac{\partial^2 H}{\partial t^2} = & \left[\frac{\tau_{\tau\tau}}{\text{Re}} - J\varphi^2(\xi, H, Z) \right] |b_\zeta| \frac{1}{\lambda^2} \frac{\partial^2 H}{\partial s^2} + \frac{\tau_\eta}{\text{Fr}^2} - b_\zeta J \ell \frac{\varphi^2(\xi, H, Z)}{\pi a} n_\xi^2 \text{sign}(n_\xi) \\ & + \ell \frac{1}{\text{Pe}} \frac{b}{a^2} \left(b_\zeta n_\eta \frac{\partial H}{\partial t} - b_\zeta n_\zeta \frac{\partial Z}{\partial t} \right) \end{aligned} \quad (8.36)$$

$$\begin{aligned} \frac{\partial^2 Z}{\partial t^2} = & \left[\frac{\tau_{\tau\tau}}{\text{Re}} - J\varphi^2(\xi, H, Z) \right] |b_\eta| \frac{1}{\lambda^2} \frac{\partial^2 Z}{\partial s^2} + \frac{(b_\eta \tau_\eta + b_\xi)}{b_\eta} \frac{1}{\text{Fr}^2} - b_\eta J \ell \frac{\varphi^2(\xi, H, Z)}{\pi a} n_\xi^2 \text{sign}(n_\xi) \\ & + \ell \frac{1}{\text{Pe}} \frac{b}{a^2} \left[-b_\eta n_\eta \frac{\partial H}{\partial t} + (1 + b_\eta n_\zeta) \frac{\partial Z}{\partial t} \right] \end{aligned} \quad (8.37)$$

The factor $\Phi = (\tau_{\tau\tau} + 1/\text{De})/\lambda^2$ involved in Eq. (8.35) satisfies the following equation if solution blowing happens in a fully saturated atmosphere and no solvent evaporation happens at all

$$\frac{\partial \Phi}{\partial t} = -\frac{\tau_{\tau\tau}}{\text{De}\lambda^2} \quad (8.38)$$

In addition, in Eq. (8.30)

$$q_{\text{total},\tau} = c\pi a \left[\tau_\xi \varphi(\xi, H) - V_\tau \right]^2 \left(\text{Re}_a a \left[\tau_\xi \varphi(\xi, H) - V_\tau \right] \right)^{-0.81} \quad (8.39)$$

The following scales have been used: L/U_{a0} for t ; L for s , ξ , H and Z ; L^{-1} for k ; $\mu U_{a0}/L$ for $\tau_{\tau\tau}$ and Φ ; U_{a0} for U_a , V_τ and V_n and V_b ; a_0 (the value obtained at the end of the straight part of the jet) for a (and πa_0^2 for f); $\rho_a U_{a0}^2 a_0$ for $q_{\text{total},\tau}$; and μ/ρ for the kinematic turbulent eddy viscosity ν_t . As a result, the following dimensionless groups arise in addition to $\ell = L/a_0$

$$\text{Re} = \frac{\rho L U_{a0}}{\mu}, \quad J = \frac{\rho_a}{\rho}, \quad \text{Fr} = \left(\frac{U_{a0}^2}{gL} \right)^{1/2}, \quad \text{Re}_a = \frac{2a_0 U_{a0}}{\nu_a}, \quad \text{De} = \frac{\theta U_{a0}}{L}, \quad \text{Pe} = \frac{U_{a0} a_0}{D_a} \quad (8.40)$$

where Re and Re_a are the corresponding Reynolds numbers, Fr is the Froude number, De is the Deborah number, θ is the polymer relaxation time, Pe is the Peclet number and D_a is the vapor diffusion coefficient in air.

In the case where solvent evaporation and jet precipitation and solidification take place, the solvent concentration C_s in the jet is governed by the following equation

$$C_s = 1 - \frac{f_0 \lambda_0}{f \lambda} C_{p0} \quad (8.41)$$

where C_{p0} is the initial polymer concentration.

The mass balance in the present case does not reduce to Eq. (8.17) and takes the following form

$$\frac{\partial f \lambda}{\partial t} = -D_a \cdot b \cdot \pi \lambda \quad (8.42)$$

where

$$b = 0.495 Re_a^{1/3} Sc^{1/2} [C_{s,eq}(T) - C_{s,\infty}] \quad (8.43)$$

[cf. Eq. (8.2)].

Correspondingly, Eqs. (8.18)-(8.20) and those following from them acquire additional terms.

Following [Yarin et al. (2001)], we assume that the viscosity and relaxation time of polymer solution vary with polymer concentration C_p according to the following expressions

$$\frac{\mu}{\mu_0} = 10^{B(C_p^m - C_{p0}^m)}, \quad \frac{\theta}{\theta_0} = \frac{C_{p0}}{C_p} \quad (8.44)$$

where μ_0 and θ_0 are the initial values of the viscosity and relaxation time and B and m are physical parameters.

The dimensionless rheological constitutive equation replacing Eq. (8.38) takes the form

$$\frac{\partial \Phi}{\partial t} = \frac{b}{De_0 Pe} \ell \frac{1}{\lambda \lambda_0} \frac{\mu}{\mu_0} \left(B \cdot m \cdot \ln 10 \cdot C_p^m - 1 \right) - \frac{\theta_0}{\theta} \frac{1}{De_0} \frac{\tau_{\tau\tau}}{\lambda^2} \quad (8.45)$$

with $\Phi = \tau_{\tau\tau} / \lambda^2 + (\theta_0 / \theta) (\mu / \mu_0) / (\lambda^2 De_0)$, and the following additional dimensionless group involved: the Deborah number $De_0 = \theta_0 U_{ao} / L$.

The boundary conditions to solve Eqs. (8.35)-(8.37) are following [Sinha-Ray, Suman et al. (2010b), Yarin et al. (2010), Yarin et al. (2011)]

$$\xi_{\text{origin}} = 0, H_{\text{origin}} = H_i + H_{0\Omega} \sin(\Omega_i t), Z_{\text{origin}} = H_{0\Omega} \cos(\Omega_i t) \quad (8.46)$$

In Eq. (8.46) H_i is the distance between the die exits located in transverse direction and this value increases with the jet number. Also, $H_{0\Omega} = \left[(0.06)^{1/2} Re^{1/4} \ell^{-1/2} \right] / (\tau_{\tau\tau 0})^{1/2}$, and the dimensionless frequency $\Omega_i = \omega_i L / U_{a0}$, with the dimensional frequency being ω_i . Following Refs. Yarin et al. (2010) and Yarin et al. (2011), the dimensionless frequency varies between 0 and 1. For non-repeatability of the frequencies they were chosen randomly.

In addition to Eqs. (8.46), the front part of the jet which is the free end provides us with the following boundary conditions

$$\xi_{\text{end}} = 1, H_{\text{end}} = 0, Z_{\text{end}} = 0 \quad (8.47)$$

Not also, that when a jet touches the screen, its ξ -coordinate becomes and stays as 1, H retains its value, whereas the Z-coordinate varies due to the screen motion as

$$Z_{\text{screen}} = Z_{\text{actual}} + V_{\text{screen}} t . \quad (8.48)$$

with V_{screen} being the dimensionless screen velocity (rendered dimensionless by U_{a0}).

8.3. Experiments

The experimental setup is sketched in Fig. 8.1. In the solution blowing experiments in the present work, the 15 wt% nylon-6 solutions in formic acid were used. The solution was supplied through a 16 gauge needle with the rate of 10 ml/h. The needle was located inside a concentric nozzle which issued a high speed air jet. The air line was connected to house pressure line operating at 40-60 psi. Polymer solution issued from the needle was entrained and stretched by the surrounding high-speed air jet. The polymer jet was significantly thinned and underwent the aerodynamically-driven bending instability [Yarin et al. (2014)]. As a result, polymer nanofibers were formed after the solvent evaporated in flight. High speed imaging of the process was done using Phantom V210 camera operating at 3100 fps and 8 μ s exposure. For a proper illumination LED light was used. A plano-convex lens was placed between the setup and the light source to render the light beam parallel for viewing through the camera.

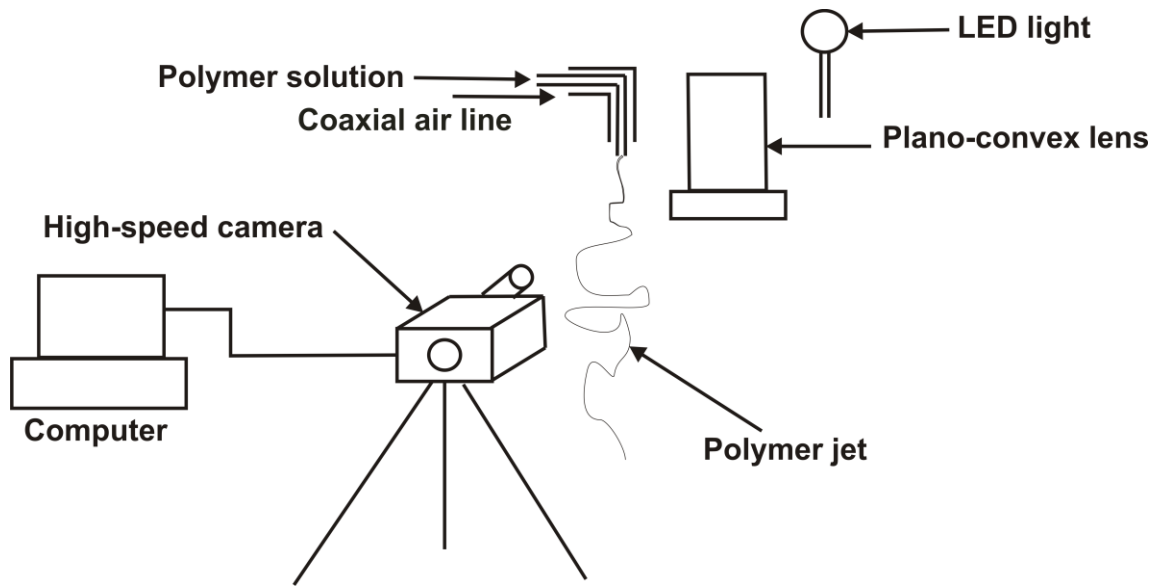


Figure 8.1: Experimental setup for high-speed recording of the solution blowing process. Polymer solution is pumped through the core of the core-shell nozzle, and air is blown at a very high speed through the annular nozzle surrounding the core one. The low-speed polymer-solution jet is entrained by the surrounding air jet and stretched and bent by the latter. LED light illumination in conjunction with a plano-convex lens renders a parallel light beam, which facilitates recording using a high speed camera 3100 fps.

8.4. Results and Discussion

The results of the numerical investigation based on the theory developed in section 8.2 are presented in this section and contrasted with the experimental findings based on section 8.3.

8.4.1 Unperturbed Straight Part of Polymer Jet

In solution blowing processes in general, and in the present experiments in particular, polymer solution is issued from a die of diameter ~ 1 mm (13-16 gauge needles) [Khansari et al. (2011)] with flow rates of 5-10 ml/h. The concentric air blowing occurs with velocities of 150-200 m/s. As the viscoelastic polymer solution is issued from the nozzle, it stays straight and experiences aerodynamically-driven stretching within a distance of 0.94 mm from the nozzle exit (Fig. 8.2), which agrees fairly well with the results in Refs. Yarin et al. (2010) and Yarin et al. (2011). The stretching cause rapid thinning of the polymer jet as it is accelerated by the surrounding air jet (Fig. 8.2). Since the polymer jet is still quite thick at this short distance from the die, it possesses a significant bending stiffness, and this does not bend here (Fig. 8.2). At such a short distance the air velocity does not diminish significantly along the polymer jet axis and for simplicity will be assumed to be constant here. It should be emphasized that the snapshots shown in Fig. 8.2 reveal a vigorous bending instability. In the process of bending the jet is always intact and never splays.

In the simulations below the values of the governing parameters were chosen to be close to the experiments of section 3. The 15 wt% polymer solution ($C_{p0}=0.15$) was issued at the feeding rate of 10 ml/h through a 16 gauge needle (diameter of 1190 μm), which corresponds to $V_0=0.249$ cm/s assuming the polymer solution density of 1 g/cm³. The speed of air blowing was taken as 150 m/s, which corresponds to the velocity ratio of $U_{a0}/V_0=60028.48$. The Reynolds number for the straight part of the jet ($Re_s=2a_0V_0/v_a$, $a_0=0.0595$ cm, $V_0=0.249$ cm/s, $v_a=0.15\text{cm}^2/\text{s}$) was equal to 0.198, and the initial straight part of the jet was taken as $L_s=1$ mm according to the experimental observation using a Phantom V210 camera at 3100 fps, as shown

in Fig. 8.2. The relaxation time θ_0 was taken as 0.01 s which corresponds to the Deborah number $De_s = \theta_0 V_0 / L_s$ of 0.0249 ($\theta_0 = 0.01$ s, $V_0 = 0.249$ cm/s, $L_s = 0.1$ cm). When polymer solution flows through a nozzle, it can acquire a longitudinal stress. The dimensional value of this stress used in the simulations $\tau_{xx0} = 0.01$ N/m², which is $0.001 \mu_0 / \theta_0$, with $\mu_0 = 1$ g/(cm×s). The simulation results were insensitive to the small values of τ_{xx0} in the range $(0.00001-0.001) \mu_0 / \theta_0$. Also, the factor c in Eq. (4) for the longitudinal aerodynamic force imposed at the straight part of the jet was taken as 65, which is of the same order as the value of 100 used in Ref. Yarin et al. (2011).

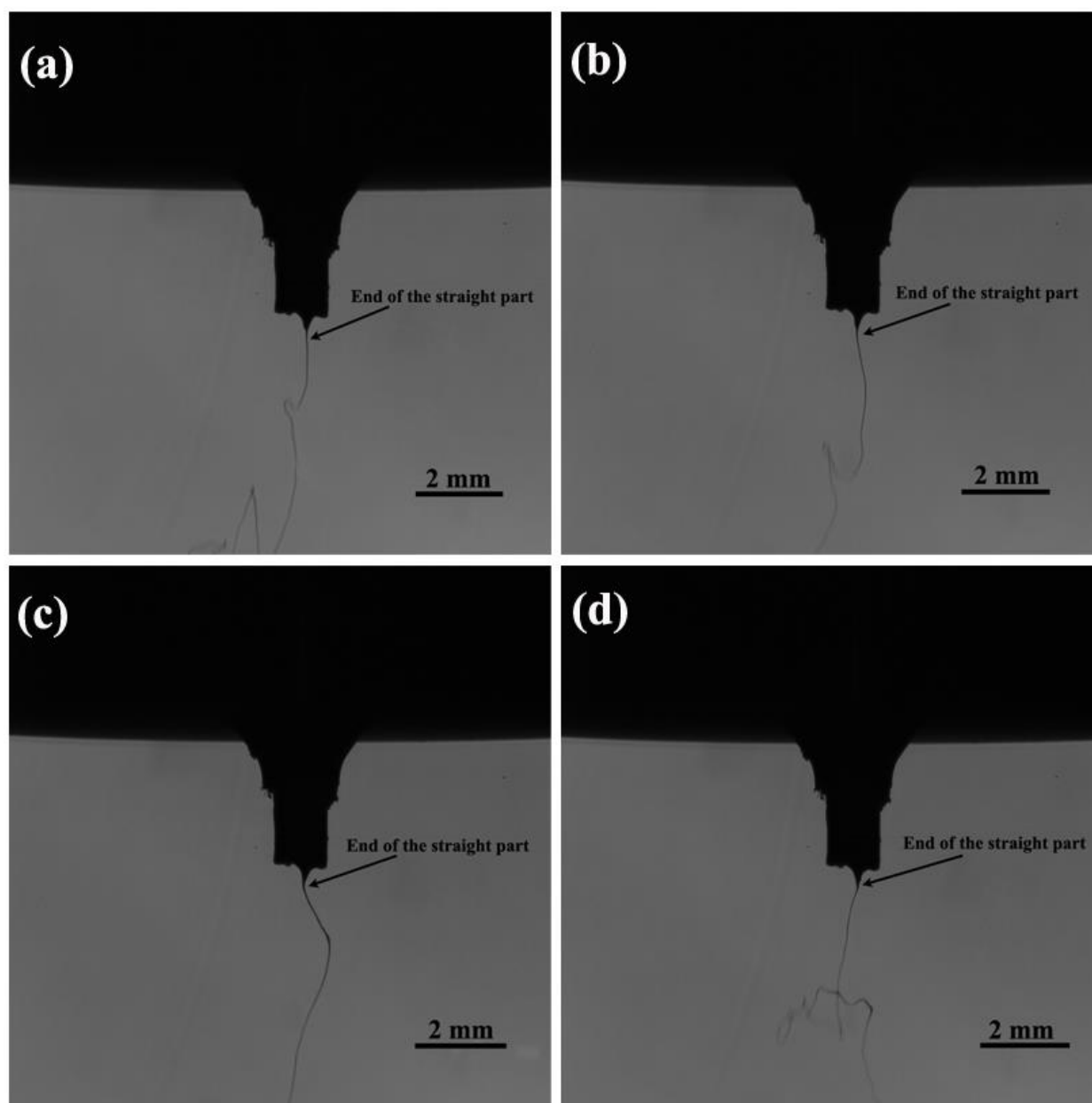


Figure 8.2. Several snapshots from a high-speed imaging of solution blowing process where the polymer solution is being issued at the flow rate of 10 ml/h into a parallel high speed air jet. The air jet velocity is 144.5 m/s. The polymer jet possesses a short thinning straight part. At the end of the straight part (indicated by arrow in all the panels) a vigorous bending begins. The imaging

was done using Phantom V210 camera operating at 3100 fps. Different panels correspond to snapshots taken at different moments of time: (a) 0.2 s, (b) 0.83 s, (c) 1.46 s, (d) 1.69 s.

In the calculations the straight part of the jet was taken as 1mm. After that the perturbations are get triggered by turbulence of the surrounding air jet, and the polymer jet starts vigorously bending and flapping.

The predicted cross-sectional radius of the polymer jet, and the distributions of the velocity and longitudinal stress along the straight part of the jet are shown in Fig. 8.3 (a-c). It can be seen that at the end of the straight part of the jet, the cross-sectional radius diminishes to 5.95 μm . Accordingly, the polymer jet velocity significantly increases and reaches of about 23% of the velocity of the surrounding air. Also, the longitudinal stress dramatically increases within the first 100 μm .

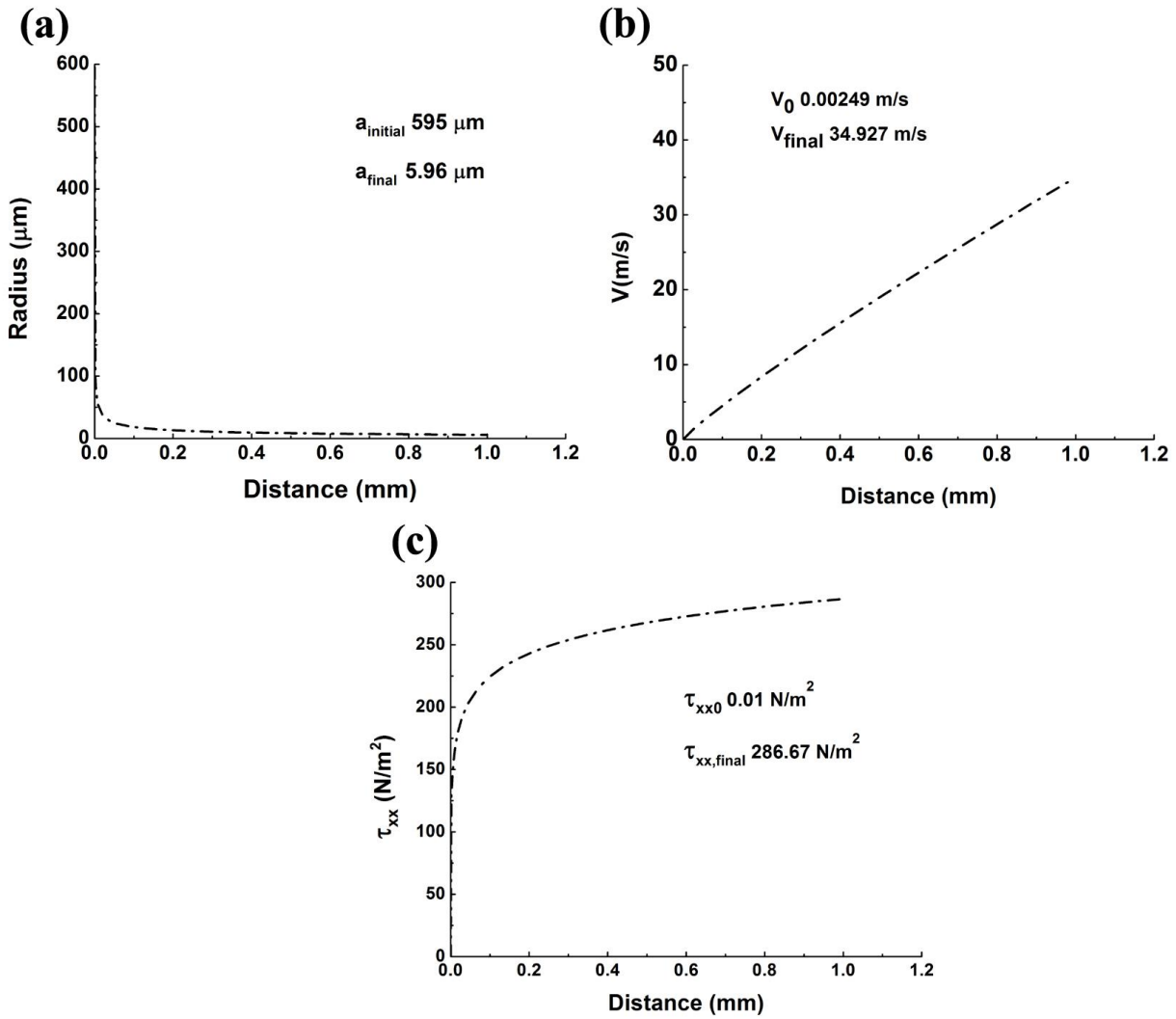


Figure 8.3. Simulation results for a straight part of polymer jet. (a) Cross-sectional radius, (b) velocity, and (c) longitudinal deviatoric stress.

The polymer concentration C_p in the straight part of the jet was predicted to increase by 10% compared to its initial value (0.166 instead of 0.15). Accordingly the solution viscosity at the end of the straight part of the polymer solution jet increased by 22%.

8.4.2 Perturbed Part of Polymer Jet

The cross-sectional radius, longitudinal stress and solvent/polymer concentration predicted at the end of the straight part of the jet were taken as initial conditions for the simulations of the perturbed part of the jet.

The velocity field in the axisymmetric air jet surrounding bending polymer jet predicted according to Eqs. (8.33) and (8.34) is shown in Fig. 8.4. Here and hereinafter all the parameters are rendered dimensionless as described in section 8.3.2.

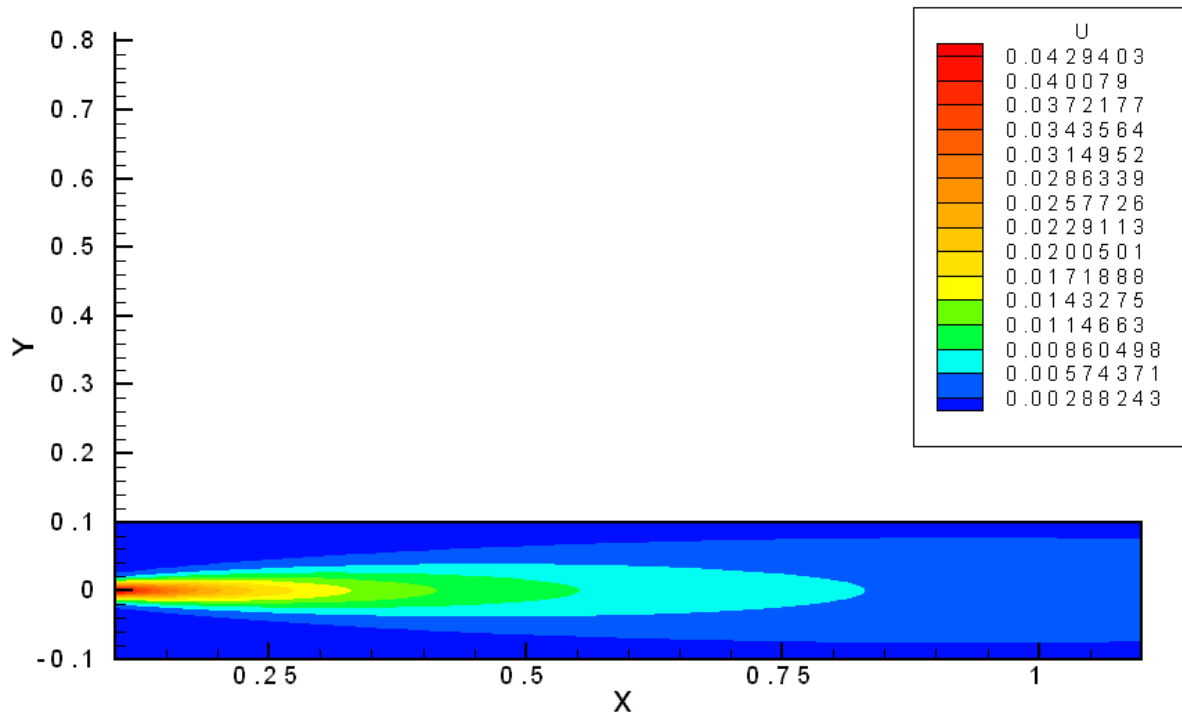


Figure 8.4. Axisymmetric velocity field in the air jet.

In our calculations the die-to-collector distance was taken as 20 cm, which makes $\ell = L/a_0 = 33613.4$. Due to numerical limitations, in the simulations the Reynolds number Re of Eq. (8.40) was kept as 40000. The value of Re_a [cf. Eq. (8.40)] corresponding to the cross-sectional radius at the end of the straight part of the jet ($5.95 \mu\text{m}$) was about 120. In the simulations we used $Re_a = 150$. In simulations of the bent part of the jet the value of the factor c in Eq. (8.24) was reduced to 30 from $c = 65$ as used in the straight part of the polymer jet, Eq. (8.4). The reduction accounts for the fact that in the bending jet the blowing direction is inclined relative to the polymer jet axis. In the simulations of the bending perturbations, the relaxation time θ_0 was taken as 0.05 s. This increase from the value of 0.01 s used in the simulations of the straight part of the polymer jet corresponds to the switch in the relaxation mechanisms when stretching rate diminishes [Yarin et al. (2001)]. Accordingly, the value of the Deborah number De_0 was 37.5. The initial value of the longitudinal stress $\tau_{\tau\tau 0}$ for bent part of the jet was found from the result obtained at the end of the straight part. Due to the different scaling used in the straight and bent part, the stress values are related as $\tau_{\tau\tau 0} = 20\tau_{xx, \text{straight-end}} / (De_0)$, which made $\tau_{\tau\tau 0} = 15.2$. The effect of gravity was negligible, so the Froude number of Eq. (8.40) was taken as $Fr = \infty$. The other parameters governing solvent evaporation, B and m in Eq. (8.44) were taken as $B = 7$ and $m = 0.1$ as in Ref. [Yarin et al. (2010)]

The simulations were carried out simultaneously for 80 jets, with the individual jets affected by turbulent pulsations according to Eq. (8.46). The basic dimensionless frequency Ω_0 , was taken from the range 0.3 following reference Yarin et al. (2010) and Yarin et al. (2011), while the corresponding pulsation frequency was calculated as $\Omega_i = \Omega_0 r_i$, where r_i was a random number from the range 0 to 1, new at each time step, and triggered by computer clock in a non-

repeatable manner. The simulation with such random frequency generator resulted in a plausible comparison with the domain of occupied by wiggling bending jets according to the experimental observations, as shown in Fig. 8.5. The simulated bending jet domain occupied a cylinder of about 0.38 cm in diameter, whereas the experimentally observed jet is located inside a cylinder of 0.33 cm in diameter.

The calculations were carried out for two dimensionless values of the screen velocity $V_{\text{screen}} = 0.05$ and 0.15 which corresponds to the dimensional velocities of 7.5 m/s and 22.5 m/s, respectively. The predicted fiber-size distribution reported below corresponded to the one occurring when jets touched the moving screen. After that, the sizes of the deposited jet sections were “frozen” and not variable anymore. Five dimensionless time moments were highlighted: $t = 35, 36, 37, 38$ and 39 which correspond to the dimensional time moments 0.047 s, 0.048 s, 0.049 s, 0.05 s and 0.052 s, respectively. The predicted jet patterns, corresponding to the two chosen screen velocities at $t = 39$ (0.052s) are shown in Figs. 8.6 and 8.8, while the corresponding predicted fiber-size distributions for the five moments of time are plotted in Figs. 8.7 and 8.9, respectively. It should be emphasized that in solution blowing solvent evaporation proceeds on the scale of 0.01 s when jets ultimately become practically rigid and cannot be stretched anymore, i.e. effectively form fibers. Comparing the predicted fiber-size distributions shown in Fig. 8.7 and 8.9, it should be emphasized that the higher is the screen velocity, the narrower becomes the fiber-size distribution. However, the effect of the screen velocity on the fiber-size distribution in solution blowing is weaker than in meltblowing [Yarin et al. (2011)]. Figure 6 corresponding to V_{screen} of 7.5 m/s reveals the mean radii values vary within the range from 1.09 to 1.28 μm with the standard deviations (SD) of 0.546 to 0.64 μm . At the higher screen velocity

of 22.5 m/s the mean fiber radii values vary from 1.01 μm to 1.24 μm with the SD of 0.474 μm to 0.59 μm .

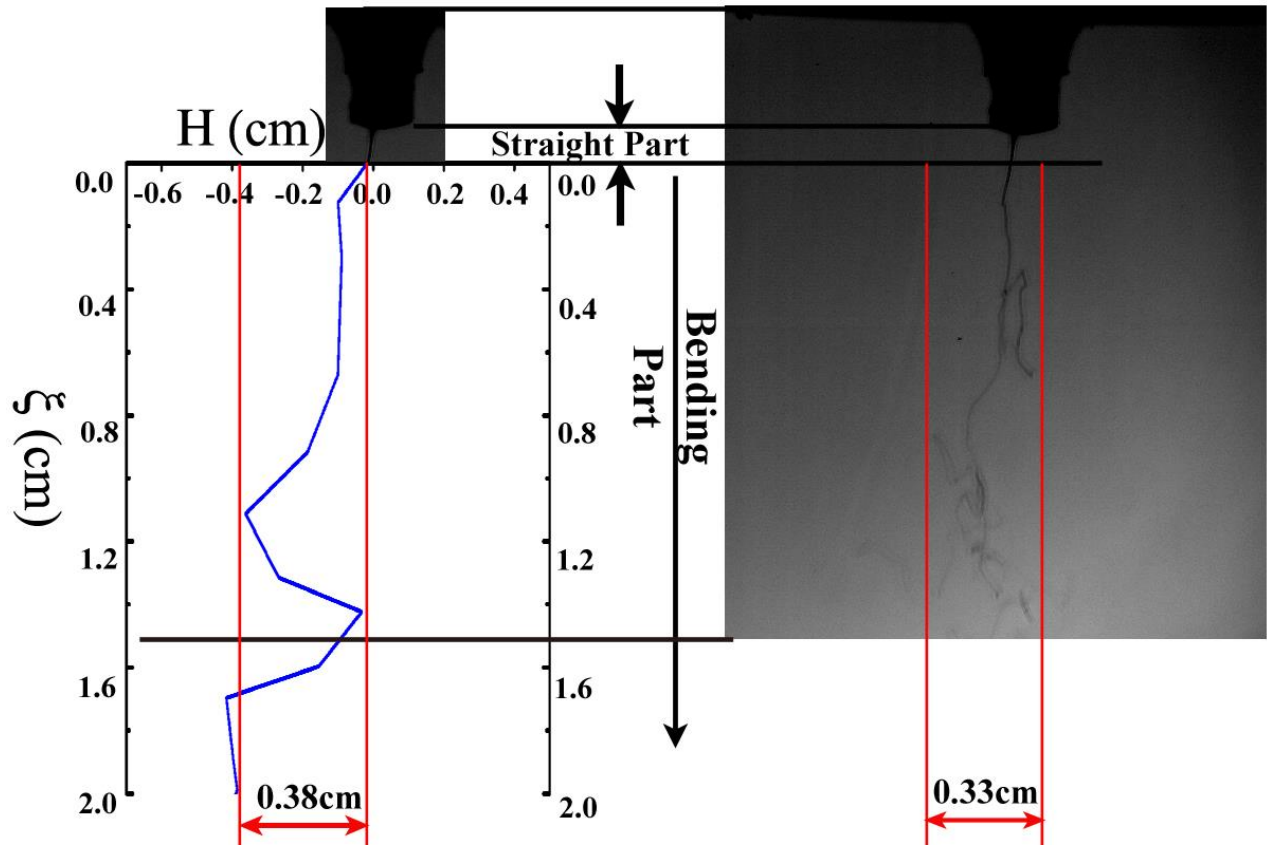


Figure 8.5. Snapshot of the observed jet configuration at the beginning of the bending part. The bending jet domain observed experimentally is delineated by two vertical straight lines. The predicted snapshot of the jet axis at the beginning of the bending part wiggles in between. The experimental data was acquired with Phantom V210 camera at 3100 fps.

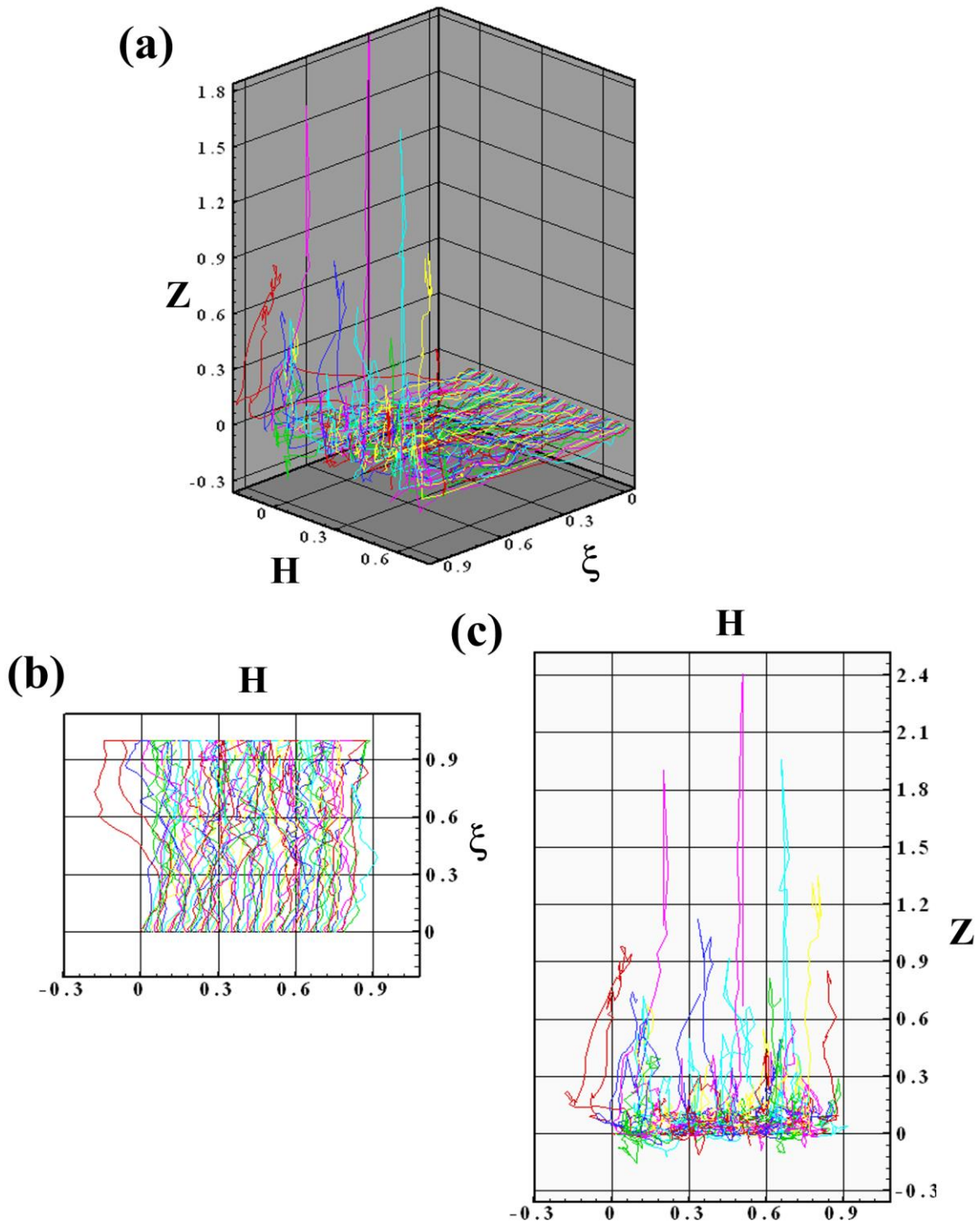


Figure 8.6. Numerically predicted snapshot for $t=39$ (the dimensional time of 0.052 s) and the screen velocity of 0.05 (the dimensional velocity of 7.5 m/s). (a) The three-dimensional view,

and (b) and (c) two two-dimensional views. In particular, panel (c) practically corresponds to the laydown on the moving screen. Here ξ denotes the direction of blowing. H and Z denote the two normal directions to the direction of blowing, where Z is the direction in which the collector screen moves.

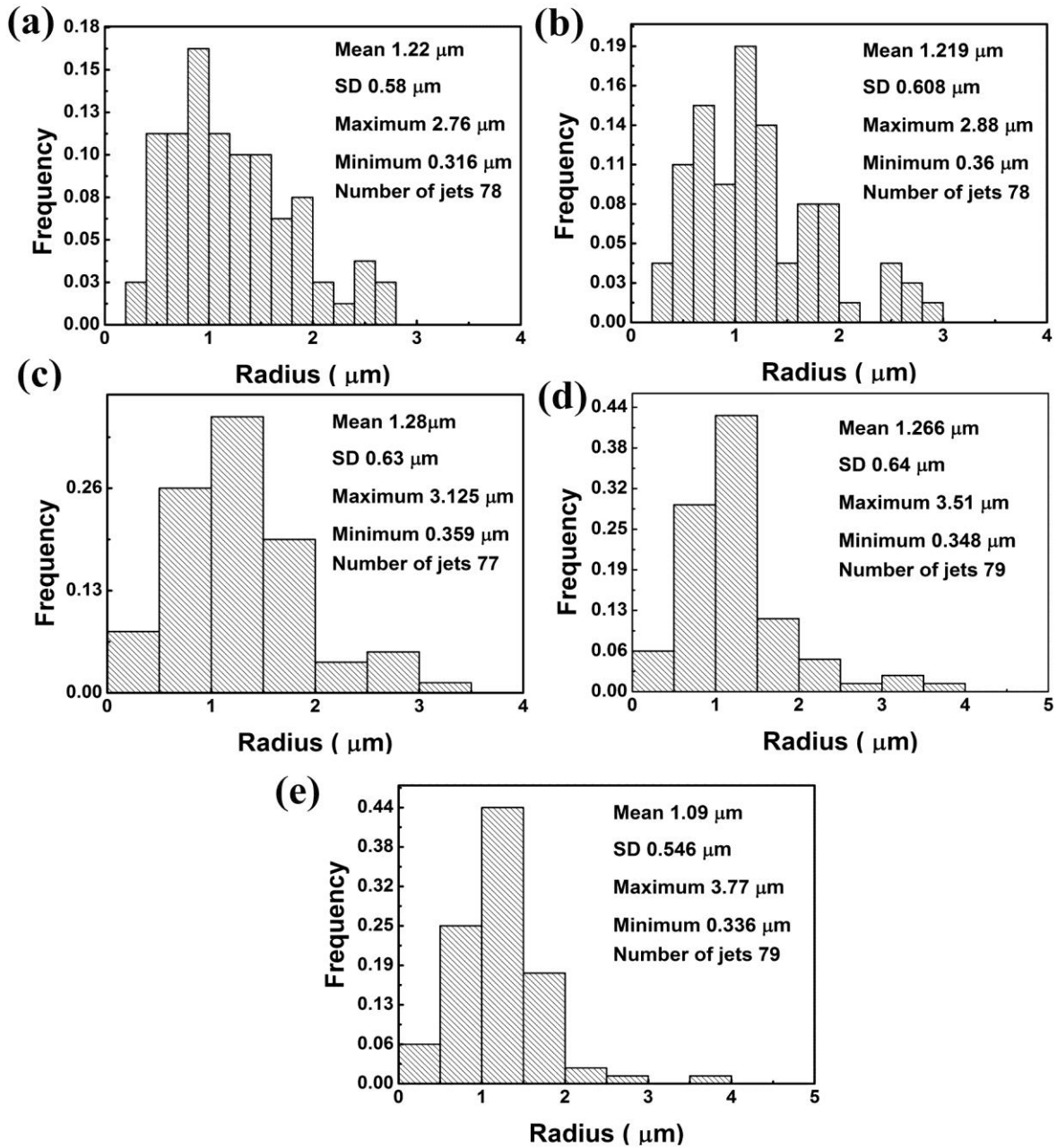


Figure 8.7. Numerically predicted fiber-size distributions for the screen velocity of 0.05 (the dimensional velocity of 7.5 m/s) at the time moments: (a) $t = 35$ (0.047 s), (b) 36 (0.048 s), (c) 37 (0.049 s), (d) 38 (0.05 s) and (e) 39 (0.052 s).

Note also, that in flight, when still being liquid, some jets can be overstretched by the air flow and break up. In such broken jets in the simulations the cross-sectional radius in a certain cross-section at a certain moment of time becomes zero. In reality, broken jets are the source of the so-called ‘fly’, while the deposited pieces of the broken jets are called ‘shots’. In the present simulations a few broken jets are not tracked further and just excluded from the consideration. In the simulations corresponding to Figs. 8.7 and 8.9 the initial jet number was 80, whereas the number of unbroken jets which were deposited on the moving screen was lower (listed in the insets in these figures as the Number of jets) by a few jets. The broken jets demonstrate the propensity to ‘fly’ formation and dripping, albeit in the cases depicted in Figs. 8.7 and 8.9 only a few jets were broken.

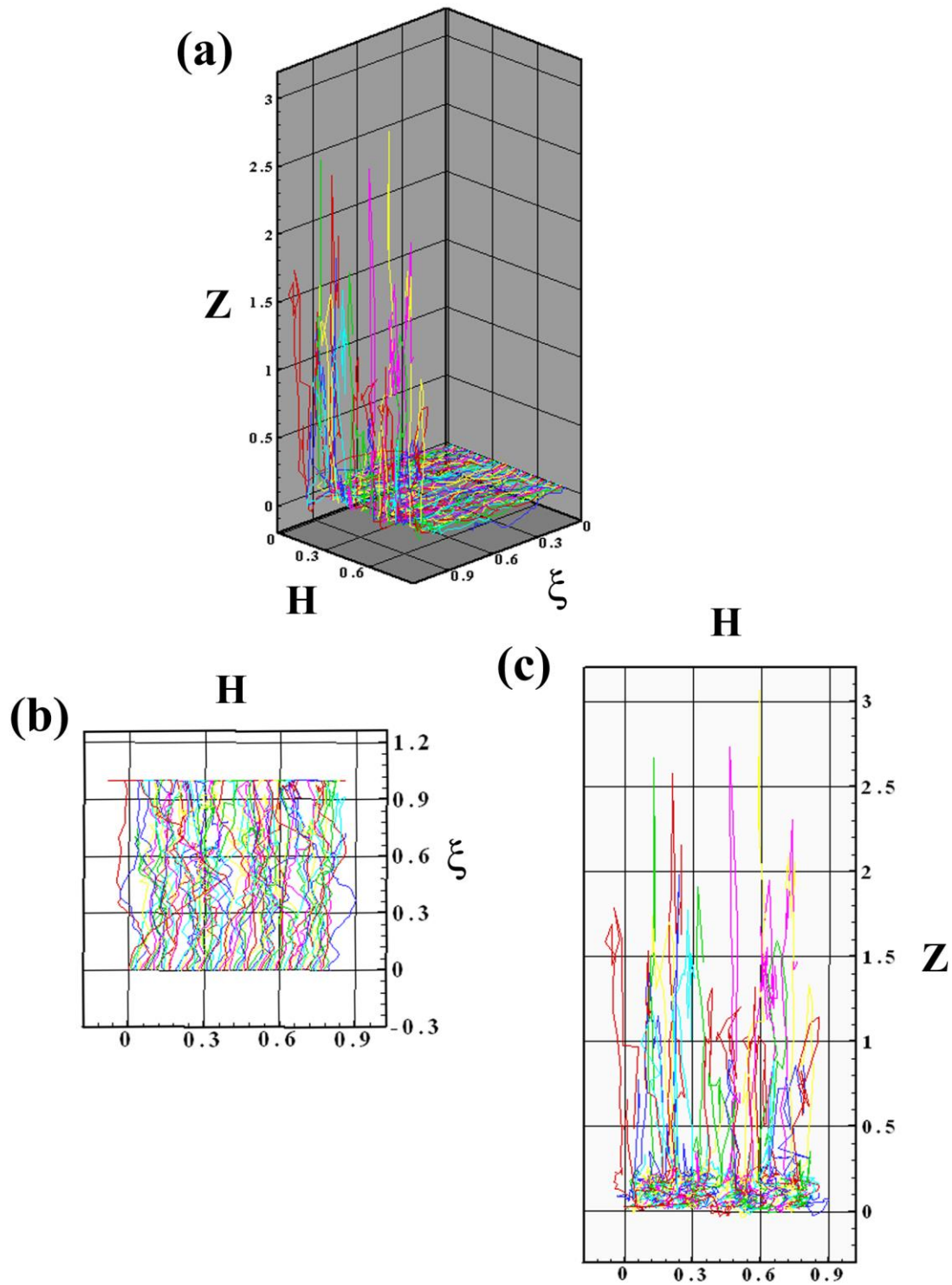


Figure 8.8. Numerically predicted snapshot for $t=39$ (the dimensional time of 0.052 s) and the screen velocity of 0.15 (the dimensional velocity of 22.5 m/s). (a) The three-dimensional view,

and (b) and (c) two two-dimensional views. In particular, panel (c) practically corresponds to the laydown on the moving screen. Here ξ denotes the direction of blowing. H and Z denote the two normal directions to the direction of blowing, where Z is the direction in which the collector screen moves.

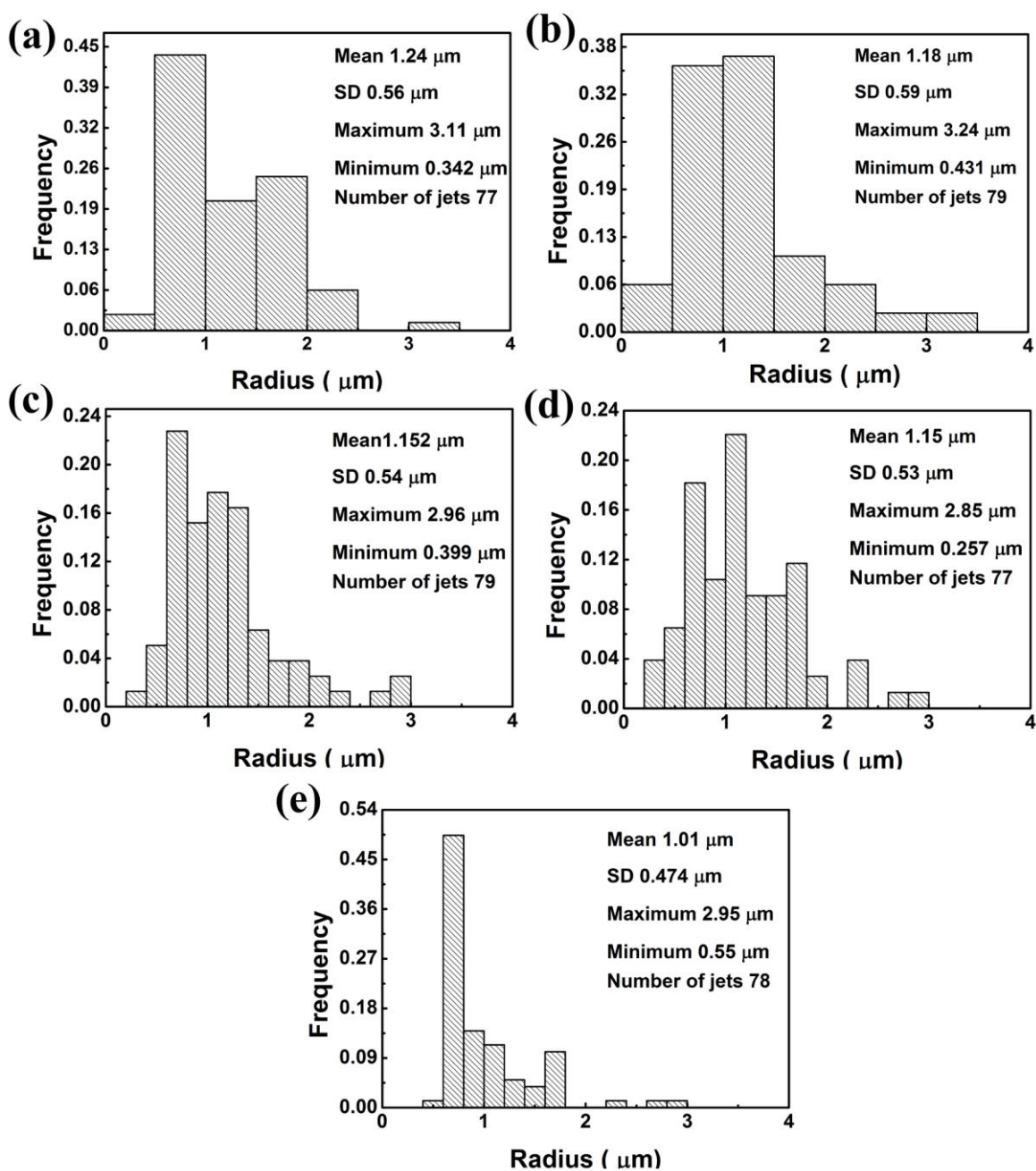


Figure 8.9. Numerically predicted fiber-size distributions for the screen velocity of 0.15 (the dimensional velocity of 22.5 m/s) at the time moments: (a) $t = 35$ (0.047 s), (b) 36 (0.048 s), (c) 37 (0.049 s), (d) 38 (0.05 s) and (e) 39 (0.052 s).

An SEM image and the corresponding fiber-size distribution established in the experiments are shown in Fig. 8.10. The fiber sizes are in the range of 100-700 nm, which overlaps with the numerical predictions in Figs. 8.7 and 8.9. Note that the polymer supply rate can have significant effect on the fiber-size distribution.

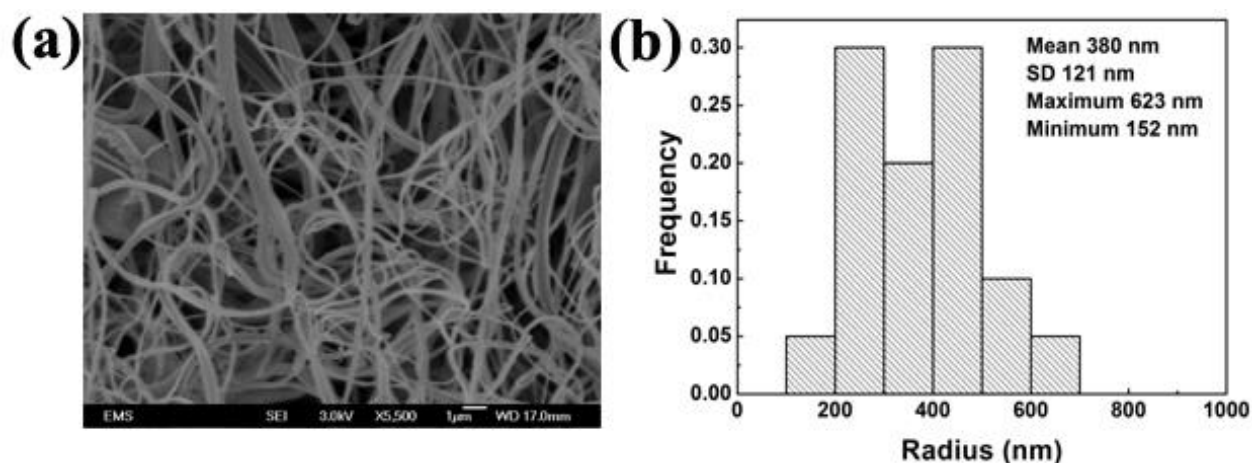


Figure 8.10. (a) SEM image of solution-blown nanofiber mat of nylon 6. (b) Fiber-size distribution. It should be emphasized that in the present case the fibers were deposited on a surface at rest.

The results obtained numerically in the present work are also in a good agreement with the data from the experimental work [Zhang et al. (2009)] where the fiber sizes varied from 300 nm to 2 µm.

8.5 Conclusion

The quasi-one dimensional model of polymer jets in solution blowing developed in the present work allows for prediction of the three-dimensional configurations of the jets as they are deposited onto a moving screen. The lay-down formed by about 80 jets was predicted, and propensity to ‘fly’ formation and dripping was demonstrated. The fiber-size distributions predicted in this work are in a reasonable overlap with the experimental data obtained here, as well those found in the literature.

CHAPTER 9

CONCLUSION

The present dissertation aims at the development and study of novel nanostructured materials useful for the enhancement of heat and mass transfer at macroscopic scales. Two basic approaches were implemented in this study. First, supersonic solution blowing was developed to form polymer nanofibers of the scale 50-100 nm for filtration and heat transfer enhancement. Second, nano-encapsulation of phase change materials, like wax and meso-erythritol, in carbon nanotubes for the indirect cooling of microelectronics was developed and explored.

The supersonic solution blowing was developed to form nanofibers of the order of 50 nm from several polymers. The applicability of the process was first demonstrated with Nylon 6 and a novel crystalline structure of Nylon 6 was discovered in the ultrafine 20-50 nm nanofibers. Furthermore, different other polymers were also spun using this method to develop the 50-100 nm nanofiber from them.

In addition, supersonically blown 50 nm Nylon 6 nanofibers were introduced to filtration applications, where such nanofibers were deposited on commercial filters in conjunction with electrospun nanofibers or alone. Such filters were then subjected to water filtration under pressure, with water being contaminated with 100 nm nanoparticles at a very low concentration. Ultrafine supersonically-blown nanofibers intercepted nanoparticles more than any other nanofibers. A detailed experimental and theoretical study proved the applicability of such nanofibers for filtration of nanoparticles in both short and long term filtration. Such nanofibers intercept nanoparticles by means of the van der Waals forces and entrap them on the windward or leeward sides.

The applicability of supersonically-blown ultrafine PAN nanofibers in thermal management applications was investigated next. A high-power surface mimicking a microelectronic a high-power substrate was coated with supersonically-blown PAN nanofibers. In one case they were metal-plated, whereas in another one pure polymer nanofibers were used. In the case of metal-plated nanofibers, it was observed that they facilitate nucleate boiling of Novec 7300 fluid at a lower surface superheat (by ~ 5 °C) than bare copper surfaces and also sustain nucleation boiling at a higher heat flux and lower surface temperature. Such metal-plated nanofibers are robust and can withstand vigorous pool boiling conditions. Pure polymer (non-metallized) nanofibers also revealed a significant enhancement of nucleation boiling, albeit less pronounced than the metal-plated ones. Such polymer nanofibers eliminate the post-processing metal-plating stage which involves an acid bath, which significantly simplifies the proposed method and extends its applicability to different substrates. Pure polymer supersonically solution-blown nanofibers also enhanced nucleate boiling by providing nucleation sites and their architectural integrity was intact even after prolonged boiling. Pure polymer electrospun nanofiber revealed lower adhesion to the substrate and delaminated too fast. This comparison showed significant benefits of supersonically-blown nanofibers compared to their electrospun counterparts.

Thermal management of high-power microelectronics was also tackled in the present work using a different approach. Nano-encapsulated phase change materials (PCM) like wax and meso-erythritol were developed and used for this aim. Such PCMs were encapsulated inside carbon nanotubes (CNTs), and such CNTs were used to form aqueous suspensions or suspensions in oil and used in throughflow in a microchannel embedded inside a high-power “microelectronics” block. The cooling effect of such suspensions was studied at different flow rates CNT contents.

It was shown that an increase in the CNT-PCM wt%, cooling via PCM melting became more and more pronounced. Such nano-encapsulation dramatically shortened the PCM thermal response time and prevented sticking to the wall.

Finally, a theoretical study of solution blowing process was conducted. A comprehensive quasi-one-dimensional model was developed for multiple polymer jets issued from a die nosepiece into a high-speed air flow and deposited onto a moving screen. The model accounts for the polymer solution viscoelasticity, jet interaction with the surrounding high-speed air flow, and solvent evaporation and jet solidification. This study is fundamental for the ongoing studies of nanofiber formation in supersonic solution blowing.

Overall, the findings of the present dissertation work resulted in a better understanding of the mechanisms available for the enhancement of the heat and mass transfer on the macroscopic scale by means of nano-objects.

CHAPTER 10

CITED LITERATURE

- Abidian, M.R., Kim, D.H., and Martin, D.C. (2006), Conducting polymer nanotubes for controlled drug release, *Advanced Materials*, 18 (4), 405–409.
- Ahn, Y.C., Park, S.K., Kim, G.T., Hwang, Y.J., Lee, C.G., Shin, H.S., and Lee, J.K. (2006), Development of high efficiency nanofilters made of nanofibers, *Current Applied Physics*, 6 (6), 1030-1035.
- Amaya, M., Kwark, S.M., Gurung, A., and You, S.M. (2013), Pool boiling heat transfer of borated (H_3BO_3) water on a nanoporous surface, *Journal of Heat Transfer*, 135 (9), 091302.
- An, S., Lee, C., Liou, M., Jo, H. S., Park, J.J., Yarin, A.L., and Yoon, S.S. (2014), Supersonically blown ultra-thin thorny devil nanofibers for efficient air cooling, *ACS Applied Materials & Interfaces*, 6 (16), 13657-13666.
- Anderson, T.M., and Mudawar, I. (1989), Microelectronic cooling by enhanced pool boiling of a dielectric fluorocarbon liquid, *Journal of Heat Transfer*, 111 (3), 752-759.
- Arik, M., and Bar-Cohen, A. (1998), Immersion cooling of high heat flux microelectronics with dielectric liquids, 4th International Symposium on Advanced Packaging Materials Processes, 229-247.
- Bandaru, P.R. (2007), Electrical properties and applications of carbon nanotube structures (2007), *Journal of Nanoscience and Nanotechnology*, 7, 1–29.
- Barhate, R.S., and Ramakrishna, S. (2007), Nanofibrous filtering media: Filtration problems and solutions from tiny material, *Journal of Membrane Science*, 296 (1), 1-8.
- Bazilevsky, A.V., Sun, K., Yarin, A.L., and Megaridis C.M. (2007), Selective intercalation of polymers in carbon nanotubes, *Langmuir*, 23, 7451–7455
- Bazilevsky, A.V., Sun, K., Yarin, A.L., and Megaridis, C.M. (2008a), Room-temperature, open-air, wet intercalation of liquids, surfactants, polymers and nanoparticles within nanotubes and microchannels, *Journal of Material Chemistry*, 18, 696-702.
- Bazilevsky, A.V., Yarin, A.L., and Megaridis, C.M. (2008b), Pressure-driven fluidic delivery through carbon tube bundles, *Lab Chip*, 8, 152-160.

Behrens, A.M., Casey, B.J., Sikorski, M.J., Wu, K.L., Tutak, W., Sandler, A.D., and Kofinas, P. (2014), In situ deposition of PLGA nanofibers via solution blow spinning, *ACS Macro Letter*, 3 (3), 249-254.

Benn, T.M., and Westerhoff, P. (2008), Nanoparticle silver released into water from commercially available sock fabrics, *Environmental Science and Technology*, 42 (11), 4133-4139.

Beratlis, N., and Smith, M. (2003), Optimization of synthetic jet cooling for micro-electronics applications, *Proceedings of 19th Semi-Therm Symposium*, San Jose, CA, 66-73.

Berber, S., Kwon, Y.K., and Tománek, D. (2000), Unusually high thermal conductivity of carbon nanotubes, *Physical Review Letter*, 84 (20), 4613-4616.

Bhattacharjee, S., Chen, J., and Elimelech, M. (2000), DLVO interaction energy between spheroidal particles and a flat surface, *Colloids and Surfaces A: Physicochemical and Engineering Aspects*, 165, 143-156.

Biondi, M., Ungaro, F., Quaglia, F., and Netti, P.A. (2008), Controlled drug delivery in tissue engineering, *Advanced Drug Delivery Reviews*, 60 (2), 229-242.

Bohn, C.R., Schaefgen, J.R., and Statton, W.O. (1961), Laterally ordered polymers: Polyacrylonitrile and poly(vinyl trifluoroacetate), *Journal of Polymer Science*, 55 (162), 531-549.

Bourdon, B., Di Marco, P., Rioboo, R., Marengo, M., and De Coninck, J. (2013), Enhancing the onset of pool boiling by wettability modification on nanometrically smooth surfaces, *International Communication of Heat and Mass Transfer*, 45, 11-15.

Calus, W.F., and Leonidopoulos, D.J. (1974), Pool boiling- binary liquid mixtures, *International Journal of Heat and Mass Transfer*, 17, 249-256.

Chalew, T.E.A., Ajmani, G.S., Huang, H., and Schwab, K.J. (2013), Evaluating nanoparticle breakthrough during drinking water treatment, *Environmental Health Perspectives*, 121, 1161-1166.

Chang, J.Y., and You, S.M. (1997), Boiling Heat Transfer Phenomena From Microporous and Porous Surfaces in Saturated FC-72, *International Journal of Heat and Mass Transfer*, 40 (18), 4437-4447.

Cheremisinoff, N.P. (1998), *Liquid Filtration*, 2nd Ed, Butterworth-Heinemann, Woburn.

Cotler, A.C., Brown, E.R., Dhir, V., and Shaw, M.C. (2004), Chip-level spray Cooling of an LD-MOSFET RF power amplifier, *IEEE Transactions on Components and Packaging Technologies*, 27, 411-416.

Cussler, E.L. (1997), *Diffusion: Mass Transfer in Fluid Systems*, 2nd Ed, Cambridge University Press, Cambridge.

Das, S.K., Putra, N. and Roetzel, W. (2003), Pool boiling characteristics of nano-fluids, *International Journal of Heat and Mass Transfer*, 46 (5), 851-862.

de Gennes, P.G. (2002), On fluid/wall slippage, *Langmuir*, 18 (9), 3413–3414.

Dees, J. R. and Spruiell, E. (1974), Structure development during melt spinning of linear polyethylene fibers, *Journal of Applied Polymer Science*, 18 (4), 1053-1078.

Deitzel, J. M., Kleinmeyer, J., Harris, D., and Beck Tan, N.C. (2001), The effect of processing variables on the morphology of electrospun nanofibers and textiles, *Polymer*, 42 (1), 261–272.

Ding, Y., Alias, H., Wen, D. and, Williams, R. A., Heat transfer of aqueous suspensions of carbon nanotubes (CNT nanofluids) (2006), *International Journal of Heat and Mass Transfer*, 49 (1-2), 240-250.

Dong, L., Quan, X., and Cheng, P. (2014), An experimental investigation of enhanced pool boiling heat transfer from surfaces with micro/nano-structures, *International Journal of Heat and Mass Transfer*, 71, 189-196.

Entov, V.M., and Yarin, A.L. (1984), The dynamics of thin liquid jets in air, *Journal of Fluid Mechanics*, 140, 91-111.

Fabris, D., Rosshirt, M., Cardenas, C., Wilhite, P., Yamada, T., and Yang, C., Y. (2011), Application of carbon nanotubes to thermal interface materials, *Journal of Electronic Packaging*, 133 (2), 020902.

Faraji, M. , Quarnia, H.E., and Lakhal, E.K. (2009), Thermal analysis of phase change material based heat sink for cooling protruding electronic chips, *Journal of Thermal Science*, 18 (3), 268-275.

Farid, M.M., Khudhair, A.M., Razcak, S.A.K., and Al-Hallaj, S. (2004), A review on phase change energy storage: Materials and applications, *Energy Conversion and Management*, 45 (9-10), 1597-1615.

Fedorova, N., and Pourdeyhimi, B. (2007), High strength nylon micro- and nanofiber based nonwovens via spunbonding, *Journal of Applied Polymer Science*, 104 (5), 3434-3442.

Feldman, D., Shapiro, M.M., Banu, D., and Fuks, C.J. (1989), Fatty acids and their mixtures as phase-change materials for thermal energy storage, *Solar Energy Materials*, 18 (2-3), 201–216.

Filatov, Y., Budyka, A., and Kirichenko, V. (2007), *Electrospinning of micro- and nanofibers: Fundamentals and applications in separation and filtration Processes*, Begell House.

Fischer, J. E., and Johnson, A.T. (1999), Electronic properties of carbon nanotubes, *Current Opinion in Solid State Material Science*, 4 (1), 28-33.

Forrest, E.C., Hu, L.W., Buongiorno, J., and McKrell, T.J. (2013), Pool boiling heat transfer performance of a dielectric fluid with low global warming potential, *Heat Transfer Engineering*, 34 (15), 1262-1277.

Freystein, M., Kolberg, F., Spiegel, L., Sinha-Ray, S., Sahu, R.P., Yarin, A.L., Gambaryan-Roisman, T., and Stephan, P. (2016), Trains of Taylor bubbles over hot nano-textured mini-channel surface, *International Journal of Heat and Mass Transfer*, 93, 827–833.

Gaertner, R.F., and Westwater, J.W. (1960), Population of active sites in nucleate boiling heat transfer, *Chemical Engineering Program Symposium*, 30, 39-48.

Gibson, P. W. , Schreuder-Gibson, H. L., and Riven, D. (1999), Electrospun fiber mats: transport properties, *American Institute for Chemical Journals*, 45 (1), 190-195.

Goel, M., Roy, S., and Sengupta, S. (1994), Laminar forced convection heat transfer in microcapsulated phase change material suspensions, *International Journal of Heat and Mass Transfer*, 37 (4), 593–604.

Gong, Z.X., and Mujumdar, A.S. (1996), Cyclic heat transfer in a novel storage unit of multiple phase change materials, *Applied Thermal Engineering*, 16 (10), 807–815.

Gopal, R., Kaur, S., Ma, Z., Chan, C., Ramakrishna, S., and Matsura, T. (2006), Electrospun nanofibrous filtration membrane, *Journal of Membrane Science*, 281, 581-586.

Grafe, T. and Graham, T. (2003b), Polymeric nanofibers and nanofiber webs: a new class of nonwovens, *International Nonwovens Journal*, 12 (1), 51-55.

Grafe, T., and Graham, K. (2003a), Polymeric nanofibers and nanofiber webs: a new class of nonwovens, *Nonwoven Technology Review INJ Spring*, 51-55.

Grafe, T., Gogins, M., Barris, M., Schafer, J., and Canepa, R. (2001), Nanofibers in filtration application in transportation, *Filtration 2001 International Conference and Expo of the Association of the Nonwovens Fabric Industry*, Chicago, Illinois, December 3–5.

Gregory, J. (1981), Approximate expressions for retarded van der Waals interaction, *Journal of Colloid Interface Science*, 83 (1), 138-145.

Groeber, H., Erk, S., and Grigull, U., (1961), *Fundamentals of heat transfer*, McGraw-Hill, New York.

Groitzsch, D., and Fahrbach, E. (1986), Microporous multilayer nonwoven material for medical applications, *US Patent*, 4,618,524.

Guo, Q., Keer, L.M., and Chung, Y.W. (1993), Thermal stress-induced open-circuit failure in microelectronics thin-film metallizations (Chapter 10) (Editor: John H. Lau), Thermal Stress and Strain in Microelectronics Packaging, Springer-Verlag.

Hallez, Y. (2012), Analytical and numerical computations of the van der Waals force in complex geometries: Application to the filtration of colloidal particles, Colloids and Surfaces A: Physicochemical and Engineering Aspects, 414, 466-476.

Hamaker, H.C. (1937), The London-van der Waals attraction between spherical particles, Physica IV, 4, 1058-1072.

Handy, R., Henry, T., Scown, T., Johnston, B., and Tyler, C. (2008), Manufactured nanoparticles: Their uptake and effects on fish—a mechanistic analysis, Ecotoxicology, 17, 396-409.

Hasnain, S.M. (1998), Review on sustainable thermal energy storage technologies, Part I: heat storage materials and techniques, Energy Conversion Management, 39 (11), 1127-1138.

Hayter, A.J. (1996), Probability and Statistics, PWS Publishing Co., Boston.

Holman, J.P. (1986), Heat Transfer, 3rd Ed., McGraw-Hill Book Company, New York.

<http://webbook.nist.gov/cgi/cbook.cgi?ID=C149326&Mask=2>

Iovleva, M.M., Smirnova, V.N., and Budnitskii, G.A. (2001), The solubility of polyacrylonitrile, Fiber Chemistry, 2001, 33 (4), 262-264.

Islam, M.F., Rojas, E., Bergey, D.M., Johnson, A.T., and Yodh, A.G. (2003), High weight fraction surfactant solubilization of single-wall carbon nanotubes in water, Nano letters, 3 (2), 269-273.

Israelachvili, J. (1997), Intermolecular and Surfaces Forces, 2nd Ed., Academic Press, London.

Janicki, M., and Napieralski, A. (2000), Modelling electronic circuit radiation cooling using analytical thermal model Microelectronics Journal, 31 (9), 781-785.

Jensen, M.K., and Jackman, D.L. (1984), Prediction of nucleate pool boiling heat transfer coefficients of refrigerant-oil mixtures, Journal of Heat Transfer, 106 (1), 184-190.

Jun, S., Sinha-Ray, S., and Yarin, A.L. (2013), Pool boiling on nano-textured surfaces, International Journal of Heat and Mass Transfer, 62 (1), 99-111.

Kandasamy, R., Wang, X., and Mujumdar, A.S. (2008), Transient cooling of electronics using phase change material (PCM)-based heat sinks, Applied Thermal Engineering, 28, 1047-1057.

Khansari S., Sinha-Ray S., Yarin A. L., and Pourdeyhimi B. (2012), Stress-strain dependence for soy-protein nanofiber mats, *Journal of Applied Physics*, 111, 044906.

Khansari, S., Duzyer, S., Sinha-Ray, S., Hockenberger, A., Yarin, A.L., and Pourdeyhimi, B. (2013a), Two-stage desorption-controlled release of fluorescent dye and vitamin from solution-blown and electrospun nanofiber mats containing porogens, *Molecular Pharmaceutics*, 10 (12), 4509-4526.

Khansari, S., Sinha-Ray, S., Yarin, A.L., and Pourdeyhimi, B. (2013b), Effect of chemical and physical cross-linking on tensile characteristics of solution-blown soy protein nanofiber mats, *Industrial & Engineering Chemistry Research*, 52 (41), 15104–15113.

Khil, M.S., Cha, D.I., Kim, H.Y., Kim, I.S., and Bhattarai, N. (2003), Electrospun nanofibrous polyurethane membrane as wound dressing, *Journal of Biomedical Material Research B: Applied Biomaterial*, 67, 675–679.

Kim, H., and Kim, M. (2009), Experimental study of the characteristics and mechanism of pool boiling chf enhancement using nanofluids, *Heat and Mass Transfer*, 45 (7), 991-998.

Kim, J., and Golliher, E. (2002), Steady state model of a micro loop heat pipe, *Proceedings of 18th Semi-Therm Symposium*, San Jose, CA, 137-144.

Kim, S.J., Bang, I.C., Buongiorno, J., and Hu, L.W. (2007), Surface wettability change during pool boiling of nanofluids and its effect on critical heat flux, *International Journal of Heat and Mass Transfer*, 50 (19-20), 4105-4116.

Kirsch, V.A. (2000), The effect of van der Waals forces on aerosol filtration with fibrous filters, *Colloid Journal*, 62 (6), 714–720.

Kirsch, V.A. (2003), Calculation of the van der Waals force between a spherical particle and an infinite cylinder, *Advanced Colloid Interface Science*, 104, 311-324.

Kochin, N.E., Kibel, I.A., and Roze, N.V. (1963), *Theoretical Hydromechanics*, vol. 2, State Publishing House of the Physico-Mathematical Literature, Moscow.

Kosmider, K., and Scott, J. (2002), Polymeric nanofibre exhibit an enhanced air filtration performance, *Filtration and Separation*, 39 (6), 20-22.

Kuravi, S., Kota, K.M., Du, J., and Chow, L.C. (2009), Numerical investigation of flow and heat transfer performance of nano-encapsulated phase change material slurry in microchannels, *Journal of Heat Transfer*, 131, 062901.

Kutateladze, S.S. (1963), *Fundamentals of heat transfer*, Academic Press, New York.

- Laceros-Mendez, S., Moreira, M.V., Mano, J.F., Schmidt, V.H., and Bohannan, G. (2002), Dielectric behavior in an oriented β -pvdf film and chain reorientation upon transverse mechanical deformation, *Ferroelectrics*, 273 (1), 15-20.
- Lauga, E., Brenner, M.P., and Stone, H.A. (2007), *Microfluidics: The No-slip Boundary Condition*, Chapter 19, (Editors: Tropea, C., Yarin, A.L., Foss, J.F.), Springer Handbook of Experimental Fluid Mechanics, Berlin, 2007
- Lee, J.K., Liu, B.Y.H., and Rubow, K. L. (1993), Latex sphere retention by microporous membranes in liquid filtration, *Journal of The Institute of Environmental Sciences and Technology*, 36 (1), 26-36.
- Li, C., and Peterson, G.P. (2010), Geometric effects on critical heat flux on horizontal microporous coatings, *Journal of Thermophysics Heat Transfer*, 24 (3), 449-455.
- Li, K., and, Chen, Y. (2012), Evaluation of DLVO interaction between a sphere and a cylinder, *Colloids and Surfaces A: Physicochemical and Engineering Aspects*, 2012, 415, 218– 229.
- Li, Y.Y., Liu, Z.H., and Zheng, B.C. (2015), Experimental study on the saturated pool boiling heat transfer on nano-scale modification surface, *International Journal of Heat and Mass Transfer*, 84, 550-561.
- Liu, Y., Cui, L., Guan, F., Gao, Y., Hedin, N.E., Zhu, L., and Fong H. (2007), Crystalline morphology and polymorphic phase transitions in electrospun nylon 6 nanofibers, *Macromolecules*, 40(17), 6283–6290.
- Loitsyanskii, L.G. (1966), *Mechanics of Liquids and Gases*, 1st Ed., Pergamon, New York.
- Ma, Z., Kotaki, M., Yong, T., Heb, W., and Ramakrishna, S. (2005), Surface engineering of electrospun polyethylene terephthalate (PET) nanofibers towards development of a new material for blood vessel engineering, *Biomaterials*, 26(15), 2527-2536
- Martines, E., Csaderova, L., Morgan, H., Curtis, A.S.G., and Riehle, M.O. (2008), DLVO interaction energy between a sphere and a nano-patterned plate, *Colloids and Surfaces A: Physicochemical and Engineering Aspects*, 318, 45–52.
- Matthews, J.A., Wnek, G.E., Simpson, D.G., and Bowlin, G L. (2002), Electrospinning of collagen nanofibers, *Biomacromolecules*, 3, 232–238.
- Mcgillis, W.R., and Carey, V.P. (1996), On the role of marangoni effects on the critical heat flux for pool boiling of binary mixtures, *Journal of Heat Transfer*, 118 (1), 103-109.
- McHale, J.P., Garimella, S.V., Fisher, T.S., and Powell, G.A. (2011), Pool boiling performance comparison of smooth and sintered copper surfaces with and without carbon nanotubes, *Nanoscale and Microscale Thermophysical Engineering*, 15 (3), 133-150.

- Medeiros, E.S., Glenn, G.M., Klamczynski, A.P., Orts, W.J., and Mattoso, L.H.C. (2009) Solution blow spinning: A new method to produce micro-and nanofibers from polymer solutions, *Journal of Applied Polymer and Science*, 113 (4), 2322-2330.
- Min, B.M., Lee, G., Kim, S.H., Nam, Y.S., Lee, T.S., and Park, W.H. (2004), Electrospinning of silk fibroin nanofibers and its effect on the adhesion and spreading of normal human keratinocytes and fibroblasts in vitro *Biomaterials*, 2, 1289–1297.
- Miner, A., and Ghoshal, U. (2004), Cooling of high-power-density microdevices using liquid metal coolants, *Applied Physics Letters*, 85 (3), 506–508.
- Miner, A., and Ghoshal, U. (2006), Limits of heat removal in microelectronic systems, *IEEE Transactions on Components and Packaging Technologies*, 29 (4), 743-749.
- Moliere, M., Verdier, Y., and Leymonie, C. (1990), Oxidation of copper on high purity water at 70 °C: application to electric generator operation, *Corrosion Science*, 30 (2-3), 183-188.
- Murphy B. L., and Kuhn R.G. (2002), Setting the terms of reference in environmental assessments: canadian nuclear fuel waste management. *Canadian Public Policy XXVII*, 249-266.
- Nguyen, N.T., and Wereley, S.T. (2007), *Fundamentals and applications of microfluidics*, Artech House, Norwood MA.
- Nishikawa, K., and Yamagata, K. (1960), On the correlation of nucleate boiling heat transfer, *International Journal of Heat and Mass Transfer*, 1 (2-3), 219-235.
- Nukiyama, S. (1966), The maximum and minimum values of the heat q transmitted from metal to boiling water under atmospheric pressure, *International Journal of Heat and Mass Transfer*, 9 (12), 1419-1433.
- Oliveira, J.E., Zucolotto, V., Mattoso, L.H.C., and Medeiros, E.S. (2012), Multi-Walled Carbon Nanotubes and Poly (lactic acid) Nanocomposite Fibrous Membranes Prepared by Solution Blow Spinning, *Journal of Nanoscience and Nanotechnology*, 12 (3), 2733-2741.
- Ona, E.P., Zhang, X., Kyaw, K., Watanabe, F., Matsuda, H., Kakiuchi, H., Yabe, M., and Chihara, S. (2001), Relaxation of supercooling of erythritol for latent heat storage, *Journal of Chemical Engineering of Japan*, 34 (3), 376–382.
- Oseen, C. (1910), Über die Stokes'sche formel, und über eine verwandte Aufgabe in der Hydrodynamik, *Arkiv för Matematik, Astron. Fysik*, 6, 1-20.
- Park, J.C., Ito, T., Kim, K.O., Kim, K.W., Kim, B.S., Khil, M.S., Kim, H.Y., and Kim, I.S. (2010), Electrospun poly (vinyl alcohol) nanofibers: effects of degree of hydrolysis and enhanced water stability, *Polymer Journal*, 42 (3), 273–276

- Parsegian, V.A., and Ninham, B.W. (1971), Toward the correct calculation of van der Waals interactions between lyophobic colloids in an aqueous medium, *Journal of Colloid and Interface Science*, 37, 332-341.
- Peng, X.F., Peterson, G.P., and Wang, B.X. (1994), Frictional flow characteristics of water flowing through microchannels, *Experimental Heat Transfer*, 7 (4), 249–264.
- Peng, X.F., Peterson, G.P., and Wang, B.X. (1994), Heat transfer characteristics of water flowing through microchannels, *Experimental Heat Transfer*, 7 (10), 265–283.
- Peresin, M.S., Habibi, Y., Zoppe, J.O., Pawlak, J.J., and Rojas, O.J. (2010), Nanofiber composites of polyvinyl alcohol and cellulose nanocrystals: manufacture and characterization, *Biomacromolecules*, 11 (3), 674–681.
- Pinchuk, L.C., Goldade, V.A., Makarevich, A.V., and Kestelman, N.V. (2002), *Meltblowing Equipment Technology and Polymer Fibrous Materials*, Berlin, Springer.
- Podgórski, A., Balazy, A., and Gradon, L. (2006), Application of nanofibers to improve the filtration efficiency of the most penetrating aerosol particles in fibrous filters, *Chemical Engineering Science*, 61 (20), 6804-6815.
- Porter, M.C. (Editor) (1990), *Handbook of Industrial Membrane Technology*, Noyes Publications, New Jersey.
- Quinn, G., and Cetegen, B.M. (2010), Effect of surfactant addition on boiling heat transfer on a liquid film flowing in a diverging open channel, *International Journal of Heat and Mass Transfer*, 53, 245–253.
- Rainey, K.N., and You, S.M. (2000), Pool boiling heat transfer from plain and microporous, square pin-finned surfaces in saturated FC-72, *Journal of Heat Transfer*, 122 (3), 509-516.
- Rakov, E.G. (2006), *Chemistry of Carbon Nano Tubes*, Chapter 3, (Editor: Y. Gogotsi), Carbon Nanomaterials, Florida.
- Reneker, D.H., and Yarin, A.L. (2008), Electrospinning jets and polymer nanofibers, *Polymer*, 2008, 49 (10), 2387-2425.
- Reneker, D.H., Yarin, A.L., Fong, H., and Koombhongse, S. (2000), Bending instability of electrically charged liquid jets of polymer solutions in electrospinning, *Journal of Applied Physics*, 87 (9), 4531-4547.
- Rioboo, R., Marengo, M., Dall'Olio, S., Voué, M., and De Coninck, J. (2009), An innovative method to control the incipient flow boiling through grafted surfaces with chemical patterns, *Langmuir*, 25 (11), 6005-6009.

Rosenfeld, J.I. , Wasan, D.T. (1974), The London force contribution to the van der Waals force between a sphere and a cylinder, *Journal of Colloid Interface Science*, 47, 27-31.

Sabbah, R., Farid, M.M., and Al-Hallaj, S. (2009), Micro-channel heat sink with slurry of water with micro-encapsulated phase change material: 3D-numerical study, *Applied Thermal Engineering* 29 (2-3), 445–454.

Sahu, R.P., Sinha-Ray, Sumit, Sinha-Ray, Suman, and Yarin, A.L. (2015), Pool boiling on nano-textured surfaces comprised of electrically-assisted supersonically solution-blown, copper-plated nanofibers: experiments and theory, *International Journal of Heat and Mass Transfer*, 87, 521-535.

Sahu, R.P., Sinha-Ray, Sumit, Sinha-Ray, Suman, and Yarin, A.L. (2016), Pool boiling of novex 7300 and self-wetting fluids on electrically-assisted supersonically solution-blown, copper-plated nanofibers, *International Journal of Heat and Mass Transfer*, 95, 83-93.

Sathyanarayana, A., Warriar, P., Im, Y., Joshi, Y., and Teja, A.S. (2012), Pool boiling of HFE 7200–C4H4F6O mixture on hybrid micro-nanostructured surface, *Journal of Nanotechnology in Engineering and Medicine*, 3 (4), 041004.

Sharma, S.D., and Sagara, K. (2005), Latent heat storage materials and systems: A review, *International Journal of Green Energy*, 2, 1-56.

Shin, C., Chase, G.G., and Reneker, D.H. (2005), Recycled expanded polystyrene nanofibers applied in filter media, *Colloids and Surfaces A: Physicochemical Engineering Aspects*, 262 (1-3), 211-215.

Shin, M., Ishii, O., Sueda, T., and Vacanti, J. (2004), Contractile cardiac grafts using a novel nanofibrous mesh, *Biomaterials*, 25, 3717–3723.

Sikorski P., Atkins E.D.T. (2001), The three-dimensional structure of monodisperse 5-amide nylon 6 crystals in the λ -phase, *Macromolecules* 34, 4788-4794.

Silverman, I., Yarin, A.L., Reznik, S.N., Arenshtam, A., Kijet, D., and Nagler, A. (2006), High heat-flux accelerator targets: cooling with liquid metal jet impingement, *International Journal of Heat and Mass Transfer*, 49 (17-18), 2782-2792.

Sinha-Ray, Suman, Yarin, A.L., and Pourdeyhyimi, B. (2010a), The production of 100/400nm inner/outer diameter carbon tubes by solution blowing and carbonization of core–shell nanofibers, *Carbon*, 48 (12), 3575–3578.

Sinha-Ray, Suman, Yarin, A.L., and Pourdeyhyimi, B. (2010b), Meltblowing: I-basic physical mechanisms and threadline model, *Journal of Applied Physics*, 108 (3), 034912.

- Sinha-Ray, Suman, Zhang, Y., and Yarin, A.L. (2011a), Thorny devil nanotextured fibers: the way to cooling rates on the order of 1 kw/cm^2 , *Langmuir*, 27 (1), 215-226.
- Sinha-Ray, Suman, Zhang, Y., Yarin, A.L., Davis, S.C., and Pourdeyhimi, B. (2011b), Solution blowing of soy protein fibers, *Biomacromolecules*, 12 (6), 2357–2363.
- Sinha-Ray, Suman, Sahu, R.P., and Yarin, A.L. (2011c), Nano-encapsulated smart tunable phase change materials, *Soft Matter*, 2011, 7, 8823-8827.
- Sinha-Ray, Suman, Lee, M.W., Sinha-Ray, Sumit, An, S., Pourdeyhimi, B., Yoon, S.S., and Yarin, A.L. (2013), Supersonic nanoblowing: a new ultra-stiff phase of nylon 6 in 20–50 nm confinement, *Journal of Material Chemistry C*, 1, 3491-3498.
- Sinha-Ray, Sumit, Sinha-Ray, Suman, Sriram, H., and Yarin, A.L. (2014), Flow of suspensions of carbon nanotubes carrying phase change materials through microchannels and heat transfer enhancement, *Lab Chip*, 2014, 14, 494-508.
- Sinha-Ray, Suman, and Yarin, A.L. (2014a), Drop impact cooling enhancement on nano-textured surfaces. part I: theory and results of the ground (1g) experiments, *International Journal of Heat and Mass Transfer*, 70, 1095-1106.
- Sinha-Ray, Suman, Sinha-Ray, Sumit, Yarin, A.L., Weickgenannt, C.M., Emmert J., and Tropea, C. (2014b), drop impact cooling enhancement on nano-textured surfaces. part II: results of the parabolic flight experiments [zero gravity (0 g) and supergravity (1.8 g)], *International Journal of Heat and Mass Transfer*, 70, 1107-1114.
- Sinha-Ray, Sumit, Sinha-Ray, Suman, Pourdeyhimi, B., and Yarin, A.L. (2015a), Application of solution-blown 20-50 nm nanofibers in filtration of nanoparticles: the efficient van der Waals collectors, *Journal of Membrane Science*, 485, 132-150.
- Sinha-Ray, Sumit, Sinha-Ray, Suman, Yarin, A.L. and Pourdeyhimi, B. (2015b), Theoretical and experimental investigation of physical mechanisms responsible for polymer nanofiber formation in solution blowing, *Polymer*, 56, 452-463.
- Sinha-Ray, Sumit, Zhang, W., Sinha-Ray, Suman, Sahu, R.P. and Yarin A.L. (2017), Pool boiling of Novec 7300 and DI water on nano-textured heater covered with supersonically blown or electrospun polymer nanofibers, *International Journal of Heat and Mass Transfer*, <http://dx.doi.org/10.1016/j.ijheatmasstransfer.2016.08.101>
- Sokolsky-Papkov, M., Agashi, K., Olaye, A., Shakesheff, K., and Domb, A.J. (2007), Polymer carriers for drug delivery in tissue engineering, *Adv. Drug Deli. Reviews*, 59 (4-5), 187–206.
- Souza Lara Leão, H.L., do Nascimento, F.J., and Ribatski, G. (2014), Flow boiling heat transfer of R407C in a microchannels based heat spreader, *Experimental Thermal and Fluid Science*, 59, 140–151.

Srikar, R., Gambaryan-Roisman, T., Steffes, C., Stephan, P., Tropea, C., and Yarin, A. L. (2010), Nanofiber coating of surfaces for intensification of drop or spray impact cooling, *International Journal of Heat and Mass Transfer*, 52 (25), 5814-5826.

Strano, M.S., Miller, M.K., Allen, M.J., Moore, V.C., O'Connell, M.J., Kittrell, C., Hauge, R.H., and Smalley, R.E. (2003), The role of surfactant adsorption during ultrasonication in the dispersion of single-walled carbon nanotubes, *Journal Nanoscience and Nanotechnology*, 3 (1-2), 81-86.

Sun, Z., Gon, M., Qi, Y., Li, Z., and Wu, J. (2004), Nucleate pool boiling heat transfer of pure refrigerants and binary mixtures, *Journal of Thermal Science*, 13 (3), 259-263.

Tien, C.L. (1962), A hydrodynamic model for nucleate pool boiling, *International Journal of Heat and Mass Transfer*, 5 (6), 533-540.

Vaisman, L., Wagner, H.D., and Marom, G. (2006), The role of surfactants in dispersion of carbon nanotubes, *Advances in Colloids and Interface Science*, 128-130, 37-46.

Velraj, R., Seeniraj, R.V., Hafner, B., Faber, C., and Schwarzer, K. (1999), Heat transfer enhancement in a latent heat storage system, *Solar Energy*, 65 (3), 171–180.

Verreck, G., Chun, I., Rosenblatt, J., Peeters, J., Dijck, A.V., Mensch, J., Noppe M. , and Brewster, M. E. (2003), Incorporation of drugs in an amorphous state into electrospun nanofibers composed of a water-insoluble, nonbiodegradable polymer, *Journal of Controlled Release*, 92, 349–360.

Wang, C., and Otani, Y. (2013), Removal of nanoparticles from streams by fibrous filters: A review, *Industrial & Engineering Chemistry Research*, 52 (1), 5-17.

Wang, E.N., Zhang, L., Jiang, L., Koo, J.M., Maveety, J.G., Sanchez, E.A., Goodson, K.E., and Kenny, T.W. (2004), Micromachined jets for liquid impingement cooling of vlsi chips, , *Journal of Microelectromechanical Systems*, 13, 833 – 842.

Wang, J., and Pui, D.Y.H. (2013), Dispersion and filtration of carbon nanotubes (CNTs) and measurement of nanoparticle agglomerates in diesel exhaust, *Chemical Engineering Science*, 85, 69-76.

Wang, X., Niu, J., Li, Y., Wang, X., Chen, B., Zeng, R., Song , Q., and Zhang, Y. (2007), Flow and heat transfer behaviors of phase change material slurries in a horizontal circular tube, *International Journal of Heat and Mass Transfer*, 50, 2480-2491.

Wang, X., Chen, X., Yoon, K., Fang, D., Hsiao, B.S., and Chu, B. (2005), High flux filtration media based on substrate with hydrophilic nanocomposite coating, *Environmental Science and Technology*, 39, 7684-7691.

Webb, R.L., and Kim, N.H. (2005), Principles of Enhanced Heat Transfer, Second Ed., Taylor & Francis, New York, 389-391.

Weber, C. (1931), On the breakdown of a fluid jet, *Zeitschrift für Angewandte Mathematik und Mechanik* (Journal of Applied Mathematics and Mechanics), 11, 136-154.

Weickgenannt, C.M., Zhang, Y., Sinha-Ray, S., Roisman, I.V., Gambaryan-Roisman, T., Tropea C., and. Yarin, A. L. (2011), Inverse-leidenfrost phenomenon on nanofiber mats on hot surfaces, *Physical Review E*, 84, 036310.

Wen, D., and Dong, Y. (2005), Experimental investigation into the pool boiling heat transfer of aqueous based γ -alumina nanofluids, *Journal of Nanoparticle Research*, 7 (2), 265-274.

Whitaker, S. (1986), Flow in porous media I: A theoretical derivation of Darcy's law, *Transport in Porous Media*, 1 (1), 3-25.

Wu, S., Zhu, D., Zhang, X., and Huang, J. (2010), Preparation and melting/freezing characteristics of Cu/Paraffin nanofluid as phase-change material (PCM), *Energy Fuels*, 24, 1894-1898.

Xu, C., Inai, R., Kotaki, M., and Ramakrishna, S. (2004), Aligned biodegradable nanofibrous structure: a potential scaffold for blood vessel engineering, *Biomaterials*, 25 (5), 877-886.

Yang, W., Elankumaran, S., and Marr L.C. (2011), Concentrations and size distributions of airborne influenza A viruses measured indoors at a health centre, a day-care centre and on aeroplanes, *Journal of the Royal Society Interface*, 8 (61), 1176-1184.

Yarin, A.L. (1993), *Free Liquid Jets and Films: Hydrodynamics and Rheology*, Longman, Harlow and John Wiley & Sons, New York.

Yarin, A.L. (2007), Self-similarity, Section 2.3 in *Springer Handbook of Experimental Fluid Mechanics* (Eds: C. Tropea, A. L. Yarin, J. Foss), 57-82, Springer, Berlin.

Yarin, A.L. (1983), Detachment of the flame of a burning liquid by an air flow, *Combustion, Explosion and Shock Waves*, 19 (1), 1-8.

Yarin, A.L., Koombhongse, S., Reneker, and D.H. (2001), Bending instability in electrospinning of nanofibers, *Journal of Applied Physics*, 89 (5), 3018-3026.

Yarin, A.L., Pourdeyhimi, B., and Ramakrishna, S. (2014), *Fundamentals and applications of micro- and nanofibers*, Cambridge University Press, Cambridge.

Yarin, A.L., Sinha-Ray, S., and Pourdeyhimi, B. (2010), Meltblowing: II-linear and nonlinear waves on viscoelastic polymer jets, *Journal of Applied Physics*, 108 (3), 034913.

Yarin, A.L., Sinha-Ray, S., and Pourdeyhimi, B. (2011), Meltblowing: Multiple polymer jets and fiber-size distribution and lay-down patterns, *Polymer*, 2011, 52 (13), 2929-2938.

Yarin, L.P., Mosyak, A., and Hetsroni, G. (2009), *Fluid flow, heat transfer and boiling in micro-channels*, Springer, Berlin.

Yoshimoto, H. , Shin, Y.M., Terai, H., and Vacanti, J.P. (2003), A biodegradable nanofiber scaffold by electrospinning and its potential for bone tissue engineering, *Biomaterials*, 24, 2077–2082.

You, S.M., Kim, J.H., and Kim, K.H. (2003), Effect of nanoparticles on critical heat flux of water in pool boiling heat transfer, *Applied Physics Letters*, 83 (16), 3374-3376.

Zalba, B., Marin, J.M., Cabeza, L.F., and Mehling, H. (2003), Review on thermal energy storage with phase change: Materials, heat transfer analysis and applications, *Applied Thermal Engineering*, 23, 251-283.

Zeldovich, Ya.B., Barenblatt, G.I., Librovich, V.B., and Makhviladze, G.M. (1985), *The mathematical theory of combustion and explosions*, Consultants Bureau, New York.

Zhang, H.Y., Pinjala, D., Wong, T.N., Toh, K.C., and Joshi, Y.K. (2005), Single-phase liquid cooled microchannel heat sink for electronic packages, *Applied Thermal Engineering*, 25 (10), 1472–1487.

Zhang, L., Cecil, J., Vasquez, D., Jones, J., and Garner, B. (2006), Modeling of van der Waals forces during the assembly of micro devices, *Automation Science and Engineering*, in: CASE'06. IEEE International Conference, 484-489.

Zhang, L., Kopperstad, P., West, M., Hedin, N., and Fong, H. (2009), Generation of polymer ultrafine fibers through solution (air-) blowing, *Journal of Applied Polymer Science*, 114 (6), 3479–3486.

Zhang, Y., and Yarin, A.L., (2010), Thermo-responsive copolymer coatings for flow regulation on demand in glass microcapillaries, *European Physical Journal E*, 33 (3), 211-218.

Zhang, Y., Lee, M.W., An, S., Sinha-Ray, S., Khansari, S., Joshi, B., Hong, S., Hong, J.H., Kim, J.J., Pourdeyhimi, B., Yoon, S.S., and Yarin, A.L. (2013), Antibacterial activity of photocatalytic electrospun titania nanofiber mats and solution-blown soy protein nanofiber mats decorated with silver nanoparticles, *Catalysis Communications*, 2013, 34, 35-40.

Zhao, R., and Wadsworth, L.C. (2003), Study of polypropylene/poly(ethylene terephthalate) bicomponent melt-blowing process: The fiber temperature and elongational viscosity profiles of the spinline, *Journal of Applied Polymer and Science*, 43 (1), 1145-1150.

Zhu, Y., and Granick, S. (2001), Rate-dependent slip of newtonian liquid at smooth surfaces, *Physical Review Letter*, 87, 096105.

Zhuang, X., Shi, L., Jia, K., Cheng, B., and Kang, W. (2013), Solution blown nanofibrous membrane for microfiltration, *Journal of Membrane Science*, 429, 66-70.

Ziabicki, A. (1976), *Fundamentals of Fibre Formation*, Wiley, London.

Ziabicki, A., Kawai, H. (Editors) (1985). *High-speed Fiber Spinning*, Wiley, New York.

Zuber, N. (1961), Nucleate boiling: the region of isolated bubbles and the similarity with natural convection, *International Journal of Heat and Mass Transfer*, 6 (1), 53-78.

Zussman, E., Rittel, D., and Yarin, A.L. (2003), Failure modes of electrospun nanofibers, *Applied Physics Letter*, 82 (22), 3958-3960

CHAPTER 11

APPENDIX

The following are the statements from the Publisher granting permission to use previously published articles of the present author in this thesis. Permission granted by Royal Society of Chemistry addresses the work on supersonic solution blowing 2.1, 3.1, as well as 4.3 of Chapter 4; on nano-encapsulated phase change materials- sections 2.4, 3.4 and Chapter 7. These sections are reproduced by permission of Royal Society of Chemistry and the links of the papers are as follows:

<http://pubs.rsc.org/en/Content/ArticleLanding/2013/TC/c3tc30248b#!divAbstract>

<http://pubs.rsc.org/en/Content/ArticleLanding/2014/LC/C3LC50949D#!divAbstract>

Permission granted by ELSEVIER addresses the work on filtration of nanoparticles from sections 2.2, 3.2, and Chapter 5, and also the work on pool boiling from Sections 2.3, 3.3, subsection 6.2.3 and subsection 6.3.1 of Chapter 6 and sections 2.3, 3.3 and the rest of Chapter 6, as well as the work on solution blowing from sections 2.5, 3.5 and Chapter 8. These sections are reproduced by permission of Elsevier and the link of the papers is as follows:

<http://www.sciencedirect.com/science/article/pii/S0376738815001404>

<http://www.sciencedirect.com/science/article/pii/S0032386114010453>

<http://www.sciencedirect.com/science/article/pii/S0376738815001404>

<http://www.sciencedirect.com/science/article/pii/S0017931016316842>

Supersonic nanoblowing: a new ultra-stiff phase of nylon 6 in 20–50 nm confinement

S. Sinha-Ray, M. W. Lee, S. Sinha-Ray, S. An, B. Pourdeyhi, S. S. Yoon and A. L. Yarin, *J. Mater. Chem. C*, 2013, **1**, 3491

DOI: 10.1039/C3TC30248B

If you are not the author of this article and you wish to reproduce material from it in a third party non-RSC publication you must formally request permission using RightsLink. Go to our [Instructions for using RightsLink page](#) for details.

Authors contributing to RSC publications (journal articles, books or book chapters) do not need to formally request permission to reproduce material contained in this article provided that the correct acknowledgement is given with the reproduced material.

Reproduced material should be attributed as follows:

- For reproduction of material from NJC:
Reproduced from Ref. XX with permission from the Centre National de la Recherche Scientifique (CNRS) and The Royal Society of Chemistry.
- For reproduction of material from PCCP:
Reproduced from Ref. XX with permission from the PCCP Owner Societies.
- For reproduction of material from PPS:
Reproduced from Ref. XX with permission from the European Society for Photobiology, the European Photochemistry Association, and The Royal Society of Chemistry.

on?msid=c3lc50949d

Flow of suspensions of carbon nanotubes carrying phase change materials through microchannels and heat transfer enhancement

S. Sinha-Ray, S. Sinha-Ray, H. Sriram and A. L. Yarin, *Lab Chip*, 2014, **14**, 494


DOI: 10.1039/C3LC50949D

If you are not the author of this article and you wish to reproduce material from it in a third party non-RSC publication you must formally request permission using RightsLink. Go to our [Instructions for using RightsLink page](#) for details.

Authors contributing to RSC publications (journal articles, books or book chapters) do not need to formally request permission to reproduce material contained in this article provided that the correct acknowledgement is given with the reproduced material.

Reproduced material should be attributed as follows:

- For reproduction of material from NJC:
Reproduced from Ref. XX with permission from the Centre National de la Recherche Scientifique (CNRS) and The Royal Society of Chemistry.
- For reproduction of material from PCCP:
Reproduced from Ref. XX with permission from the PCCP Owner Societies.
- For reproduction of material from PPS:
Reproduced from Ref. XX with permission from the European Society for Photobiology, the European Photochemistry Association, and The Royal Society of Chemistry.

 **CONTRACTS-COPYRIGHT (shared)** <Contracts-Copyright@rsc.org> Aug 23 ☆ ↶ ↷
to me ▾

Dear Sumit,

The Royal Society of Chemistry (RSC) hereby grants permission for the use of your paper(s) specified below in the printed and microfilm version of your thesis. You may also make available the PDF version of your paper(s) that the RSC sent to the corresponding author(s) of your paper(s) upon publication of the paper(s) in the following ways: in your thesis via any website that your university may have for the deposition of theses, via your university's Intranet or via your own personal website. We are however unable to grant you permission to include the PDF version of the paper(s) on its own in your institutional repository. The Royal Society of Chemistry is a signatory to the STM Guidelines on Permissions (available on request).

Please note that if the material specified below or any part of it appears with credit or acknowledgement to a third party then you must also secure permission from that third party before reproducing that material.

Please ensure that the thesis states the following:

Reproduced by permission of The Royal Society of Chemistry

and include a link to the paper on the Royal Society of Chemistry's website.

Please ensure that your co-authors are aware that you are including the paper in your thesis.

Regards
Antonella

Antonella Tesoro
Customer Sales Support
Royal Society of Chemistry
Thomas Graham House,
Science Park, Milton Road,
Cambridge CB4 0WF
Tel: +44 (0) 1223 432 675
tesora@rsc.org

Main Reception Tel. +44 (0) 1223 42 0066
www.rsc.org

Winner of The Queen's Awards for Enterprise, International Trade 2013



DISCLAIMER:

This communication (including any attachments) is intended for the use of the addressee only and may contain confidential, privileged or copyright material. It may not be relied upon or disclosed to any other person without the consent of the Royal Society of Chemistry. If you have received it in error, please contact us immediately. Any advice given by the Royal Society of Chemistry has been carefully formulated but is necessarily based on the information available, and the Royal Society of

**ELSEVIER LICENSE
TERMS AND CONDITIONS**

Sep 08, 2016

This Agreement between Sumit Sinha Ray ("You") and Elsevier ("Elsevier") consists of your license details and the terms and conditions provided by Elsevier and Copyright Clearance Center.

License Number	3934421326590
License date	Aug 22, 2016
Licensed Content Publisher	Elsevier
Licensed Content Publication	Polymer
Licensed Content Title	Theoretical and experimental investigation of physical mechanisms responsible for polymer nanofiber formation in solution blowing
Licensed Content Author	Sumit Sinha-Ray,Suman Sinha-Ray,Alexander L. Yarin,Behnam Pourdeyhimi
Licensed Content Date	15 January 2015
Licensed Content Volume Number	56
Licensed Content Issue Number	n/a
Licensed Content Pages	12
Start Page	452
End Page	463
Type of Use	reuse in a thesis/dissertation
Portion	full article
Format	both print and electronic
Are you the author of this Elsevier article?	Yes
Will you be translating?	No
Order reference number	
Title of your thesis/dissertation	HEAT AND MASS TRANSFER ENHANCEMENT BY CARBON NANOTUBES AND SUPERSONICALLY-BLOWN NANOFIBERS
Expected completion date	Dec 2016
Estimated size (number of pages)	250
Elsevier VAT number	GB 494 6272 12
Requestor Location	Sumit Sinha Ray 842 W. Taylor Street 2039 Engineering Research Facility CHICAGO, IL 60607 United States Attn: Sumit Sinha Ray
Total	0.00 USD

[Terms and Conditions](#)

**ELSEVIER LICENSE
TERMS AND CONDITIONS**

Sep 08, 2016

This Agreement between Sumit Sinha Ray ("You") and Elsevier ("Elsevier") consists of your license details and the terms and conditions provided by Elsevier and Copyright Clearance Center.

License Number	3944330904161
License date	Sep 08, 2016
Licensed Content Publisher	Elsevier
Licensed Content Publication	Journal of Membrane Science
Licensed Content Title	Application of solution-blown 20–50nm nanofibers in filtration of nanoparticles: The efficient van der Waals collectors
Licensed Content Author	Sumit Sinha-Ray,Suman Sinha-Ray,Alexander L. Yarin,Behnam Pourdeyhimi
Licensed Content Date	1 July 2015
Licensed Content Volume Number	485
Licensed Content Issue Number	n/a
Licensed Content Pages	19
Start Page	132
End Page	150
Type of Use	reuse in a thesis/dissertation
Portion	full article
Format	both print and electronic
Are you the author of this Elsevier article?	Yes
Will you be translating?	No
Order reference number	
Title of your thesis/dissertation	HEAT AND MASS TRANSFER ENHANCEMENT BY CARBON NANOTUBES AND SUPERSONICALLY-BLOWN NANOFIBERS
Expected completion date	Dec 2016
Estimated size (number of pages)	250
Elsevier VAT number	GB 494 6272 12
Requestor Location	Sumit Sinha Ray 842 W. Taylor Street 2039 Engineering Research Facility CHICAGO, IL 60607 United States Attn: Sumit Sinha Ray
Total	0.00 USD

ELSEVIER LICENSE TERMS AND CONDITIONS

Sep 08, 2016

This Agreement between Sumit Sinha Ray ("You") and Elsevier ("Elsevier") consists of your license details and the terms and conditions provided by Elsevier and Copyright Clearance Center.

License Number	3944331212510
License date	Sep 08, 2016
Licensed Content Publisher	Elsevier
Licensed Content Publication	International Journal of Heat and Mass Transfer
Licensed Content Title	Pool boiling of Novec 7300 and self-rewetting fluids on electrically-assisted supersonically solution-blown, copper-plated nanofibers
Licensed Content Author	Rakesh P. Sahu,Sumit Sinha-Ray,Suman Sinha-Ray,Alexander L. Yarin
Licensed Content Date	April 2016
Licensed Content Volume Number	95
Licensed Content Issue Number	n/a
Licensed Content Pages	11
Start Page	83
End Page	93
Type of Use	reuse in a thesis/dissertation
Portion	figures/tables/illustrations
Number of figures/tables/illustrations	6
Format	both print and electronic
Are you the author of this Elsevier article?	Yes
Will you be translating?	No
Order reference number	
Original figure numbers	Figures 2,3,7
Title of your thesis/dissertation	HEAT AND MASS TRANSFER ENHANCEMENT BY CARBON NANOTUBES AND SUPERSONICALLY-BLOWN NANOFIBERS
Expected completion date	Dec 2016
Estimated size (number of pages)	250
Elsevier VAT number	GB 494 6272 12
Requestor Location	Sumit Sinha Ray 842 W. Taylor Street 2039 Engineering Research Facility CHICAGO, IL 60607 United States Attn: Sumit Sinha Ray
Total	0.00 USD
Terms and Conditions	



RightsLink®

[Account Info](#)
[Help](#)


Title: Pool boiling of Novec 7300 and DI water on nano-textured heater covered with supersonically-blown or electrospun polymer nanofibers

Author: Sumit Sinha-Ray, Wenshuo Zhang, Rakesh P. Sahu, Suman Sinha-Ray, Alexander L. Yarin

Publication: International Journal of Heat and Mass Transfer

Publisher: Elsevier

Date: Dec 31, 1969

Copyright © 1969, Elsevier

Logged in as:
Sumit Sinha Ray
Account #: 3001056526

[LOGOUT](#)

Order Completed

Thank you for your order.

This Agreement between Sumit Sinha Ray ("You") and Elsevier ("Elsevier") consists of your order details and the terms and conditions provided by Elsevier and Copyright Clearance Center.

License number	Reference confirmation email for license number
License date	Sep 11, 2016
Licensed Content Publisher	Elsevier
Licensed Content Publication	International Journal of Heat and Mass Transfer
Licensed Content Title	Pool boiling of Novec 7300 and DI water on nano-textured heater covered with supersonically-blown or electrospun polymer nanofibers
Licensed Content Author	Sumit Sinha-Ray, Wenshuo Zhang, Rakesh P. Sahu, Suman Sinha-Ray, Alexander L. Yarin
Licensed Content Date	Available online 9 September 2016
Licensed Content Volume	n/a
Licensed Content Issue	n/a
Licensed Content Pages	1
Type of Use	reuse in a thesis/dissertation
Portion	full article
Format	both print and electronic
Are you the author of this Elsevier article?	Yes
Will you be translating?	No
Order reference number	
Title of your thesis/dissertation	HEAT AND MASS TRANSFER ENHANCEMENT BY CARBON NANOTUBES AND SUPERSONICALLY-BLOWN NANOFIBERS
Expected completion date	Dec 2016
Estimated size (number of pages)	250
Elsevier VAT number	GB 494 6272 12
Requestor Location	Sumit Sinha Ray 842 W. Taylor Street 2039 Engineering Research Facility CHICAGO, IL 60607 United States Attn: Sumit Sinha Ray
Billing Type	Invoice
Billing address	Sumit Sinha Ray 842 W Taylor St 2039 ERF Department of Mechanical and Industrial Engineering Chicago, IL 60607 United States Attn: Sumit Sinha Ray
Total	0.00 USD

CHAPTER 12

CURRICULUM VITAE

SUMIT SINHA RAY

Department of Mechanical and Industrial Engineering University of Illinois at Chicago (UIC)
842 West Taylor Street, M/C 251, Room 2039ERF Chicago, Illinois 60607-7022
Tel: (312) 714-3910 Fax: (312) 413-0447
ssinha20@uic.edu

Research Interests

Experimental and Theoretical Thermal-Fluid Sciences at the Micro/Nanoscale, Characteristics and new methodologies of manufacturing Nonwoven Micro/Nanofiber Mat, Bio-materials, Optical and Thermal Material Characterization Techniques, Super Capacitors, Water Purification and Filtration, Experimental and Theoretical Study of Production Methods of Nonwovens.

Education

Doctoral Candidate, Mechanical and Industrial Engineering, University of Illinois at Chicago, Chicago Illinois, Jan 2012-present.

Advisor: Prof. Alexander L. Yarin. GPA: 3.91/4.0

B.S., Metallurgical Engineering, Jadavpur University, Kolkata, India, May, 2011 GPA: 7.78/10.

Teaching Experience

Teaching Assistant

- Introduction to Thermodynamics (ME 205), Fall 2012- Graded students' performances of class and held regular office hours.
- Fluid mechanics I (ME 211), Spring 2014, Spring 2015- Conducted and coordinated laboratory experiments and held regular problem solving sessions. Graded students' performances of class.
- Air Pollution Engineering (ME 450) Spring 2016- Graded students' performances of class and held regular office hours.

Professional Experience

University of Illinois at Chicago – IL

- Teaching Assistant, 2012,2014, 2015.
- Research Assistant, 2012-13, 2015-Present.

PUBLISHED WORK

- Suman Sinha-Ray, Min Wook Lee, Sumit Sinha-Ray, Seongpil An, Behnam Pourdeyhimi, Sam S. Yoon and Alexander L. Yarin, Supersonic nanoblowing: a new ultra-stiff phase of nylon 6 in 20–50 nm confinement, *Journal of Material Chemistry C*, 2013, 1, 3491.
- Sumit Sinha-Ray, Suman Sinha-Ray, Hari Sriram, Alexander L. Yarin, Flow of

- suspensions of carbon nanotubes carrying phase change materials through microchannels and heat transfer enhancement, *Lab Chip*, 2014, 14, 494-508 (This article was chosen as 'Hot Article' on *Lab on a Chip*).
- Suman Sinha-Ray, Sumit Sinha-Ray, Alexander L. Yarina, Christina M. Weickgenannt, Johannes Emmert, Cameron Tropea, Drop impact cooling enhancement on nano-textured surfaces. part ii: results of the parabolic flight experiments [zero gravity (0 g) and supergravity (1.8 g)], *International Journal of Heat and Mass Transfer*, 2014, 70, 1107-1114. (Widely covered in UIC NEWS and CNN UK)
 - Sumit Sinha-Ray, Suman Sinha-Ray, Alexander L Yarin, Behnam Pourdeyhimi, Application of solution-blown 20–50nm nanofibers in filtration of nanoparticles: The efficient van der Waals collectors, *Journal of Membrane Science*, 2015, 485, 132-150.
 - Sumit Sinha-Ray, Suman Sinha-Ray, Alexander L Yarin, Behnam Pourdeyhimi, Theoretical and experimental investigation of physical mechanisms responsible for polymer nanofiber formation in solution blowing, *Polymer*, 2015, 56, 452-463.
 - Rakesh P Sahu, Sumit Sinha-Ray, Suman Sinha-Ray, Alexander L Yarin, Pool boiling on nano-textured surfaces comprised of electrically-assisted supersonically solution-blown, copper-plated nanofibers: Experiments and theory, *International Journal of Heat and Mass Transfer*, 2015, 87, 521-535.
 - Martin Freystein, Felix Kolberg, Lucas Spiegel, Sumit Sinha-Ray, Rakesh P. Sahu, Alexander L. Yarin, Tatiana Gambaryan-Roisman, Peter Stephan, Trains of Taylor bubbles over hot nano-textured mini-channel surface, *International Journal of Heat and Mass Transfer*, 2016, 93, 827-833.
 - Rakesh P. Sahu, Sumit Sinha-Ray, Suman Sinha-Ray, Alexander L. Yarin, Pool Boiling of Novec 7300 and Self-Rewetting Fluids on Electrically-Assisted Supersonically Solution-Blown, Copper-Plated Nanofibers, *International Journal of Heat and Mass Transfer*, 2016, 95, 83-93.
 - Viral K. Patel, Jamal Seyed-Yagoobi, Suman Sinha-Ray, Sumit Sinha-Ray, Alexander L. Yarin, EHD conduction pumping driven liquid film flow boiling on bare- and nanofiber-enhanced surfaces, *Journal of Heat Transfer*, 2016, 138(4), 041501-07.
 - Spela Zupancic, Sumit Sinha-Ray, Suman Sinha-Ray, Julijana Kristl, Alexander L Yarin, Long-term Sustained Ciprofloxacin Release from PMMA and Hydrophilic Polymer Blended Nanofibers, *Molecular Pharmaceutics*, 2016, 13 (1), 295–305.
 - Spela Zupancic, Sumit Sinha-Ray, Suman Sinha-Ray, Julijana Kristl, Alexander L Yarin, Controlled Release of Ciprofloxacin from Core-shell Nanofibers with Monolithic or Blended Core, *Molecular Pharmaceutics*, 2016, 13 (4), 1393–1404.
 - Sumit Sinha-Ray, Wenshuo Zhang, Rakesh P. Sahu, Suman Sinha-Ray, Alexander L. Yarin, Pool boiling of Novec 7300 and DI water on nano-textured heater covered with supersonically blown or electrospun polymer nanofibers, *International Journal of Heat and Mass Transfer* (<http://dx.doi.org/10.1016/j.ijheatmasstransfer.2016.08.101>)

Academic Achievement

- Scholarship from Govt. of India for all India ranking 68 in GATE 2011 (Entrance examination for Masters' Studies in Indian Institute of Technology).

- Ranked 30th out of 0.5 million (approx.) students and 3rd out of 102 students in school in state level examination for high school.
- Ranked 72nd out of 0.6 million (approx.) students in state level examination for 10th grade.
- Received honorarium for scoring perfect marks in mathematics in high school level in state examination.

Awards and Honors

- Awarded with **Litvin Graduate Honor Award** (2014) in recognition of academic achievement and service to the department and graduate student community.
- Awarded with **Best Technical Merit Award** (2015) by The Nonwovens Institute in NCRC-IAB consortium.
- Travel award for one of best selected poster presentation at INDA-IDEA(2013, Miami) conference.
- Honorarium for scoring perfect score in mathematics from WB State Board.
- Two time inter-school debate champion, one time inter-school recitation champion and several times won prizes for debate, recitation and writing competitions in school level.

BS Students Mentored

- Hari Sriram – Summer 2012
- Nicholas McCartney – Fall 2013
- Mustafa Wahid– Spring 2014
- Chris Staszal- Spring 2014
- Barak Stoltz- Summer 2015- Till Date
- Christopher Kim- Spring 2015

Computational Skills

FORTRAN, MATLAB, Origin Pro.

Characterization Skills

- Scanning Electron Microscopy.
- Transmission Electron Microscopy.
- Atomic Absorption Spectroscopy.

Extracurricular Activities

- Active member of the MIE Graduate Student Council: Spring 2012-Present.
- Was an active member of Indian Institute of Metals (Kolkata Chapter) during undergraduate studies.
- Was an active member of NSS (National Social Service, India) during High School studies.
- Was chief editor of little magazine “Pratyoy”(Determination) in school.